Clay Templated Semiconductor Hybrids for (Photo)catalytic Wastewater Remediation

Thesis Submitted for
the Fulfilment of the Degree

Doctor rerum Naturalium
(Dr. rer. nat.)

by

Sanjay Jatav

Universität Hamburg
DER FORSCHUNG | DER LEHRE | DER BILDUNG

to
Institute of Physical Chemistry
University of Hamburg

Hamburg
March 2023

to Aayush, who'll forever live in our memories....

Reviewers of Dissertation:	Prof. Dr. Alf Mews
	Dr. Eric H. Hill
Reviewers of Disputation:	Prof. Dr. Alf Mews
	Prof. Dr. Michael Fröba
	Dr. Tobias Vossmeyer
Date of Disputation:	26.05.2023

This dissertation was carried out from November 2018 to March 2023 in Hamburg.

List of Publications

Published during PhD.

First author publications

1. Jatav, S.; Xiang H.; Herber, M.; Paineau E.; Hill, E. H. In_2S_3 Growth Templated by Aluminogermanate Nanotubes towards Efficient Visible Light Photocatalysts. *Solar RRL*, **2023**, 7 (4), 2200947. (IF: 8.582)
2. Jatav, S.; Herber, M.; Xiang H.; Hill, E. H. Layered Double Hydroxide-Bismuth Molybdate Hybrids toward Water Remediation via Selective Adsorption of Anionic Species. *ACS Applied Materials & Interfaces.* **2022**, 14 (46), 51921-51930. (IF: 9.229)
3. Jatav, S.; Kao, M. C.; Graf M.; Hill, E. H. Colloidal growth of titania in nanoporous gold toward electrochemical applications. *Colloids and Surfaces A: Physicochemical and Engineering Aspects.* **2022**, 651, 129700. (IF: 5.518)
4. Jatav, S.; Herber, M.; Xiang H.; Hill, E. H. Surface-Encapsulated Bismuth Molybdate-Layered Silicate Hybrids as Sorbents for Photocatalytic Filtration Membranes. *ACS Applied Materials & Interfaces.* **2022**, 14 (20), 22790-22798. (IF: 9.229)
5. Jatav, S.; Liu, J.; Herber, M.; Hill, E. H. Facet Engineering of Bismuth Molybdate via Confined Growth in a Nanoscale Template toward Water Remediation. *ACS Applied Materials & Interfaces.* **2021**, 13(16), 18713-18723. (IF: 10.383)
6. Jatav, S.; Furlan, K. P.; Liu, J.; Hill, E. H. Heterostructured Monolayer MoS_2 Nanoparticles toward Water-Dispersible Catalysts. *ACS Applied Materials & Interfaces.* **2020**, 12(17), 19813-19822. (IF:9.229)

Publications as a contributing author

1. Liu, J.; Jatav, S; Hill, E. H. Templating Unidirectional Bismuth Oxyiodide Crystal Growth with Layered Silicates for Enhanced Photocatal-

ysis. *The Journal of Physical Chemistry C.* **2022**, 126(10), 4975-4983.

2. Liu, J.; Jatav, S; Herber, M.; Hill, E. H. Few-Layer $ZnIn_2S_4$/Laponite Heterostructures: Role of Mg^{2+} Leaching in Zn Defect Formation. *Langmuir.* **2021**, 37(15), 4727-4735.

3. Liu, J.; Jatav, S; Hill, E. H. Few-layer In_2S_3 in Laponite Interlayers: A Colloidal Route Toward Heterostructured Nanohybrids with Enhanced Photocatalysis. *Chemistry of Materials.* **2020**, 32 (23), 10015-10024.

Previous publications

1. Suresh, G.; Jatav, S.; Mallikarjunachari, G.; Rao, M. R.; Ghosh, P.; Satapathy, D. K. Influence of Microstructure on the Nanomechanical Properties of Polymorphic Phases of Poly(vinylidene fluoride). *Journal of Physical Chemistry B.* **2018**, 122(36), 8591-8600

2. Suresh, G.; Jatav, S.; Geethu, P. M.; Rephung, Y.; Ramachandra Rao, M. S.; Satapathy, D. K. Poly(vinylidene fluoride)– Formvar blends: Dielectric, Miscibility and Mechanical studies". *Journal of Physics D: Applied Physics.* **2018**, 51(6), 065604

3. Suresh, G.; Mallikarjunachari, G.; Jatav, S.; Thirmal, C.; Ramachandra Rao, M. S.; Satapathy, D. K. Evolution of Morphology, Ferroelectric and Mechanical Properties in Poly(vinylidene fluoride) – Poly(vinylidene fluoride-trifluoroethylene) Blends. *Journal of Applied Polymer Science.* **2018** ,(10), 45955

4. Suresh, G.; Jatav, S.; Ramachandra Rao, M. S.; Satapathy, D. K. Enhancement of Dielectric and Ferroelectric Properties in Cobalt Ferrite doped Poly(vinylidene fluoride) Multiferroic Polymer Composites". *Materials Research Express.* **2017**, 4(7), 075301

ABSTRACT

The inability to cease the steady drip of pollutants into the biosphere has led to the breaching of the "planetary boundary" for chemical pollution. This thesis aimed at exploiting the rich chemistry of clays to synthesize semiconductor hybrid materials and study their viability toward water decontamination. By carefully controlling the growth of metal sulphides and oxides (MoS_2, In_2S_3 and Bi_2MoO_6) on the different clays, hybrids with enhanced (photo)catalytic and adsorption capabilities were obtained. In the laponite-MoS_2 and imogolite-In_2S_3 nanohybrids, the clay-substrates were able to enhance the functional property (catalysis and photocatalysis, respectively) of the over-grown semiconductor, whereas Bi_2MoO_6 growth onto the clays (laponite and CoAl layered double hydroxide) resulted in improving the adsorptivity of the underlying clay substrates, in addition to rendering these clay-Bi_2MoO_6 hybrids photocatalytic.

The improvement in the functional performance of these hybrids was concomitant with changes in the semiconductor growth and morphology; which in turn were affected by the introduction of clays. For instance, in laponite-MoS_2 and imogolite-In_2S_3 hybrids, the clays confined and curtailed growth of MoS_2 and In_2S_3 crystals, respectively. Laponite, however, altered the default crystal growth habit of Bi_2MoO_6 and resulted in the formation of faceted single-crystal particles. Interestingly, these improvements in the performance of the semiconductor-clay hybrids were contingent upon the organic modification of the clays. Since clays are abundant and the syntheses were carried out in aqueous medium this work demonstrates that high performance hybrid materials can be obtained by environmentally benign means.

Keywords: environmental remediation; water decontamination; adsorption; (photo)catalysis; confined-growth; surface engineering; clay-based hybrids

Zusammenfassung

Das Ausbleiben eines stetigen Eintrags von Schadstoffen in die Biosphäre hat dazu geführt, dass die “planetarische Grenze” für chemische Verschmutzung überschritten wurde. Ziel dieser Arbeit war es, die vielseitige Chemie von Tonen, sogenannte clays, zu nutzen, um Halbleiter-Hybridmaterialien zu synthetisieren und ihre Eignung zur Wasserdekontaminierung zu untersuchen. Durch sorgfältige Kontrolle des Wachstums von Metallsulfiden und -oxiden (MoS_2, In_2S_3 and Bi_2MoO_6) auf den verschiedenen clays wurden Hybride mit verbesserten (photo)katalytischen und adsorptiven Fähigkeiten erhalten. Bei den laponite-MoS_2 and imogolite-In_2S_3 Nanohybriden konnten die clay-Substrate die funktionellen Eigenschaften (Katalyse bzw. Photokatalyse) des aufgewachsenen Halbleiters verbessern, während das Wachstum von Bi_2MoO_6 auf clay (Laponit und CoAl-Doppelschichthydroxid) zu einer Verbesserung der Adsorptionsfähigkeit der darunter liegenden clay-Substrate führte und diese clay-Bi_2MoO_6-Hybride zusätzlich photokatalytisch aktiv waren.

Die Verbesserung der funktionellen Leistung dieser Hybride ging mit einer Veränderungen des Halbleiterwachstums und der Morphologie einher, die ihrerseits durch die Einführung von clays beeinflusst wurden. Zum Beispiel hat der clay in laponit- MoS_2- und imogolith-In_2S_3-Hybriden zu einem eingeschränkten und verkürzten Wachstum von MoS_2- bzw. In_2S_3-Kristallen geführt. Laponit hingegen veränderte das ursprüngliche Kristallwachstum von Bi_2MoO_6 und führte zur Bildung facettierter einkristalliner Partikel. Interessant ist, dass die Verbesserungen der Leistung der Halbleiter-clay-Hybride von der organischen Modifikation der eingesetzten clays abhängig waren. Diese Arbeit zeigt, dass hochleistungsfähige Hybridmaterialien mit umweltfreundlichen Mitteln hergestellt werden können, da clays reichlich vorhanden sind und die Synthesen in wässrigem Medium stattfinden.

Keywords: environmental remediation; water decontamination; adsorption; (photo)catalysis; confined-growth; surface engineering; clay-based hybrids

Contents

List of Figures

Chapter 1

Introduction

The primary thrust of this thesis was to use surfactant-modified clays to template the growth of semiconductor photocatalysts and study their (photo)catalytic performance. These high-performance clay-semiconductor hybrid materials were then tested for their efficacy toward decontamination of water polluted with molecular species. This chapter is intended to provide a concise background to the problem of pollution, its scale and consequences for our species. In addition, the basics of semiconductor photocatalysis are presented and the materials used herein for the purpose of water decontamination are also reviewed. The discussion presented in this chapter also serves as the motivation for this oeuvre.

1.1 The Contamination of the Earth

Pollution: An Entropic Perspective

The human industrial economy represents a sub-system which functions within the confines of a larger biophysical system of the biosphere. From the Figure 1.1 it can be seen that energy and matter can flow into and out of the human economic sphere (or sub-system) making it an open system with regard to both energy and matter. However, the biosphere is materially closed since matter cannot enter or leave this system, but energy can easily flow into and out of this system. The human economy functions by obtaining raw materials or natural resource as inputs from the biosphere. These are transformed by manufacturing processes into usable commodities, which at a later stage are expelled in the environment for assimilation or decomposition. Since human activities are not exempt from the laws of thermodynamics, a grasp of these principles becomes essential for understanding the fundamental cause(s) of pollution.

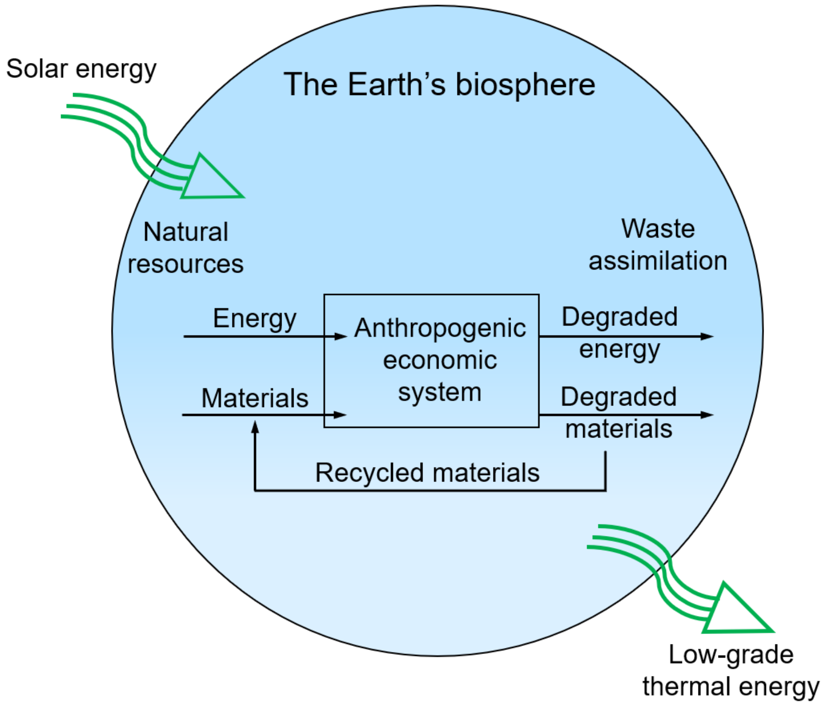

Figure 1.1: Material and energy flow pertaining to anthropogenic economic system.

The law that concerns us the most is the second law of thermodynamics, also known as the entropy law. Entropy is formally defined as heat exchanged and transferred at a given temperature, but for the purpose of our discussion it can be assumed as a reliable measure of the *disorderliness* of a system. The entropy law maintains that the entropy of any isolated system or by extension that of the universe, increases persistently and irrevocably.[1] Hence, all the anthropogenic activities by the virtue of the entropy law, transform low entropy matter (natural resources) into high entropy matter or waste (Figure

1.1). Since, all the physical and material processes are subject to the entropy law this implies that the end product of all the anthropogenic industrial activities is high-entropy waste (waste heat or residues etc.).[2] Therefore, any growth in the economic activity is bound to increase the quantity of high entropy matter or waste generated and thus, expelled into the environmental sink for assimilation. Hence, the scale of pollutions grows in tandem with innovations in the human enterprise.[3] Anthropogenic pollution becomes a concern when the amount and nature of high-entropy waste thus generated cannot be assimilated by the biosphere. This is a grave problem because an organism cannot live in a medium of its own waste-products.[4]

Scale of Contamination

An understanding of the scale and extent of a problem is essential for framing or implementing effective intervention measures. The scale of anthropogenic contamination, in the context of our discussion, can be best understood by looking at the concept of planetary boundaries proposed by Rockström and colleagues.[5] The authors defined 9 different boundaries pertaining to the self-regulating biophysical capacity of the planet (Figure 1.2). The simple idea being that crossing any of these thresholds would undermine the ability of our planet to regulate and maintain the conditions responsible for the existence of complex lifeforms on earth (especially the stable climatic conditions that have persisted since past $\sim$ 10,000 years [6]). The planetary boundary that interests us the most is the one pertaining to chemical pollution/ novel entities. Rockström et al. deemed that the unchecked release of chemicals or novel entities can disrupt the regulatory feedback of the planet. A good example would be the anthropogenic emission of greenhouse gases responsible for climate change.[7]

In a 2022 study, Persson and colleagues quantified the above-mentioned planetary boundary and concluded that the chemical pollution planetary boundary has been breached.[8] The primary reason they cited was the high rate of production of novel chemicals and ineffective screening protocols for assessing these chemicals. In other words, the dams constructed to safeguard public health against chemical substances during the last century are rendered largely ineffective against the 21st century chemical deluge. Taking the example of European Union REACH (Registration, Evaluation, Authorization and Restriction of Chemicals) for instance, one finds $\sim$23,000

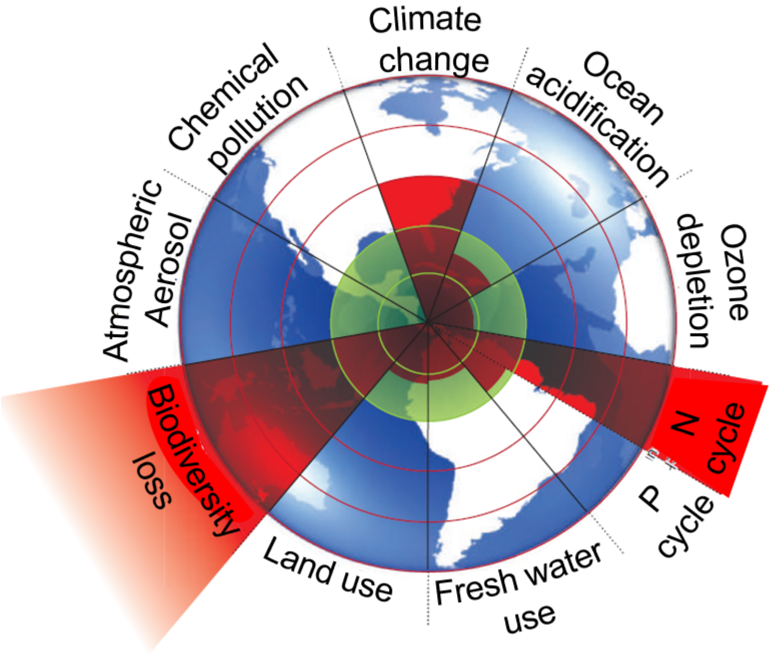

Figure 1.2: Planetary boundaries concept. The green region corresponds to the safe operating space for human activities. Whereas the red color represents present scale of human activities. This figure is adapted from ref [5].

chemicals substances registered as of December 2020 with the agency. Over 12,000 among them were registered as nonintermediates (intermediates have reduced safety data requirements), of which 2,400 chemicals have been or are being evaluated and assessed. Ergo, even in this small space, close to 10,000 substances (80%) are still waiting to be examined after more than 10 years of functioning of REACH. (Never mind that there are more than 350,000 different chemicals registered for commercial use, globally[9])!

Let us now look at the on-ground implication of breaching the chemical pollution planetary boundary. The magnitude of anthropogenic chemical discharge is estimated to be in excess of 200 billion tons per year; only a fifth of which is due to greenhouse gas emissions.[10] Many of these chemical substances can migrate great distance either via waterways or through atmosphere.[11] As a consequence, many pollutants like plastics and PFAS can be found in unforgiving geographies ranging from the summit of Mt

Everest,[12] which lies at 8,440 m above sea level to Marianas Trench lying at a depth of 10,898 m below sea level.[13] Over-reliance on plastic products has also resulted in a situation where now in some regions of ocean plastic outweighs plankton by 36:1 by weight.[14, 15] Due to their ubiquity these chemical pollutants have now penetrated most of the marine and terrestrial food webs.[16] Apart from there ubiquity on land, persistent organic chemicals like PFAS are now a common constituent of rainwater all over the globe.[17]

Costs borne by humanity

From the above discussion it is clear that the entire earth is straddled with waste generated by human activities, and as a result the human habitat and enclaves have not remained unscathed from its effects. Consequently, the chemical contamination of the human habitat has been implicated in reproductive, cognitive, and developmental disorders as well as premature deaths.[18] The costs borne by our species can be roughly divided into two categories. First, the effects due to direct exposure to these pollutants, for example by consuming food laden with toxins, exposure to toxic vapors at workplace etc. and second, the damage done to the environment or other species which are crucial for sustaining the complex functions of biosphere. Examples of the latter are, decline in the population of plankton (which form the basis of marine life) threatens the collapse of underwater ecosystem and the decimation of bee population due to profligate pesticide usage, which threatens global food security.[19] For the sake of brevity and due to the limitation of space only the first category would be discussed here.

These industrial chemicals, including many known carcinogens and their residues, have been detected in all human populations, including the fetus and infants,[20, 21] and in mothers milk.[22, 23] It was also reported that the human body is now host to around 700 different kinds of anthropogenic chemicals.[24] But the pregnant women and infants are especially vulnerable to the effects of these chemicals. It was assumed for the longest of times that the developing fetus were immune from the effects of pollutants in the mother's body and that the placenta worked as a shield against these chemical intruders. But recent studies have found otherwise.[20] In many cases the effects are felt most drastically by the developing fetus.[25] For instance a class of chemicals can act as teratogens and alter the morphology of the developing fetus.[26] Apart from such tangible effects many chemical pollutants act in a much more pernicious manner. For instance they've been implicated in the serious decline in male fertility recorded in the developed world for the past half century and affecting sexual orientation in humans.[27, 28]. Since pharmaceuticals are being routinely detected in water bodies, the immunity of our species is also being jeopardized by the emergence of antibiotic-resistant strain of microorganisms in the environment.[29]

1.2 Photocatalysis: A Short Introduction

Since most of the semiconductors explored in this thesis were used as photocatalysts to degrade the model pollutants, this section discusses the fundamental principles of semiconductor photocatalysis and presents a brief historical account of the advancements in the design of these photocatalysts. From an application point of view, photocatalysis presents a low cost and environmentally benign means for decontaminating water polluted with synthetic organic moieties.[30] Its primary advantage being the possibility to utilize solar energy to bring about the degradation of organic molecules and transform them into less toxic products.

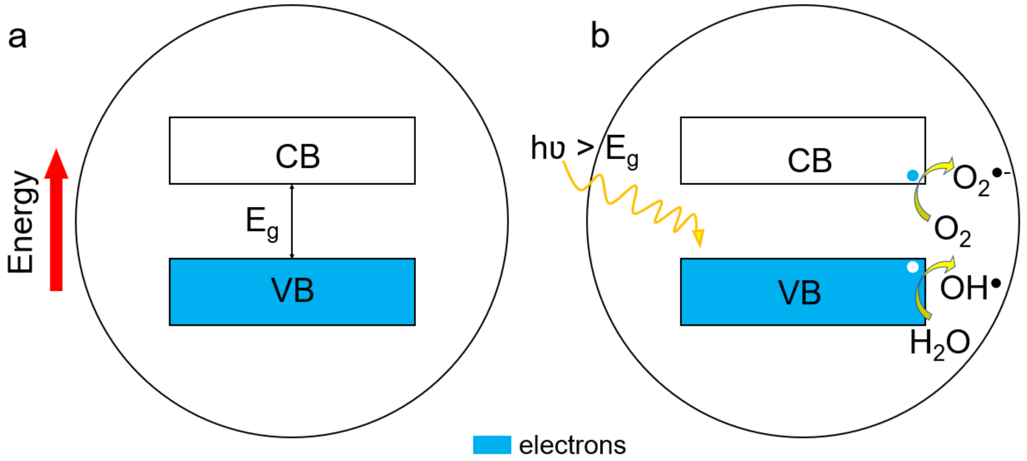

Figure 1.3: Semiconductor photocatalyst (a) band structure, (b) mechanism of photocatalytic action.

Semiconductors are characterized by the presence of an energy band gap, which is the measure of the energy difference between the top of valence band (VB) and the bottom of the conduction band (CB). The electronic bands or bands refer to the energy states within a material which are densely populated with electrons.[31] The VB represents the highest occupied energy band which is separated by an energy bandgap from the CB, the lowest unoccupied energy band (Figure 1.3a). The bandgap between these two energy bands refers to the energy states that cannot be populated by the electrons. The photocatalytic process in a semiconductor is comprised of the following steps: charge generation upon illumination, charge separation, migration of these charges to the surface of the photocatalyst and reaction with the target species.

The electrons in the VB can be excited across the bandgap to CB by optically illuminating the semiconductor with radiation having energy greater than the bandgap. The electrons and holes thus generated by the optical excitation, in the CB and VB, respectively, can be used for carrying out chemical reactions and hence function as photocatalyst. For instance, if the bandgap of a semiconductor straddles the redox potential for water oxidation and reduction, it can be used for splitting water directly into hydrogen and oxygen. Another application where semiconductor photocatalysts find use is the degradation of organic pollutants. When used in aqueous dispersion, the photogenerated charges in the semiconductor can react with dissolved molecular species in water and form reactive species like superoxide anion radical or hydroxyl radicals (Figure 1.3b), which are much better oxidants compared to conventional ones like ozone. Depending on the redox potential of the different functional groups present on the target pollutant, these radicals can result in complete mineralization of the organic contaminants into CO_2 and water.[32]

The one of the first photocatalyst that could degrade organic molecules was reported by Müller and Steinbach in 1969. They tested the efficacy of ZnO for photodegradation of isopropanol under UV light.[33] Subsequently, under similar conditions of UV irradiation, Carey et al were able to achieve photodechlorination of different polychlorinated biphenyls (PCB) in the aqueous suspension of TiO_2.[34] Since, the UV radiation covers only 5% of the entire solar spectrum, the practical use of these semiconductors was thus limited. Hence, further developments focused on harvesting light from the visible region of solar spectrum. For extending the light absorption of these semiconductor photocatalysts various strategies were employed. In the case of TiO_2, for instance, sensitization with dye molecules like eosin allowed Heleg and Willner to extend the photocatalytic action of TiO_2 in to visible region.[35] Also doping with metallic and non-metallic elements can narrow the bandgap, making visible light absorption feasible.[36, 37]

Another issue plaguing the widespread application of semiconductor photocatalysts has been the recombination of charges after their photo-excitation. Although having a narrow bandgap allows for greater light absorption, the reduced bandgap also leads to greater instances of charge recombination. To tackle this bottleneck researchers have relied on combining semiconductors photocatalysts with other semiconductors or metals (especially the ones showing strong plasmonic activities).[38, 39] The advantage of composite photocatalysts is that they allow for the separation of electrons holes in different materials of the composite system. In addition, morphology control and enhancing internal electric fields have also shown success in improving photocatalytic performance of semiconductor photocatalysts. In the former case, it has been shown that certain facets of semiconductor crystals have more affinity toward either holes or electrons.[40, 41] This results in spatial separation of the charges on the surface of the photocatalyst allowing for higher photocatalytic efficiency. Also, hollow photocatalyst nanoparticles offer the benefit of reduced the volume available for charge recombination which shortens the distance charge transfer distance and improves the surface area available for reaction, which ultimately improves their photocatalytic performance over conventional photocatalytic nanoparticles.[42]

The presence of electric field within a photocatalyst is also conducive towards segregation of charges. In this regard, ferroelectric materials seems promising since they possess intrinsic and spontaneous polarization which can be further enhanced by poling.[43, 44]

1.3 Materials

This section provides a short introduction to the materials used during the course of this dissertation and reviews their application towards water decontamination.

1.3.1 Clays

Clays are anisotropic charged particles which are composed of a layered structure, made of oxides and hydroxides of inorganic elements such as silicon, aluminum, magnesium or lithium.[45] Clays occur naturally and are produced by geological processes like chemical weathering of silicate-bearing rocks. The particles of clay can have aspect ratio ranging anywhere from 10 to 1000. The charge on each particle is balanced by the presence of cations like Na or Ca in the interlayer space between these particles. Clays can be categorized in two types based on the stacking of the tetrahedral and octahedral layer.

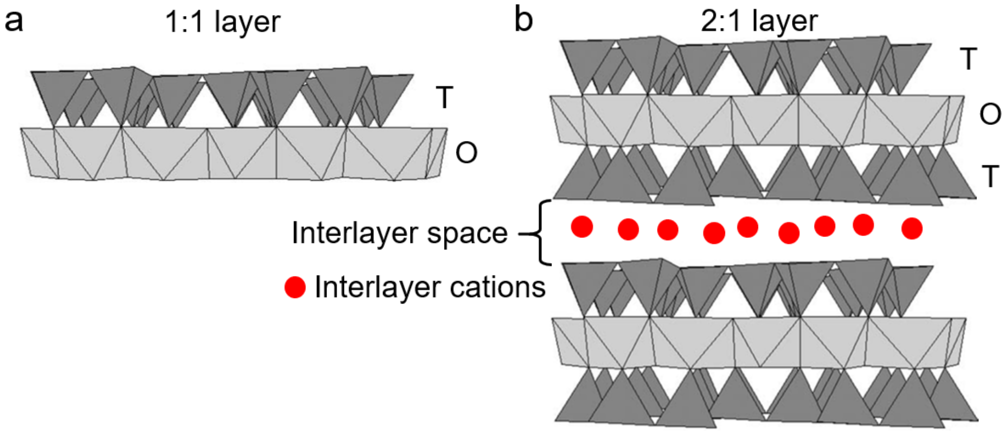

Figure 1.4: The arrangement of tetrahedral (T) and octahedral (O) layers in, (a) 1:1 type and (b) 2:1 type clays. Adapted from ref [31].

In the 1:1 type clay, tetrahedral sheet lies atop the octahedral sheet. The examples for this kind are kaolinite, lizardite, whereas for the 2:1 type, also called smectite clays, the octahedral layer is sandwiched between the two tetrahedral (Figure 1.4). Each tetrahedron (T) is comprised of a cation at the center, coordinated to four oxygen atoms. Individual tetrahedron is linked to the neighboring tetrahedra by sharing three corner basal oxygen atoms. This pattern is repeated ad-infinitum along the *a, b* crystallographic directions. The common cations occupying the tetrahedral sites include Si^{4+}, Al^{3+} and Fe^{3+}. In the octahedral layer, each octahedron is linked to the adjacent one by sharing edges. The usual octahedral cations are $Mg^{2+}, Al^{3+}, Fe^{2+}$ and Fe^{3+}, but many other cations, namely, Cu^{2+}, Li^{+}, Co^{2+}, Mn^{2+}, Ni^{2+}, Zn^{2+},

Cr^{3+}, Ti^{4+} and Cr^{3+} have also been identified. Moreover, in the tetrahedral layer, all the tetrahedra are aligned such that their free corners lie on the same side of the sheet. These free corners comprising of tetrahedral apical oxygen atoms, link the tetrahedral and octahedral sheets constituting a common plane with octahedral anionic position.

In addition, clays can also be classified based on their swelling behavior. The clays which show an expansion of the interlayer space upon hydration are termed swelling clays which include smectites like montmorillonite; whereas, clays which during hydration show no such expansion of interlayer space are termed non-swelling clays.[46] Examples of non-swelling clays include kaolinite and illite, where the latter also belongs to the category of smectites. Since the swelling smectite clay, laponite, was used most frequently during the course of this dissertation, it is discussed at length below.

Laponite

Laponite is a synthetic magnesio-silicate smectite clay. Its industrial production was first pioneered by Barbara Neumann in 1962.[47, 48] Since then the synthetic strategy for obtaining laponite has been optimized and different grades of laponite have been developed for specific applications. For instance, it has been used for applications like rheology modifier in personal care products like toothpaste, cosmetics; and as a film forming agent in antistatic and barrier coatings, to name a few.[48]

The laponite particle possesses a disc shape with a diameter of 25 nm and a thickness of 0.92 nm.[49, 50] In this particle, the octahedral layer is composed of Mg or Li and the tetrahedral layer is composed of Si. The isomorphic substitution of Mg in octahedral by Li and the presence of vacancies impart a negative charge to the face of laponite particles which is compensated by the presence of Na cations in the interlayer space. When dispersed in aqueous media, the face of laponite becomes permanently negatively charged[51] as the intergallery Na cations dissociate in the surrounding media and form an electrical double layer. However, the charge on the edges of the laponite particle depends on the protonation and de-protonation of –OH groups, where neutral conditions result in partial positive charge.[52] The aqueous dispersion of laponite displays rich phase behavior and can form dispersions ranging from sol to gel phase.[53] The gel phase is obtained by the face–to–edge as-

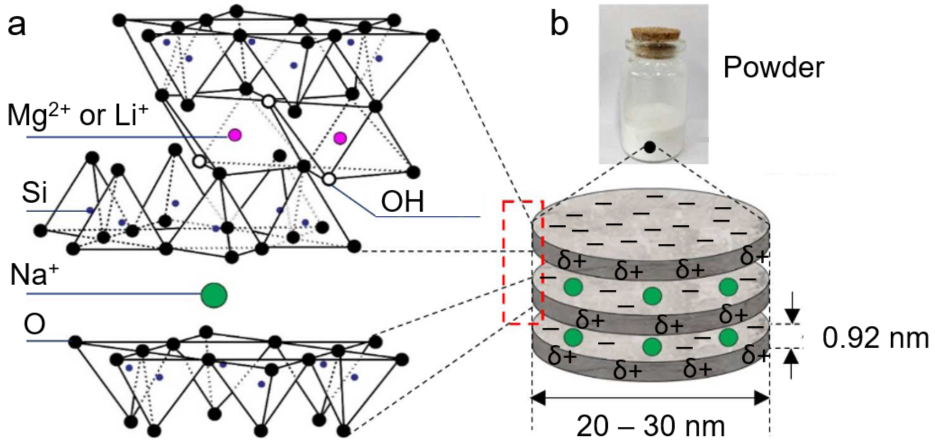

Figure 1.5: (a) The unit cell of laponite. (b) Laponite powder and the arrangement of laponite platelets in stacks called tactoids. The face of these platelets is negatively charged, whereas the edges are partially positively charged under neutral conditions. Adapted from ref [51].

sociation of the Lap particles.

Another important property of clays in general and laponite in particular is their cation exchange capacity (CEC). Cation exchange refers (in the context of laponite) to the substitution of the intergallery Na cations with other cations. The CEC of laponite is estimated to be ranging from 0.55–0.8 mequiv/g of dry laponite.[54, 55] This corresponds to around 450 substitutable Na cations per laponite particle.

Because of their charged surfaces and edges, and the presence of exchangeable interlayer cations, clays in general and laponite in particular lend themselves easily to chemical functionalization.[56, 57] Some of these functionalizations render the clays useful for molecular adsorption, which motivates their use in wastewater remediation applications.[58] Their sorbent action primarily stems from a combination of a highly charged surface superimposed on a sizable surface area.[59]

Pillared Smectite Clays

Pillaring is defined as a process which transforms a layered compound into a thermally stable micro-and or mesoporous material while preserving the layer structure.[60] Whereas a pillaring agent is any compound which can intercalate and maintain the spacing between adjacent layers upon the removal of the solvent. The resulting porous structure obtained thereafter should be able to accommodate molecules at least as large as N_2. Since organic compounds belonging to the family of quaternary ammonium surfactants (or salts) were used as pillaring agents in the course of this thesis, the role of these compounds in the adsorption performance of pillared-clays towards organic molecules is discussed.

Cowan and White conducted a systematic study of phenol removal from water by using montmorillonite pillared with different quaternary ammonium cations (QACs). These QAC derivatives having carbon chains ranging from 2 up to 18 C turned out to be proficient phenol adsorbents.[61] The maximum uptake was achieved using dodecylammonium (having 12 C atoms) pillared montmorillonite. In other separate studies, Mortland et al. and Boyd et al., reported that smectites modified with long-chain QACs like hexadecylpyridinium (HDPY) and hexadecyltri-methyl ammonium (CTA) adsorb more of these organic contaminants (OC) like phenol, trichlorophenol and pentachlorophenol from water compared to their short-chain counterparts like trimethylphenyl ammonium (TMPA), and tetramethylammonium (TMA).[62, 63] The reason being that intercalation with larger molecules imparts greater hydrophobicity to the QAC pillared clays.

The removal of OC from aqueous solutions also depends on the amount of QAC present in the pillared smectite clay. In addition, this relationship between QAC amount (in the pillared smectite) and OC uptake varies according to the alkyl chain length of the different QACs. For instance, increasing the concentration of short-chain QACs, such as TMA, in the smectite clay resulted in reducing in the amount of OC removed from the solution.[64] However, in the case of long-chain QACs, like CTA, the removal of any particular OC improved with increasing concentration of QAC in the pillared smectite.[65] The corresponding adsorption isotherms of OC sorption by short-chain QAC pillared clay exhibited typical curvilinear form, pointing towards both high- and low-energy sites.[64] In contrast, essentially linear isotherms were obtained for their long-chain QAC derivatives, suggesting that all sites are energetically equivalent.[66] This behavior can be explained mechanistically in the following way, the intercalation of long-chain QACs like HDPY or CTA, provides a microscopic organic phase which functions as a solvent, able to dissolve OC. Whereas, TMA or TPMA like short-chain QACs form ‘pillars’ or ‘columns’ in the interlayer space, hence providing only pores for the sorption of OC.[67]

Size of the pillaring agent is also known affect the sorption capacity of pillared clays. For instance, Jaynes and Vance observed a general increment in the sequestration of OC like benzene, toluene, ethylbenzene and xylene (collectively called BTEX) hydrocarbons as the C content of the QAC was increased from 15 C atoms (in cyclododecyl trimethylammonium, CDTA, molecular weight $M_W = 226$ and dodecyl trimethylammonium, DTA, $M_W = 228$) to 38 (dioctadecyl trimethylammonium, DODA, $M_W = 551$).[68] However, the comparison between CDTMA and DTA revealed that the QAC having straight-chain alkyl groups, was much more proficient at sequestering BTEX than the former, containing cyclic groups having almost identical M_W and the same number of C atoms. Along the similar vein, building up from the particulate system, researchers have demonstrated free-standing membranes of vermiculite modified amines have interesting properties when it comes to wastewater filtration. By changing the size of the pillaring diamines, channel/ pore size in the vermiculite membrane could be varied, which allows for selective removal of molecular species from water.[69]

1.3.2 Molybdenum Disulfide

MoS_2 is a 2D van der Waals material where the individual MoS_2 layer has a thickness of 0.31 nm and is separated from the adjacent layers by a van der waals gap of 0.32 nm. Due to its layered structure, bulk MoS_2 has been used as a solid lubricant for high temperature applications.[70] However, the recent excitement and upsurge of interest in this material is driven by the realization that monolayer MoS_2 exhibits behavior not otherwise seen in bulk or few layer MoS_2. For instance, the electronic band structure transitions to a direct bandgap type in monolayer MoS_2, whereas bulk and few layer MoS_2 possess an indirect bandgap.[71] This transition in bandgap structure is also accompanied by the emergence of photoluminescence in single layer MoS_2.[72]

Apart from its exotic behavior, single or few layer MoS_2 have also shown to be proficient in clean energy generation and wastewater remediation. For instance, its performance as a hydrogen evolution catalyst was found to rival that of the best-known noble metal catalysts.[73] The primary role of the edge sites in this process was recognized and exploited by Jaramillo et al.[74] These authors, by synthesizing MoS_2 nanoparticles of different sizes, demonstrated that electrocatalytic hydrogen evolution increases in proportion to

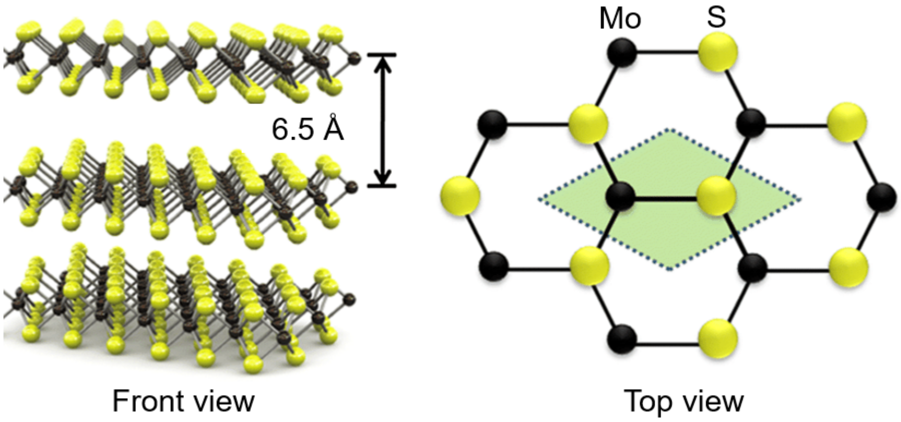

Figure 1.6: Left, the atomic structure of MoS_2. Right, top view of the honey comb structure of MoS_2. Adapted from ref [72].

the edge sites on the MoS_2 catalysts. Along similar vein, exclusively edge exposed MoS_2 thin films were grown by Kong et al. They reported 10-fold enhancement in the exchange current density which is a metric for gauging the electrocatalytic performance.[75] This insight into the role of exposed Mo-edge sites led researchers to investigate chemically exfoliated single/ few layer MoS_2 as a catalyst for aqueous reduction reactions.[76] Mo-edge sites function as catalytic sites because of the under-coordination of Mo present at the edges of MoS_2.

Researchers since then have sought to use MoS_2-composites with reduced dimensions towards catalytic water decontamination.[77, 78] In these studies, Peng et al used a layered silicate clay substrate, montmorillonite to template and restrain the size of hydrothermally grown MoS_2 nanosheets. They found that the montmorillonite substrate prevented the agglomeration of MoS_2 nanosheets during growth and resulted in greater number of exposed edge sites in the hybrid. They reported a 300 % enhancement in the catalytic degradation rate constant of the surfactant-pillared montmorillonite hybrid compared to pristine MoS_2.[78]

1.3.3 Bismuth Molybdate

Bi_2MoO_6 (BMO) is the simplest member of the Aurivillius perovskite group and possesses a layered structure. These layers are composed of $(MoO_4)^{2-}$

octahedra and $(Bi_2O_2)^{2+}$ tetrahedra stacked alternately along the b-axis of the crystal (Figure 1.7). This layered structure underpins many important functionalities of BMO. For instance, this layered structure provides such high oxide ion mobility that BMO has been termed as an oxide ion conductor.[79] This high oxide ion mobility is also the reason why BMO is used as a catalyst for oxidation and ammoxidation of propylene.[80] Another property resulting from this structure is the piezoelectric behavior of these crystals.[81] In addition, BMO has also proven successful in capacitor,[82, 83] sensing,[84] and environmental remediation applications.[85, 86] This same layered structure also provides a narrow band gap that can be further expanded to 500 nm i.e. to the visible region of the solar spectrum.[87]

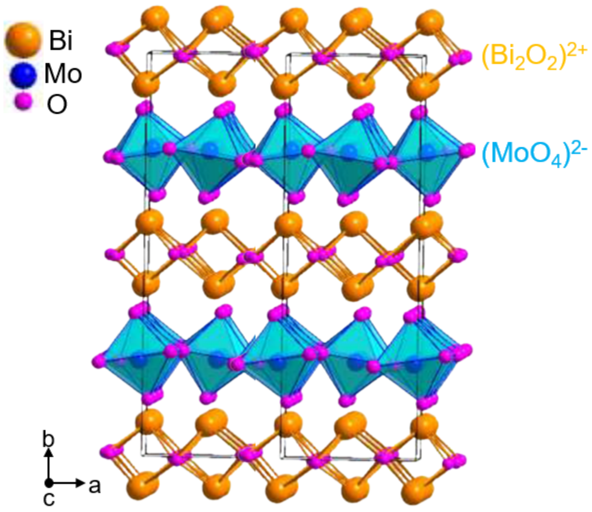

Figure 1.7: Atomic structure of Bi_2MoO_6. $(Bi_2O_2)^{2+}$ and $(MoO_4)^{2-}$ layers are stacked along the b direction. Adapted from ref [82].

The recent burgeoning of interest in BMO is primarily due to its photocatalytic activity which extends in the visible region of electromagnetic spectrum.[88] BMO is also interesting because its functional properties can be controlled by modifying particle growth and morphology.[89] For instance, the reduction in the thickness of BMO nanosheets has been reported to influence the photocatalytic performance.[90] In another study, by reducing the thickness of BMO particles from 40 nm to 3 nm, Li et al were able to enhance the internal electric field in BMO nanoparticles resulting in a 10-fold enhancement in the photocatalytic reduction of CO_2.[86] Apart from these environmental applications BMO has also been investigated for wastewater remediation. BMO has proven effective in degrading contaminants ranging from organic and inorganic substances to biological matter like bacteria.[89] For instance, Cruz and Alfaro studied the photocatalytic performance of BMO towards the degradation of different dyes, namely rhodamine-B, methyl orange and indigo carmen.[91] They found that the performance of BMO photocatalyst to decrease in the order, indigo carmen   rhodamine-B   methyl orange. This trend was attributed to the difference in the average bond strengths of –N=N– (420 kJ/mol) and –N–C– (286 kJ/mol) bonds. In more recent time, the application of BMO-based photocatalysts have also been extended to photodegrade pharmaceutical compounds. Xu et al studied the photodegradation of ciprofloxacin with BMO photocatalyst and examined the toxicity of the photodegradation products.[92] They reported that the presence of O vacancies in BMO improves their photodegradation performance and that over time these BMO photocatalysts eliminated toxicity from the photodegradation products with degree of mineralization. Furthermore, Ce-doped BMO was used by Dai and colleagues to efficiently decompose toxic nerve agent simulants like methyl paraoxon and bis(4-nitrophenyl) phosphate and they reported complete mineralization of the photodegradation products.[93] Since semiconductor photocatalysts exhibit stronger oxidation ability than oxygen ions and ozone,[94, 95] they're being also studied for water disinfection applications. In this regard, BMO-AgI composite has also shown significant bactericidal action toward both Gram-positive and Gram-negative strains.[96]

1.3.4 Indium Sulfide

In_2S_3 belongs to the family of III–VI semiconductors. It commonly exists in three different polymorphic forms, namely, α-In_2S_3 (defect cubic), β-In_2S_3 (defect spinel), and γ-In_2S_3 (layered hexagonal).[97, 98] Among these three forms, β-In_2S_3 is stable at room temperature and exists in the tetragonal and cubic form with bandgap range 1.9–2.4 eV.[99, 100] Since, β-In_2S_3 was synthesized during this work, rest of the discussion would focus on this phase. The unit cell of β-In_2S_3 is comprised of tetrahedral and octahedral sites, where two-third of the tetrahedral sites and all of the octahedral sites are occupied by In^{3+}.[101] β-In_2S_3 is a typical n-type semiconductor. Due to its favorable band structure In_2S_3 has been endowed with luminescent properties and because of which it has also been investigated as phosphor in display devices.[102] Since its bandgap corresponds to absorption in visible light, this has allowed In_2S_3 to be useful for solar energy harvesting applications. For instance, In_2S_3 has been investigated as a buffer layer in thin film photovoltaics and is also explored as a replacement of more toxic CdS which is more commonly used for the same purpose in photovoltaics.[103]

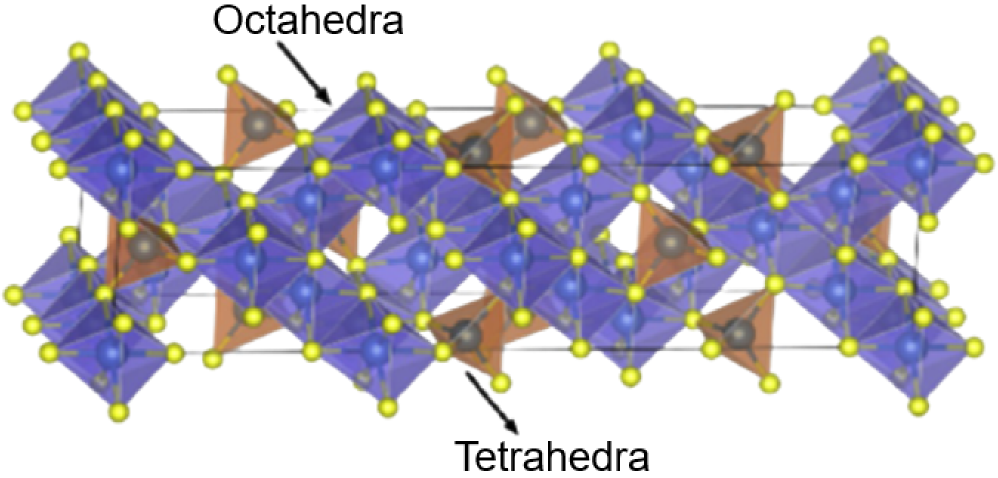

Figure 1.8: Atomic structure of β-In_2S_3. Adapted from ref [101].

Because of its light harvesting capacity, In_2S_3 has been widely used as a photocatalyst for degrading pollutants. Previously, In_2S_3 nanoparticles have been used to destroy model pollutants like dyes via photocatalytic oxidation of the target contaminant.[104] In another study, Wu et al focused on the remediation of wastewater polluted with Cr(VI) and the dye rhodamine-B. They reported that the co-doping of In_2S_3 nanoparticles with Yb^{3+} and Tm^{3+} further improves the photocatalytic reduction of Cr(VI) and photocatalytic oxidation of rhodamine-B.[105] Co-doping allowed these authors to extend the light absorption by In_2S_3 across UV-near infrared region. In addition, In_2S_3 nanoparticles also turned out to be effective at degrading antibiotics like tetracyline and its derivatives.[106, 107] Apart from their action on chemical moieties, In_2S_3 photocatalysts have also proven successful in destroying bacteria present in contaminated water.[108]

1.4 Motivation

Particles exhibiting anisotropic surface chemistry can provide an avenue to adsorb molecules differentially onto their specific facets, depending on their charge or surface chemistry. Such colloidal control of molecular adsorption at interfaces can direct and template the growth of other materials, such as semiconductor photocatalysts. Since the performance of photocatalysts, is dependent on their size, where thinner and smaller particles exhibit better photocatalytic performance due to their direct bandgap and high surface area, it becomes critical to control their growth. The conventional colloidal growth strategies result in the agglomeration of photocatalysts and post-synthesis exfoliation to obtain thin sheets can introduce detrimental defects in these materials. These shortcomings can be overcome by using clay-like materials possessing anisotropic surface chemistry, to template the growth of photocatalysts. Apart from controlling photocatalyst growth, these clay-templated photocatalysts also benefit from the intrinsic aqueous dispersibility of clay-like materials which can further improve their catalytic and photocatalytic performance in aqueous media by improving their dispersibility.

In the course of this dissertation, the surfactant-modified clay templated growth strategy explored here was found to improve the catalytic, photocatalytic and adsorption performance of these clay-semiconductor hybrids compared to their pristine (photo)catalyst and clay counterparts. Moreover, the pressing issue of water pollution (discussed previously in section 1.1) and the inability of present wastewater treatment facilities to tackle bioactive, non-biodegradable chemicals like pharmaceuticals and dyes,[109] further motivated the use of these novel clay-semiconductor hybrids for water decontamination applications. Anti-fouling filtration membranes with the ability to sieve out molecular moieties were fashioned out of these clay-semiconductor hybrids to offer point-of-use water decontamination solutions, which further motivated us to explore nanofiltration with the aim of achieving selectivity along with high flow rate in these membranes.

Chapter 2

Heterostructured Monolayer MoS_2 Nanoparticles toward Water-Dispersible Catalysts

This chapter has been published as: Jatav, S.; Furlan, K. P.; Liu, J.; Hill, E. H. Heterostructured Monolayer MoS_2 Nanoparticles toward Water-Dispersible Catalysts. *ACS Applied Materials & Interfaces.* **2020**, 12(17), 19813-19822.

In this work, laponite-MoS_2 nanoparticles were synthesized, and tested for the catalytic degradation of water soluble model pollutants like synthetic organic dyes. The surfactant-pillared laponite template was able to confine and restrict the growth of MoS_2, which resulted in the formation of smaller MoS_2 particles leading to the presence of greater number of Mo edge sites compared to pristine MoS_2. In contrast to MoS_2 control, the incorporation of laponite was shown to significantly improve the water dispersibility of these laponite-MoS_2 nanohybrids, in addition to retaining the surface chemistry of laponite. The presence of greater number of catalytic sites, due to smaller size and improved water dispersibility resulted in significantly higher catalytic pollutant degradation performance of the laponite-MoS_2 nanoparticles compared to pristine MoS_2.

ACS APPLIED MATERIALS & INTERFACES

www.acsami.org Research Article

Heterostructured Monolayer MoS_2 Nanoparticles toward Water-Dispersible Catalysts

Sanjay Jatav, Kaline P. Furlan, Junying Liu, and Eric H. Hill*

Cite This: ACS Appl. Mater. Interfaces 2020, 12, 19813−19822 Read Online

ABSTRACT: MoS_2 is a 2D semiconductor where exfoliation to a single layer results in improved catalytic properties. However, its high surface energy can lead to extensive aggregation, resulting in degraded catalytic performance and stability. Combined with a lack of dispersibility in water, this represents a pitfall for catalysis in the aqueous phase. Herein, we present the use of nanoscopic layered silicates pillared with a cationic surfactant to template the growth of MoS_2 in the interlayer space. This provides heterostructured layered nanoparticles ~25 nm wide by 3−8 nm thick containing isolated MoS_2 layers. The resulting nanohybrids retain the disc-like morphology and surface chemistry of the clays, providing good aqueous stability, while also providing access to the catalytic edge-sites of the MoS_2 layer. In addition to significant enhancement of catalytic dye degradation, molecular aggregation on the highly charged clay interface is comparable to unmodified clays. These particles are ideal for studies of charge-transport properties in confined semiconductor layers, as well as hierarchical self-assembly into functional materials. This study paves the way to colloidal synthesis of nanoparticulate heterostructures with other functional layered materials, particularly where particle exfoliation, covalent modification, and aqueous stability are concerns.

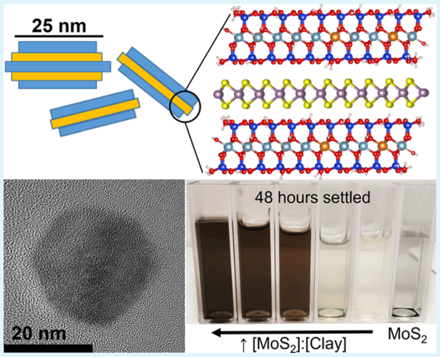

KEYWORDS: *nanohybrids, 2D materials, hybrid materials, nanocomposites, transition metal dichalcogenides, laponite,* MoS_2*, vdW heterostructure*

INTRODUCTION

Recent advances in synthesis of ultrathin 2D materials including transition-metal dichalcogenides (TMDs) and oxides provide the impetus to apply these materials in composite layered materials. TMDs are among the numerous 2D nanomaterials which have recently attracted global attention and extensive research.[1−3] Many TMDs are semiconductors with ~1−2 eV indirect band gap, which becomes a direct bandgap after exfoliation into a few layers or a single layer (in the 1T phase).[4−7] In the case of MoS_2, their high surface energy can lead to extensive aggregation, resulting in degraded catalytic performance and stability. Combined with their lack of colloidal stability in water, this represents a pitfall when using MoS_2 composites for catalysis in the aqueous phase.[8,9] The absorbed photon-to-current conversion efficiencies of MoS_2 thin films has been shown to decrease at thicknesses greater than a single layer, where the efficiency drops from 8 to 2% as the thickness increases from 1.7 to 2.5 nm.[6]

Layered silicate clays have a wide range of aspect ratios and diameters (25 nm to 3.5 μm) and desirable properties including gas-barrier, transparency, and cation-exchange capacity.[10] The faces of these clay particles are able to load a variety of molecules at the surface, and aggregation of molecules occurs upon binding to the surface of the clay.[11−14] The use of TMDs in composites with layered silicate clays have yielded high-performance materials that combine the benefits of both.[1,8] It was also shown that a layered silicate clay in a hybrid perovskite solar cell could serve as a bifunctional buffer layer that limited charge recombination and improved overall efficiency by 32%.[15] The lamellar configuration and a large surface area both lead to improved hydrogen generation due to easy access for electrolytes to facilitate interfacial charge transfer and electrochemical reactions.[2] Furthermore, a number of recent studies have shown that layered silicate clays are useful for nanoscale self-assembly toward solution-processed materials with high material strength.[16−19]

In a recent study by Peng et al., the layered silicate clay montmorillonite was used to stabilize the synthesis of MoS_2 in the interlayer space of the clay.[20] Cationic surfactants can be used to cause "pillaring" in layered smectites.[21,22] It was also shown by Peng et al. that without pillaring, MoS_2 is grown on the external basal surfaces of montmorillonite.[23] Although

Received: February 5, 2020
Accepted: March 31, 2020
Published: March 31, 2020

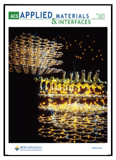

https://dx.doi.org/10.1021/acsami.0c02246
ACS Appl. Mater. Interfaces 2020, 12, 19813−19822

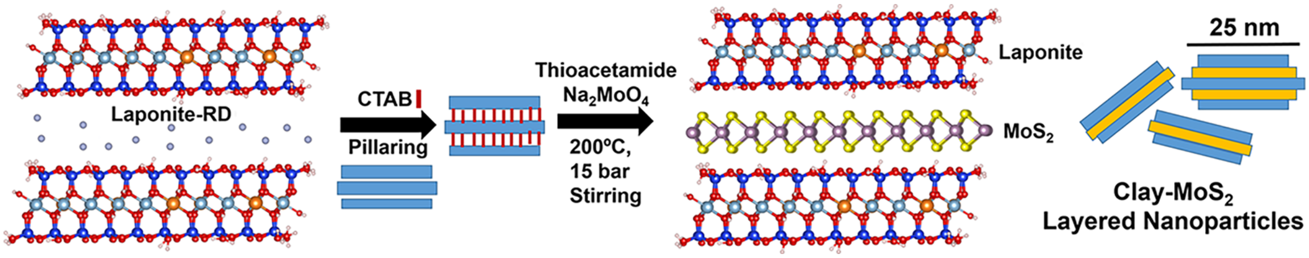

Figure 1. Hydrothermal synthesis of Lap−MoS$_2$ hybrid nanoparticles.

these studies serve as good motivation for further studies of reactions in the clay interlayer space, they focus on the preparation of a bulk composite material rather than a nanoparticulate system. Because of its natural origin, montmorillonite can also have a wide size distribution and dispersity ranging from hundreds of nanometers to several microns, further complicating systematic studies of templated growth.[24,25] The templated growth of 2D materials in a nanoparticulate layered silicate to achieve a hybrid nanoparticle containing exfoliated MoS$_2$ nanosheets has not been reported. Laponite-RD (Lap), a synthetic clay, has a diameter of 25 nm and a thickness of 0.92 nm, and has a rich phase behavior ranging from completely exfoliated particles to glasses and gels.[26] It has been previously used for shape-templated synthesis of gold−clay hybrid nanoparticles.[27] As the diameter of Lap is much smaller than that of montmorillonite (25 nm vs 0.1 to >1 μm), and with a smaller size and shape dispersity, the resulting nanohybrid would provide greater accessible surface area, increased number of catalytic edge-sites[28] per clay particle, and better control over the synthesis. Furthermore, such water-dispersible nanohybrids can be used for additional colloidal assembly approaches that require a sub-100 nm particle size. Finally, this small size is ideal for investigations of charge-transport properties of isolated MoS$_2$ layers, which is critical for electronics applications.

Herein, the templated growth of MoS$_2$ in the interlayer space of Lap is carried out (Figure 1). The mechanism of growth relies on the expansion of the Lap interlayer space by pillaring using the surfactant cetyltrimethylammonium bromide (CTAB), followed by impregnation of the interlayer by MoS$_2$ precursors. The direct adsorption of the MoO$_4^{2-}$ anion on the surface of unmodified Lap is unlikely due to electrostatic repulsion. However, the hydrophobic cavity of the surfactant-loaded interlayer eases the entry of molybdate ions into the interlayer space.[20] Osmotic pressure and hydration effects have been shown to aid the movement of ions and molecules in clay films.[29] Insertion of anions into the interlayer is particularly favorable in clays pillared with long-chain organocations such as CTAB, which can result in the strong uptake of anionic species such as Mo(CN)$_8^{4-}$, Fe(C$_2$O$_4$)$_3^{3-}$, and Fe(CN)$_6^{4-}$ by electrostatic interactions.[30,31] Such pillaring with CTAB has been shown to even accommodate the subsequent addition of anionic surfactants, drastically expanding the interlayer space from 2.0 to 5.7 nm.[32]

Earlier studies show that S sources such as cysteine, thiourea, and thioacetamide associate strongly with montmorillonite,[33,34] and recent studies report templating of WS$_2$ and MoS$_2$ growth by adsorbed thioacetamide on the surface of montmorillonite.[23,35] Interestingly, thioacetamide was shown to intercalate more strongly at basic pH, whereas acidic pH led to only minimal intercalation.[33] As our synthesis is carried out at basic pH, a similar templating effect is likely. Furthermore, the combination of CTAB with thioacetamide has been shown to absorb strongly in the interlayer space of montmorillonite, supporting the idea that MoS$_2$ growth in the interlayer space is indeed templated by the combination of the hydrophobic interlayer and bound thioacetamide within.[36,37] The S source, thioacetamide, will easily decompose and form H$_2$S above 150°C, which can then reduce Mo(VI) in situ.[38] In addition, thioacetamide has been shown to template the growth of MoS$_2$ due to the closed hydrogen chain generated by reaction of the azyl group and water, leaving MoO$_4^{2-}$ anions to react with the generated H$_2$S.[38,39]

Under 200 °C and 15 bar over 20 h, the organic components (including thioacetamide) degrade, allowing crystallization of MoS$_2$. First, we compared how stirring influences the resulting particle morphology. Conditions which led to the formation of hybrid nanoparticles of alternating layers of MoS$_2$ and Lap with a morphology resembling the clay particle were determined. The surface chemistry of the particles was then studied via molecular aggregation to clarify whether there was more clay-like or MoS$_2$-like character. Finally, the catalysis of dye reduction by BH$_4^-$ was compared for Lap−MoS$_2$ and MoS$_2$, showing a drastic increase in catalytic activity of Lap−MoS$_2$ against MoS$_2$, and also when comparing with previous studies of montmorillonite−MoS$_2$ heterostructures. The templated growth of MoS$_2$ in the interlayer space of Lap shows the relevance of nanoscopic layered silicates for model studies of nanohybrid synthesis.

RESULTS AND DISCUSSION

The UV−vis spectra of the Lap−MoS$_2$ particles at different ratios of MoS$_2$−Lap show a broadband absorption that decreases with the MoS$_2$−Lap ratio (Figure 2a). The Lap−MoS$_2$ particles have decreasing absorbance as wavelength increases, showing a broad absorbance spectrum not unlike that of the MoS$_2$ control. Their UV−vis spectra resemble those of Li-intercalated MoS$_2$, exfoliated MoS$_2$ nanosheets, or small MoS$_2$ particles.[40−42] Although the lack of the typical A and B exciton bands of MoS$_2$ in the control sample is conspicuous, this may result from a reduced number of layers due to the influence of stirring, as hydrothermal synthesis is typically performed under static conditions. The aqueous stability of the particles was significantly improved over MoS$_2$, remaining in suspension for over 48 h compared with MoS$_2$ which precipitates within an hour (Figure 2b, UV−vis spectra shown in Figure S1).

In contrast with a previous study of montmorillonite clay with MoS$_2$ grown in the interlayer space where synthesis was carried out under static conditions, stirring was carried out during the hydrothermal synthesis. This prevents large flocs from forming due to settling during the reaction, resulting in

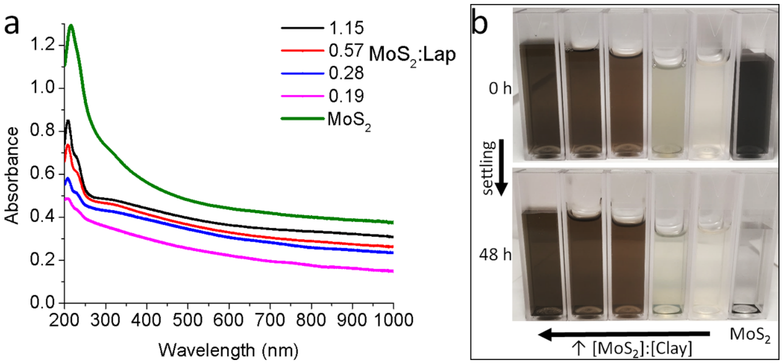

Figure 2. (a) UV−vis spectra of Lap−MoS$_2$ nanoparticles and MoS$_2$ (0.1 mg/mL). (b) Photographs of Lap−MoS$_2$ and MoS$_2$ dispersions at 0.5 mg/mL before and after 48 h of settling time. Corresponding UV−vis spectra of (b) are shown in Figure S1.

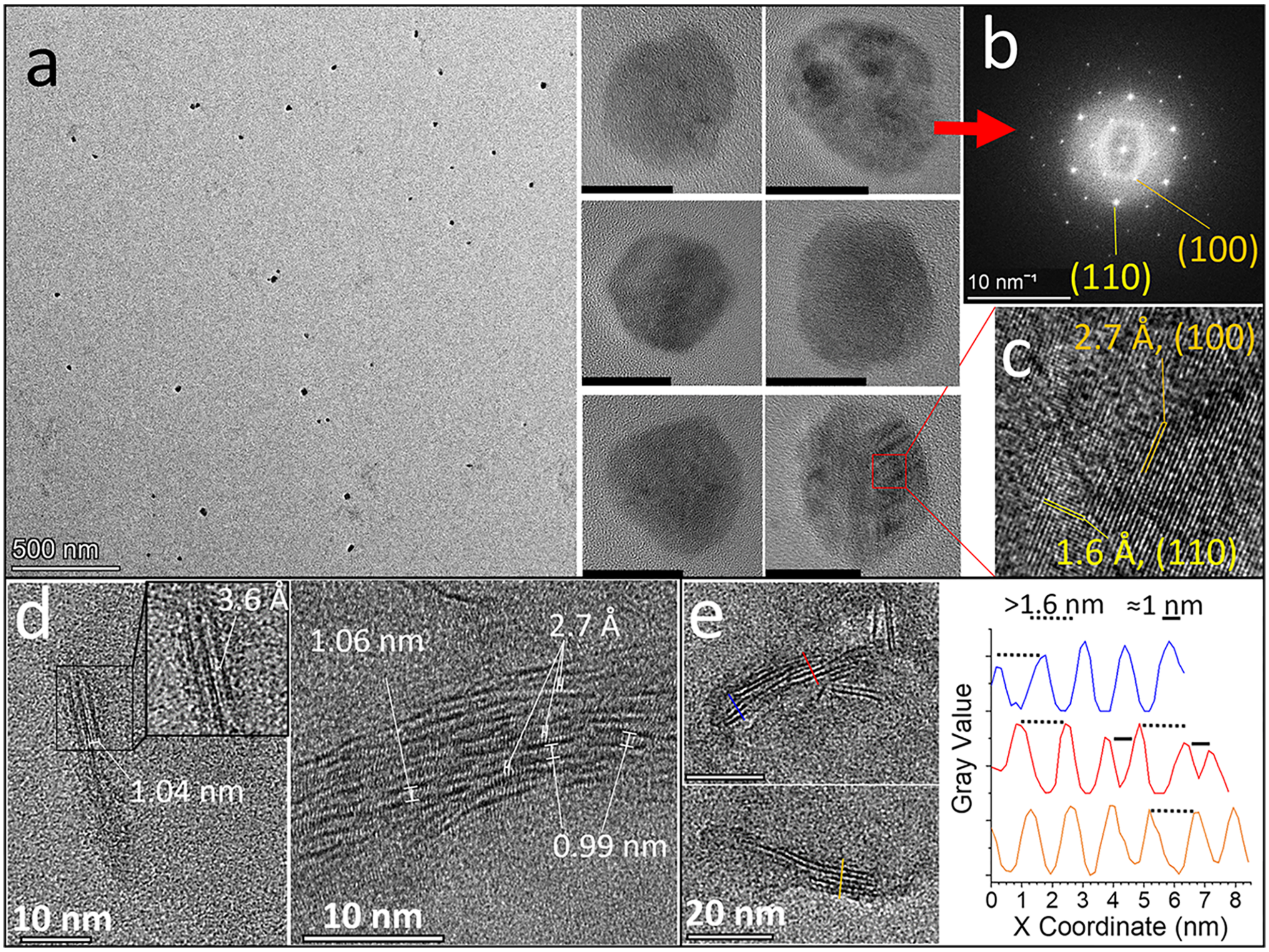

Figure 3. High resolution-TEM micrographs. (a) Lap−MoS$_2$ nanoparticles showing Lap-like morphology; particle scale bars are 20 nm. (b) Electron diffraction and (c) lattice fringes of MoS$_2$(100) and (110) facets. (d) Edge-on view of particles and a particle aggregate (right); lattice spacings of (100) facets within some of the layers are labeled accordingly. (e) Line-scans showing variations in interlayer spacing; layers with spacing outside the range 1.2−1.3 nm are labeled accordingly.

smaller nanohybrids. Comparing electron microscopy images of MoS$_2$−Lap with and without stirring shows clear differences in their structure (Figure S2). In the case of the sample that is not stirred, particles of ∼100 nm have the morphology of discs intersecting at 90°, suggesting that multiple clay platelets are aggregated during the synthesis. Furthermore, in the features perpendicular to the TEM grid surface, the lattice spacing of 0.31 nm indicates the growth of multiple layers of MoS$_2$, a feature which is not present in the stirred sample (Figure S3). A MoS$_2$ control synthesized with stirring, but without Lap, has a typical flower-like morphology in a size range of ∼100−500 nm (Figure S4). Transmission electron microscopy (TEM) revealed that Lap−MoS$_2$ particles resemble Lap in size and

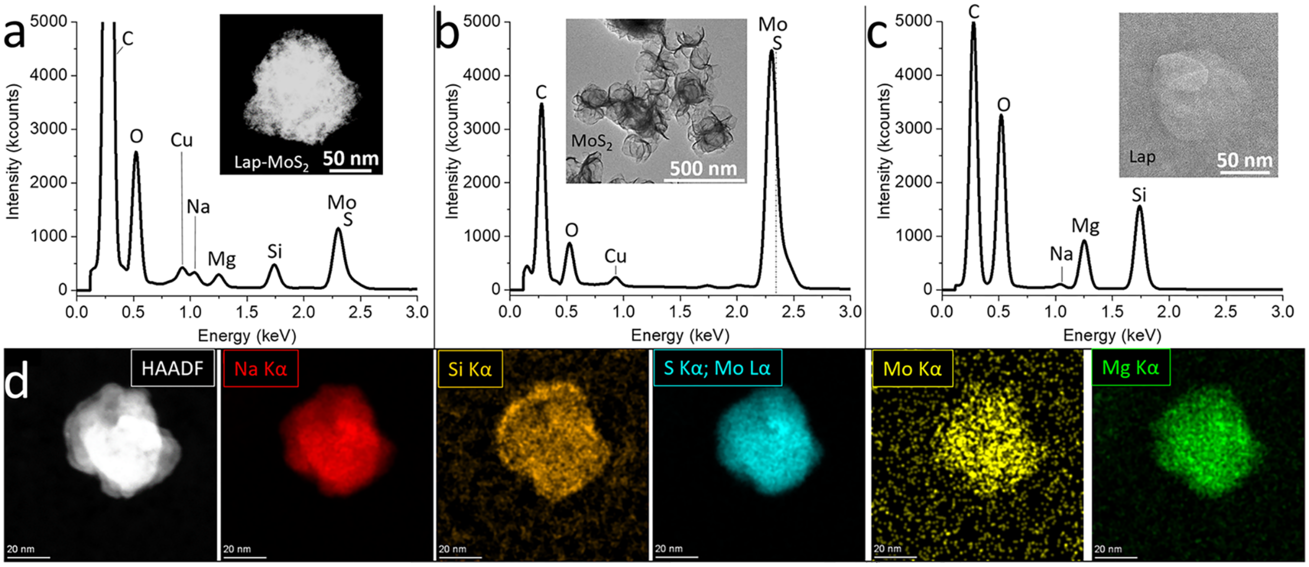

Figure 4. EDX spectra of (a) Lap−MoS$_2$, (b) MoS$_2$, and (c) Lap. (d) HAADF−STEM EDX mapping of a Lap−MoS$_2$ particle; scale bars are 20 nm. The complete range of the measured spectra in (a−c), including the Mo K*α* line when present, are given in Figure S9. HAADF−STEM EDX maps of additional particles are shown in Figure S10.

shape, but with greater contrast compared with unmodified Lap (Figure 3).

Zooming into individual Lap−MoS$_2$ particles, the (100) and (110) planes of MoS$_2$ are clearly visible and can be observed by diffraction (Figures 3c and S5). Furthermore, although unmodified Lap is difficult to observe clearly by electron microscopy (Figure S6), these particles have greater contrast, enabling confirmation of their diameter to be similar to that of unmodified Lap (∼25 ± 10 nm).[29] The presence of both Lap and MoS$_2$ is further supported by EDS measurements (Figure 4). The interlayer spacings of the layered structure were largely centered around 1.3 nm (Figure 3e), corresponding to the Lap basal spacing of 1.30 nm measured by X-ray diffraction (XRD) (Figure 5). The occurrence of >1.6 and <1.1 nm layer spacings was also observed, and although Bragg reflections of ∼1.04 nm were observed by XRD, those on the order of 1.6 nm were not (Figure 5). Measurement of 48 interlayer spacings imaged by TEM showed that the majority (∼40%) were between 1.2 and 1.36 nm, with ∼15% each for bins of 0.97−1.06, 1.12−1.18, 1.42−1.48, and >1.6 nm (Figure S7). Not only was the interlayer space confirmed by TEM, but some of the alternating layers clearly show 0.27 nm lattice spacings, corresponding to the (100) plane of MoS$_2$. As Lap viewed edge-on shows little structure other than a thin dark line (Figure S6), we infer that these observed lattice fringes represent the MoS$_2$ layers within the layered structure.

Because of the lack of nonaggregated particles observed edge-on, particle thickness was uncertain. Atomic force microscopy (AFM) was used to survey 217 particles, which showed thicknesses from 3 to 9 nm (average 5.1 ± 1.5 nm) (Figure S8). Using the measured value of Lap basal spacing of 1.3 nm from XRD, this suggests that the particles consist of heterogeneous multilayer stacks with a number of MoS$_2$ layers from 1 to 6. Although the TEM images could only reveal the structure and crystallinity of the Lap−MoS$_2$ particles, their elemental composition was confirmed by energy-dispersive X-ray spectroscopy (EDX) (Figure 4).

EDX spectroscopy of Lap−MoS$_2$ clearly shows the presence of both Mg and Si of Lap and Mo and S from MoS$_2$. Na was also clearly observed, suggesting that the Na$^+$ ions from the Mo precursor, Na$_2$MoO$_4$ associated with the anionic faces of Lap during the formation of the MoS$_2$ layer. The presence of Na is logical, as the organocation CTAB is not expected to survive the high temperature and pressure of the hydrothermal reaction conditions. In fact, Raman spectroscopy showed that in the case of MoS$_2$−montmorillonite using CTAB as a pillaring surfactant, an amorphous carbon phase is formed.[20] In addition to EDX spectroscopy, spectral mapping was performed by using high-angle annular dark-field scanning TEM (HAADF−STEM) in order to resolve the composition of the Lap−MoS$_2$ nanoparticles spatially. The close overlap of the Mo L*α* line (2.293 keV) and the S K*α* line (2.307 keV) leads to the formation of a peak with a broadened base (e.g., Figure 4b). To overcome this, the Mo K*α* line (17.44 keV) was used to further confirm the presence of Mo (Figure S9). Furthermore, for EDX mapping by HAADF−STEM, the Mo K*α* line can also be used to indicate the presence of Mo independent of an S signal, although the signal intensity of this line is limited by the EBSD detectors used for the measurement because of their relatively lower detection of X-ray lines >10 keV. Although EDX confirmed the presence of both Lap and MoS$_2$, further information about the crystalline phases present in the nanohybrids was obtained by XRD (Figure 5).

XRD shed light on the state of both the Lap and MoS$_2$ components in the Lap−MoS$_2$ nanoparticles and further information about their layered structure. The MoS$_2$ control sample showed broad diffraction peaks corresponding to (002), (100), and (102) crystal planes (JCPDS card 03-065-0160). Such broad peaks are characteristic of MoS$_2$ nanoparticles, in agreement with the previous studies.[43] Broad peaks are also observed in the Laponite-RD sample related to its nanocrystalline nature and are identified at values 7.10, 19.34, 28.07, and 34.93°, corresponding to (001), (02,11), (005), and (20,13) crystal planes, respectively.[44,45] In the XRD pattern of

Lap−MoS_2, the peak at $2\theta \approx 35°$ consists of the (102) crystal plane of MoS_2 overlapping with the (20,13) band of Lap. The d-spacing of the (001) crystal plane, otherwise known as the basal spacing, for unmodified Lap is 1.24 nm. After pillaring with CTAB, the d_{001}-spacing is increased to 1.47 nm. Hydrothermal synthesis leads to a reduction of the d-spacing relative to pillared Lap, the amount of which depends on the amount of MoS_2 precursor added. With ratios of 0.19 and 0.28 Mo−Lap, the d-spacing compared to pillared Lap reduces from 1.47 to 1.39 nm. A further decrease in the d-spacing to 1.33 and 1.30 nm is noted as the Mo−Lap ratio is increased to 0.57 and 1.15, respectively (Figure 5b). This corroborates the d-spacing in MoS_2−montmorillonite of 1.29 nm reported by Peng et al.[20] However, in both cases the spacing is smaller than would be expected for a van der Waals (vdW) heterostructure, as the vdW gap of MoS_2 is 0.3 nm. Thus, if a vdW gap was present, one would expect a d_{001}-spacing of ∼1.6 nm. Although this spacing is observed by TEM (Figures 3e and S7), no peak corresponding to this d-spacing value is observed by XRD. It is envisioned that future studies using more advanced electron microscopy methods such as double aberration-corrected TEM may provide a better understanding of this result.

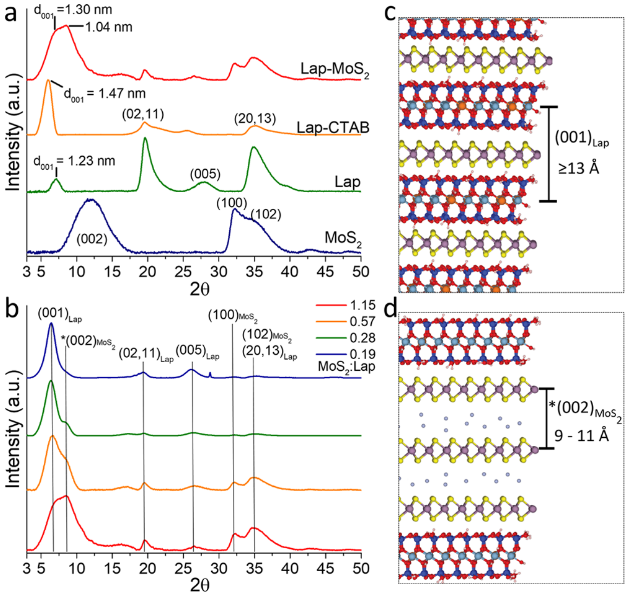

Figure 5. (a) X-ray diffractograms of Lap−MoS_2 and controls; (b) X-ray diffractograms of Lap−MoS_2 synthesized at different MoS_2−Lap ratios (by Mo mass), showing a decrease in Lap interlayer spacing (d_{001}) with increasing MoS_2 content. Schematic illustrating the observed d-spacings of (c) $(001)_{Lap}$ and (d) $(002)_{MoS_2}$ with an expanded interlayer space from Lap−MoS_2.

As the amount of MoS_2 precursors are increased, the peaks related to the (100) and (102) planes of MoS_2 become more prominent (Figure 5b). Furthermore, increased MoS_2 content leads to a peak at 8.4° emerging next to the Lap d_{001} peak at 6.4°. A decrease in the Lap d-spacing from 1.38 to 1.04 nm is unlikely, as subtracting the Lap thickness (0.92 nm) gives an interlayer spacing of 1.2 Å, which is not even half of a single MoS_2 layer. Rather, this peak likely represents a reflection caused by expanded MoS_2 layers grown on or inside Lap. Notably, the typical (002) reflection of MoS_2 around 14°, which is present in typical multilayer MoS_2 but not in monolayer MoS_2, was not observed in the Lap−MoS_2 samples. Although the majority of chemically synthesized MoS_2 has a (002) spacing of ∼0.65 nm, increased spacings up to 1.45 nm have been observed when the layers are intercalated with molecules, ions, or graphene.[46−49] In our case, the increase in basal spacing could result from either intercalation of Na^+, incorporation of oxygen in the vdW gap of MoS_2, or a combination of both. It has been shown previously that the presence of Na^+ ions can result in an increase in basal spacing from 0.64 nm up to 1.5 nm when intercalated Na^+ ions are solvated.[46,50−52] Considering that there are two sources of Na^+ ions, Na_2MoO_4 and Lap, and that Na is clearly detected by EDS (Figure 4d), this is the most likely cause of the expanded layer spacing of MoS_2. The incorporation of oxygen can also occur due to the incomplete decomposition of Na_2MoO_4 precursor,[49] increasing the (002) spacing to 0.95 nm, though this is unlikely as this peak at 8.4° is absent in the MoS_2 control sample. Considering that the sulfur source thioacetamide can be incorporated into clay interlayers,[34] we expect that the growth of MoS_2 occurs on the basal surfaces of Lap when MoS_2 precursors exceed the space provided by the expanded Lap interlayer. Interestingly, this peak is not observed with MoS_2 grown in pillared montmorillonite, suggesting dependence of the growth process on particle edge-length.[20]

The increase in Lap interlayer spacing shown by XRD (Figure 5), along with the confirmation of the (100) lattice spacing in Lap−MoS_2 particles by TEM (Figure 3d) indicate the growth of monolayer MoS_2 within the interlayer space of Lap. Although the XRD measurements were not extended to the range required to observe the (110) spacing of MoS_2 (2θ = 58°) in Lap−MoS_2, this lattice spacing was regularly observed via TEM (Figures 3b,c and S5).

Examining Surface Chemistry by Molecular Absorption. As mentioned in the introduction, layered silicate clays are effective at absorbing a variety of organic and ionic species, particularly cations. MoS_2 has also been shown to be an effective sorbent of heavy metal ions and organic contaminants, including a wide variety of organic dye molecules.[53−55] Considering that both components of the Lap−MoS_2 nanohybrids are good sorbents for similar molecules and both are anionic, one would expect difficulty in differentiating which material caps the faces of the layered structure. As the synthesis is based on growth in the interlayer space, one would assume that the Lap−MoS_2 nanocomposites are terminating stacks of varying numbers of formerly pillared clay particles with MoS_2 layers in between. Significant past research on the electronic structure of dye molecules and aggregates bound to layered silicates allows us to ascertain which surface terminates the nanohybrid.[12−14] Methylene blue (MB) is a good candidate for determining interactions with the layered silicate interface, as Cenens and Schoonheydt reported in 1988 the different absorptive molecular species and their extinction coefficients when adsorbed on clays including Lap-B.[13]

In order to better understand the aggregation of molecules on the Lap−MoS_2 nanohybrids, the absorption of MB on both MoS_2 and Lap−MoS_2 was studied by UV−vis spectroscopy and ζ-potential measurements. It was observed that titration of a solution of MB with Lap−MoS_2 leads to drastic changes in both color and colloidal stability (Figure 6). Calculated using the average molecular weight of Lap of 7.1 to 9.3 × 10^5 g/mol,[56] charge-equivalency is reached at a MB/Lap−MoS_2 molar ratio of 150, resulting in the formation of a bluish-green precipitate. As shown by UV−vis spectroscopy (Figure

https://dx.doi.org/10.1021/acsami.0c02246
ACS Appl. Mater. Interfaces 2020, 12, 19813−19822

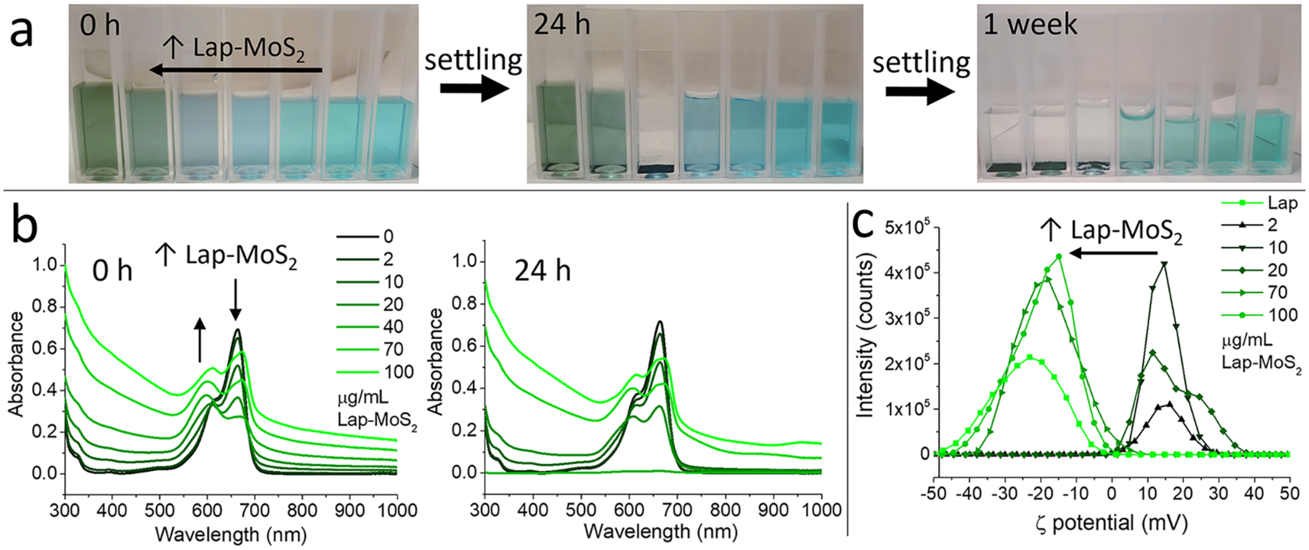

Figure 6. Absorption and aggregation of MB on Lap−MoS$_2$. (a) Photographs of a 7.3 μM solution of MB with different amounts of Lap−MoS$_2$ added (2−100 μg/mL), directly after addition, 1 day later, and 1 week later. (b) Corresponding UV−vis spectra of 0 and 24 h samples from (a). (c) Zeta-potentials measured after 24 h, excluding the 40 μg/mL sample due to colloidal instability. "Lap" in the legend of (c) refers to a 0.1 mg/mL suspension of Lap at pH 10, without any added MB.

6b), addition of Lap−MoS$_2$ results in the formation of a prominent absorbance band at 596 nm, which is attributed to the formation of an H-dimer on the clay interface.[13] However, MB trimer bound to the clay interface which was previously reported at 570 nm was not observed at the concentrations studied. In the control study of MoS$_2$, although the typical absorbance bands observed for MB in solution were observed (monomer at ~664 nm, dimer as a shoulder at ~605 nm), no surface aggregates were observed. With increasing addition of MoS$_2$, the MB spectrum is reduced, whereas beyond 40 μg/mL MoS$_2$, the spectrum of MB completely disappears and only the spectrum of MoS$_2$ is visible (Figure S11).

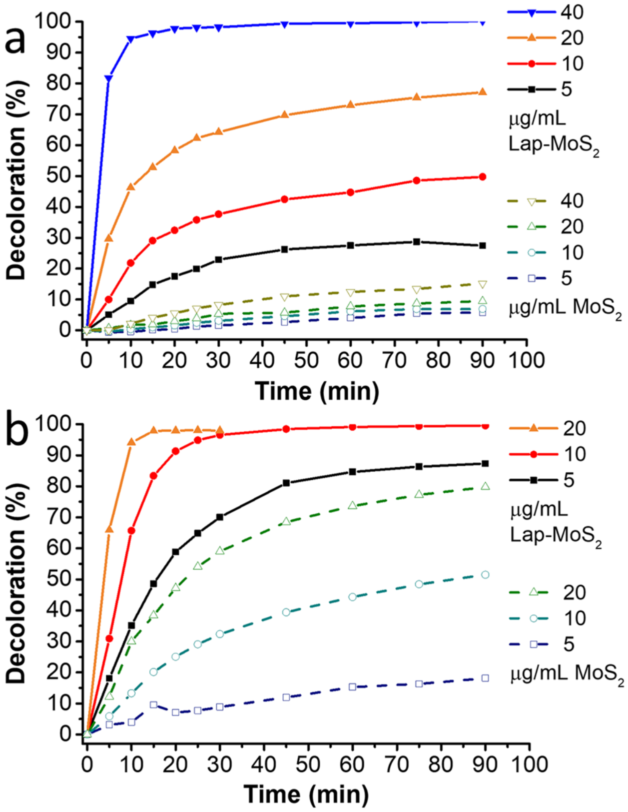

Figure 7. Catalytic degradation of (a) MO (67 μM) and (b) 4-NA (0.12 mM) at different catalyst concentrations. Lap−MoS$_2$ is indicated by solid lines; MoS$_2$ by dashed lines and open symbols.

The change in colloidal stability observed in the form of a precipitate at 0.183 nmol MB per μg Lap−MoS$_2$ suggested that ζ-potential may reveal the change of surface charge brought about by the change from a cationic MB-rich system to an anionic clay-rich system. Indeed, a MB/Lap−MoS$_2$ molar ratio above 150 resulted in a cationic surface charge of ~15 mV, indicating that the layered silicate surface of Lap−MoS$_2$ is covered with MB at an amount exceeding the cation exchange capacity (CEC). A MB/Lap−MoS$_2$ ratio less than 150 showed a negative zeta potential, which is ascribed to the lack of MB molecules sufficient to compensate for the surface charge of the layered silicate clay. This would result in the aggregation of the Lap−MoS$_2$ particles with the cationic MB molecules sandwiched between the exposed Lap surfaces. The Lap−MoS$_2$ itself was measured to have a zeta potential of ~−20 mV, where unmodified Lap has a zeta potential of −25 mV (Figure 6c).

Catalytic Dye Degradation. The reactions of 4-nitroaniline (4-NA) and methyl orange (MO) with NaBH$_4$ were chosen to evaluate the catalytic performance of the samples. The reduction of 4-NA and MO with NaBH$_4$ is a common measure of catalytic activity, as it is thermodynamically feasible but kinetically hindered by a high activation barrier.[20,23,57] Borohydride ions transfer surface−hydrogen species in a reversible manner to the surface of the particles, which can readily react with the adsorbed dye molecules.[58,59] In the case of MO, catalytic reduction leads to the formation of sulfanilic acid and *N*,*N*-dimethyl-*p*-phenylenediamine, whereas 4-NA is reduced to *p*-phenylenediamine. Without the presence of a catalyst, there is no generation of surface−hydrogen species

https://dx.doi.org/10.1021/acsami.0c02246
ACS Appl. Mater. Interfaces 2020, 12, 19813−19822

from BH_4^-, resulting in little reduction of the organic species. Control experiments where only catalyst or only $NaBH_4$ were used yield a decoloration of no more than 5% over 90 min (Figure S12). UV−vis spectra taken over the course of the reactions are shown in Figure S13.

There was a significant increase in catalytic activity of Lap−MoS_2 over that of MoS_2 (Figure 7). Although 40 μg/mL Lap−MoS_2 was required to fully react a solution of 67 μM MO, an equivalent amount of MoS_2 only removed 15%. 4-NA was more easily reduced, and 10 μg/mL Lap−MoS_2 was sufficient to fully react 0.12 mM 4-NA, where 10 μg/mL MoS_2 achieved no more than 50%. Furthermore, the Lap−MoS_2 particles gave significant enhancement in catalytic dye degradation compared with a previous hybrid system of montmorillonite−MoS_2. In the case of MO degradation, Lap−MoS_2 degraded 96% of the dye within 15 min, whereas a montmorillonite−MoS_2 hybrid degraded around 90% of the dye in the same time while using 5 times the catalyst concentration used herein.[23] There are several possible contributions to the improved performance of the Lap−MoS_2 compared to pristine MoS_2. First, the clay-like surface chemistry of the Lap−MoS_2 hybrids provides increased water dispersibility compared to MoS_2, resulting in higher effective surface area due to improved exfoliation. Second, small lateral dimensions of the Lap−MoS_2 particles (∼25 nm) means a greater proportion of catalytically active edge-sites of the intercalated MoS_2 than the larger (100−500 nm) MoS_2 particles. Finally, as Laponite can readily absorb a number of organic dyes, the dye molecules bound to the clay surface can be attacked by the surface hydrogen species, resulting in improved catalytic performance compared to pure MoS_2. Interestingly the difference between the dye degradation performance of the hybrid particles and pure MoS_2 becomes more pronounced for the case of the more complex molecule, MO, suggesting that these hybrid nanoparticles may be useful for water decontamination applications.

CONCLUSIONS

Many 2D semiconducting materials such as MoS_2 can be exfoliated to achieve a direct bandgap,[4,60−62] but suffer from extensive aggregation and are unstable in aqueous solution, hindering their application in photocatalysis and water purification. In addition, the majority of catalytic activity of MoS_2 is provided by the edge-sites,[63] allowing modification of the basal surfaces. The use of stirring during hydrothermal synthesis led to reduced settling and aggregation, and thereby smaller particles. These hybrid nanoparticles showed several features that have not been previously reported. Not only did the Lap−MoS_2 particles resemble Lap morphologically, but electron diffraction, EDX spectroscopy, and XRD show that the particle is a hybrid of alternating layers of MoS_2 and Lap. In addition to heterostructured layers, a positive correlation between the MoS_2 precursor concentration and the formation of expanded MoS_2 multilayers with a spacing of ∼1.04 nm was observed.

The surface chemistry of the nanohybrids was shown to be clay-like, as their surface charge and the molecular aggregation behavior of MB resemble that of Lap. Furthermore, their improved stability in aqueous solution compared to MoS_2 was evident. Finally, catalytic degradation of 4-NA and MO revealed significant enhancement of the activity of Lap−MoS_2 compared with MoS_2. The improved dispersibility, aqueous stability, ease of exfoliation, molecular absorption properties of the clay surface, and small particle diameter increasing surface area and proportion of catalytic Mo edge sites are all probable origins of the improvement of catalytic properties over MoS_2.

These results show that Lap is an ideal model system for the study of surfactant-templated growth of nanoscopic 2D materials, in part because of its small size and size distribution, optical transparency, and colloidal stability. Systematic studies of the synthesis are currently underway in order to understand how choice of pillaring surfactant, tuning of micelle geometry, and the reaction pH influence the final nanohybrid morphology and structure. It has also been shown that the surfactant, cetylpyridinium chloride can effectively pillar layered silicate clays,[64] and that CTAC/CTAB mixtures can give rise to wormlike or ellipsoidal micelles.[65] Furthermore, layered silicate clays can form a gel phase via a "house of cards"-type aggregation at low pH, suggesting that this work may present an approach to synthesize a bulk gel-phase hybrid material for photo- or electrocatalysis.[66] Finally, the successful growth of a 2D material on a nanoscopic template gives impetus to synthesize other 2D materials in the interlayer space, particularly where prevention of aggregation and aqueous stability is a concern. As the majority of synthetic approaches for monolayer MoS_2 are top-down, this presents a colloidal hydrothermal approach which should be applicable for the growth of other 2D materials. We look forward to future developments of such hybrid nanomaterials for applications in photocatalysis, sensing, and self-assembled materials for electronics and energy.

MATERIALS AND METHODS

Materials. Lap was provided by BYK additives (Germany). Sodium molybdate, Na_2MoO4 (99%), thioacetamide (99%), NaOH pellets (99%), MB, MO, 4-NA, and CTAB (>99%) were obtained from Sigma-Aldrich and used without further purification. All solutions and dispersions were prepared using Millipore-filtered water with a resistivity of 18.2 MΩ·cm. Lap dispersions are prepared by first adding the Lap powder to water under stirring, followed by addition of NaOH to reach a pH of 10. Following 24 h of stirring, the Lap dispersion is stored at 23 °C, and prior to use in the synthetic procedures, the dispersion is sonicated in a bath sonicator (480 W, Sonorex RK106, Bandelin, Berlin, DE) for 15 min.

Hydrothermal Synthesis of Lap−MoS_2 Nanohybrids. A dispersion of Lap (42 mL, 5 mg/mL) is added to a 100 mL Teflon beaker. Under magnetic stirring at 50 °C (700 rpm), CTAB (2.1 mL, 0.1 M) is added to the Lap dispersion. The flocculation of Lap by CTAB is immediately visible by increased opacity and turbidity of the dispersion. Assuming a CEC of Lap in the range of 0.55−0.8 mequiv/g,[26] there is an 18 to 26× excess of CTA^+ (4.4 mmol) over the total exchangeable cations (0.18 mequiv), which ensures the pillaring of all Lap present. After 10 min of stirring, a previously prepared solution of Na_2MoO_4 (24 mg/mL) and thioacetamide (30 mg/mL) is added to the dispersion to reach a final Mo−Lap ratio of 1.15, 0.57, 0.25, or 0.19, and the Teflon beaker is then inserted into the hydrothermal autoclave (BR-100, Berghof Instruments, Eningen, DE). The reactor is evacuated with argon gas, and magnetic stirring (700 rpm) is controlled by a hotplate below the reactor. The temperature is increased from 30 to 200 °C in 70 min, at which time the pressure of the reactor reached ∼15 bar. The reaction is carried out for 20 h, after which the heating is turned off and the reactor is allowed to cool to room temperature (∼23 °C) at a rate not exceeding 2 °C/min. The product is cleaned three times by centrifugation at 7500 rpm for 25 min and rinsing with water, and the cleaned product is collected and then dried in a vacuum oven (60 °C for 24 h). An MoS_2 control was synthesized following the same procedure as that of 1.15 Mo−Lap ratio (4.6 mg/mL Na_2MoO_4, 5.8 mg/mL thioacetamide) without the addition of Lap.

Characterization. UV−vis absorbance spectra were obtained using a Cary 60 UV−Vis spectrometer (Agilent, Santa Clara, CA, USA). Samples for electron microscopy were prepared by vacuum-drying 5−10 μL of a particle dispersion onto the carbon film of a copper TEM grid (300 mesh size, Formvar film, Ted Pella Inc., Redding, CA, USA). High-resolution TEM imaging, including EDX, was performed using a FEI Talos F200X transmission electron microscope (Thermo Scientific, Waltham, MA, USA) operated at 200 kV. XRD was performed on dried powder samples placed on top of Si(100) wafer (Bruker AXS D8 ADVANCE, Cu Kα, 40 kV, 40 mA, step size 0.01°, step time 3 s). The XRD spectra were analyzed using Diffrac.EVA software from Bruker, and the *d*-spacing values were calculated according to the peak positions obtained in the software. AFM was carried out using a Dimension 3000 atomic force microscope system (Digital Instruments, Santa Barbara, CA), with an SSS-NCLR cantilever (Nanosensors, Neuchatel, Switzerland) in the noncontact mode (f_r = 151 kHz, k = 48 N/m). AFM images were processed with Gwyddion software. Heightmaps were leveled using mean plane subtraction, followed by polynomial background subtraction, and correction of the zero set point. Line scans were made across different particles, and their height profiles were fitted using the step height function.

Catalytic Dye Degradation. The catalytic activity of the samples was examined using model reactions of reduction of 4-NA and MO with $NaBH_4$. Catalyst dispersions were prepared by first sonicating 20 mg of the catalyst powder in 2 mL of deionized (DI) water for 15 min, followed by further addition of DI water and a brief sonication to achieve the desired concentration. For a given experiment, 0.5 mg/mL MoS_2−Lap solution was added to an aqueous solution of MO (100 mL, 67 μM) or 4-NA (50 mL, 0.12 mM) to achieve the desired final concentration of the catalyst. After 15 min of stirring, $NaBH_4$ was added to reach 72 mM, initiating the reduction reaction. As a large excess of $NaBH_4$ is present, its concentration can be assumed to be constant. Concentrations of MO (λ = 464 nm, ε = 23,400 $M^{-1}\cdot cm^{-1}$) and 4-NA (λ = 380 nm, ε = 13,500 $M^{-1}\cdot cm^{-1}$) were calculated using the Beer−Lambert law. Two milliliter aliquots were taken at different times and their UV−vis spectra were recorded. Decoloration was evaluated as follows: decoloration (%) = $C_0 - C/C_0$, C_0 is the initial concentration of the dye and C is the concentration at a given time. The same procedure was used to evaluate the catalytic activity of the MoS_2 control, and control experiments with no catalyst and no $NaBH_4$ were also performed.

Dye Aggregation. MB was added to 20 mL of water to a final concentration of 10 μM. Different amounts of Lap−MoS_2 or MoS_2 dispersions (1 mg/mL) were then added to 2 mL aliquots of the dye solution to result in a final catalyst concentration ranging from 2 μg/mL to 0.2 mg/mL. UV−visible spectra were recorded and the samples were photographed at 0 and 24 h timepoints. In the case of MB, after 24 h of settling, the samples were diluted 10-fold and their zeta potentials were obtained with a Zetasizer ZS-Nano (Malvern Instruments, Malvern, United Kingdom).

■ ASSOCIATED CONTENT

Supporting Information

The Supporting Information is available free of charge at https://pubs.acs.org/doi/10.1021/acsami.0c02246.

> UV−vis spectra of Lap-MoS_2 and MoS_2 before and after settling for 48 h; TEM images of control particles, Lap-MoS_2 particles synthesized without stirring, MoS_2 control sample, individual Lap-MoS_2 particles, and Lap; statistics of measured interlayer spaces from TEM; AFM characterization of particle thickness; full range of EDX spectra; additional EDX maps of Lap-MoS_2 particles; UV−vis spectra of Methylene Blue with MoS_2 control; catalysis control experiments; and UV−vis spectra taken over the course of catalysis (PDF)

■ AUTHOR INFORMATION

Corresponding Author

Eric H. Hill − *Institute of Advanced Ceramics, Hamburg University of Technology, Hamburg 21073, Germany;* orcid.org/0000-0003-3063-1447; Email: eric.hill@tuhh.de

Authors

Sanjay Jatav − *Institute of Advanced Ceramics, Hamburg University of Technology, Hamburg 21073, Germany*

Kaline P. Furlan − *Institute of Advanced Ceramics, Hamburg University of Technology, Hamburg 21073, Germany;* orcid.org/0000-0003-4032-2795

Junying Liu − *Institute of Advanced Ceramics, Hamburg University of Technology, Hamburg 21073, Germany*

Complete contact information is available at: https://pubs.acs.org/10.1021/acsami.0c02246

Notes

The authors declare no competing financial interest.

■ ACKNOWLEDGMENTS

This research was funded by the DAAD from funds of the German Federal Ministry of Education and Research (BMBF), under the MOPGA-GRI program (57429511). We thank the Central Division of Electron Microscopy (BEEM) of the Hamburg University of Technology for providing a FEI Talos F200X, and Dr. Tobias Krekeler for informative discussions. We thank Gerold Schneider of the Institute of Advanced Ceramics for providing access to an X-ray Diffractometer. We thank BYK GmbH for providing the Laponite used in this study. We also thank the reviewers for their helpful suggestions, particularly regarding the XRD analysis.

■ REFERENCES

(1) Coleman, J. N.; Lotya, M.; O'Neill, A.; Bergin, S. D.; King, P. J.; Khan, U.; Young, K.; Gaucher, A.; De, S.; Smith, R. J.; Shvets, I. V.; Arora, S. K.; Stanton, G.; Kim, H.-Y.; Lee, K.; Kim, G. T.; Duesberg, G. S.; Hallam, T.; Boland, J. J.; Wang, J. J.; Donegan, J. F.; Grunlan, J. C.; Moriarty, G.; Shmeliov, A.; Nicholls, R. J.; Perkins, J. M.; Grieveson, E. M.; Theuwissen, K.; McComb, D. W.; Nellist, P. D.; Nicolosi, V. Two-Dimensional Nanosheets Produced by Liquid Exfoliation of Layered Materials. *Science* **2011**, *331*, 568−571.

(2) Voiry, D.; Mohite, A.; Chhowalla, M. Phase Engineering of Transition Metal Dichalcogenides. *Chem. Soc. Rev.* **2015**, *44*, 2702−2712.

(3) Li, C.; Cao, Q.; Wang, F.; Xiao, Y.; Li, Y.; Delaunay, J.-J.; Zhu, H. Engineering Graphene and TMDs Based van Der Waals Heterostructures for Photovoltaic and Photoelectrochemical Solar Energy Conversion. *Chem. Soc. Rev.* **2018**, *47*, 4981−5037.

(4) Shen, J.; He, Y.; Wu, J.; Gao, C.; Keyshar, K.; Zhang, X.; Yang, Y.; Ye, M.; Vajtai, R.; Lou, J.; Ajayan, P. M. Liquid Phase Exfoliation of Two-Dimensional Materials by Directly Probing and Matching Surface Tension Components. *Nano Lett.* **2015**, *15*, 5449−5454.

(5) Dong, R.; Zhang, T.; Feng, X. Interface-Assisted Synthesis of 2D Materials: Trend and Challenges. *Chem. Rev.* **2018**, *118*, 6189−6235.

(6) King, L. A.; Zhao, W.; Chhowalla, M.; Riley, D. J.; Eda, G. Photoelectrochemical Properties of Chemically Exfoliated MoS2. *J. Mater. Chem. A* **2013**, *1*, 8935−8941.

(7) Mahler, B.; Hoepfner, V.; Liao, K.; Ozin, G. A. Colloidal Synthesis of 1T-WS2 and 2H-WS2 Nanosheets: Applications for Photocatalytic Hydrogen Evolution. *J. Am. Chem. Soc.* **2014**, *136*, 14121−14127.

(8) Lu, Q.; Yu, Y.; Ma, Q.; Chen, B.; Zhang, H. 2D Transition-Metal-Dichalcogenide-Nanosheet-Based Composites for Photocata-

lytic and Electrocatalytic Hydrogen Evolution Reactions. *Adv. Mater.* **2016**, *28*, 1917−1933.

(9) Guardia, L.; Paredes, J. I.; Munuera, J. M.; Villar-Rodil, S.; Ayán-Varela, M.; Martínez-Alonso, A.; Tascón, J. M. D. Chemically Exfoliated MoS2 Nanosheets as an Efficient Catalyst for Reduction Reactions in the Aqueous Phase. *ACS Appl. Mater. Interfaces* **2014**, *6*, 21702−21710.

(10) Das, P.; Malho, J.; Rahimi, K.; Schacher, F. H.; Wang, B.; Demco, D. E.; Walther, A. Nacre-Mimetics with Synthetic Nanoclays up to Ultrahigh Aspect Ratios. *Nat. Commun.* **2015**, *6*, 5967.

(11) Hill, E. H.; Zhang, Y.; Whitten, D. G. Aggregation of Cationic P-Phenylene Ethynylenes on Laponite Clay in Aqueous Dispersions and Solid Films. *J. Colloid Interface Sci.* **2015**, *449*, 347−356.

(12) López Arbeloa, F.; Martínez Martínez, V. Orientation of Adsorbed Dyes in the Interlayer Space of Clays. 2 Fluorescence Polarization of Rhodamine 6G in Laponite Films. *Chem. Mater.* **2006**, *18*, 1407−1416.

(13) Cenens, J.; Schoonheydt, R. A. Visible Spectroscopy of Methylene Blue on Hectorite, Laponite B, and Barasym in Aqueous Suspension. *Clays Clay Miner.* **1988**, *36*, 214−224.

(14) Grauer, Z.; Malter, A. B.; Yariv, S.; Avnir, D. Sorption of Rhodamine B by Montmorillonite and Laponite. *Colloids Surf.* **1987**, *25*, 41−65.

(15) Li, W.; Dong, H.; Wang, L.; Li, N.; Guo, X.; Li, J.; Qiu, Y. Montmorillonite as Bifunctional Buffer Layer Material for Hybrid Perovskite Solar Cells with Protection from Corrosion and Retarding Recombination. *J. Mater. Chem. A* **2014**, *2*, 13587−13592.

(16) Mäkiniemi, R. O.; Das, P.; Hönders, D.; Grygiel, K.; Cordella, D.; Detrembleur, C.; Yuan, J.; Walther, A. Conducting, Self-Assembled, Nacre-Mimetic Polymer/Clay Nanocomposites. *ACS Appl. Mater. Interfaces* **2015**, *7*, 15681−15685.

(17) Zhao, H.; Yue, Y.; Zhang, Y.; Li, L.; Guo, L. Ternary Artificial Nacre Reinforced by Ultrathin Amorphous Alumina with Exceptional Mechanical Properties. *Adv. Mater.* **2016**, *28*, 2037−2042.

(18) Zhu, J.; Liu, X.; Geier, M. L.; McMorrow, J. J.; Jariwala, D.; Beck, M. E.; Huang, W.; Marks, T. J.; Hersam, M. C. Layer-by-Layer Assembled 2D Montmorillonite Dielectrics for Solution-Processed Electronics. *Adv. Mater.* **2016**, *28*, 63−68.

(19) Hill, E. H.; Hanske, C.; Johnson, A.; Yate, L.; Jelitto, H.; Schneider, G. A.; Liz-Marzán, L. M. Metal Nanoparticle Growth within Clay-Polymer Nacre-Inspired Materials for Improved Catalysis and Plasmonic Detection in Complex Biofluids. *Langmuir* **2017**, *33*, 8774−8783.

(20) Peng, K.; Fu, L.; Yang, H.; Ouyang, J.; Tang, A. Hierarchical MoS2 Intercalated Clay Hybrid Nanosheets with Enhanced Catalytic Activity. *Nano Res.* **2017**, *10*, 570−583.

(21) Negrete; Letoffe, J.-M.; Putaux, J.-L.; David, L.; Bourgeat-Lami, E. Aqueous Dispersions of Silane-Functionalized Laponite Clay Platelets. A First Step toward the Elaboration of Water-Based Polymer/Clay Nanocomposites. *Langmuir* **2004**, *20*, 1564−1571.

(22) Zhang, J.; Zhou, C. H.; Petit, S.; Zhang, H. Hectorite: Synthesis, Modification, Assembly and Applications. *Appl. Clay Sci.* **2019**, *177*, 114−138.

(23) Peng, K.; Fu, L.; Ouyang, J.; Yang, H. Emerging Parallel Dual 2D Composites: Natural Clay Mineral Hybridizing MoS 2 and Interfacial Structure. *Adv. Funct. Mater.* **2016**, *26*, 2666−2675.

(24) Fornes, T. D.; Hunter, D. L.; Paul, D. R. Effect of Sodium Montmorillonite Source on Nylon 6/Clay Nanocomposites. *Polymer* **2004**, *45*, 2321−2331.

(25) Poli, A. L.; Batista, T.; Schmitt, C. C.; Gessner, F.; Neumann, M. G. Effect of Sonication on the Particle Size of Montmorillonite Clays. *J. Colloid Interface Sci.* **2008**, *325*, 386−390.

(26) Suman, K.; Joshi, Y. M. Microstructure and Soft Glassy Dynamics of an Aqueous Laponite Dispersion. *Langmuir* **2018**, *34*, 13079−13103.

(27) Hill, E. H.; Claes, N.; Bals, S.; Liz-Marzán, L. M. Layered Silicate Clays as Templates for Anisotropic Gold Nanoparticle Growth. *Chem. Mater.* **2016**, *28*, 5131−5139.

(28) Karunadasa, H. I.; Montalvo, E.; Sun, Y.; Majda, M.; Long, J. R.; Chang, C. J. A Molecular MoS2 Edge Site Mimic for Catalytic Hydrogen Generation. *Science* **2012**, *335*, 698−702.

(29) Lee, S. A.; Fitch, A. Conductivity of Clay-Modified Electrodes: Alkali Metal Cation Hydration and Film Preparation Effects. *J. Phys. Chem.* **1990**, *94*, 4998−5004.

(30) Falaras, P.; Petridis, D. Incorporation of Anionic Species in Organoclay-Modified Electrodes. *J. Electroanal. Chem.* **1992**, *337*, 229−239.

(31) Navrátilová, Z.; Kula, P. Cation and Anion Exchange on Clay Modified Electrodes. *J. Solid State Electrochem.* **2000**, *4*, 342−347.

(32) Liao, L.; Lv, G.; Cai, D.; Wu, L. The Sequential Intercalation of Three Types of Surfactants into Sodium Montmorillonite. *Appl. Clay Sci.* **2016**, *119*, 82−86.

(33) De Santana, H.; Paesano, A.; Da Costa, A. C. S.; Di Mauro, E.; De Souza, I. G.; Ivashita, F. F.; De Souza, C. M. D.; Zaia, C. T. B. V.; Zaia, D. A. M. Cysteine, Thiourea and Thiocyanate Interactions with Clays: FT-IR, Mössbauer and EPR Spectroscopy and X-Ray Diffractometry Studies. *Amino Acids* **2010**, *38*, 1089−1099.

(34) Khaorapapong, N.; Kuroda, K.; Ogawa, M. Incorporation of Thioacetamide into the Interlayer Space of Montmorillonite by Solid-Solid Reactions. *Clay Sci.* **2002**, *11*, 549−564.

(35) Peng, K.; Wang, H.; Li, X.; Wang, J.; Cai, Z.; Su, L.; Fan, X. Emerging WS2/Montmorillonite Composite Nanosheets as an Efficient Hydrophilic Photocatalyst for Aqueous Phase Reactions. *Sci. Rep.* **2019**, *9*, 16325.

(36) Ngassa, G. B. P.; Tonlé, I. K.; Walcarius, A.; Ngameni, E. One-Step Co-Intercalation of Cetyltrimethylammonium and Thiourea in Smectite and Application of the Organoclay to the Sensitive Electrochemical Detection of Pb(II). *Appl. Clay Sci.* **2014**, *99*, 297−305.

(37) Ngassa Piegang, G. B.; Tonle, I. K.; Walcarius, A.; Ngameni, E. An Inorganic-Organic Hybrid Material from the Co-Intercalation of a Cationic Surfactant and Thiourea within Montmorillonite Layers: Application to the Sensitive Stripping Voltammetric Detection of Pb2+ and Cd2+ Ions. *C. R. Chim.* **2016**, *19*, 789−797.

(38) Li, X.-L.; Li, Y.-D. MoS_2 Nanostructures: Synthesis and Electrochemical Mg^{2+} Intercalation. *J. Phys. Chem. B* **2004**, *108*, 13893−13900.

(39) Su, X.; Wang, D.; Yan, Q.; Guo, X.; Fang, S.; Liu, Y. Preparation, Microstructure, Electromagnetic Property and Microwave Absorption Property of MoS2 Nanopowder by Hydrothermal Method at Various Reaction Temperatures. *J. Mater. Sci.: Mater. Electron.* **2018**, *29*, 4020−4029.

(40) Shi, Y.; Wang, J.; Wang, C.; Zhai, T.-T.; Bao, W.-J.; Xu, J.-J.; Xia, X.-H.; Chen, H.-Y. Hot Electron of Au Nanorods Activates the Electrocatalysis of Hydrogen Evolution on MoS2 Nanosheets. *J. Am. Chem. Soc.* **2015**, *137*, 7365−7370.

(41) Li, B.; Jiang, L.; Li, X.; Ran, P.; Zuo, P.; Wang, A.; Qu, L.; Zhao, Y.; Cheng, Z.; Lu, Y. Preparation of Monolayer MoS2 Quantum Dots Using Temporally Shaped Femtosecond Laser Ablation of Bulk MoS2 Targets in Water. *Sci. Rep.* **2017**, *7*, 11182.

(42) Visic, B.; Dominko, R.; Gunde, M. K.; Hauptman, N.; Skapin, S. D.; Remskar, M. Optical Properties of Exfoliated MoS 2 Coaxial Nanotubes - Analogues of Graphene. *Nanoscale Res. Lett.* **2011**, *6*, 593.

(43) Lei, B.; Li, G. R.; Gao, X. P. Morphology Dependence of Molybdenum Disulfide Transparent Counter Electrode in Dye-Sensitized Solar Cells. *J. Mater. Chem. A* **2014**, *2*, 3919−3925.

(44) Daniel, L. M.; Frost, R. L.; Zhu, H. Y. Edge-Modification of Laponite with Dimethyl-Octylmethoxysilane. *J. Colloid Interface Sci.* **2008**, *321*, 302−309.

(45) Silva, J. M.; Maturi, F. E.; Barud, H. S.; Constantino, V. R. L.; Ribeiro, S. J. L. New Organic-Inorganic Hybrid Composites Based on Cellulose Nanofibers and Modified Laponite. *Adv. Opt. Technol.* **2018**, *7*, 327−334.

(46) Zheng, J.; Zhang, H.; Dong, S.; Liu, Y.; Tai Nai, C.; Suk Shin, H.; Young Jeong, H.; Liu, B.; Ping Loh, K. High Yield Exfoliation of

Two-Dimensional Chalcogenides Using Sodium Naphthalenide. *Nat. Commun.* **2014**, *5*, 2995.

(47) Li, Y.; Liang, Y.; Robles Hernandez, F. C.; Deog Yoo, H.; An, Q.; Yao, Y. Enhancing Sodium-Ion Battery Performance with Interlayer-Expanded MoS2-PEO Nanocomposites. *Nano Energy* **2015**, *15*, 453−461.

(48) Zhao, C.; Wang, X.; Kong, J.; Ang, J. M.; Lee, P. S.; Liu, Z.; Lu, X. Self-Assembly-Induced Alternately Stacked Single-Layer MoS2 and N-Doped Graphene: A Novel van Der Waals Heterostructure for Lithium-Ion Batteries. *ACS Appl. Mater. Interfaces* **2016**, *8*, 2372−2379.

(49) Xie, J.; Zhang, J.; Li, S.; Grote, F.; Zhang, X.; Zhang, H.; Wang, R.; Lei, Y.; Pan, B.; Xie, Y. Controllable Disorder Engineering in Oxygen-Incorporated MoS_2 Ultrathin Nanosheets for Efficient Hydrogen Evolution. *J. Am. Chem. Soc.* **2013**, *135*, 17881−17888.

(50) Wang, S.; Tu, J.; Yuan, Y.; Ma, R.; Jiao, S. Sodium Modified Molybdenum Sulfide via Molten Salt Electrolysis as an Anode Material for High Performance Sodium-Ion Batteries. *Phys. Chem. Chem. Phys.* **2016**, *18*, 3204−3213.

(51) Zak, A.; Feldman, Y.; Lyakhovitskaya, V.; Leitus, G.; Popovitz-Biro, R.; Wachtel, E.; Cohen, H.; Reich, S.; Tenne, R. Alkali Metal Intercalated Fullerene-like MS2 (M = W, Mo) Nanoparticles and Their Properties. *J. Am. Chem. Soc.* **2002**, *124*, 4747−4758.

(52) Wang, X.; Shen, X.; Wang, Z.; Yu, R.; Chen, L. Atomic-Scale Clarification of Structural Transition of MoS2 upon Sodium Intercalation. *ACS Nano* **2014**, *8*, 11394−11400.

(53) Song, Y.; Lu, M.; Huang, B.; Wang, D.; Wang, G.; Zhou, L. Decoration of Defective MoS2 Nanosheets with Fe3O4 Nanoparticles as Superior Magnetic Adsorbent for Highly Selective and Efficient Mercury Ions (Hg2+) Removal. *J. Alloys Compd.* **2018**, *737*, 113−121.

(54) Ai, K.; Ruan, C.; Shen, M.; Lu, L. MoS2 Nanosheets with Widened Interlayer Spacing for High-Efficiency Removal of Mercury in Aquatic Systems. *Adv. Funct. Mater.* **2016**, *26*, 5542−5549.

(55) Wang, Z.; Sim, A.; Urban, J. J.; Mi, B. Removal and Recovery of Heavy Metal Ions by Two-Dimensional MoS2 Nanosheets: Performance and Mechanisms. *Environ. Sci. Technol.* **2018**, *52*, 9741−9748.

(56) Avery, R. G.; Ramsay, J. D. F. Colloidal Properties of Synthetic Hectorite Clay Dispersions. II. Light and Small Angle Neutron Scattering. *J. Colloid Interface Sci.* **1986**, *109*, 448−454.

(57) Lin, T.; Wang, J.; Guo, L.; Fu, F. Fe3O4@MoS2 Core-Shell Composites: Preparation, Characterization, and Catalytic Application. *J. Phys. Chem. C* **2015**, *119*, 13658−13664.

(58) Zhang, H.; Li, X.; Chen, G. Ionic Liquid-Facilitated Synthesis and Catalytic Activity of Highly Dispersed Ag Nanoclusters Supported on TiO2. *J. Mater. Chem.* **2009**, *19*, 8223−8231.

(59) Wunder, S.; Polzer, F.; Lu, Y.; Mei, Y.; Ballauff, M. Kinetic Analysis of Catalytic Reduction of 4-Nitrophenol by Metallic Nanoparticles Immobilized in Spherical Polyelectrolyte Brushes. *J. Phys. Chem. C* **2010**, *114*, 8814−8820.

(60) Rizvi, R.; Nguyen, E. P.; Kowal, M. D.; Mak, W. H.; Rasel, S.; Islam, M. A.; Abdelaal, A.; Joshi, A. S.; Zekriardehani, S.; Coleman, M. R.; Kaner, R. B. High-Throughput Continuous Production of Shear-Exfoliated 2D Layered Materials Using Compressible Flows. *Adv. Mater.* **2018**, *30*, 1800200.

(61) Nicolosi, V.; Chhowalla, M.; Kanatzidis, M. G.; Strano, M. S.; Coleman, J. N. Liquid Exfoliation of Layered Materials. *Science* **2013**, *340*, 1226419.

(62) Tan, C.; Cao, X.; Wu, X.-J.; He, Q.; Yang, J.; Zhang, X.; Chen, J.; Zhao, W.; Han, S.; Nam, G.-H.; Sindoro, M.; Zhang, H. Recent Advances in Ultrathin Two-Dimensional Nanomaterials. *Chem. Rev.* **2017**, *117*, 6225−6331.

(63) Zhang, J.; Wu, J.; Guo, H.; Chen, W.; Yuan, J.; Martinez, U.; Gupta, G.; Mohite, A.; Ajayan, P. M.; Lou, J. Unveiling Active Sites for the Hydrogen Evolution Reaction on Monolayer MoS_2. *Adv. Mater.* **2017**, *29*, 1701955.

(64) Xu, Z.; Lv, F.; Zhang, Y.; Fu, L. Synthesis and Characterization of CPC Modified Magnetic MMT Capable of Using as Anisotropic Nanoparticles. *Chem. Eng. J.* **2013**, *215-216*, 755−762.

(65) Han, S.; Hou, W.; Dang, W.; Xu, J.; Hu, J.; Li, D. Synthesis of Rod-like Mesoporous Silica Using Mixed Surfactants of Cetyltrimethylammonium Bromide and Cetyltrimethylammonium Chloride as Templates. *Mater. Lett.* **2003**, *57*, 4520−4524.

(66) Cummins, H. Z. Liquid, Glass, Gel: The Phases of Colloidal Laponite. *J. Non-Cryst. Solids* **2007**, *353*, 3891−3905.

Chapter 3

Facet Engineering of Bismuth Molybdate via Confined Growth in a Nanoscale Template toward Water Remediation

This chapter has been published as: Jatav, S.; Liu, J.; Herber, M.; Hill, E. H. Facet Engineering of Bismuth Molybdate via Confined Growth in a Nanoscale Template toward Water Remediation. *ACS Applied Materials & Interfaces*. **2021**, 13(16), 18713-18723.

After obtaining the growth of isolated monolayers of MoS_2 confined by the organically-modified laponite interlayers (chapter 2), the subsequent task was to extend this synthetic methodology for obtaining thin/ confined growth of other semiconductors. Hence, in this study, organically-modified laponite was used for templating the growth of photocatalytic Bi_2MoO_6 for obtaining thin platelets of the latter, since thin platelets exhibit better photocatalytic performance. Our investigations revealed that Bi_2MoO_6 growth on laponite can improve the adsorption capacity of the underlying clay substrate. Herein, we were able to remove model pollutants from water by their adsorption onto these laponite-Bi_2MoO_6 hybrids and photodegrade the adsorbed pollutant later by exploiting the photocatalytic activity of Bi_2MoO_6.

ACS APPLIED MATERIALS & INTERFACES

www.acsami.org Research Article

Facet Engineering of Bismuth Molybdate via Confined Growth in a Nanoscale Template toward Water Remediation

Sanjay Jatav, Junying Liu, Marcel Herber, and Eric H. Hill*

Cite This: *ACS Appl. Mater. Interfaces* 2021, 13, 18713−18723

Read Online

ACCESS | Metrics & More | Article Recommendations | Supporting Information

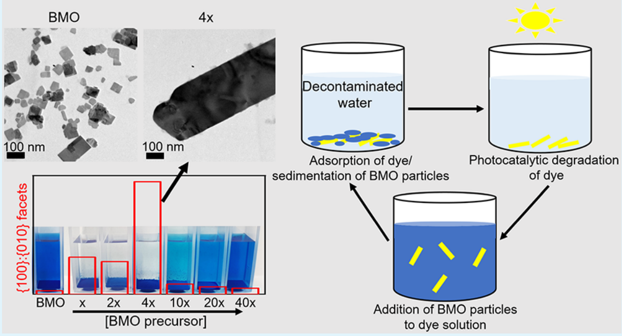

ABSTRACT: Certain nanomaterials can filter and alter unwanted compounds due to a high surface area, surface reactivity, and microporous structure. Herein, γ-Bi_2MoO_6 particles are synthesized via a colloidal hydrothermal approach using organically modified Laponite as a template. This organically modified Laponite interlayer serves as a template promoting the growth of the bismuth molybdate crystals in the [010] direction to result in hybrid Laponite−Bi_2MoO_6 particles terminating predominantly in the {100} crystal facets. This resulted in an increase in particle size from lateral dimensions of <100 nm to micron scale and superior adsorption capacity compared to bismuth molybdate nanoparticles. These {100}-facet terminated particles can load both cationic and anionic dyes on their surfaces near-spontaneously and retain the photocatalytic properties of Bi_2MoO_6. Furthermore, dye-laden hybrid particles quickly sediment, rendering the task of particle recovery trivial. The adsorption of dyes is completed within minutes, and near-complete photocatalytic degradation of the adsorbed dye in visible light allowed recycling of these particles for multiple cycles of water decontamination. Their adsorption capacity, facile synthesis, good recycling performance, and increased product yield compared to pure bismuth molybdate make them promising materials for environmental remediation. Furthermore, this synthetic approach could be exploited for facet engineering in other Aurivillius-type perovskites and potentially other materials.

KEYWORDS: *Bi_2MoO_6, dye adsorption, Laponite, layered silicates, environmental remediation*

■ INTRODUCTION

A pressing global problem on par with anthropogenic climate change is anthropogenic contamination of soil and water.[1,2] A consequence of our reliance on fossil fuel-powered facilities to manufacture products at scale is the emission of greenhouse gases along with the release of toxic byproducts into the environment.[3,4] These pollutants include simple atomic entities like heavy metal ions of As, Cd, Cs, Hg, and Pb[5,6] as well as molecules such as per- and polyfluoroalkyls.[7] Moreover, pollutants composed of complex molecules like plastics, synthetic dyes, pesticides, and pharmaceutical waste also contribute toward contaminating the environment.[8−10] An account of how these chemicals interact and cause harm to the human body can be found elsewhere.[3,11] One of the primary contributors in this vein is the highly visible wastewater effluents from textile, printing, cosmetic, and pharmaceutical industries.[4,12] Dye-contaminated water reduces or in extreme cases completely blocks sunlight being transmitted through water, which in turn adversely affects underwater ecosystems.[13] Furthermore, many industrial dyes are toxic, having mutagenic and carcinogenic effects.[14,15] As the discharge of such pollutants hinders attempts to keep the toxicity of the environment in check, measures should be taken to ensure proper treatment of contaminated water before its release into the environment.

Most industrial dyes are non-biodegradable or biodegrade very slowly, which makes contaminated water treatment necessary.[15,16] They are challenging to remove because of their high solubility and stability in water.[17] Traditional wastewater treatment methods employ physicochemical,[18] biological, and advanced oxidative processes (AOPs).[19] Recently, electrochemical processes have also been explored for treating wastewater.[20] All these techniques suffer from limitations that make their deployment on a large scale difficult or slow. For example, biological processes that employ bacteria/algae, etc. are time-consuming, require large operational areas, and are ineffective against barely biodegradable and recalcitrant industrial pollutants. Physicochemical processes for example require coagulation, flocculation, and

Received: January 18, 2021
Accepted: April 5, 2021
Published: April 15, 2021

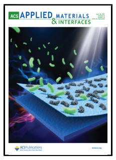

Scheme 1. Hydrothermal Synthesis of Pillared Lap−BMO Particles

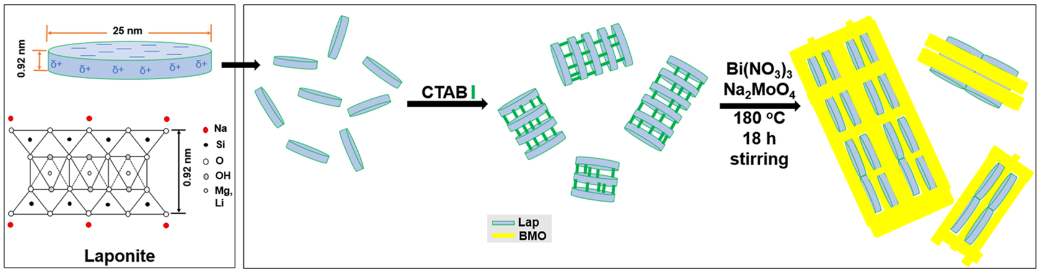

sedimentation stages for their action, which are expensive and ineffective and cause secondary pollution due to formation of sludge.[21] AOPs, which include wet oxidation, ozonation, heterogeneous photocatalysis, and the Fenton process, require high energy for operation, are costly, and cannot always degrade all recalcitrant compounds.[22] Mycoremediation has also shown limited success in breaking down recalcitrant compounds.[23] Another physical process that has been explored is adsorption onto a dispersed solid. Adsorption has an advantage over the other techniques in that it is a spontaneous process and cheap and can allow easy recycling of the sorbent. Activated carbon has been widely studied in this regard, but its widespread deployment is hindered by material and regeneration costs.[24]

Laponite (Lap) is a synthetic hectorite layered silicate clay with an octahedral Mg layer between two tetrahedral silica layers.[25] These disk-shaped particles are 25−30 nm in diameter and are 0.92 nm thick.[26] Because of the isomorphic substitution of divalent Mg by monovalent Li (in the octahedral layer), the faces of these discoidal particles acquire a negative charge, which is compensated by Na^+ ions associated with the basal surface.[27,28] One of the most intriguing properties of layered silicate clays in general and Lap in particular is the high cation exchange capacity (CEC),[28] which allows the exchange of Na^+ ions with cationic surfactants and molecules.[29−31] Meanwhile, the exchange of Na^+ by cetyltrimethylammonium chloride can result in exfoliation;[32] cetyltrimethylammonium bromide and cetylpyridiunium chloride cause "pillaring" or aggregation of Lap into vertically stacked floccules. This results in an expanded interlayer space, the size of which is also dependent on the length of the hydrocarbon tail of the exchanged entity.[28] As a consequence of their high surface area and surface charge, pillared clays have been shown to strongly adsorb dyes and heavy metal cations.[33,34] The expanded, organophilic interlayer space in pillared Lap has opened up an avenue for the growth of nanoscopic layered materials in the intergallery space.[35−37]

Bismuth-based mixed oxides with a layered structure belong to the Aurivillius group. Bismuth molybdate, Bi_2MoO_6 (BMO), from this group is composed of alternating $(Bi_2O_2)^{2+}$ and $(MoO_4)^{2-}$ layers, stacked along the *b*-axis of the unit cell. This layered structure, apart from being conducive to oxide ion mobility,[38] also confers a narrow band gap that can be extended to 500 nm.[39] Nanoparticles of BMO have been studied for catalytic,[40−43] gas sensing,[44,45] photocatalytic[46−48] and supercapacitor applications.[49] BMO is interesting not only due to its good performance in these applications but also because its properties and performance are closely related to particle structures and morphology.[50,51] It has been shown that the morphology of BMO nanoparticles can be controlled by changing reaction pH or introducing surfactants into the synthesis.[52] Recently, Xing et al. synthesized ultrathin BMO particles that selectively adsorbed cationic dye and enhanced photocatalytic activity by introducing mannitol into the precursor solution.[53]

Herein, bismuth molybdate was grown in the pillared interlayer space of Lap, resulting in the formation of particles with drastically altered morphology that could efficiently adsorb and photodegrade dye molecules. This synthetic approach yielded changes in the crystalline growth direction of BMO, which resulted in the formation of particles predominantly capped with {100}-crystal facets. With the dominance of {100} facets emerged greatly enhanced adsorption kinetics and the capacity to adsorb both cationic and anionic dyes. Interestingly, their adsorption capacity surpasses that of pillared Lap (clays), which are known to be effective sorbents of various molecules and ions.[33,54,55] The photocatalytic activity and sedimentation of these particles (laden with dye molecules) provide a facile means to reuse and recover these particles. Furthermore, the size of these {100} faceted particles can be tailored by controlling the pH of the precursor dispersion. Overall, apart from increased product yield, this strategy provides a facile means to tailor the crystal growth direction and studying crystal-facet-dependent properties.

■ EXPERIMENTAL METHODS

Materials. Laponite-RD was provided by BYK Additives (Germany). Sodium molybdate, Na_2MoO_4 (99%), bismuth nitrate, $Bi(NO_3)_3$ (99%), NaOH pellets (99%), rhodamine B (RhB), methylene blue (MB) and methyl orange (MO), and cetyl trimethylammonium bromide (CTAB, >99%) were obtained from Sigma-Aldrich and used without further purification. Nitric acid (HNO_3, 65% w/w) was obtained from Chemsolute and used without further purification. Polyvinyl alcohol (PVA), 87−89% hydrolyzed with an average molecular weight of 88k−97k g/mol, was obtained from Alfa Aesar. All solutions and dispersions were prepared using Millipore-filtered water with a resistivity of 18.2 MΩ·cm. Lap powder was dried at 120 °C for 4 h prior to preparing any dispersion. A total of 2.5 g of Lap powder was added to 500 mL of water under stirring followed by addition of 0.2 mL of 1 M NaOH to reach a pH of 10. After 24 h of stirring, the Lap dispersion was stored at 23 °C, and prior to use in synthesis, the Lap dispersion was sonicated in a bath sonicator (480 W, Sonorex RK106, Bandelin, Berlin, DE) for 15 min.

Hydrothermal Synthesis of Lap−Bi_2MoO_6. A dispersion of Lap (11 mL, 5 mg/mL) was added to a 50 mL Teflon beaker containing 17 mL of deionized water (Scheme 1). Under magnetic stirring, CTAB (0.560 mL, 0.1 M) was added to the Lap dispersion. The flocculation of Lap by CTAB is immediately visible by increased opacity and turbidity of the dispersion. Assuming a CEC of Lap in a range of 0.55−0.8 mequiv/g,[54] there is 1.25 times excess of CTA^+ cations over the total exchangeable cations, allowing complete pillaring of Lap. After 10 min of stirring, a previously prepared solution of Na_2MoO_4 (3 mg/mL) and $Bi(NO_3)_3$ (10 mg/mL) was

https://doi.org/10.1021/acsami.1c01144
ACS Appl. Mater. Interfaces 2021, 13, 18713−18723

added to the dispersion to reach final Bi concentrations of 0.25, 0.5, 1, 2.5, 5, or 10 mM, always keeping the Bi:Mo precursor ratio constant. This solution was prepared by adding the desired amount of Bi_2MoO_6 precursors to 6.7 mL of water and subsequently sonicating it for 10 min. After the addition of precursors to the Lap−CTAB dispersion, the beaker was sonicated for 10 min. These samples have been labeled as PLB-0.05x, PLB-0.1x, PLB-0.2x, PLB-0.5x, PLB-1x, and PLB-2x, respectively. The pH values prior to synthesis were measured to be 8.17, 6.4, 3.48, 2.74, 2.18, and 1.81 for the aforementioned samples, respectively. The Teflon beaker was then inserted into a hydrothermal autoclave (DAB-2, Berghof Instruments, Eningen, DE). The autoclave was placed in an oven over a heat-resistant magnetic stirring plate (MIXdrive 6, 2mag, Muenchen, DE) stirring at 720 rpm. The temperature was maintained at 180 °C for 18 h, after which the reactor was allowed to cool to room temperature. The yellow precipitates were rinsed seven times with water and two times with ethanol and centrifuged at 7500 rpm for 10 min, and the cleaned product was then dried at 60 °C for 24 h. A BMO control was synthesized following the same procedure without the addition of Lap, and it is labeled as BMO. Here, the pH was measured to be 1.85. Hydrothermally treated CTAB-pillared Lap was also synthesized following the same procedure without the addition of precursors and is labeled as PL. For studying the effect of reaction duration on the templated growth of BMO, PLB-0.2x samples were synthesized with reaction times of 30 min, 1 h, 3 h, and 5 h. For studying the influence of pH on BMO growth, PLB-0.2x samples were synthesized at pH values of 2.04, 4.24, 6.3, and 8.24, adjusted using 0.2 M NaOH or 0.2 M HNO_3. Samples were also prepared by varying the concentration of all the reactants by 1.5× and 2.5× compared with PLB-1.0, labeled as PLB_1.5 and PLB_2.5, respectively.

Characterization. UV−Vis absorbance spectra were obtained using a Cary 60 UV−Vis spectrometer (Agilent, Santa Clara, CA, USA). High-resolution transmission electron microscopy was carried out on a Phillips CM300 HRTEM (Phillips, Netherlands) to investigate the morphologies of the different samples. High-resolution transmission electron microscopy (Talos F200X, FEI, USA) was also performed to obtain HAADF-STEM mappings of the samples. Samples for electron microscopy were prepared by drying 5−10 μL of a particle dispersion onto the carbon film of a copper TEM grid (300 mesh size, Formvar film, Ted Pella Inc., Redding, CA, USA). The crystal structure of the as-prepared samples was determined using a PANalytical X'PERT Pro diffractometer (Phillips, Netherlands). Aqueous suspensions of the samples were pipetted onto a Si ⟨100⟩ wafer and heated till the powders were completely dried. Crystal plane intensity ratios were evaluated after subtracting the baseline from the corresponding X-ray diffractograms. Zeta potential was measured using a Malvern Zeta-sizer Nano ZS (Malvern Instruments, UK). N_2 adsorption−desorption isotherms were measured on an Autosorb iQ automated gas sorption analyzer (Quantacore instruments, Boynton Beach, FL, USA). Samples were degassed at 150 °C for 6 h prior to commencing N_2 adsorption. A total of 100 mg of powder was used for analysis. The isotherms were obtained at 77 K, and the surface area was estimated using the Brunauer−Emmett−Teller (BET) equation by choosing seven points on the isotherms between 0.05 and 0.30 relative pressure values to ensure a good fit. Diffuse reflectance UV−visible (UV−Vis) spectra were obtained using a Cary 5000 UV−Vis−NIR Spectrometer (Agilent Inc., Santa Clara, CA, USA).

Dye Adsorption. RhB, MB, and MO dyes were used to study the adsorption behavior of Lap−BMO particles. Sorbent dispersions were prepared by first sonicating 20 mg of the powder in 2 mL of deionized (DI) water for 15 min. For a given experiment, 0.2 mL of the abovementioned particle dispersion was added to a 75 μM aqueous solution of MB, MO, and RhB to achieve a final sorbent concentration of 1 mg/mL (2 mL). These dispersions were left undisturbed in the dark for 36 h, following which their UV−Vis spectra were recorded. Concentrations of MB (λ = 664 nm), MO (λ = 464 nm), and RhB (λ = 554 nm) were calculated using the Beer−Lambert law. To study the kinetics of dye adsorption, UV−Vis spectra were recorded at specific time points after the addition of the particles. Dye and particle concentrations in these experiments were fixed at 75 μM and 1 mg/mL, respectively. At specific time points, 2 mL aliquots were taken from the dye suspension and centrifuged at 7500 rpm for 2 min to sediment any suspended particles, after which the spectrum was recorded.

Particle Recycling via Photocatalytic Dye Degradation. For the recycling experiments, 0.05 mL of 10 mg/mL PLB-0.2x particle dispersion was added to 1.950 mL of RhB solution, resulting in final concentrations of RhB and PLB-0.2x of 5 μM and 0.25 mg/mL, respectively. This dispersion was left undisturbed for 24 h, and a UV−Vis spectrum of the supernatant was recorded, after which it was discarded. Then, 2 mL of water was added to the sedimented particles, and after 2 min stirring, they were sonicated for 1 min. This cuvette was then irradiated with light under constant stirring (Dolan-Jenner Mi-150 Fiber-lite, 170 mW at 400 nm), and UV−Vis spectra were recorded at specific time points. The dispersion was sonicated for a minute prior to recording the spectrum. After a total of 300 min of irradiation, the particles were loaded with 50 μL of RhB (210 μM) to attain a final concentration of 5 μM. This was allowed to sit overnight, and after the adsorption of dye, the process was repeated to determine the recyclability of the particles. The kinetics of RhB degradation were calculated using the Langmuir−Hinshelwood first-order kinetic model.

Photoelectrochemical Characterization. Transient photocurrent response of the samples was measured on a Zahner Zennium XC electrochemical workstation in a three-electrode cell. Ag/AgCl (with 3 M KCl) and platinum wire were used as a reference electrode and counter electrode, respectively. For fabricating the working electrode, 15 mg of sample powder was sonicated in 1.5 mL of PVA (10 mg/mL) for 15 min and then drop-casted on a clean fluorine-doped tin oxide substrate. This was left for drying under ambient conditions for 24 h. The working electrode was illuminated with a steady-state solar simulator (SS-F5-3A, Enli Tech Company, 110 mW/cm^2 at 400 nm), and 0.2 M Na_2SO_4 was used as an electrolyte.

RESULTS AND DISCUSSION

Under hydrothermal conditions, $(Bi_2O_2)^{2+}$ and $(MoO_4)^{2-}$ ions are generated from the precursors, which subsequently attach to each other because of the electrostatic interactions, gradually morphing into nucleation sites.[56,57] Figure 1 shows the X-ray diffractograms of BMO prepared with CTAB (labeled as BMO) and the different BMO samples prepared using CTAB-pillared Lap (labeled as PLB). The peaks at 10.89, 28.28, 32.64, 33.13, 36.04, 46.83, 47.12, 55.60, 56.23, and 58.51° correspond to the reflections from the (020), (131), (200), (060), (151), (202), (062), (331), (133), and (262)

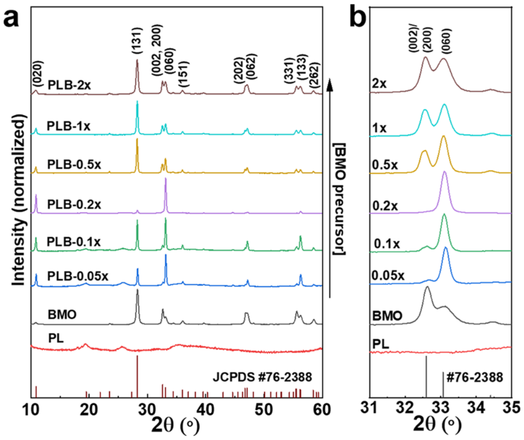

Figure 1. (a) X-ray diffractograms of samples prepared with varying amounts of BMO precursors (1x = 5 mM Bi). (b) Enlarged view of regions of the (200), (002), and (060) peaks.

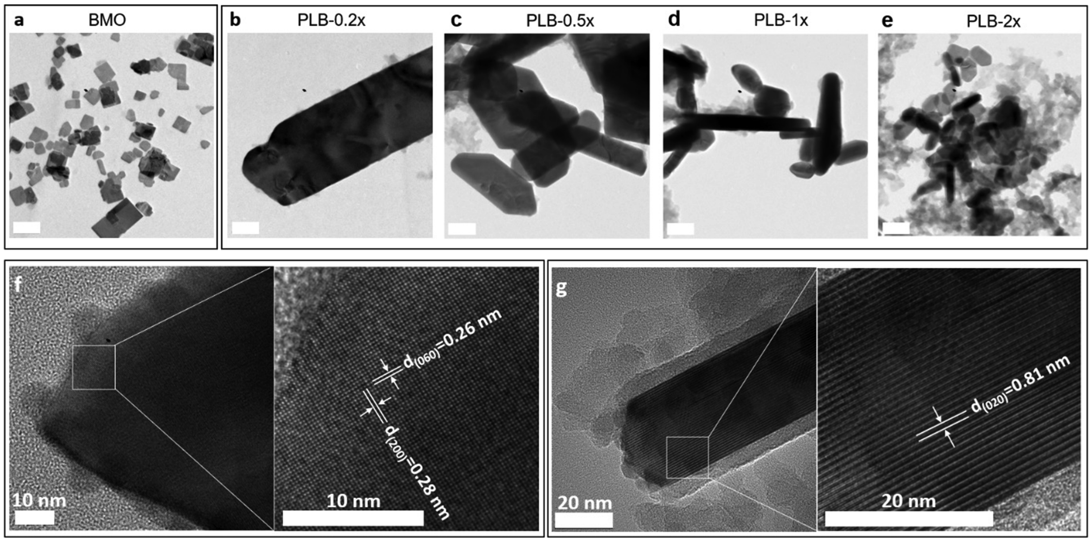

Figure 2. TEM images of Lap−BMO hybrids prepared at different BMO precursor concentrations with [Lap] and [CTAB] fixed. (a) BMO control prepared with CTAB and no Lap. PLB samples prepared at (b) 1 mM, (c) 2.5 mM, (d) 5 mM, and (e) 10 mM BMO precursor concentration (Bi basis) using CTAB-pillared Lap. (f) HR-TEM image of PLB-0.2x particles (images on the right show zoomed-in lattice planes). (g) HR-TEM image of PLB-1x with the (020) stacking plane of BMO indicated. Scale bars in (a)−(e) are 100 nm. HR-TEM images of BMO, PLB-0.05x, and 0.1x are shown in Figure S2.

planes of BMO, respectively.[39] These peaks correspond to γ-Bi_2MoO_6 (γ-BMO), and the absence of peaks from α and β phases confirms the formation of a pure γ-BMO phase. Upon comparison of X-ray scattering from the different samples shown in Figure 1a, it can be seen that the introduction of CTAB-modified Lap results in the preferential growth of certain planes and changes the most prominent Bragg reflection from the (131) plane to the (060) plane in samples with a [Bi]:[Lap] ratio of up to 0.63 mM:mg/mL. A significant modification in the crystal growth orientation can be seen in the case of PLB-0.2x, where the ratio of (060) to (131) peak intensity is drastically shifted from 0.23 to 10.86. This clearly demonstrates that CTAB−Lap strongly influences the preferential growth orientation of the γ-BMO crystal, which suggests that the interaction of CTAB-modified Lap with $(Bi_2O_2)^{2+}$ and $(MoO_4)^{2-}$ ions generated from the precursors is conducive to the growth of bismuth molybdate in the [010] direction, which is the direction along which $(Bi_2O_2)^{2+}$ and $(MoO_4)^{2-}$ layers are stacked. On the other hand, growth along this direction is drastically reduced for BMO synthesized with only CTAB and no Lap. Similar changes in crystal growth orientation were reported by Liu et al. where the growth of In_2S_3 in the expanded interlayer space of pillared Lap resulted in the elimination of the (400) and (511) peaks observed in pristine In_2S_3.[36]

The peaks from PL can be seen in samples prepared with low BMO precursor concentration (PLB-0.05x, PLB-0.1x, and PLB-0.2x); however, their relative intensity decreases with increasing BMO precursor concentration (Figure 1a). The intensity of the (131) peak increases with BMO precursor amount, with the exception of PLB-0.2x, which shows the lowest intensity of the (131) peak. Moreover, the intensity of the (020) reflection is greater for all PLB samples as compared to BMO, maxing out for PLB-0.2x and reducing with increasing BMO precursor beyond this. The intensity of the (002)/(200) reflection reduces with the amount of BMO precursor and is greatly diminished in the diffractograms of PLB-0.05x, PLB-0.1x, and PLB-0.2x (Figure 1b). This decrease in the (002, 200) peak intensity is accompanied with an increase in the intensities of the (020) and (060) peaks. A similar pattern of change in the intensity is also seen in the peak pairs corresponding to the (202)/(062) and (331)/(133) crystal planes, where (331) and (202) peaks are nearly absent in PLB-0.2x. The influence of scaling was studied at 2.5× the concentration of reactants used in PLB-1x, where no significant change in the (060):(020, 200) intensity ratio was observed (Figure S1a). However, in a control sample synthesized with unpillared Lap at the same concentrations as PLB-1x, a slight decrease in the (060):(020, 200) intensity ratio was observed (Figure S1b). The anisotropy in the growth of different samples can be compared by looking at the intensity ratio of peaks belonging to mutually orthogonal crystal planes. These results indicate that templated growth in pillared Lap effectively switches the crystalline growth direction, which can be controlled by varying the ratio of [Bi]:[Lap] used during the synthesis. Thus, at a certain ratio of [Bi]:[Lap] (0.16−0.63 mM:mg/mL), CTAB-pillared Lap promotes growth in the [010] direction and hinders the growth of the (131) and (200, 002) crystal planes.

Figure 2 shows the TEM micrographs of BMO control and PLB particles prepared with different BMO precursor concentrations. The particles from the PLB series clearly display larger size (up to microns in edge length) and higher anisotropy compared to BMO particles, which assume a square sheet-like shape with edge lengths of around 50 nm. The size of the particles reduces upon increasing [BMO precursor] to approach similar lateral dimensions to BMO control. Selected area electron diffraction (SAED) patterns of PLB-0.2x show the growth of a single crystal, with the (060) and (062) reflections clearly visible (Figure S3). This trend in the size change suggests that at an optimal concentration of BMO precursor, the [Bi]:[Lap] ratio is such that edge−edge aggregation of pillared Lap flocs can occur, providing a template for such lateral growth. By stopping the synthesis at different time points, the growth process could be monitored. Single-crystalline particles are already observed after 30 min of

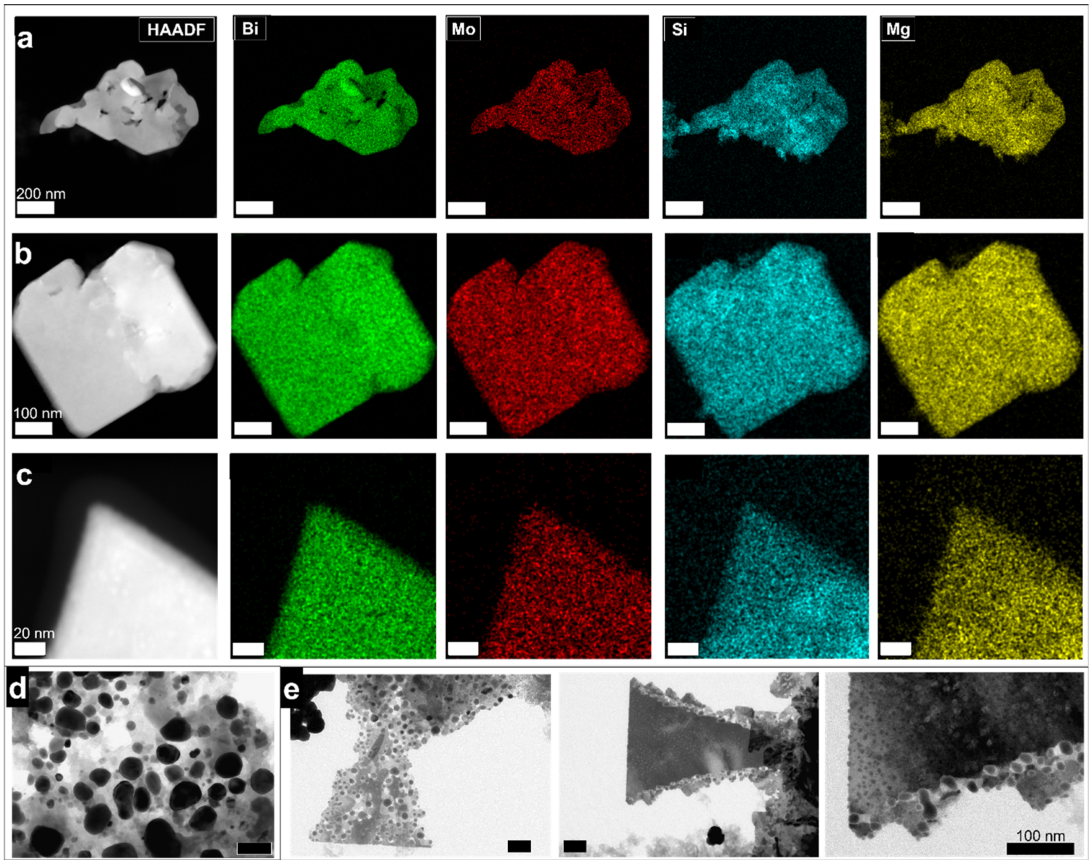

Figure 3. (a−c) HAADF-STEM mappings of PLB-0.2x particles. Elements Bi, Mo, Si, and Mg are shown from left to right (corresponding EDX spectra are shown in Figure S7). TEM micrographs of PLB-0.2x synthesized for (d) 30 min and (e) 1 h, showing progression from the initial nucleation to lateral growth.

synthesis, and by 1 h, large crystals with single-crystalline domains are formed (Figure S4). After 1 h, the particle shape and morphology are quite different from those synthesized for 3 and 5 h (which resemble those in Figure 2b), looking more like a christmas tree. After 1 h, the transition from the initial nucleation to lateral growth can be clearly observed (Figure 3d,e). It should be noted that since the crystallographic phase of the initial seed critically influences further crystal growth,[58] the orientation of the particles observed after 30 min likely dictates the crystalline orientation after complete growth. X-ray diffractograms of these samples show that with increasing reaction time, the (060) reflection peak becomes sharper and shifts toward a higher angle (Figure S5).

The different polymorphs of BMO, namely, α-$Bi_2Mo_3O_{12}$, β-$Bi_2Mo_2O_9$, and γ-Bi_2MoO_6, can be synthesized by varying the Bi:Mo precursor ratio.[47] In their study, Li and co-workers also showed that pH plays a crucial role in directing the crystal growth of bismuth molybdate. They found that pH > 7 favors the formation of γ-Bi_2MoO_6 (koechlinite) exclusively, regardless of the Bi:Mo ratio. This was attributed to OH^- ions causing depolymerization of molybdate anions like $(Mo_2O_7)^{2-}$ and $(Mo_3O_{10})^{2-}$, making $(MoO_4)^{2-}$ the only stable molybdate species in the solution.[59] The selective adsorption of H^+ on certain facets of the BMO crystal also directs the crystal growth.[60] Therefore, to study the influence of pH on the synthesis carried out in pillared Lap, PLB-0.2x was synthesized at different pH values ranging from 2 to 8. Interestingly, PLB-0.2x samples retain their habit of growth along [010] even at acidic pH (Figure S6a), in contrast to the aforementioned studies.[47,60] Particle size increased with pH, as observed by TEM and the narrowing of the (131) reflection peak observed by XRD (Figure S6). Therefore, while templating the growth with pillared Laponite maintained the growth habit along [010] independent of pH, adjusting the pH provided a means to tailor particle size.

While the external surface is dominated by the {010} facets in the BMO control, a preferential growth orientation in PLB samples along the [010] direction would result in external surfaces terminating predominantly in the {100} facet. It is plausible that at low [Bi]:[Lap] (0.16−0.63 mM:mg/mL), high proportions of $(Bi_2O_2)^{2+}$ and $(MoO_4)^{2-}$ ions are present in close vicinity of CTAB-pillared Lap floccules because of the attractive electrostatic interactions between CTA^+ (associated with Lap) and $(MoO_4)^{2-}$ and $(Bi_2O_2)^{2+}$ and the basal plane of Lap. We posit that these electrostatic interactions would facilitate the nucleation and growth of BMO crystals to begin primarily from CTAB−Lap floccules. The increase in particle size and anisotropy also suggests that edge−edge aggregation of pillared Lap flocs is driven in part by BMO precursors. Of the potential molecules involved in the synthesis, $(MoO_4)^{2-}$ would be able to coordinate two Lap edge sites. This aggregation of pillared Lap driven by $(MoO_4)^{2-}$ might explain the decrease in the (131) peak intensity observed in the diffractogram of PLB-0.2x. If the precursor:Lap ratio is such that a certain aggregation of pillared Lap flocs occurs, this would be likely to influence the orientation of interfloc and

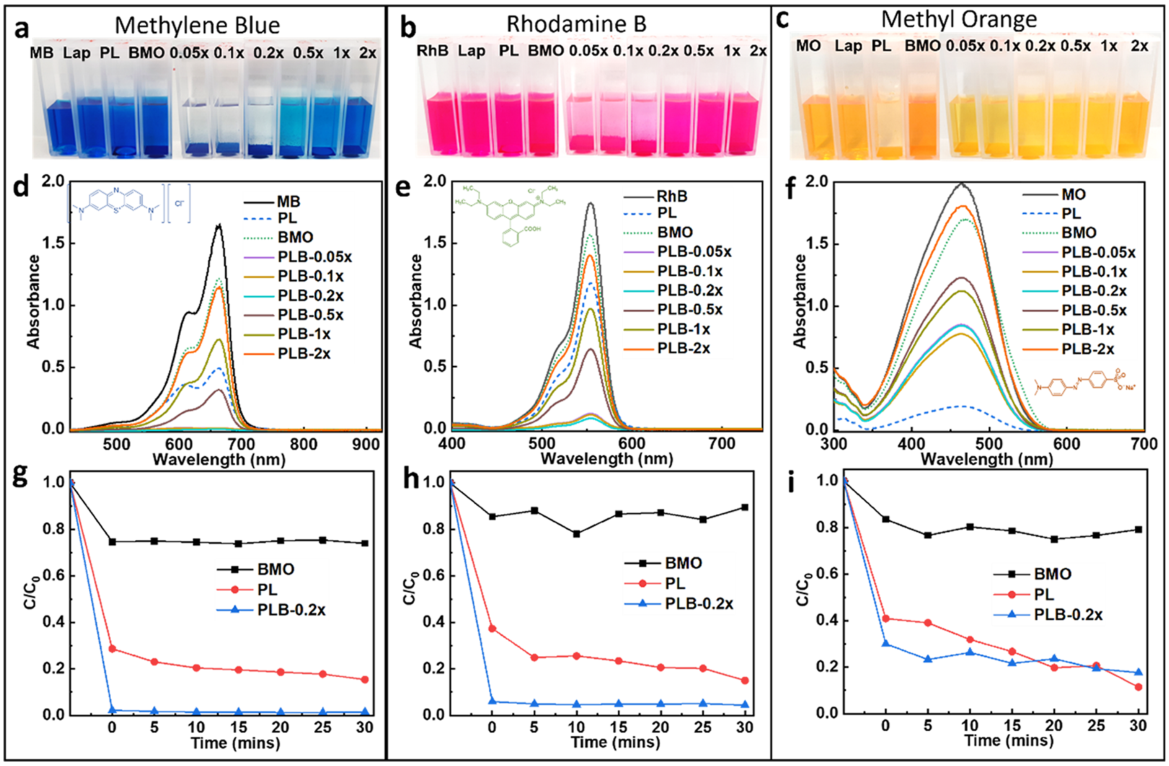

Figure 4. (a−c) Photographs, (d−f) UV−Vis spectra, and (g−i) adsorption kinetics of dyes (a, d, g) MB, (b, e, h) RhB, and (c, f ,i) MO; [dye] = 75 μM and [particles] = 1 mg/mL. Insets in the middle panel show the chemical structure of the different dyes. Full UV−Vis spectra of (g)−(i) are shown in Figure S8.

intergallery spaces and thus growth of the BMO crystal. As particle edge length decreases with increased precursor concentration, it is likely that an excess of precursors either leads to greater repulsion between pillared Lap flocs or an increased likelihood of nucleation and growth occurring in solution away from the CTAB−Lap interface. Since low precursor concentration favors the growth of the crystal over the process of nucleation,[61] it might also be a contributing factor toward the formation of particles with such enlarged edge lengths (Figure 2b).

A detailed in situ study of the formation of different BMO crystals under hydrothermal conditions was carried out by Beale and Sankar by time-resolved energy-dispersive X-ray diffraction.[62] They found that the crystallization of γ-BMO commences by growth along the [131] and [001, 100] directions, and thereafter, diffusion-controlled uniform crystal growth along two dimensions ensues without a preferred crystallographic direction, resulting in the formation of γ-BMO sheets. Since the growth of the crystal is influenced by the surface energies of the different crystal planes, the preferred growth along the [100, 001] directions means that the corresponding (100, 001) planes have a higher surface energy compared to the (010) crystal planes.[63] The normal habit of BMO crystal growth seems to break down in the PLB samples prepared with [Bi]:[Lap] < 0.63 mM:mg/mL, namely, PLB-0.05x, PLB-0.1x, and PLB-0.2x (Figure 1). The inhibition of growth along the [001, 100] directions results from the reduction in the surface energy of the (100, 001) crystal planes, which is suspected to be a consequence of the interactions between BMO precursors and pillared Lap. In order to establish the colocalization of Lap with BMO, HAADF-STEM elemental mappings were carried out for PLB-0.2x (Figure 3).

From the HAADF-STEM mappings of PLB-0.2x particles presented in Figure 3a−c, it can be seen that the elements from BMO, namely, Bi and Mo, and elements from Lap, namely, Si and Mg, are present throughout the particles. The transition between the initial nucleation observed after only 30 min of growth (Figure 3d) and such "christmas tree"-shaped particles can be observed in some instances after 1 h of synthesis (Figure 3e). Taking the above characterization into account, a mechanism of the growth of BMO with CTAB−Lap was proposed. During the initial stages of the reaction, BMO precursors impregnate the interlayer space of the CTAB−Lap floccules. As the reaction proceeds, $(Bi_2O_2)^{2+}$ and $(MoO_4)^{2-}$ ions generated from the BMO precursors nucleate, likely at the basal surface of Lap. Since the basal surface of Lap is negatively charged and given that $(Bi_2O_2)^{2+}$ layers are formed prior to the $(MoO_4)^{2-}$ layer,[64] it seems likely that Lap initially provides a platform for $(Bi_2O_2)^{2+}$ layers to grow atop, potentially dislodging some CTA^+ ions in the process. However, at lower pH, $(MoO_4)^{2-}$ may interact more strongly with the Lap edge sites, which may be the cause of the decrease in (131) intensity in Figure S6a. These nuclei then grow in the interlayer space where pillared Lap not only alters the surface energy of embryonic crystallites but also provides a confined environment during the initial stages of BMO crystal growth. The crystal growth proceeds, consuming the intergallery space and ultimately growing out of the interlayer.

Dye Adsorption. Figure 4 shows the photographs of the dye solutions 36 h after the addition of different sorbent particles and the UV−Vis spectra from the dye adsorption

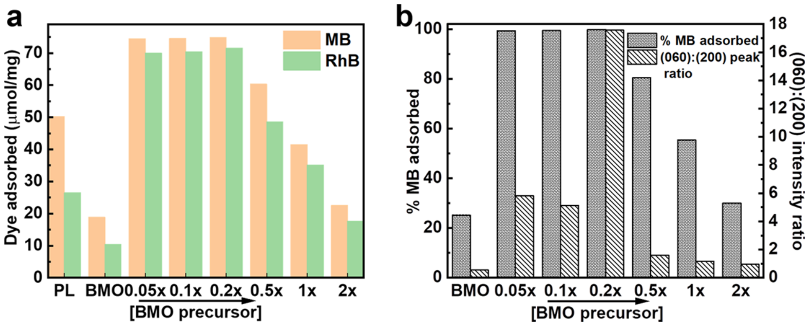

Figure 5. (a) Specific dye adsorption by different particles. (b) Percentage of total amount of MB adsorbed from the dispersion and ratio of intensity of reflections from the (060) and (200) planes measured by XRD for different samples. [dye] = 75 μM and [particles] = 1 mg/mL.

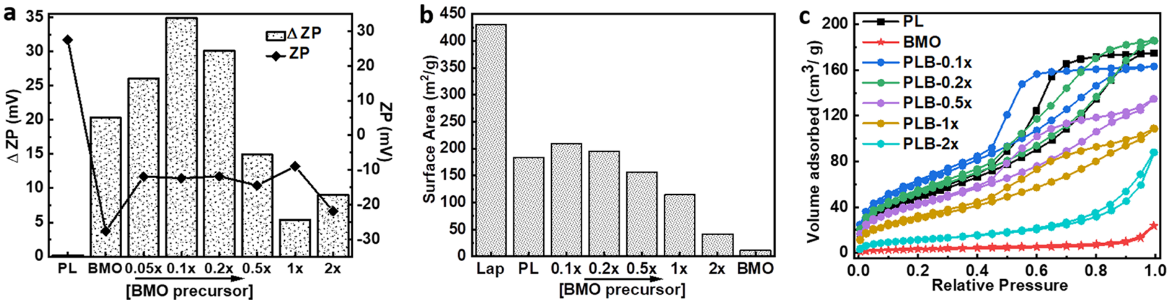

Figure 6. (a) Zeta potential of PLB particles and change in zeta potential after the adsorption of MB. (b) Surface area of different PLB samples estimated using BET. (c) N_2 adsorption−desorption isotherms obtained at 77 K.

experiments. In the case of cationic dyes MB and RhB, it can be clearly seen from the photographs that PLB-0.05x, PLB-0.1x, and PLB-0.2x adsorb the highest amount of dye, especially in the case of dye MB where colorless water can be clearly observed after the sedimentation of dye laden-particles (Figure 4a−c). In the case of the anionic dye MO, the greatest adsorption after 36 h is achieved by PL (Figure 4f), although PLB-0.2x adsorbs more immediately upon dye addition (Figure 4i). In Figure 4d,e, it can be seen that RhB is adsorbed substantially, and MB is completely removed in PLB-0.05x, PLB-0.1x, and PLB-0.2x. Notably, all PLB samples showed greater dye adsorption compared to BMO, demonstrating that particles terminating in the {100} facets have greatly enhanced dye adsorption capacity. On the other hand, dye adsorption capacity decreased as the [Bi]:[Lap] ratio is increased past 0.63 mM:mg/mL. The adsorption of MO on PLB samples revealed a similar trend, where samples PLB-0.05x, PLB-0.1x, and PLB-0.2x were most proficient at adsorbing the anionic dye and the adsorption performance decreased as the BMO precursor was increased beyond this. Control dye adsorption experiments using pristine Lap as the sorbent are shown in Figure S9.

To further investigate the adsorption process, kinetics of dye adsorption was also studied by recording UV−Vis spectra at specific time points after the addition of the sorbent particles to the dye solution (Figure 4g−i). BMO removes 26% of MB and 10% of RhB after 30 min, while PL adsorbs 85% of both MB and RhB. PLB-0.2x adsorbs 98% of MB and 94% of RhB within just the first few seconds after their addition to the dye solution. In the case of the anionic dye MO, BMO adsorbs only 20% during 30 min of adsorption (Figure 4i). Interestingly, in the first seconds of adsorption, PLB-0.2x adsorbs 70% of MO, compared with only 60% adsorbed by PL in the same time frame, although by 30 min, PL has adsorbed more.

Figure 5a shows the amount of cationic dye adsorbed per gram of the sorbent particle estimated from the UV−Vis spectra presented in Figure 4d−f. The adsorption performance begins to decline in the samples prepared with [Bi]:[Lap] greater than 0.63 mM:mg/mL, namely, PLB-0.5x, PLB-1x, and PLB-2x. Among the different PLB samples, the amount of dye adsorbed by the particles decreases as the [Bi]:[Lap] ratio is increased. Interestingly, enhanced adsorption is accompanied with an increase in growth along the [010] direction (Figure 5b). The intensity ratio of the (060):(200) peaks for BMO is 0.55, whereas for the samples showing the best adsorption performance, namely, PLB-0.05x, PLB-0.1x, and PLB-0.2x, it is 5.81, 5.12, and 17.57, respectively. The (060):(200) peak intensity ratio approaches values closer to the BMO control in PLB-1x and PLB-2x. It has been shown previously that the {100} facets in BMO are more conducive to photocatalytic O_2 evolution as compared to the {010} facets.[52] The {010} facet of BMO is composed exclusively of O atoms, whereas the chains of $(MoO_4)^{2-}$ and $(Bi_2O_2)^{2+}$ are present equally along the {100} and {001} facets of BMO.[63] This results in the chemical potential of the {100}/{001} facets being higher than the {010} facets.[65] Thus, we suspect that this difference in the chemical potential between the {010} and {100} facets is responsible for the latter being more conducive toward dye adsorption. Comparing the different cationic dyes, MB is adsorbed to a greater extent than RhB, which could be due to the smaller size of MB molecules, allowing more MB per unit surface area compared to RhB.

Further insights into the interaction between the surface of the particles and different dyes were gained by measuring the surface charge of the particles before and after the adsorption of dye (Figure 6a). It can be clearly seen that as [Bi]:[Lap] is

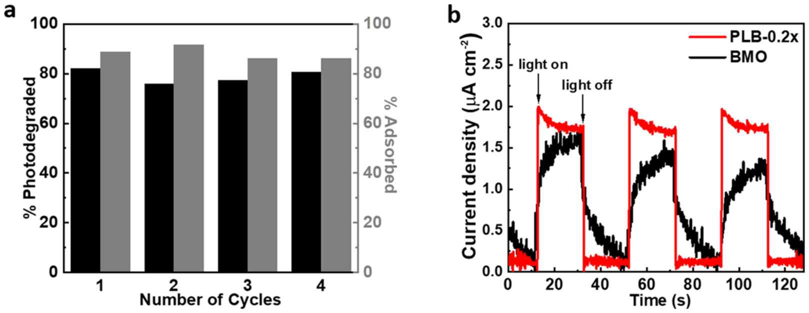

Figure 7. (a) Removal of RhB after consecutive adsorption/photodegradation cycles using PLB-0.2x particles. [RhB] = 5 μM and [particles] = 0.25 mg/mL. (b) Transient photocurrent measurements of BMO and PLB-0.2x. Full UV−Vis spectra are shown in Figure S10.

increased, the zeta potentials of the particles become less negative compared to BMO. However, upon a further increase in the BMO precursor concentration, the zeta potential becomes more negative (−21.93 mV) and approaches the value for BMO (−27.7 mV). The surface charge of PLB particles upon addition to MB dye solution changes from negative to positive (Figure 6a), which results from the adsorption of the cationic dye molecules onto the negatively charged surface of PLB particles. The change in surface charge after MB adsorption was the greatest for the PLB-0.05x, PLB-0.1x, and PLB-0.2x samples (>20 mV) and most pronounced for PLB-0.1x (34.9 mV). Although BMO adsorbed only 25% of MB, it still showed a significant change of 20 mV in zeta potential, a consequence of BMO particles having a smaller surface area and thus becoming saturated with a reduced amount of MB compared with the PLB samples. Interestingly, even though PL adsorbed more than 65% of MB from the solution, there is little change in zeta potential (0.2 mV), suggesting that the surface charge is dominated by CTAB.

Gas adsorption−desorption isotherms can be used to discern the presence and nature of porosity in a material and can be used to estimate the surface area of materials.[66] Figure 6b shows the surface area of the different particles as estimated from N_2 adsorption−desorption isotherms using the Brunauer−Emmett−Teller (BET) method. Earlier studies revealed that pillared clay can have 40 times the surface area compared to unpillared clay.[33] In the case of Lap, pillaring with CTAB reduced the surface area of Lap from 430 to 184 m^2/g. For PLB samples, it was observed that upon increasing BMO precursor concentration the surface area of the particles decreases, which is an interesting finding considering the reduced particle size observed by TEM. The surface areas of PLB-0.1x, PLB-0.2x, PLB-0.5x, PLB-1x, and PLB-2x were estimated to be 209, 196, 156, 115, and 41.7 m^2/g, respectively, whereas BMO was found to have a surface area of only 11.1 m^2/g. The isotherm for PL shows a type-IV behavior and an H2-type hysteresis, which is typical of mesoporous materials[33] (Figure 6c). Interestingly, for most PLB samples, the isotherms look like a combination of PL and BMO, which could be due to the presence of free PL. On the other hand, with increasing BMO precursor concentration, hysteresis in the adsorption−desorption curves becomes successively less pronounced, and PLB-2x shows a type-II behavior with H3 hysteresis,[44] which is similar to that of BMO control. Since PLB-0.05x, PLB-0.1x, and PLB-0.2x show almost identical dye adsorption capacity, we suspect that this enhancement in adsorption is primarily driven by a combination of changes in crystal facet terminating these particles along with an increase in their surface area. The preponderance of the {100} facet in the samples PLB-0.05x, PLB-0.1x, and PLB-0.2x can be inferred from Figure 5b, where the (060):(200) intensity ratios of the aforementioned samples are at least an order of magnitude greater than BMO control. Furthermore, a similar trend is followed by the adsorption surface area in which a 10 times increase was observed in the aforementioned PLB particle surface area over BMO control. Therefore, we suspect that upon obtaining a threshold number of surfaces terminated in the {100} crystal facet, the adsorption capacity can be dominated by the surface area.

An important aspect for evaluating the overall performance of any functional material/particle system for water decontamination and dye removal is to study their reuse and recycling performance. Common techniques for recycling of sorbents involve desorbing the attached molecules from the sorbent using certain reagents like $NaNO_3$ and NaOH.[67] The possibility of surface damage due to the action of these reagents is the major shortcoming of these methods. As BMO has intrinsic photocatalytic activity, dye molecules can be photocatalytically degraded directly, circumventing the need for reagents to remove dye molecules from the surface to achieve reusability of these particles. To study the recycling performance of these materials, RhB was allowed to adsorb on the particle surface, and following sedimentation, the particles were exposed to visible light under stirring.

Figure 7 shows the cyclic adsorption/photodegradation performance of PLB-0.2x particles and the comparison of transient photocurrent response with control BMO. PLB-0.2x particles retain their adsorption and photocatalytic activity even after four cycles of use, although the adsorption performance shows a slight decline with subsequent cycles (Figure 7a). During the first adsorption cycle, almost 89% of RhB was adsorbed onto PLB-0.2x. In the first photodegradation cycle, close to 82% of RhB adsorbed was degraded in 300 min. While no significant change in the photocatalytic degradation performance was observed from one cycle to another (Figure S11c), only 86% of RhB was removed by adsorption in the fourth cycle compared to the 89% in the first. This slight reduction in adsorption performance with successive cycles could be due to saturation of particle surface with RhB or its photoproducts or structural damage caused by long exposure to light, although no change in crystallinity or morphology could be observed (Figure S12). Despite this slow degradation of performance with repeated cycling, the PLB-0.2x particles were able to adsorb and degrade a total of 54.16 nmol of dye per mg particles after a total of four cycles. Photocurrent measurements showed little change from PLB-

https://doi.org/10.1021/acsami.1c01144
ACS Appl. Mater. Interfaces 2021, 13, 18713−18723

0.2x to BMO, with a slight increase for PLB-0.2x observed (Figure 7b). While the same performance of these two samples is unsurprising, it is interesting that PLB-0.2x has a higher photocurrent, considering that it would absorb less light due to the slight blue-shift of the absorption band edge from ~460 nm in BMO to 440 nm in PLB-0.2x (Figure S11a).

■ CONCLUSIONS

In this study, the layered silicate nanoclay Laponite pillared with the cationic surfactant CTAB was used for templating the growth of γ-Bi_2MoO_6. The morphologies of these PLB samples were anisotropic, elongated, and up to microns in length, whereas BMO synthesized with only CTAB formed square sheets with 50−100 nm edge lengths. This contrasts with syntheses of MoS_2,[35] In_2S_3,[36] and $ZnIn_2S_4$[37] in the pillared Lap interlayer, in which thin semiconductor layers formed a heterolayered structure. Interestingly, CTAB-modified Lap was found to alter the growth orientation of BMO crystals, promoting preferential growth along the [010] direction, which otherwise does not occur in the BMO control. This shift in the crystal growth orientation manifests as an increase in the predominance of the {100} crystal facets terminating these particles, as opposed to {010} facets in BMO synthesized without Lap. The amount of BMO precursor controlled this shift, where the formation of larger, more anisotropic particles occurred at lower precursor concentrations. Tuning the BMO precursor concentration also provides a facile synthetic strategy to facet-engineer bismuth molybdate particles. Between the [Bi]:[Lap] ratio of 0.16−0.63 mM:mg/mL, the particle size and growth orientation of BMO are altered drastically, inferred from the change in the presentation of the prominent reflection peak from the (131) crystal plane to the (060) crystal plane. In addition, pH provided a facile means to tailor the size of these {100} faceted particles, with low pH resulting in the formation of smaller-sized particles. The examination of particles synthesized at different time points further revealed that the growth of PLB-0.2x particles proceeds via an initial nucleation of nanocrystals followed by lateral growth along the same crystalline direction, forming extended single-crystalline particles.

The emergence of {100} faceted particles also led to a drastically improved capacity for adsorption of cationic dye molecules that was lacking in the control samples (namely, BMO and PL). Also, the CTAB−Lap templated synthesis significantly increased the surface area of BMO particles, which is more than an order of magnitude greater for samples PLB-0.2x, PLB-0.5x, and PLB-1x than BMO. The adsorption of dye on the surface of these particles is accomplished within few seconds after their addition to the dye solution, and quick sedimentation of these particles (along with adsorbed dye molecules) allows for their easy recovery after use. Furthermore, the photocatalytic activity of BMO provided a facile means to degrade dye molecules adsorbed onto the particle surface, which allowed cyclic adsorption/photodegradation on the same particles with limited loss to cycle performance. These particles maintained their adsorption and photodegradation performance over multiple cycles, making them appealing for practical applications in both stationary and continuous-flow wastewater decontamination settings.

Therefore, this synthetic approach might be useful for studying the facet-dependence of different properties in BMO and may even be broadly applicable to a range of other materials in the Aurivillius family and beyond. Surface engineering of nanomaterials is a useful strategy for tailoring their functionality and also plays an important role in the synthesis of heterostructures. This work provides a simple route for tailoring the surface chemistry and anisotropy in nanomaterials via colloidal interactions between the surfactant-modified clay and Bi/Mo precursors. In addition to the recyclable photocatalytic sorbent described herein, this synthetic methodology could potentially be adapted for tailoring the crystalline growth orientation of a variety of different materials with applications beyond water decontamination.

■ ASSOCIATED CONTENT

Supporting Information

The Supporting Information is available free of charge at https://pubs.acs.org/doi/10.1021/acsami.1c01144.

> Additional X-ray diffractograms, SEM images, HR-TEM images, selected area electron diffraction (SAED) patterns, EDX spectra, and UV−Vis diffuse reflectance spectra of PLB samples and BMO control; UV−Vis spectra from dye adsorption and photocatalytic degradation experiments; and first-order kinetics of RhB photodegradation (PDF)

■ AUTHOR INFORMATION

Corresponding Author

Eric H. Hill − *Institute of Physical Chemistry, University of Hamburg, 20146 Hamburg, Germany; The Hamburg Center for Ultrafast Imaging (CUI), 22761 Hamburg, Germany;* orcid.org/0000-0003-3063-1447; Email: eric.hill@chemie.uni-hamburg.de

Authors

Sanjay Jatav − *Institute of Physical Chemistry, University of Hamburg, 20146 Hamburg, Germany*

Junying Liu − *Institute of Physical Chemistry, University of Hamburg, 20146 Hamburg, Germany*

Marcel Herber − *Institute of Physical Chemistry, University of Hamburg, 20146 Hamburg, Germany*

Complete contact information is available at: https://pubs.acs.org/10.1021/acsami.1c01144

Notes

The authors declare no competing financial interest.

■ ACKNOWLEDGMENTS

This research was funded by the DAAD from the funds of German Federal Ministry of Education and Research (BMBF), under the MOPGA-GRI program (57429511). E.H.H. is supported by the Cluster of Excellence "Advanced Imaging of Matter" of the Deutsche Forschungsgemeinschaft (DFG)—EXC 2056—project ID 390715994. We thank Stefan Werner and Robert Schön at the Institute of Physical Chemistry for providing XRD and SEM characterization, respectively. We thank Dr. Hauke Heller of the Institute of Physical Chemistry for providing access to the gas sorption analyzer for BET surface area measurements. We thank the Central Division of Electron Microscopy (BEEM) of TUHH for providing an FEI Talos F200X. We thank Prof. Manfred Eich of the Institute of Optical and Electronic Materials of TUHH for providing the PEC setup. We thank BYK GmbH for providing the Laponite-RD used in this study.

■ REFERENCES

(1) Cribb, J. *Poisoned Planet: How Constant Exposure to Man-Made Chemicals Is Putting Your Life at Risk*; Allen & Unwin: 2014.

(2) Cribb, J. *Surviving the 21st Century: Humanity's Ten Great Challenges and How We Can Overcome Them*; 1st ed.; Springer: 2016.

(3) Rhind, S. M. Anthropogenic Pollutants: A Threat to Ecosystem Sustainability? *Philos. Trans. R. Soc., B* **2009**, *364*, 3391−3401.

(4) Tkaczyk, A.; Mitrowska, K.; Posyniak, A. Synthetic Organic Dyes as Contaminants of the Aquatic Environment and Their Implications for Ecosystems: A Review. *Sci. Total Environ.* **2020**, *717*, 137222.

(5) Alam, R.; Ahmed, Z.; Howladar, M. F. Evaluation of Heavy Metal Contamination in Water, Soil and Plant around the Open Landfill Site Mogla Bazar in Sylhet, Bangladesh. *Groundwater Sustainable Dev.* **2020**, *10*, 100311.

(6) Hoang, H.-G.; Lin, C.; Tran, H.-T.; Chiang, C.-F.; Bui, X.-T.; Cheruiyot, N. K.; Shern, C.-C.; Lee, C.-W. Heavy Metal Contamination Trends in Surface Water and Sediments of a River in a Highly-Industrialized Region. *Environ. Technol. Innovation* **2020**, *20*, 101043.

(7) Liu, L.; Qu, Y.; Huang, J.; Weber, R. Per- and Polyfluoroalkyl Substances (PFASs) in Chinese Drinking Water : Risk Assessment and Geographical Distribution. *Environ. Sci. Eur.* **2021**, *33*, 6.

(8) Peterson, E. M.; Green, F. B.; Smith, P. N. Pesticides Used on Beef Cattle Feed Yards Are Aerially Transported into the Environment Via Particulate Matter. *Environ. Sci. Technol.* **2020**, *54*, 13008−13015.

(9) Hassaan, M. A.; El Nemr, A.; Hassaan, A. Health and Environmental Impacts of Dyes: Mini Review. *Am. J. Environ. Sci. Eng.* **2017**, *1*, 64−67.

(10) Yu, X.; Sui, Q.; Lyu, S.; Zhao, W.; Liu, J.; Cai, Z.; Yu, G.; Barcelo, D. Municipal Solid Waste Landfills: An Underestimated Source of Pharmaceutical and Personal Care Products in the Water Environment. *Environ. Sci. Technol.* **2020**, *54*, 9757−9768.

(11) Tchounwou, P. B.; Yedjou, C. G.; Patlolla, A. K.; Sutton, D. J. Heavy Metal Toxicity and the Environment. *Mol. Clin. Environ. Toxicol.* **2012**, *101*, 133−164.

(12) Yusuf, M. Synthetic Dyes: A Threat to the Environment and Water Ecosystem. *Text. Clothing* **2019**, 11−26.

(13) Gita, S.; Hussan, A.; Choudhury, T. G. Impact of Textile Dyes Waste on Aquatic Environments and Its Treatment. *Environ. Ecol.* **2017**, *35*, 2349−2353.

(14) Przystaś, W.; Zabłocka-Godlewska, E.; Grabińska-Sota, E. Biological Removal of Azo and Triphenylmethane Dyes and Toxicity of Process By-Products. *Water, Air, Soil Pollut.* **2012**, *223*, 1581−1592.

(15) Carmen, Z.; Daniela, S. Textile Organic Dyes − Characteristics, Polluting Effects and Separation/Elimination Procedures from Industrial Effluents − A Critical Overview. In *Organic Pollutants Ten Years After the Stockholm Convention- Environmental and Analytical Update*; IntechOpen: 2012; 55−86.

(16) Ali, H. Biodegradation of Synthetic Dyes- A Review. *Water, Air, Soil Pollut.* **2010**, *213*, 251−273.

(17) Brillas, E.; Martínez-Huitle, C. A. Decontamination of Wastewaters Containing Synthetic Organic Dyes by Electrochemical Methods. An Updated Review. *Appl. Catal., B* **2015**, *166-167*, 603−643.

(18) Hor, K. Y.; Chee, J. M. C.; Chong, M. N.; Jin, B.; Saint, C.; Poh, P. E.; Aryal, R. Evaluation of Physicochemical Methods in Enhancing the Adsorption Performance of Natural Zeolite as Low-Cost Adsorbent of Methylene Blue Dye from Wastewater. *J. Cleaner Prod.* **2016**, *118*, 197−209.

(19) Oller, I.; Malato, S.; Sánchez-Pérez, J. A. Combination of Advanced Oxidation Processes and Biological Treatments for Wastewater Decontamination- A Review. *Sci. Total Environ.* **2011**, *409*, 4141−4166.

(20) Martínez-Huitle, C. A.; Rodrigo, M. A.; Sirés, I.; Scialdone, O. Single and Coupled Electrochemical Processes and Reactors for the Abatement of Organic Water Pollutants: A Critical Review. *Chem. Rev.* **2015**, *115*, 13362−13407.

(21) Kurniawan, T. A.; Chan, G. Y. S.; Lo, W.-H.; Babel, S. Physico-Chemical Treatment Techniques for Wastewater Laden with Heavy Metals. *Chem. Eng. J.* **2006**, *118*, 83−98.

(22) Mirzaei, A.; Chen, Z.; Haghighat, F.; Yerushalmi, L. Removal of Pharmaceuticals from Water by Homo/Heterogonous Fenton-Type Processes− A Review. *Chemosphere* **2017**, *174*, 665−688.

(23) Akhtar, N.; Mannan, M. A. Mycoremediation: Expunging Environmental Pollutants. *Biotechnol. Rep.* **2020**, *26*, No. e00452.

(24) Newcombe, G. Adsorption from Aqueous Solutions: Water Purification. *Adsorpt. Carbons* **2008**, 679−709.

(25) Suman, K.; Joshi, Y. M. Microstructure and Soft Glassy Dynamics of an Aqueous Laponite Dispersion. *Langmuir* **2018**, *34*, 13079−13103.

(26) Kroon, M.; Vos, W. L.; Wegdam, G. H. Structure and Formation of a Gel of Colloidal Disks. *Phys. Rev. E* **1998**, *57*, 1962−1970.

(27) Van Olphen, H. *An Introduction to Clay Colloidal Chemistry: For Clay Technologists, Geologists, and Soil Scientists*; 2nd ed.; Wiley: 1963.

(28) Bergaya, F., Lagaly, G., *Handbook of Clay Science*; 2nd ed.; Newnes: 2013; 19−86.

(29) Negrete; Letoffe, J. M.; Putaux, J. L.; David, L.; Bourgeat-Lami, E. Aqueous Dispersions of Silane-Functionalized Laponite Clay Platelets. A First Step toward the Elaboration of Water-Based Polymer/Clay Nanocomposites. *Langmuir* **2004**, *20*, 1564−1571.

(30) Zhang, J.; Zhou, C. H.; Petit, S.; Zhang, H. Hectorite: Synthesis, Modification, Assembly and Applications. *Appl. Clay Sci.* **2019**, *177*, 114−138.

(31) Hill, E. H.; Zhang, Y.; Whitten, D. G. Aggregation of Cationic p-Phenylene Ethynylenes on Laponite Clay in Aqueous Dispersions and Solid Films. *J. Colloid Interface Sci.* **2015**, *449*, 347−356.

(32) Hill, E. H.; Claes, N.; Bals, S.; Liz-Marzán, L. M. Layered Silicate Clays as Templates for Anisotropic Gold Nanoparticle Growth. *Chem. Mater.* **2016**, *28*, 5131−5139.

(33) Gil, A.; Assis, F. C. C.; Albeniz, S.; Korili, S. A. Removal of Dyes from Wastewaters by Adsorption on Pillared Clays. *Chem. Eng. J.* **2011**, *168*, 1032−1040.

(34) Zhao, S.; Meng, Z.; Fan, X.; Jing, R.; Yang, J.; Shao, Y.; Liu, X.; Wu, M.; Zhang, Q.; Liu, A. Removal of Heavy Metals from Soil by Vermiculite Supported Layered Double Hydroxides with Three-Dimensional Hierarchical Structure. *Chem. Eng. J.* **2020**, *390*, 124554.

(35) Jatav, S.; Furlan, K. P.; Liu, J.; Hill, E. H. Heterostructured Monolayer MoS_2 Nanoparticles toward Water-Dispersible Catalysts. *ACS Appl. Mater. Interfaces* **2020**, *12*, 19813−19822.

(36) Liu, J.; Jatav, S.; Hill, E. H. Few-Layer In_2S_3 in Laponite Interlayers: A Colloidal Route Toward Heterostructured Nanohybrids with Enhanced Photocatalysis. *Chem. Mater.* **2020**, *32*, 10015−10024.

(37) Liu, J.; Jatav, S.; Herber, M.; Hill, E. H. Few-Layer $ZnIn_2S_4$/Laponite Heterostructures: Role of Mg^{2+} Leaching on Zn Defect Formation. *Langmuir* **2021**, DOI: 10.1021/acs.langmuir.1c00684.

(38) Sim, L. T.; Lee, C. K.; West, A. R. High Oxide Ion Conductivity in Bi_2MoO_6 Oxidation Catalyst. *J. Mater. Chem.* **2002**, *12*, 17−19.

(39) Chankhanittha, T.; Somaudon, V.; Watcharakitti, J.; Piyavarakorn, V.; Nanan, S. Performance of Solvothermally Grown Bi_2MoO_6 Photocatalyst toward Degradation of Organic Azo Dyes and Fluoroquinolone Antibiotics. *Mater. Lett.* **2020**, *258*, 126764.

(40) Snyder, T. P.; Hill, C. G., Jr. The Mechanism For The Partial Oxidation of Propylene Over Bismuth Molybdate Catalysts. *Catal. Rev.* **1989**, *31*, 43−95.

(41) Batist, P. A. Bismuth Molybdates: Preparation and Catalysis. *J. Chem. Technol. Biotechnol.* **1979**, *29*, 451−466.

(42) Schuh, K.; Kleist, W.; Høj, M.; Trouillet, V.; Beato, P.; Jensen, A. D.; Grunwaldt, J.-D. Bismuth Molybdate Catalysts Prepared by Mild Hydrothermal Synthesis: Influence of pH on the Selective Oxidation of Propylene. *Catalysts* **2015**, *5*, 1554−1573.

(43) Sprenger, P.; Kleist, W.; Grunwaldt, J.-D. Recent Advances in Selective Propylene Oxidation over Bismuth Molybdate Based Catalysts: Synthetic, Spectroscopic, and Theoretical Approaches. *ACS Catal.* **2017**, *7*, 5628−5642.

(44) Kulkarni, A. K.; Tamboli, M. S.; Nadargi, D. Y.; Sethi, Y. A.; Suryavanshi, S. S.; Ghule, A. V.; Kale, B. B. Bismuth Molybdate (α-$Bi_2Mo_3O_{12}$) Nanoplates via Facile Hydrothermal and Its Gas Sensing Study. *J. Solid State Chem.* **2020**, *281*, 121043.

(45) Din, S. U.; Haq, M. u.; Khatoon, R.; Chen, X.; Li, L.; Zhang, M.; Zhu, L. A Novel Ethanol Gas Sensor Based on α-$Bi_2Mo_3O_{12}$/Co_3O_4 nanotube-Decorated Particles. *RSC Adv.* **2020**, *10*, 21940−21953.

(46) Ren, J.; Wang, W.; Shang, M.; Sun, S.; Gao, E. Heterostructured Bismuth Molybdate Composite: Preparation and Improved Photocatalytic Activity under Visible-Light Irradiation. *ACS Appl. Mater. Interfaces* **2011**, *3*, 2529−2533.

(47) Li, H. H.; Li, K. W.; Wang, H. Hydrothermal Synthesis and Photocatalytic Properties of Bismuth Molybdate Materials. *Mater. Chem. Phys.* **2009**, *116*, 134−142.

(48) Kumar, R.; Sudhaik, A.; Raizada, P.; Hosseini-Bandegharaei, A.; Thakur, V. K.; Saini, A.; Saini, V.; Singh, P. An Overview on Bismuth Molybdate Based Photocatalytic Systems: Controlled Morphology and Enhancement Strategies for Photocatalytic Water Purification. *J. Environ. Chem. Eng.* **2020**, *8*, 104291.

(49) Hussain, S. K.; Dudem, B.; Yu, J. S. Enhanced Electrochemical Performance via PPy Encapsulated 3D Flower-like Bismuth Molybdate Nanoplates for High-Performance Supercapacitors. *Appl. Surf. Sci.* **2019**, *478*, 846−856.

(50) Zhang, Y.; Li, L.; Han, Q.; Tang, L.; Chen, X.; Hu, J.; Li, Z.; Zhou, Y.; Liu, J.; Zou, Z. Bi_2MoO_6 Nanostrip Networks for Enhanced Visible-Light Photocatalytic Reduction of CO_2 to CH_4. *ChemPhysChem* **2017**, *18*, 3240−3244.

(51) Yang, Z.; Shen, M.; Dai, K.; Zhang, X.; Chen, H. Controllable Synthesis of Bi_2MoO_6 Nanosheets and Their Facet-Dependent Visible-Light-Driven Photocatalytic Activity. *Appl. Surf. Sci.* **2018**, *430*, 505−514.

(52) Wu, X.; Ng, Y. H.; Saputera, W. H.; Wen, X.; Du, Y.; Dou, S. X.; Amal, R.; Scott, J. The Dependence of Bi_2MoO_6 Photocatalytic Water Oxidation Capability on Crystal Facet Engineering. *ChemPhotoChem* **2019**, *3*, 1246−1253.

(53) Xing, Y.; Cheng, R.; Li, H.; Liu, Z.; Du, C. Mannitol-Assisted Synthesis of Ultrathin Bi_2MoO_6 Architectures: Excellent Selective Adsorption and Photocatalytic Performance. *J. Nanopart. Res.* **2019**, *21*, 40.

(54) Baigorria, E.; Cano, L.; Alvarez, V. Nanoclays as Eco-Friendly Adsorbents of Arsenic for Water Purification. In *Handbook of Nanomaterials and Nanocomposites for Energy and Environmental Applications*; Springer: 2020; *2*, 1−17, DOI: 10.1007/978-3-030-11155-7_61-1.

(55) Thompson, D. W.; Butterworth, J. T. The Nature of Laponite and Its Aqueous Dispersions. *J. Colloid Interface Sci.* **1992**, *151*, 236−243.

(56) Zhang, L.; Wang, W.; Chen, Z.; Zhou, L.; Xu, H.; Zhu, W. Fabrication of Flower-like Bi_2WO_6 Superstructures as High Performance Visible-Light Driven Photocatalysts. *J. Mater. Chem.* **2007**, *17*, 2526−2532.

(57) Samdani, K. J.; Park, J. H.; Joh, D. W.; Lee, K. T. Self-Assembled Bi_2MoO_6 Nanopetal Array on Carbon Spheres toward Enhanced Supercapacitor Performance. *ACS Sustainable Chem. Eng.* **2018**, *6*, 16702−16712.

(58) Jun, Y.-w.; Choi, J.-s.; Cheon, J. Shape Control of Semiconductor and Metal Oxide Nanocrystals through Nonhydrolytic Colloidal Routes. *Angew. Chem., Int. Ed.* **2006**, *45*, 3414−3439.

(59) Keulks, G. W.; Hall, J. L.; Daniel, C.; Suzuki, K. The Catalytic Oxidation of Propylene: IV. Preparation and Characterization of α-Bismuth Molybdate. *J. Catal.* **1974**, *34*, 79−97.

(60) Zhang, L.; Xu, T.; Zhao, X.; Zhu, Y. Controllable Synthesis of Bi_2MoO_6 and Effect of Morphology and Variation in Local Structure on Photocatalytic Activities. *Appl. Catal., B* **2010**, *98*, 138−146.

(61) Sugimoto, T. Preparation of Monodispersed Colloidal particles. *Adv. Colloid Interface Sci.* **1987**, *28*, 65−108.

(62) Beale, A. M.; Sankar, G. In Situ Study of the Formation of Crystalline Bismuth Molybdate Materials under Hydrothermal Conditions. *Chem. Mater.* **2003**, *15*, 146−153.

(63) Wu, M.; Wang, Y.; Xu, Y.; Ming, J.; Zhou, M.; Xu, R.; Fu, Q.; Lei, Y. Self-Supported Bi_2MoO_6 Nanowall for Photoelectrochemical Water Splitting. *ACS Appl. Mater. Interfaces* **2017**, *9*, 23647−23653.

(64) Beale, A. M.; Reilly, L. M.; Sankar, G. Watching the Crystallisation of Complex Oxides by in Situ X-Ray Techniques. *Appl. Catal., A* **2007**, *325*, 290−295.

(65) Peng, Z. A.; Peng, X. Nearly Monodisperse and Shape-Controlled CdSe Nanocrystals via Alternative Routes: Nucleation and Growth. *J. Am. Chem. Soc.* **2002**, *124*, 3343−3353.

(66) Kopinke, F. D.; Stottmeister, U. Comment on "Adsorption of CO_2 and N_2 on Soil Organic Matter: Nature of Porosity, Surface Area, and Diffusion Mechanism". *Environ. Sci. Technol.* **1996**, *30*, 3634−3635.

(67) Li, F.; Jin, J.; Shen, Z.; Ji, H.; Yang, M.; Yin, Y. Removal and Recovery of Phosphate and Fluoride from Water with Reusable Mesoporous Fe_3O_4@mSiO_2@mLDH Composites as Sorbents. *J. Hazard. Mater.* **2020**, *388*, 121734.

Chapter 4

Surface-Encapsulated Bismuth Molybdate-Layered Silicate Hybrids as Sorbents for Photocatalytic Filtration Membranes

This chapter has been published as: Jatav, S.; Herber, M.; Xiang H.; Hill, E. H. Surface-Encapsulated Bismuth Molybdate-Layered Silicate Hybrids as Sorbents for Photocatalytic Filtration Membranes. *ACS Applied Materials & Interfaces.* **2022**, 14 (20), 22790-22798.

In chapter 3, it was shown that the organically modified laponite interlayer templates the growth of Bi_2MoO_6 and results in the formation of photocatalytic sorbent laponite-Bi_2MoO_6 hybrid particles. This subsequent study aimed at further improving the adsorption capacity of these laponite-Bi_2MoO_6 hybrid by encapsulating these particles with a thin shell of polymer. Herein, the encapsulation of laponite-Bi_2MoO_6 hybrids with a thin shell of crosslinked polymer blend of styrene and butyl acrylate resulted in the enhancement of adsorption capacity of the former. Furthermore, since the laponite-Bi_2MoO_6 hybrids exhibit near-instantaneous molecular sorption, their polymer encapsulated counterparts also turned out to be effective at sequestering model pollutants when used in a filtration setup.

ACS APPLIED MATERIALS & INTERFACES

www.acsami.org Forum Article

Surface-Encapsulated Bismuth Molybdate-Layered Silicate Hybrids as Sorbents for Photocatalytic Filtration Membranes

Sanjay Jatav, Marcel Herber, Hongxiao Xiang, and Eric H. Hill*

Cite This: *ACS Appl. Mater. Interfaces* 2022, 14, 22790−22798 Read Online

ACCESS | Metrics & More | Article Recommendations | Supporting Information

ABSTRACT: Groundwater is being depleted globally at an average rate of more than one meter per year, during a period when more than a quarter of the human population has no access to potable water. Aside from overexploitation, freshwater security is also threatened by climate change and chemical pollution. The contamination of surface and groundwater by industrial substances is also undermining the vitality of ecosystems. It was previously shown that {100}-faceted Bi_2MoO_6−Laponite hybrids effectively bind and photodegrade molecular species, aiding in the decontamination of water. In this study, the encapsulation of Bi_2MoO_6−Laponite particles with the polymers butyl acrylate and styrene further enhanced adsorption of methylene blue by 31.4%, with a specific adsorption capacity of 192 μmol/g. The polymer−particle composites were deposited to form membranes and their efficacies in water filtration and photodegradation were examined. Among the different surface modifications examined, the highest dye sorption was obtained by butyl acrylate and styrene (3:2) with a 5 mol % cross-linker. This study provides a method for enhancing the molecular adsorption of composite particles used in membranes capable of multiple cycles of adsorption and photodegradation, advancing the application of such systems to water filtration.

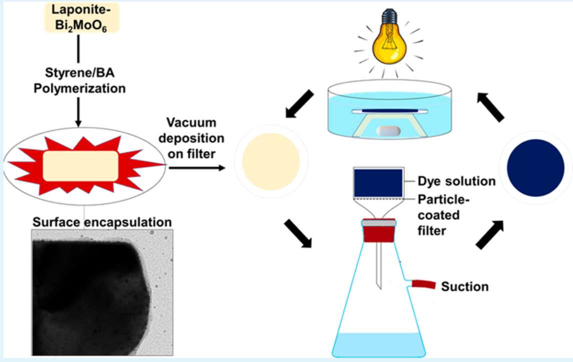

KEYWORDS: *Bi_2MoO_6, Laponite, surface modification, dye adsorption, self-cleaning membranes, water remediation*

INTRODUCTION

The exploitation and consumption of resources has resulted in the indiscriminate release of greenhouse gases and more than 350 000 different anthropogenic/industrial chemicals.[1,2] The magnitude of anthropogenic chemical discharge is estimated to be in excess of 200 billion tons per year−only a fifth of which is due to greenhouse gas emissions.[3] The chemical footprint of humanity has been found in the stratosphere, summits of high mountains,[4] in the deepest point in the oceans,[5] across the geosphere[6] and hydrosphere,[7] and in the human food chain.[8] These industrial chemicals, including many known carcinogens and their residues, have been detected in all human populations, including the fetus and infants,[9,10] and in mothers' milk.[11,12] There is mounting evidence implicating chemical contamination of the human habitat in reproductive, cognitive, and developmental disorders as well as premature deaths.[13] Not only does chemical poisoning today constitute the greatest form of preventable mortality, it also aggravates the problem of biodiversity loss[14] by extirpating insects and animals involved in pollination and water filtration, which are crucial for human survival and well-being.[15]

Most notable among these industrial chemicals are synthetic organic dyes. The worldwide production of these dyes as of 2009 was 700 000 t annually, and they are used primarily by the textile, printing, cosmetic, and pharmaceutical industries.[16] The untreated discharge of dyes into local water streams changes the color of water, altering the amount of sunlight that passes through, which can have adverse consequences for the aquatic biota.[17] In addition, some are toxic, mutagenic, and carcinogenic because of the presence of compounds such as benzidine, naphthalene, and other aromatics.[18] Apart from this, these dyes are essentially nonbiodegradable and remain in the biosphere for extended periods of time, raising the risk of bioaccumulation.[19,20] Because dye molecules possess a small size and high solubility and stability in water, it presents a challenge to filter or remove these molecules by conventional means.[21]

Filtration and reverse osmosis by polymer-based membranes represent one of the most thoroughly investigated material systems for water decontamination, mainly because of their high removal efficiency of small organic molecule, salt rejection, and high permeation flux.[22,23] Many different inorganic materials are now being explored toward the same

Special Issue: Early Career Forum

Received: October 23, 2021
Accepted: December 29, 2021
Published: January 11, 2022

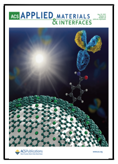

https://doi.org/10.1021/acsami.1c20503

end. Recent studies aimed toward decontaminating water polluted with atomic and molecular species have explored materials ranging from 2D systems like g-C_3N_4[24] and MXenes[25] to carbon organic frameworks (COFs)[26] and metal organic frameworks (MOFs)[27] and have investigated their efficacy in a filtration setup. For instance, Ren et al. used Fe-based MOFs (MIL-53(Fe)) in combination with polyvinyidene fluoride (PVDF) to fabricate a water filtration membrane and tested it by filtering dye-contaminated water, going on to show that the addition of H_2O_2 further improves methylene blue (MB) removal due to the catalytic activity of MIL-53(Fe).[27] They showed that 75% of MB could be removed from an aqueous solution (6.25 μM) by a combination of adsorption and catalytic degradation. In another study, Kim et al. found $Ti_3C_2T_x$ MXene-coated polyamide membranes to be effective at adsorbing cationic dyes, showing a maximum specific adsorption capacity of 131.31 μmol/g for MB.[28]

A major hindrance toward the wide-scale adoption of these technologies is the fouling of filtration membranes. The loss of performance during early stages of fouling can render filtration membranes useless if mitigatory actions are not taken. The present day processes required for overcoming the problem of fouling are highly energy intensive and involve laborious and expensive cleanup.[29] Researchers have responded to the challenge of membrane fouling by striving to incorporate multiple functionalities in membrane-based filtration systems. The use of photocatalytic particles that can degrade the adsorbate without requiring any energy intensive inputs is a critical area for advancement toward a level where their real application becomes feasible.[30] In this vein, TiO_2 particles immobilized on a filter substrate have been investigated previously as antifouling/self-cleaning water filtration membranes. In one study of these TiO_2 water filtration membranes, Lee et al. found that the reduction of the band gap due to N-doping of TiO_2 results in notable improvements in permeance, photocatalytic activity, and self-cleaning action under solar illumination,[31] whereas, Zhang et al. reported the enhancement of humic acid degradation and fouling resistance upon hydrogenation-assisted Ti^{3+} self-doping of TiO_2.[32]

Previous studies have shown that the surfactant-pillared nanoscopic clay Laponite-RD (Lap) can template the growth of a number of semiconductors as thin layers within the Lap intergallery space, strongly influencing both the morphology and the crystalline growth orientation.[33−35] Interestingly, in the case of Bi_2MoO_6 (BMO), self-assembly of pillared Lap template particles resulted in micrometer-sized particles with surfaces terminating in predominantly {100}-facets, which were found to be effective at quickly sequestering molecular dyes.[36] In addition, their reuse was achieved by photocatalytic degradation of an aqueous particle dispersion following dye adsorption. The characteristics of high adsorption capacity, fast adsorption kinetics, and reuse by photocatalytic degradation motivated further efforts to optimize this system for a real application.

Herein, Lap-BMO particles were modified with hydrophobic polymers butyl acrylate (BA) and styrene (Sty) and immobilized on a cellulose acetate filter to fabricate a filtration membrane. The polymer blends which grant the Lap-BMO particles increased adsorption were identified, and the influence of surface modification on photocatalytic performance was shown to be negligible for the best case, which was 3:2 butyl acrylate:styrene with a 5 mol % cross-linker. This study shows that certain polymer coatings can provide further enhancement of dye adsorption, with negligible loss of photodegradation and the added benefit of facile deposition to form membranes. This will pave the way for further advances in sorbent-based water filtration systems utilizing light-based decontamination.

■ MATERIALS AND METHODS

Materials. Laponite-RD was provided by BYK additives (Germany). Sodium molybdate, Na_2MoO_4 (99%), bismuth nitrate, $Bi(NO_3)_3$ (99%), NaOH pellets (99%), methylene blue trihydrate (MB), and methyl orange (MO), butyl acrylate (99%), *N*,*N*-methylenebis(acrylamide) (BIS) and cetyltrimethylammonium bromide, CTAB (>99%) were obtained from Sigma-Aldrich and used without further purification. Styrene (Sty), ammonium persulfate (APS), and 3-(trimethoxysilyl)propyl methacrylate (MPS) were procured from Roth, Alfa-Aesar and J&K scientific, respectively. Solutions and dispersions were prepared using filtered water (resistivity of 18.2 MΩ cm). Lap-BMO particles were synthesized according to the previously reported method using 2 mM Bi and 3.2 mg/mL Lap.[36]

Surface Functionalization of Lap-BMO with MPS. Three hundred milligrams of Lap-BMO particles were dispersed in 10 mL of ethanol with sonication for 10 min. Then, 88.8 μL of MPS was added under stirring and the reaction was carried out for 36 h. These particles were washed via centrifugation and redispersed in water. These particles are labeled Lap-BMO-MPS.

Surface Polymerization of Lap-BMO Particles. One hundred milligrams of Lap-BMO particles were dispersed in 10 mL of water by sonication (15 min). This particle dispersion was added to a three-neck flask containing 90 mL of water under stirring. Then 0.750 and 0.4 mL of BA and Sty, respectively, were added to this, followed by 64 mg of BIS as the cross-linker (5 mol % of the monomer amount). Upon reaching 70 °C, 10 mg of APS (initiator) was added, and the reaction was carried out for 2 h under reflux conditions. N_2 was bubbled during the entire course of the reaction. These samples were labeled as BS-C. The same procedure was carried out with Lap-BMO-MPS particles, labeled as M-BS-C. Samples modified without the cross-linker BIS were labeled BS. A control reaction was carried out without any Lap-BMO particles to obtain just the polymer blend of cross-linked butyl acrylate and styrene and was labeled BS-C-NoLB. For studying the role of cross-linking, we prepared sample BS-C using 2.5 and 10% mole ratios of BIS:monomer. Following the procedure as above, the polymer blend composition was also varied from a 3:2 molar ratio of BA:Sty to 1:0, 1:1, and 0:1.

Preparation of Filter Membranes. Cellulose acetate membrane filters (47 mm dia., 0.45 μm pore size) were obtained from Labsolute (Th. Geyer GmbH & Co, Germany). A filtration assembly (47 mm, Wheaton, DWK Life Sciences, NJ, USA) was used carrying out the membrane preparation and filtration studies (Figure S1). Filters were placed onto the vacuum filtration setup and moistened with water, after which 10 mL of particle−polymer dispersion (1 mg/mL) was poured onto the filter and left for 2−3 min to dry.

Filtration Experiments. Following the deposition of particles on the filter, 53.4 μM dye solution were poured through particle−polymer-modified filter paper under a vacuum. The filtrate was then diluted 4-fold before recording UV−vis spectra. Typically, 20 mL of dye solution was used, aside from the experiment where the particle amount was varied, in which 100 mL was used.

Photodegradation of Dye on Filter Membranes. A photograph of the filtration setup is shown in Figure S2. Particles were first deposited as per the procedure described above, then removed from the setup and left to dry overnight in ambient conditions. The particle-coated membrane was then loaded on the filtration setup and 2.5 mL of 53.4 μM MB was poured through the filter under vacuum. The dye-stained membrane was then fixed onto a homemade immersion fixture and immersed in water (1 cm depth) before irradiating it with a 300 W Xe solar simulator (LSE340, LOT-Oriel GmbH & Co. KG, Germany) for an hour. The lamp power was measured to be 126 mW/cm^2 at 400 nm. The filter was then removed from the fixture and dried at ambient conditions before recording the UV−vis diffuse spectra. The same amount of dye was filtered through these membranes and photodegraded for recycling experiments and UV−vis spectra were recorded after each adsorption and photodegradation cycle. For evaluating the amount of MB adsorbed in subsequent runs of recycling experiments, the amount of MB adsorbed by the filter during the first cycle (74 nmol) was taken as 100% for reference. For comparing the effect of surface encapsulation on photocatalysis, we carried out photodegradation by depositing Lap-BMO and BS-C on the filter. For this experiment 5 mL of 53.4 μM MB was poured through the filters. For these recycling and photodegradation experiments, the amount of dye photodegraded or adsorbed on the filter was estimated/measured by means of a calibration curve of adsorbed concentration relative to absorbance measured by DRS UV−vis spectrometer (Figure S3). For generating the calibration curve, a known amount of MB was deposited on the particle-coated filter, after which their DRS UV−vis spectra were recorded. The value of the absorbance at 664 nm was used for these calculations.

The photocatalytic activity of Lap-BMO, pure polymer BS-C-NoLB, BS-C, and Lap-BMO with BS-C-NoLB in aqueous solution was measured; 15.8 mg of Lap-BMO, 10 mg of BS-C-NoLB, 15.8 mg of Lap-BMO, 10 mg of BS-C-NoLB, and 25.8 mg of BS-C were separately dispersed in 15 mL of MB (13.35 μM) and irradiated for an hour.

Characterization. Transmission electron microscopy was carried out on a Phillips CM300 HRTEM (Phillips, Netherlands) to investigate the morphologies of the different samples. High-resolution transmission electron microscopy (Talos F200X, FEI, USA) was also used to obtain HAADF-STEM mappings of the samples. UV−vis absorbance spectra were obtained using a Cary 60 UV−vis spectrometer (Agilent, Santa Clara, CA, USA). FTIR measurements were performed on Bruker Invenio R using golden gate ATR; 128 scans were averaged and recorded at a resolution of 4 cm^{-1}. TGA was carried out on a Netzsch TG 209 F1 from room temperature to 800 °C at a heating rate of 10 K/min and N_2 was purged at a rate of 40 mL/min. Organic content was calculated by taking the difference in weight loss from 150 to 600 °C. N_2 adsorption−desorption isotherms were measured on an Autosorb iQ automated gas sorption analyzer (Quantacore instruments, Boynton Beach, FL, USA) for measuring the surface area. Prior to commencing N_2 adsorption, samples (100 mg of powder) were degassed at 100 °C for 2 h. The isotherms were obtained at 77 K and the surface area was estimated using the Brunauer−Emmett−Teller (BET) equation. Seven points were chosen on the isotherms between 0.05 to 0.30 relative pressure to ensure a good fit. A Cary 5000 UV−vis−NIR spectrometer (Agilent Inc., Santa Clara, CA, USA) was used to measure diffuse reflectance UV−visible (UV−vis) spectra. Scanning electron microscopy was performed on a FEI Quanta 3D (ThermoFisher Scientific, Hillsboro, Oregon, USA) at an operating voltage of 2 kV.

■ RESULTS AND DISCUSSION

A detailed discussion on the growth and morphology of Lap-BMO particles can be found in the previous report.[36] TEM micrographs show the polymer encapsulated particles (Figure 1). With cross-linking, a uniform thin coating of polymer is observed at the particle interface (Figure 1a). With surface modification of the particles by MPS, a notable increase in the thickness of polymer layer at the interface is observed, suggesting that MPS is able to bind effectively to the −OH groups of Lap in Lap-BMO and template polymerization (Figure 1b). The samples without either MPS or cross-linking show sparse and irregular coating at the interface (Figure 1c). SEM characterization showed a change in porosity in the membranes loaded with different surface-modified Lap-BMO particles (Figure 1d−f). Among the polymer-modified samples, the cross-linked BS showed dense packing with the occurrence of small pores (Figure 1d). On the other hand, M-BS-C showed much larger pore dimensions, presumably due to the thick polymer shell (Figure 1e). Non-cross-linked BS shows a smoother cross-section compared to samples BS-C and M-BS-C, which can be attributed to the lack of coating (Figure 1f). The filter coated with unmodified Lap-BMO particles showed the smoothest surface compared to the filters coated with surface-modified Lap-BMO particles, and the similarity to BS supports the low amount of polymer at the interface of the latter (Figure S4). Energy-dispersive X-ray spectroscopy (EDX) was performed using high-angle annular dark-field scanning transmission electron microscopy (HAADF-STEM) to confirm the organic nature of the surface coating, corroborating the TEM results (Figure S5).

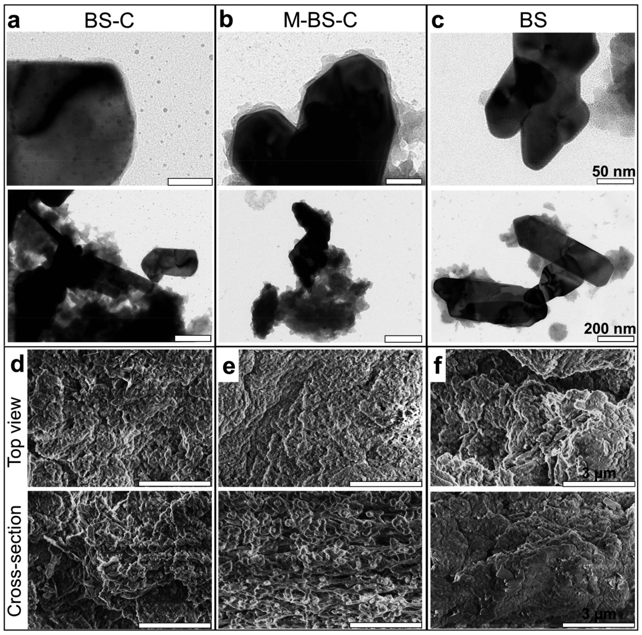

Figure 1. TEM images of the different surface-modified Lap-BMO particles. (a) BS-C, (b) M-BS-C, and (c) BS. The scale bars in a−c in the top and bottom panels correspond to 50 and 200 nm, respectively. (d−f) SEM images of the top surface and cross-section of the filters coated with different surface-modified Lap-BMO particles. Scale bars in d−f are 3 μm.

Although the electron micrographs show that cross-linking with BIS results in the formation a thin shell of BA-Sty polymers on the surface of Lap-BMO particles, further characterization of the polymer shell was carried out by FT-IR and TGA. It can be seen from the FT-IR spectra that all samples show an intense and broad peak at 649 and 970 cm^{-1} with the exception of the polymer blend BS-C-NoLB (Figure 2a). These bands correspond to the Si−O−Si stretch of Laponite[37,38] which is present in the Lap-BMO particles.[36] The band at 698 cm^{-1} is due to the deformation of the phenyl ring in styrene.[39] The bands at 1377 and 1452 cm^{-1} can be assigned to the C−H bending mode.[40] The bands at 1523 and 3920 cm^{-1} can be assigned to the N−H bend in the cross-linker BIS,[41] whereas the bands at 1651 and 1728 cm^{-1} in the spectrum of BS-C-NoLB are due to the C═O stretching mode in BA and BIS.[40−42] The bands at 2872 and 2931 cm^{-1} correspond to the symmetric and asymmetric stretching of the methylene group (−CH_2).[39,40,43] In summary, vibrational peaks due to the polymers are most pronounced with cross-linked samples M-BS-C and BS-C. Among the polymer-

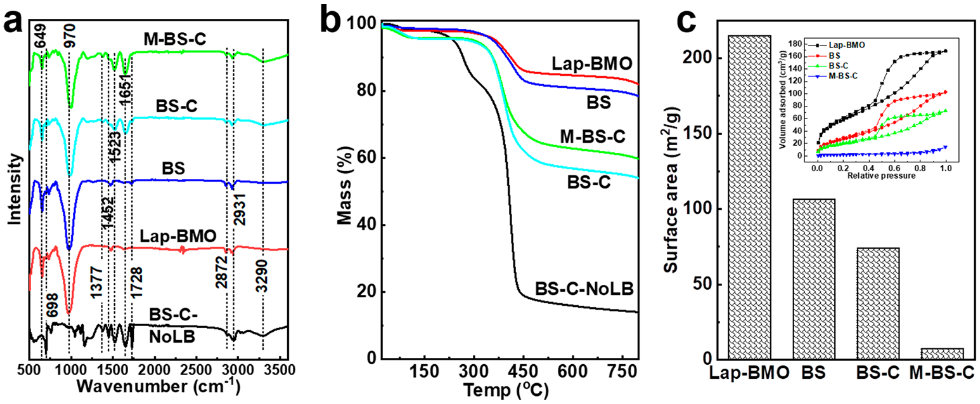

Figure 2. (a) FT-IR spectra and (b) TGA curves (c) Surface area determined by BET; inset shows the N_2 adsorption−desorption isotherms for the different samples.

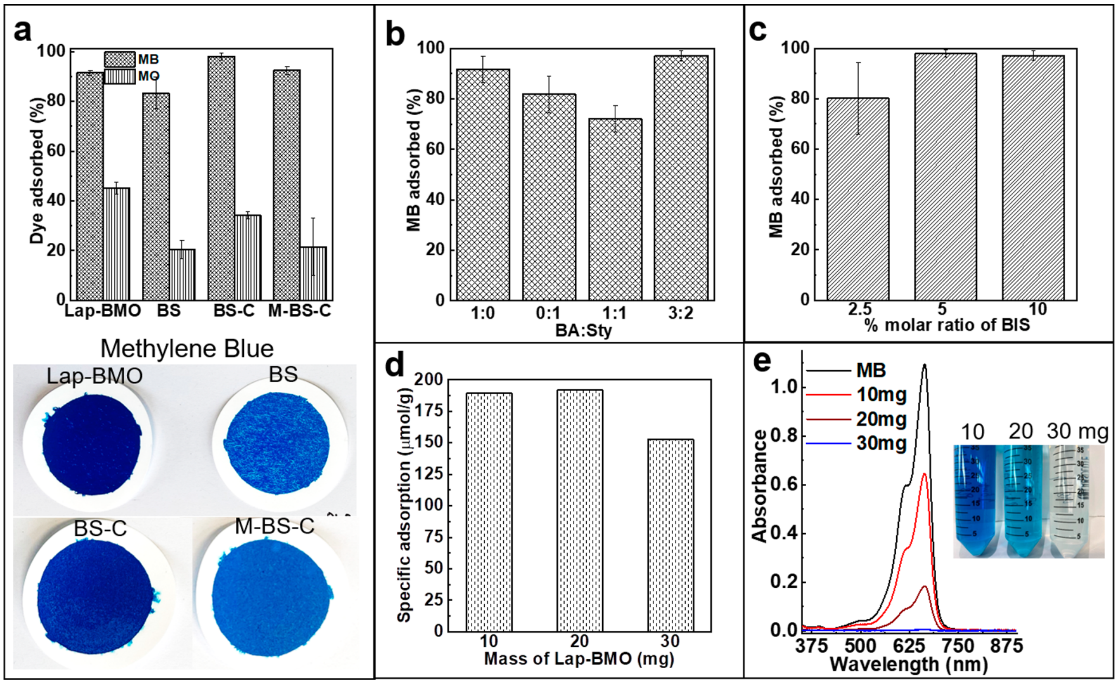

Figure 3. (a) Dye filtration experiment carried out with MB and MO. Photograph shows MB-loaded filters. (b) Dye filtered by particles prepared using different polymer compositions with BIS fixed at 5 mol %. (c) Effect of cross-linker BIS concentration on the dye adsorption performance of filters, BA:Sty 3:2. (d) Specific dye adsorption of BS-C particles measured using 100 mL of MB (53.4 μM) and (e) corresponding UV−vis spectra (image of filtrate inset). Full UV−vis spectra for a−c are shown in Figure S6.

modified samples, BS is quite similar to the Lap-BMO particles, suggesting a low amount of polymerization.

TGA was carried out to quantify the amount of polymer present on the surface-modified particles (Figure 2b). A noticeable onset of mass loss begins from 150 °C onward and saturates after 400 °C, which is attributed to organic content. The greatest loss is seen in the cross-linked polymer blend BS-C-NoLB, which lost 82% of its initial mass. Mass loss of 13% observed in the case of Lap-BMO is likely due to the decomposition of the surfactant CTAB, which was used in the Lap-BMO synthesis for pillaring Laponite. BS shows a 4.6% increased mass loss compared to Lap-BMO, which suggests that only this amount of polymer ends up coating Lap-BMO without MPS or cross-linking. In contrast, the cross-linked samples M-BS-C and BS-C show a mass loss of 32.9 and 38.7%, respectively, which is more than twice of that observed in BS. The amount of organic content for each of the measured samples is presented in Table S1.

The surface area of the different surface-modified Lap-BMO particles was measured using the Brunauer−Emmett−Teller method from the N_2 adsorption−desorption curves (Figure 2c). Not surprisingly, modification of the surface of the particles results in a decreased surface area. Sample Lap-BMO has a surface area of 216 m^2/g, whereas polymer-modified samples BS, BS-C, and M-BS-C have a surface area of 104, 74, and 7 m^2/g, respectively. Moreover, from the N_2 adsorption−desorption isotherms presented in the inset of Figure 2c, it is seen that the samples Lap-BMO, BS, and BS-C show type-IV behavior with an H2-type hysteresis, typical of mesoporous materials.[44] On the other hand, the isotherm for M-BS-C shows no such hysteresis and hence lacks porosity as opposed to all the other samples, suggesting a negative effect of surface modification by MPS. The mesoporosity of the polymer-

https://doi.org/10.1021/acsami.1c20503

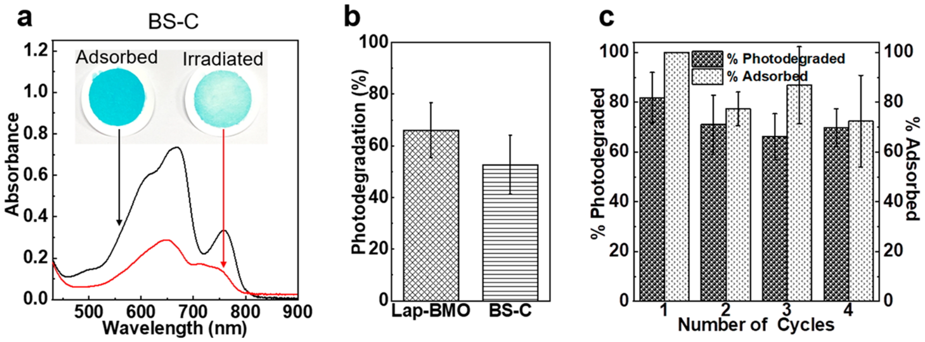

Figure 4. (a) UV−vis diffuse spectra of BS-C filters loaded with 5 mL of MB (53.4 μM) before and after 1 h of irradiation. (b) Photodegradation of MB adsorbed on filter with unmodified Lap-BMO and BS-C. (c) Cyclic filtration/photodegradation of 2.5 mL of MB (53.4 μM) over 4 cycles, adsorption in the first step taken as 100%. The quantity of MB on the filter was estimated from diffuse reflectance UV−vis (Figure S3).

coated samples BS-C and BS makes it unlikely that the removal of molecular species is the result of a size exclusion effect.

Summarizing the above findings, the degree of surface encapsulation of the particles with polymer is corroborated by TEM, FT-IR, TGA, and N_2 adsorption−desorption isotherms. Although overall polymerization is increased by cross-linking, polymer growth without MPS modification is more conducive to the growth of a thin polymer shell. On the other hand, modification of Lap-BMO with MPS led to denser growth of polymer at the particle surface. This significantly reduced the accessible surface area of the Lap-BMO particles, which plummeted from 104 m^2/g without MPS to 7 m^2/g with MPS modification (Figure 2c). Interestingly, this reduced surface area led to only a slight reduction in dye adsorption, as discussed in the following section.

Dye Adsorption on Lap-BMO Filter Membranes. It was previously shown that the improved adsorption capacity of the Lap-BMO hybrid particles was closely associated with the growth of the BMO crystal along the [010] direction.[36] This resulted in the termination of the Lap-BMO crystal in predominantly {100}-facets, which possess a higher surface energy as compared to {010}-facets.[36,45] Dye filtration experiments were carried out using a cationic dye, MB, and an anionic dye, MO. Lap-BMO and its surface-modified counterparts are more effective at sequestering the cationic dye MB than the anionic dye MO (Figure 3a). Samples Lap-BMO, BS, BS-C, and M-BS-C removed 91.4, 83.3, 97.9, and 92.4% of MB, respectively, whereas, in the case of MO, these membranes removed only 45.0, 20.4, 34.1, and 21.6%, respectively. The increased adsorption of cations compared to anions is reasonable considering the negative surface zeta potential (approximately −12 mV) of Lap-BMO.[36] In the case of MB, unmodified Lap-BMO and M-BS-C show similar dye adsorption (91.4 and 92.4%, respectively), whereas non-cross-linked BS showed a relatively poor performance (83.3%) (Figure 3a). The sample BS-C adsorbed all MB added (0.916 μmol), resulting in clean water with no MB absorption peak in the UV−vis spectrum (Figure S6). The specific adsorptions of these surface-modified particles (related to the mass of Lap-BMO) were calculated (Table S2). In the case of MB, samples Lap-BMO, BS, BS-C, and M-BS-C showed specific adsorption capacity of ∼95, 90, 125, and 113 μmol/g, respectively. This suggests that surface passivation of particles might occur in the absence of a cross-linker. Furthermore, the cross-linked samples BS-C and M-BS-C showed an enhancement of specific adsorption of ∼31 and 16% over unmodified Lap-BMO particles, respectively. Without cross-linking, a 15% reduction in adsorption performance was observed for BS compared to Lap-BMO. However, in the case of MO, surface encapsulation resulted in a reduction of the adsorption capacity of Lap-BMO particles, where samples Lap-BMO, BS, BS-C, and M-BS-C showed specific adsorption capacities of ∼57, 27, 53, and 32 μmol/g, respectively (Table S2).

The effect of polymer blend composition on adsorption effectiveness was also investigated. As can be seen from Figure 3b, pure cross-linked Sty-functionalized particles adsorb ∼82% of MB, which is less than the cross-linked-BA-coated samples, which adsorb 91.6% of MB. Particles coated with a 1:1 molar ratio of BA to Sty only adsorbed 72% of the dye. The best performance was shown by the sample prepared at a BA:Sty of 3:2, which adsorbed 97.9% of the dye that passed through. Furthermore, the effect of the cross-linker amount on the filtration performance was studied by varying BIS from 2.5 to 10% molar ratio of monomers (Figure 3c). A 5% molar ratio of BIS gave the best adsorption, whereas at 2.5 and 10%, samples adsorbed 80.1 and 97.1% of MB, respectively. Interestingly, because the samples prepared at 5 and 10% molar ratio of BIS, which adsorb ∼98 and 97% of the dye, filter more dye than Lap-BMO itself (∼91%), these results indicate that more cross-linking is beneficial for adsorption (Figure 3c). In the case of MO, maximum dye is adsorbed by Lap-BMO, followed by BS-C, BS, and M-BS-C.

To determine the maximum specific adsorption capacity of the highest-performing composition (BS-C), we filtered 100 mL of MB solution (53.4 μM) through membranes containing 10, 20, and 30 mg of Lap-BMO particles (Figure 3d). From these results and the corresponding UV−vis spectra (Figure 3e), the maximum specific adsorption can be observed in samples with 10 and 20 mg particles. The maximum adsorption capacity increases marginally at first, from 189.3 to 191.8 μmol/g with the doubling of the quantity of Lap-BMO from 10 to 20 mg and then dips to 152.7 μmol/g. This drop in the 30 mg sample results from an excess of particles, which is clear from the completely colorless filtrate (Figure 3e). These results indicate an upper limit to dye adsorption, which is consistent as particle amount is increased. Thus, with higher particle loading, the sorbent action of the particle surface is not compromised.

Photodegradation and Recycling of Membranes. To find out whether the surface coating affected the dye photodegradation performance of these filters, we carried out a comparative study between the unmodified Lap-BMO and the most effective sample, BS-C. A substantial amount of MB was photodegraded by sample BS-C in an hour of irradiation

(Figure 4a.) The emergence of an extra peak at 757 nm in the spectra of Figure 4a as compared to the spectra Figure S6a, c, and d may be due to the formation of MBH^{2+} entities on the surface of the particles.[46] Unmodified Lap-BMO degraded 66.1% of the adsorbed MB, whereas the surface-modified BS-C degraded 52.7% within an hour of light exposure (Figure 4b). Because Lap-BMO particles are the source of photocatalytic activity, the diminished performance of BS-C could be due to the actual amount of Lap-BMO particles present in the sample BS-C (61%). BS-C comprised ∼39% organic content by weight, whereas Lap-BMO had only 10% (Table S1). Considering this, the actual amount degraded per milligram of Lap-BMO was increased by ∼10% for BS-C, which is an improvement considering the reduced surface area measured by BET. To study the role of polymer in the photocatalytic degradation of dye, we performed control photodegradation experiments in MB solution (Figure S7). The polymer alone degraded 24.5% of MB, which is marginally above the photodegradation of MB control (22.8%), whereas Lap-BMO degraded ∼85% alone, showing that there is only a minor contribution of the polymer itself to the degradation. Interestingly, the sample BS-C showed better performance than Lap-BMO and Lap-BMO and polymer mixed, indicating that the polymer shell has a synergistic effect toward photocatalytic degradation.

As stated in the introduction, a major factor limiting the performance of any membrane-based system is fouling due to saturation with filtrate over time, which can shorten the membrane lifetime. In the extreme case, foulants stuck in pores or on the membrane surface can make it difficult to restore flux through the membrane even after employing physical and chemical antifouling treatments.[47] Conventional means of tackling this problem along the lines of chemical/physical cleaning and replacement of faulty membrane modules lead to significant increases in capital.[30] Therefore, photocatalytic degradation of these foulants presents a low-cost and environmentally benign solution to the problem of membrane fouling. Photocatalytic membrane systems can be irradiated ex situ, which requires its removal from the filtration apparatus, or in situ, entailing irradiation of the membrane under continuous flow conditions, conferring the advantage of interruption-free filtration and regeneration of the membrane.[48] The system presented here falls into the former category; however, the latter could be easily achieved if the requisite equipment were available.

To study the potential real-world use of these membranes in decontamination applications, we subjected the particle-coated membranes to repeated cycles of adsorption and photocatalytic degradation of the adsorbed dye (Figure 4c). The amount of dye adsorbed after the first adsorption cycle decreased by 22.7, 13.2, and 27.6% in cycles 2−4, respectively. During the first cycle, 82% of the dye adsorbed onto the filter was photodegraded, whereas 71, 66, and 70% was degraded in subsequent cycles 2−4, respectively. In a previous study, we reported that Lap-BMO particles do not undergo any observable structural changes (based on TEM and X-ray diffractograms) after four cycles of photocatalysis and adsorption.[36] Therefore, to evaluate the state of surface polymer coating after use, we deposited 20 mg of BS-C onto the filter and irradiated with light for 5 h. The FT-IR spectra are essentially unchanged after irradiation except for the emergence of a small peak at 1227 cm^{-1} (Figure S8a). This peak can be ascribed to the $\gamma_t(CH_2)$ methylene twisting mode of butyl acrylate, and its emergence might be related to the photodegradation of polymer directly by light or by the photocatalytic BMO.[49] TGA showed that the organic content in the light irradiated sample decreases to 29.2% from 38.7%, which may indicate damage to the polymer shell (Figure S8b).

■ CONCLUSIONS

This work represents an extension of the usage of highly sorbent Lap-Bi_2MoO_6 particles from dispersion[36] to a membrane filter toward continuous-flow wastewater decontamination. The focus of this study was to exploit the fast adsorption kinetics and further enhance the high adsorption capacity of Lap-BMO particles by surface functionalization with hydrophobic polymers BA, Sty, or both. In addition to determining the optimal polymer blend and amount of cross-linker BIS, it was found that the organosilane MPS, which covalently attaches to the −OH groups of the Lap edge, increased polymer grafting at the particle surface and marginally improved the adsorption of MB while greatly reducing the available surface area. The polymer-modified Lap-BMO particles were then deposited on a cellulose acetate filtration membrane, toward removal of a cationic thiazine dye, methylene blue, and an anionic azo dye, methyl orange. Although these membranes were able to sieve both MB and MO, polymer-modified particles were found to be more effective toward adsorbing cationic dye MB than MO, in line with results from the unmodified Lap-BMO particles.[36]

Furthermore, the regeneration of these membrane filters by photocatalytic degradation of the adsorbed dye provided a facile means for mitigating membrane fouling. One of the major shortcomings of this filtration system is the rate at which water was filtered through them (2 mL/min). Therefore, applying them in a real system would require studying these filters in a stacked configuration to optimize liquid flow and tuning membrane porosity to improve flow without sacrificing decontamination efficiency. Also, photocatalytic degradation on the filter surface could be easily improved by the growth of plasmonic metal nanoparticles such as Ag, Au, or Pt on the Lap-BMO particles.[50,51] This could potentially be achieved by a previously reported method where metal salts complexed with poly(vinyl alcohol)-modified Lap were dried to form films directly, followed by nanoparticle formation in situ with a weak reducing agent.[52]

Moreover, these results strongly suggest that surface encapsulation of the particles can enhance their specific adsorption capacity. In fact, the specific adsorption capacity of 191.83 μmol/g during filtration measured herein exceeds that of other extant sorbent-based filters under flow conditions in the literature, with the next best being 171.87 μmol/g for powdered activated carbon (Table S3). It may be useful to further tailor the surface modifications of these sorbent particles for more specific purposes, such as sequestering per-polyfluoroalkyl compounds.[53] Also, as the synthesis and deposition of these polymer-encapsulated Lap-BMO particles is simple, it presents a relatively straightforward and low-cost means to upgrade existing water filtration membranes to tackle molecular entities in the water stream. Finally, considering that the total weight percent of BMO in polymer-modified Lap-BMO is a mere 13.46% (with 9.23 and 2.1 wt % of Bi and Mo per BS-C sample), this represents a cheap and efficient means of producing highly adsorbent photocatalysts.

Because the products of photocatalytic degradation are relatively benign,[54,55] this fouling mitigation approach, apart from reducing operational costs, also minimizes secondary pollution. Aside from water decontamination, the same sorbent particle system could potentially be adapted for nutrient and metal mining from the waste stream.[56−58] A better understanding of adsorption and controlled desorption of molecules at the {100}-facet-rich Bi_2MoO_6 particle surface may also provide avenues toward applications in separation and controlled release. Finally, such efforts in water decontamination and molecular separation may benefit from combining both sorbent activity at specific crystalline facets and nanofiltration approaches utilizing 2D materials.[59]

ASSOCIATED CONTENT

Supporting Information

The Supporting Information is available free of charge at https://pubs.acs.org/doi/10.1021/acsami.1c20503.

> Organic content in the different samples; specific dye adsorption; SEM images of Lap-BMO-coated filter; UV−vis spectra from dye adsorption experiments; calibration curve for estimating quantity of dye from DRS-UV−vis; photographs of the vacuum filtration and photodegradation setup; UV−vis spectra of MB adsorption by polymer control; MB degradation in aqueous dispersions of polymer/particle controls; FT-IR and TGA curves of BS-C before and after 5 h of irradiation; HAADF-STEM EDX elemental maps; literature comparison of maximum adsorption capacities (PDF)

AUTHOR INFORMATION

Corresponding Author

Eric H. Hill − *Institute of Physical Chemistry, University of Hamburg, Hamburg 20146, Germany; The Hamburg Center for Ultrafast Imaging (CUI), Hamburg 22761, Germany;* orcid.org/0000-0003-3063-1447; Email: eric.hill@chemie.uni-hamburg.de

Authors

Sanjay Jatav − *Institute of Physical Chemistry, University of Hamburg, Hamburg 20146, Germany*

Marcel Herber − *Institute of Physical Chemistry, University of Hamburg, Hamburg 20146, Germany*

Hongxiao Xiang − *Institute of Physical Chemistry, University of Hamburg, Hamburg 20146, Germany*

Complete contact information is available at: https://pubs.acs.org/10.1021/acsami.1c20503

Notes

The authors declare no competing financial interest.

ACKNOWLEDGMENTS

This research was funded by the DAAD from the funds of German Federal Ministry of Education and Research (BMBF), under the MOPGA-GRI program (57429511). E.H.H. is supported by the Cluster of Excellence “Advanced Imaging of Matter” of the Deutsche Forschungsgemeinschaft (DFG)—EXC 2056—project ID 390715994. H.X. is supported by funds from the DFG−project ID 447787198. We thank Dr. Charlotte Ruhmlieb for assisting with SEM characterization. We thank the Weller/Vossmeyer groups for providing access to a Cary 5000 UV−vis−NIR spectrometer. We thank Dr. Hauke Heller of the Institute of Physical Chemistry for providing access to the gas sorption analyzer for BET surface area measurements.

REFERENCES

(1) Naidu, R.; Biswas, B.; Willett, I. R.; Cribb, J.; Kumar Singh, B.; Paul Nathanail, C.; Coulon, F.; Semple, K. T.; Jones, K. C.; Barclay, A.; Aitken, R. J. Chemical Pollution: A Growing Peril and Potential Catastrophic Risk to Humanity. *Environ. Int.* **2021**, *156*, 106616.

(2) Wang, Z.; Walker, G. W.; Muir, D. C. G.; Nagatani-Yoshida, K. Toward a Global Understanding of Chemical Pollution: A First Comprehensive Analysis of National and Regional Chemical Inventories. *Environ. Sci. Technol.* **2020**, *54* (5), 2575−2584.

(3) Cribb, J. *Surviving the 21st Century: Humanity's Ten Great Challenges and How We Can. Overcome Them*, 1st ed.; Springer, 2017.

(4) Napper, I. E.; Davies, B. F. R.; Clifford, H.; Elvin, S.; Koldewey, H. J.; Mayewski, P. A.; Miner, K. R.; Potocki, M.; Elmore, A. C.; Gajurel, A. P.; Thompson, R. C. Reaching New Heights in Plastic Pollution—Preliminary Findings of Microplastics on Mount Everest. *One Earth* **2020**, *3* (5), 621−630.

(5) Chiba, S.; Saito, H.; Fletcher, R.; Yogi, T.; Kayo, M.; Miyagi, S.; Ogido, M.; Fujikura, K. Human Footprint in the Abyss: 30 Year Records of Deep-Sea Plastic Debris. *Mar. Policy* **2018**, *96*, 204−212.

(6) Alam, R.; Ahmed, Z.; Howladar, M. F. Evaluation of Heavy Metal Contamination in Water, Soil and Plant around the Open Landfill Site Mogla Bazar in Sylhet, Bangladesh. *Groundw. Sustain. Dev.* **2020**, *10*, 100311.

(7) Hoang, H. G.; Lin, C.; Tran, H. T.; Chiang, C. F.; Bui, X. T.; Cheruiyot, N. K.; Shern, C. C.; Lee, C. W. Heavy Metal Contamination Trends in Surface Water and Sediments of a River in a Highly-Industrialized Region. *Environ. Technol. Innov.* **2020**, *20*, 101043.

(8) Gruber, K. Cleaning up Our Future Health. *Nature* **2018**, *555* (7695), S20−S22.

(9) Mathiesen, L.; Buerki-Thurnherr, T.; Pastuschek, J.; Aengenheister, L.; Knudsen, L. E. Fetal Exposure to Environmental Chemicals; Insights from Placental Perfusion Studies. *Placenta* **2021**, *106*, 58−66.

(10) Soleman, S. R.; Fujitani, T.; Fujii, Y.; Harada, K. H. Levels of Octachlorostyrene in Mothers' Milk and Potential Exposure among Infants in Sendai City, Japan 2012. *Int. J. Environ. Res. Public Health* **2020**, *17* (9), 3064.

(11) Hu, L.; Luo, D.; Wang, L.; Yu, M.; Zhao, S.; Wang, Y.; Mei, S.; Zhang, G. Levels and Profiles of Persistent Organic Pollutants in Breast Milk in China and Their Potential Health Risks to Breastfed Infants: A Review. *Sci. Total Environ.* **2021**, *753*, 142028.

(12) van den Berg, M.; Kypke, K.; Kotz, A.; Tritscher, A.; Lee, S. Y.; Magulova, K.; Fiedler, H.; Malisch, R. WHO/UNEP Global Surveys of PCDDs, PCDFs, PCBs and DDTs in Human Milk and Benefit-Risk Evaluation of Breastfeeding. *Arch. Toxicol.* **2017**, *91* (1), 83−96.

(13) Diamanti-Kandarakis, E.; Bourguignon, J. P.; Giudice, L. C.; Hauser, R.; Prins, G. S.; Soto, A. M.; Zoeller, R. T.; Gore, A. C. Endocrine-Disrupting Chemicals: An Endocrine Society Scientific Statement. *Endocr. Rev.* **2009**, *30* (4), 293−342.

(14) Bradshaw, C. J. A.; Ehrlich, P. R.; Beattie, A.; Ceballos, G.; Crist, E.; Diamond, J.; Dirzo, R.; Ehrlich, A. H.; Harte, J.; Harte, M. E.; et al. Underestimating the Challenges of Avoiding a Ghastly Future. *Front. Conserv. Sci.* **2021**, *1*, 1−10.

(15) Goulson, D. An Overview of the Environmental Risks Posed by Neonicotinoid Insecticides. *J. Appl. Ecol.* **2013**, *50* (4), 977−987.

(16) Soloman, P. A.; Basha, C. A.; Velan, M.; Ramamurthi, V.; Koteeswaran, K.; Balasubramanian, N. Electrochemical Degradation of Remazol Black B Dye Effluent. *Clean - Soil, Air, Water* **2009**, *37* (11), 889−900.

(17) Gita, S.; Hussan, A.; Choudhury, T. G. Impact of Textile Dyes Waste on Aquatic Environments and Its Treatment. *Environ. Ecol.* **2017**, *35* (3), 2349−2353.

(18) Zaharia, C.; Suteu, D.; Muresan, A.; Muresan, R.; Popescu, A. Textile Wastewater Treatment by Homogeneous Oxidation with Hydrogen Peroxide. *Environ. Eng. Manag. J.* **2009**, *8* (6), 1359−1369.

(19) Ali, H. Biodegradation of Synthetic Dyes - A Review. *Water. Air. Soil Pollut.* **2010**, *213*, 251−273.

(20) Chaturvedi, A.; Rai, B. N.; Singh, R. S.; Jaiswal, R. P. A Comprehensive Review on the Integration of Advanced Oxidation Processes with Biodegradation for the Treatment of Textile Wastewater Containing Azo Dyes. *Rev. Chem. Eng.* **2021**, DOI: 10.1515/revce-2020-0010.

(21) Brillas, E.; Martínez-Huitle, C. A. Decontamination of Wastewaters Containing Synthetic Organic Dyes by Electrochemical Methods. An Updated Review. *Appl. Catal. B Environ.* **2015**, *166*, 603−643.

(22) Lau, W. J.; Ismail, A. F. Polymeric Nanofiltration Membranes for Textile Dye Wastewater Treatment: Preparation, Performance Evaluation, Transport Modelling, and Fouling Control - a Review. *Desalination* **2009**, *245* (1), 321−348.

(23) Tul Muntha, S.; Kausar, A.; Siddiq, M. Advances in Polymeric Nanofiltration Membrane: A Review. *Polym. - Plast. Technol. Eng.* **2017**, *56* (8), 841−856.

(24) Liu, Y.; Yu, Z.; Li, X.; Shao, L.; Zeng, H. Super Hydrophilic Composite Membrane with Photocatalytic Degradation and Self-Cleaning Ability Based on LDH and g-C3N4. *J. Membr. Sci.* **2021**, *617*, 118504.

(25) Kim, S.; Gholamirad, F.; Shin, B.; Taheri-Qazvini, N.; Cho, J.; Yu, M.; Park, C. M.; Heo, J.; Yoon, Y. Application of a $Ti_3C_2T_X$ MXene-Coated Membrane for Removal of Selected Natural Organic Matter and Pharmaceuticals. *ACS ES&T Water* **2021**, *1* (9), 2164−2173.

(26) Li, G.; Ye, J.; Shen, Y.; Fang, Q.; Liu, F. Covalent Triazine Frameworks Composite Membrane (CdS/CTF-1) with Enhanced Photocatalytic in-Situ Cleaning and Disinfection Properties for Sustainable Separation. *Chem. Eng. J.* **2021**, *421*, 127784.

(27) Ren, Y.; Li, T.; Zhang, W.; Wang, S.; Shi, M.; Shan, C.; Zhang, W.; Guan, X.; Lv, L.; Hua, M.; Pan, B. MIL-PVDF Blend Ultrafiltration Membranes with Ultrahigh MOF Loading for Simultaneous Adsorption and Catalytic Oxidation of Methylene Blue. *J. Hazard. Mater.* **2019**, *365*, 312−321.

(28) Kim, S.; Yu, M.; Yoon, Y. Fouling and Retention Mechanisms of Selected Cationic and Anionic Dyes in a $Ti_3C_2T_X$ MXene-Ultrafiltration Hybrid System. *ACS Appl. Mater. Interfaces* **2020**, *12* (14), 16557−16565.

(29) Ning, R. Y.; Troyer, T. L. Colloidal Fouling of RO Membranes Following MF/UF in the Reclamation of Municipal Wastewater. *Desalination* **2007**, *208*, 232−237.

(30) Zhang, H.; Wan, Y.; Luo, J.; Darling, S. B. Drawing on Membrane Photocatalysis for Fouling Mitigation. *ACS Appl. Mater. Interfaces* **2021**, *13* (13), 14844−14865.

(31) Lee, A.; Libera, J. A.; Waldman, R. Z.; Ahmed, A.; Avila, J. R.; Elam, J. W.; Darling, S. B. Conformal Nitrogen-Doped TiO_2 Photocatalytic Coatings for Sunlight-Activated Membranes. *Adv. Sustainable Syst.* **2017**, *1*, 1600041.

(32) Zhang, L.; Ng, T. C. A.; Liu, X.; Gu, Q.; Pang, Y.; Zhang, Z.; Lyu, Z.; He, Z.; Ng, H. Y.; Wang, J. Hydrogenated TiO_2 Membrane with Photocatalytically Enhanced Anti-Fouling for Ultrafiltration of Surface Water. *Appl. Catal. B Environ.* **2020**, *264*, 118528.

(33) Jatav, S.; Furlan, K. P.; Liu, J.; Hill, E. H. Heterostructured Monolayer MoS_2 Nanoparticles toward Water-Dispersible Catalysts. *ACS Appl. Mater. Interfaces* **2020**, *12* (17), 19813−19822.

(34) Liu, J.; Jatav, S.; Hill, E. H. Few-Layer In_2S_3 in Laponite Interlayers: A Colloidal Route Toward Heterostructured Nanohybrids with Enhanced Photocatalysis. *Chem. Mater.* **2020**, *32* (23), 10015−10024.

(35) Liu, J.; Jatav, S.; Herber, M.; Hill, E. H. Few-Layer $ZnIn_2S_4$/Laponite Heterostructures: Role of Mg^{2+} Leaching on Zn Defect Formation. *Langmuir* **2021**, *37* (15), 4727−4735.

(36) Jatav, S.; Liu, J.; Herber, M.; Hill, E. H. Facet Engineering of Bismuth Molybdate via Confined Growth in a Nanoscale Template toward Water Remediation. *ACS Appl. Mater. Interfaces* **2021**, *13* (16), 18713−18723.

(37) Tao, L.; Zhonglong, L.; Ming, X.; Zezheng, Y.; Zhiyuan, L.; Xiaojun, Z.; Jinwu, W. In Vitro and in Vivo Studies of a Gelatin/Carboxymethyl Chitosan/LAPONITE® Composite Scaffold for Bone Tissue Engineering. *RSC Adv.* **2017**, *7* (85), 54100−54110.

(38) Fenero, M.; Palenzuela, J.; Azpitarte, I.; Knez, M.; Rodríguez, J.; Tena-Zaera, R. Laponite-Based Surfaces with Holistic Self-Cleaning Functionality by Combining Antistatics and Omniphobicity. *ACS Appl. Mater. Interfaces* **2017**, *9* (44), 39078−39085.

(39) Wang, W.; Zhang, Q.; Guo, F.; Gu, J.; Yin, C. Preparation of Diblock Copolymer PBA-b-PSt by DPE Method in Emulsion. *J. Polym. Res.* **2011**, *18* (5), 1229−1235.

(40) Kim, S. H.; Son, W. K.; Kim, Y. J.; Kang, E. G.; Kim, D. W.; Park, C. W.; Kim, W. G.; Kim, H. J. Synthesis of Polystyrene/Poly(Butyl Acrylate) Core-Shell Latex and Its Surface Morphology. *J. Appl. Polym. Sci.* **2003**, *88* (3), 595−601.

(41) Reddy, B. V.; Rao, G. R. Vibrational Spectra and Modified Valence Force Field for N,N'-Methylenebisacrylamide. *Indian J. Pure Appl. Phys.* **2008**, *46* (9), 611−616.

(42) Naghash, H. J.; Karimzadeh, A.; Momeni, A. R.; Massah, A. R.; Alian, H. Preparation and Properties of Triethoxyvinylsilane-Modified Styrene - Butyl Acrylate Emulsion Copolymers. *Turkish J. Chem.* **2007**, *31* (3), 257−269.

(43) Wang, W.; Zhang, Q. Synthesis of Block Copolymer Poly (n-Butyl Acrylate)-b-Polystyrene by DPE Seeded Emulsion Polymerization with Monodisperse Latex Particles and Morphology of Self-Assembly Film Surface. *J. Colloid Interface Sci.* **2012**, *374* (1), 54−60.

(44) Gil, A.; Assis, F. C. C.; Albeniz, S.; Korili, S. A. Removal of Dyes from Wastewaters by Adsorption on Pillared Clays. *Chem. Eng. J.* **2011**, *168* (3), 1032−1040.

(45) Peng, Z. A.; Peng, X. Nearly Monodisperse and Shape-Controlled CdSe Nanocrystals via Alternative Routes: Nucleation and Growth. *J. Am. Chem. Soc.* **2002**, *124* (13), 3343−3353.

(46) Cenens, J.; Schoonheydt, R. A. Visible Spectroscopy of Methylene Blue on Hectorite, Laponite B, and Barasym in Aqueous Suspension. *Clays Clay Miner.* **1988**, *36* (3), 214−224.

(47) Guo, W.; Ngo, H. H.; Li, J. A Mini-Review on Membrane Fouling. *Bioresour. Technol.* **2012**, *122*, 27−34.

(48) Zhang, H.; Mane, A. U.; Yang, X.; Xia, Z.; Barry, E. F.; Luo, J.; Wan, Y.; Elam, J. W.; Darling, S. B. Visible-Light-Activated Photocatalytic Films toward Self-Cleaning Membranes. *Adv. Funct. Mater.* **2020**, *30* (34), 2070230.

(49) Kawasaki, A.; Furukawa, J.; Tsuruta, T.; Wasai, G.; Makimoto, T. Infrared Spectra of Poly (Buty1 Acrylates). *Die Makromol. Chemie Macromol. Chem. Phys.* **1961**, *49* (1), 76−111.

(50) Hill, E. H.; Claes, N.; Bals, S.; Liz-Marzán, L. M. Layered Silicate Clays as Templates for Anisotropic Gold Nanoparticle Growth. *Chem. Mater.* **2016**, *28* (14), 5131−5139.

(51) Aihara, N.; Torigoe, K.; Esumi, K. Preparation and Characterization of Gold and Silver Nanoparticles in Layered Laponite Suspensions. *Langmuir* **1998**, *14* (17), 4945−4949.

(52) Hill, E. H.; Hanske, C.; Johnson, A.; Yate, L.; Jelitto, H.; Schneider, G. A.; Liz-Marzán, L. M. Metal Nanoparticle Growth within Clay-Polymer Nacre-Inspired Materials for Improved Catalysis and Plasmonic Detection in Complex Biofluids. *Langmuir* **2017**, *33* (35), 8774−8783.

(53) Andrews, D. Q.; Hayes, J.; Stoiber, T.; Brewer, B.; Campbell, C.; Naidenko, O. V. Identification of Point Source Dischargers of Per- and Polyfluoroalkyl Substances in the United States. *AWWA Water Science* **2021**, *3* (5), No. e1252.

(54) Amornpitoksuk, P.; Intarasuwan, K.; Suwanboon, S.; Baltrusaitis, J. Effect of Phosphate Salts (Na_3PO_4, Na_2HPO_4, and NaH_2PO_4) on Ag_3PO_4 Morphology for Photocatalytic Dye Degradation under Visible Light and Toxicity of the Degraded Dye Products. *Ind. Eng. Chem. Res.* **2013**, *52* (49), 17369−17375.

(55) Rasheed, T.; Bilal, M.; Iqbal, H. M. N.; Hu, H.; Zhang, X. Reaction Mechanism and Degradation Pathway of Rhodamine 6G by Photocatalytic Treatment. *Water. Air. Soil Pollut.* **2017**, *228* (8), 1−10.

(56) Drapanauskaite, D.; Buneviciene, K.; Silva, M.; Slepetiene, A.; Baltrusaitis, J. Phosphate Removal from Simulated Wastewater Using Industrial Calcium-Containing Solid Waste. *J. Environ. Chem. Eng.* **2021**, *9*, 106575.

(57) Mostajeran, M.; Bondy, J.-M.; Reynier, N.; Cameron, R. Mining Value from Waste: Scandium and Rare Earth Elements Selective Recovery from Coal Fly Ash Leach Solutions. *Miner. Eng.* **2021**, *173*, 107091.

(58) Zeng, X.; Mathews, J. A.; Li, J. Urban Mining of E-Waste Is Becoming More Cost-Effective Than Virgin Mining. *Environ. Sci. Technol.* **2018**, *52* (8), 4835−4841.

(59) Zhang, H.; He, Q.; Luo, J.; Wan, Y.; Darling, S. B. Sharpening Nanofiltration: Strategies for Enhanced Membrane Selectivity. *ACS Appl. Mater. Interfaces* **2020**, *12* (36), 39948−39966.

https://doi.org/10.1021/acsami.1c20503
ACS Appl. Mater. Interfaces 2022, 14, 22790−22798

Chapter 5

Layered Double Hydroxide-Bismuth Molybdate Hybrids toward Water Remediation via Selective Adsorption of Anionic Species

This chapter has been published as: Jatav, S.; Herber, M.; Xiang H.; Hill, E. H. Layered Double Hydroxide-Bismuth Molybdate Hybrids toward Water Remediation via Selective Adsorption of Anionic Species. *ACS Applied Materials & Interfaces*. **2022**, 14 (46), 51921-51930.

One of the shortcomings of the laponite-Bi_2MoO_6 photocatalytic hybrids explored in chapters 3 and 4, was their inability to sequester anionic species as effectively as their cationic counterparts. Hence, the aim of this subsequent study was to extend the applicability of clay-Bi_2MoO_6 hybrid towards the sorption of anionic molecules. Herein, the Bi_2MoO_6 growth was templated using the organically modified cationic clay-like particles called Co-Al layered double hydroxides (LDH). This substitution to a cationic template for an anionic clay, laponite, resulted in the formation of LDH-Bi_2MoO_6 hybrids, which selectively adsorbed anionic species from aqueous medium.

ACS APPLIED MATERIALS & INTERFACES

www.acsami.org Research Article

Layered Double Hydroxide−Bismuth Molybdate Hybrids toward Water Remediation via Selective Adsorption of Anionic Species

Sanjay Jatav,* Marcel Herber, Hongxiao Xiang, and Eric H. Hill*

Cite This: ACS Appl. Mater. Interfaces 2022, 14, 51921−51930 Read Online

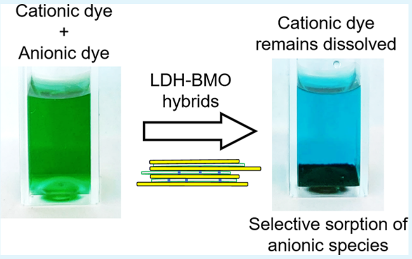

ABSTRACT: The steady release of anthropogenic toxins into the biosphere is compromising water security globally. Herein, CoAl layered double hydroxide, a clay-like layered material with a cationic surface charge, was organically modified and used to template the growth of Bi_2MoO_6. The resulting nanohybrid selectively removed the anionic dye methyl orange from aqueous solution and showed an enhancement of greater than 300% in the maximum adsorptivity (1.95 mmol/g) compared to modified CoAl layered double hydroxide (0.42 mmol/g). Interestingly, the observed improvement in adsorption occurs without any significant increase in the surface area of the hybrids. Furthermore, these hybrids exhibit increased broadband visible light absorption, and their photoactivity is slightly improved compared to CoAl layered double hydroxide. This study demonstrates that composites of clay-like materials with Aurivillius oxides are promising sorbent materials for water decontamination and photocatalytic antifouling membranes and shows that the synthetic strategy that was first established with an anionic layered silicate nanoclay can be generalized to other ionic layered materials.

KEYWORDS: *Bi_2MoO_6, dye adsorption, clays, layered double hydroxides, environmental remediation*

INTRODUCTION

Rampant anthropogenic pollution, sluggish screening protocols for evaluating chemicals, and a high rate of production of novel chemicals have led to the breaching of the "planetary boundary" for chemical pollution.[1] The most recent estimate of the global chemical inventory showed that more than 350,000 chemicals have been registered for production and use.[2] Many chemicals and their breakdown products end-up in reservoirs, rivers, oceans, and even percolate through to the water table, thereby polluting them.[3,4] Many chemical contaminants are non-biodegradable, which can result in bioaccumulation, as has been reported with pesticides, synthetic organic dyes, and perfluoroalkyl substances, among others.[5−8] Some of these chemicals act as endocrine disruptors, which can adversely affect the development of a wide array of organisms even at trace concentrations.[9,10] For instance, in the case of estradiol, a natural estrogen, organisms are sensitive to variations in the concentration of the order of few parts per trillion.[11−13] It is a significant and increasing concern that such chemicals can cover great distances and accumulate even in the most remote pockets of the planet.[14]

Conventional water treatment processes have many limitations. For instance, biological methods require large areas, and oxidative processes are energy-intensive, expensive, and not able to degrade recalcitrant compounds.[15] Furthermore, physicochemical processes, in addition to being energy-intensive, can result in the formation of highly polluting sludge.[16] Most conventional water filtration/decontamination systems do not primarily focus on the removal of molecular species.[17] These shortcomings can be overcome by employing adsorption-based methods, which have several advantages over such conventional water decontamination processes. Since adsorption is a spontaneous process, apart from being energetically favorable, adsorption onto a solid surface also provides an avenue for the selective removal of chemical species and allows for the realization of multiple functionalities.[18,19] Moreover, most water treatment plants use chlorine to remove pathogens from the water, but chlorine can react with the natural organic matter present in the water and form toxic products.[20,21] Such scenarios can be circumvented by employing adsorption onto a solid surface for disinfecting and filtering water.[22] Considering the different anthropogenic processes that leave behind varying chemical species, adsorption provides an effective strategy to develop sorbents that can selectively sequester the target compound(s).

In previous studies, we established that the organically modified interlayer of layered silicate clays can be exploited for the templated growth of semiconductors for realizing enhanced catalysis and photocatalysis.[23−27] Layered double hydroxides (LDHs) are clay-like particles, composed of brucite-type layers of mixed metal hydroxides.[28] The isomorphic substitution of

Received: August 20, 2022
Accepted: November 1, 2022
Published: November 10, 2022

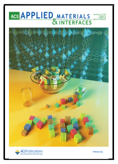

ACS Publications

https://doi.org/10.1021/acsami.2c14979

bivalent cations (M^{2+} sites) by trivalent cations impart a positive charge to the brucite layer.[29] The positive charge of the brucite layer is balanced by the presence of counterions such Cl^-, $(CO_3)^{2-}$, etc., which can be exchanged with other anionic species.[30] The major advantage of LDHs is the plethora of combinations of different elements that can be incorporated in the LDH structure. Hence, unsurprisingly, LDHs have been used in applications ranging from controlled drug release[31] to water decontamination.[32] For the present study, CoAl LDH was chosen since it has been used previously for removing anionic species for water decontamination.[32−34] Moreover, apart from being good sorbents, LDHs are also photocatalytic, which allows for the possibility of photocatalytically degrading the adsorbed dye.[35] Bismuth-based materials in general, and oxides in particular, have garnered immense interest recently due to their visible light photocatalytic properties.[36,37] Bismuth molybdate, Bi_2MoO_6 (BMO), the simplest Aurivillius oxide, is composed of alternating layers of $(Bi_2O_2)^{2+}$ and $(MoO_4)^{2-}$. This layered structure, apart from conferring high oxide ion mobility,[38] can also absorb light in the visible region of the spectrum.[39] This has motivated several studies exploring the photocatalytic behavior of BMO and its hybrids with different materials.[40−42]

Lately, composites of BMO with other LDHs such as NiAl,[43] ZnAl,[44] and ZnTi[45] have been explored in the vein of photocatalytic water remediation. However, the aforementioned studies overlook the fact that LDHs as clay-like materials are also good sorbents of molecular entities.[46] Hence, it is also possible to employ sorption in tandem with photocatalysis for the purpose of water remediation. In our previous work, the anionic layered silicate nanoclay Laponite was organically modified to template the growth of bismuth molybdate, resulting in the formation of highly sorbent Laponite−Bi_2MoO_6 hybrids, which could be reused by photocatalytically degrading the adsorbed dye.[26] Herein, organically modified cationic platelets of CoAl LDH were used to template the growth of Bi_2MoO_6. The resulting LDH−Bi_2MoO_6 hybrids were found to selectively adsorb anionic dye and showed an enhancement of greater than 3× in their dye adsorption capacity compared to organically modified LDH. A detailed investigation of the adsorption performance of the different LDH−Bi_2MoO_6 hybrids revealed that this emergence and enhancement of adsorption capacity only occurs when the synthesis is carried out with [Bi/Mo]:[LDH] of 0.315 to 1.58 mmol:g and near neutral pH. Furthermore, O vacancies can be introduced in Bi_2MoO_6 in the composites by varying the pH of the reaction. This allows for the broadband absorption of the light by these LDH−Bi_2MoO_6 composites, and retention of photoactivity was shown by photo-electrochemical measurements. This work signifies that this synthetic strategy can be generalized to other clay-like or layered materials to obtain high-performance functional composites.

EXPERIMENTAL SECTION

Materials. Sodium molybdate, $Na_2MoO_4\cdot 2H_2O$ (99%), bismuth nitrate, $Bi(NO_3)_3\cdot 5H_2O$ (99%), NaOH pellets (99%), methylene blue (MB) and methyl orange (MO), and butyl acrylate (99%) were obtained from Sigma-Aldrich and used without further purification. Aluminum nitrate nonahydrate ($Al(NO_3)_3\cdot 9H_2O$, ≥98%) was obtained from Honeywell, cobalt nitrate hexahydrate ($Co(NO_3)_2\cdot 6H_2O$, ≥98%), polyvinyl alcohol, (PVA, molecular weight: 88,000−97,000 g/mol, 87−89% hydrolyzed), and sodium dodecyl sulfate (SDS, 99%) were obtained from Alfa Aesar. Hexamethylenetetramine (HMT, ≥99%) was obtained from PanReac AppliChem. Sodium sulfate (Na_2SO_4,>99%) and nitric acid (HNO_3, >65%) were procured from Chemsolute. Millipore-filtered water with a resistivity of 18.2 MΩ·cm was used in all experiments.

Hydrothermal Synthesis of Co-Al LDH. $Al(NO_3)_3\cdot 9H_2O$ (0.70 g, 1.87 mmol), $Co(NO_3)_2\cdot 6H_2O$ (1.64 g, 5.63 mmol), and HMT (0.91165 g, 6.50 mmol) were added to 50 mL of N_2-degassed Milli-Q water. This was then stirred until complete dissolution of the powders (∼15 min). The mixture was transferred to a Teflon-lined autoclave (BR-100, Berghof Instruments, Germany) and degassed with N_2 for 10 min prior to sealing the reactor. The autoclave was inserted in a heating block and placed on a heating plate set to achieve a temperature of 140 °C inside the autoclave (monitored with a thermocouple inside the reactor). The reaction was carried out under stirring for 12 h, after which the reactor was allowed to cool to room temperature. The product was washed with water and collected by centrifugation (6000 rpm, 10 min) five times followed by drying at 60 °C for 24 h.

Hydrothermal Synthesis of CoAl-BMO Composites. A dispersion of CoAl LDH (11 mL, 5 mg/mL) was added to a 50 mL Teflon vessel containing 17 mL of deionized water. The dispersion of LDH was prepared by adding 55 mg of LDH to 11 mL of water followed by sonication for 10−15 min (until complete dispersion). Under magnetic stirring, SDS (0.560 mL, 0.1 M) was added to the LDH dispersion, allowing pillaring of CoAl-LDH. After 10 min of stirring, a previously prepared solution of Na_2MoO_4 (3 mg/mL) and $Bi(NO_3)_3$ (10 mg/mL) was added to the dispersion to reach final Bi concentrations of 0.5, 1, 2.5, or 5 mM, always keeping the Bi:Mo molar ratio constant at 1.64:1. This solution was prepared by adding the desired amount of Bi_2MoO_6 precursors to 7 mL of water and subsequently sonicating it for 10 min. After the addition of BMO precursors to the CoAl-SDS dispersion, the vessel was sonicated for 10 min. These samples have been labeled as CAB-0.1x, CAB-0.2x, CAB-0.5x, and CAB-1x, respectively. The Teflon vessel was then inserted into the hydrothermal autoclave (DAB-2, Berghof Instruments, Eningen, DE). The autoclave was placed in an oven over a heat-resistant magnetic stirring plate (MIXdrive 6, 2mag, Muenchen, DE) stirring at 720 rpm. The temperature was maintained at 180 °C for 18 h, after which the reactor was allowed to cool to room temperature. The dark gray or yellow precipitates were rinsed seven times with water and two times with ethanol and centrifuged at 7500 rpm for 10 min, and the cleaned product was then dried at 60 °C for 24 h. The synthesis of BMO with LDH is depicted in Scheme 1.

Scheme 1. Hydrothermal Synthesis of LDH−BMO Composites

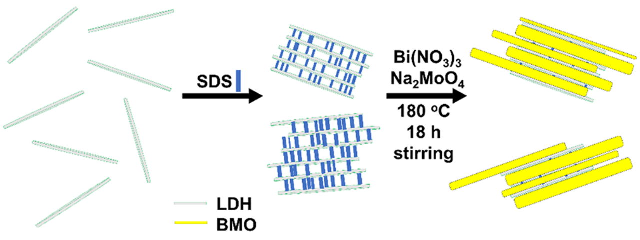

A BMO control was synthesized following the same procedure as that for CAB-1x without the addition of LDH, and it is labeled as BMO. SDS-pillared CoAl was synthesized following the same procedure without the addition of precursors and hydrothermal treatment, and it is labeled as CAS. For studying the influence of pH on the growth, CAB-0.2x samples were synthesized at pH values of 2.81, 6.3, and 11.9, adjusted using 5 M HNO_3 and 5 M NaOH. An identical pH study was done using CAB-1x. A series of CAB-0.2x samples were also synthesized at different SDS concentration of 0, 0.4, 0.8, 1.6, and 3.2 mM. They have been labeled as CAB-0S, CAB-0.25S, CAB-0.5S, CAB-1S (same as CAB-0.2x), and CAB-2S, respectively. The yields of CAB-0.1x, CAB-0.2x, CAB-0.5x, CAB-1x, and CoAl LDH were 59.2, 58.5, 41.7, 49.8, and 30.1%, respectively.

https://doi.org/10.1021/acsami.2c14979

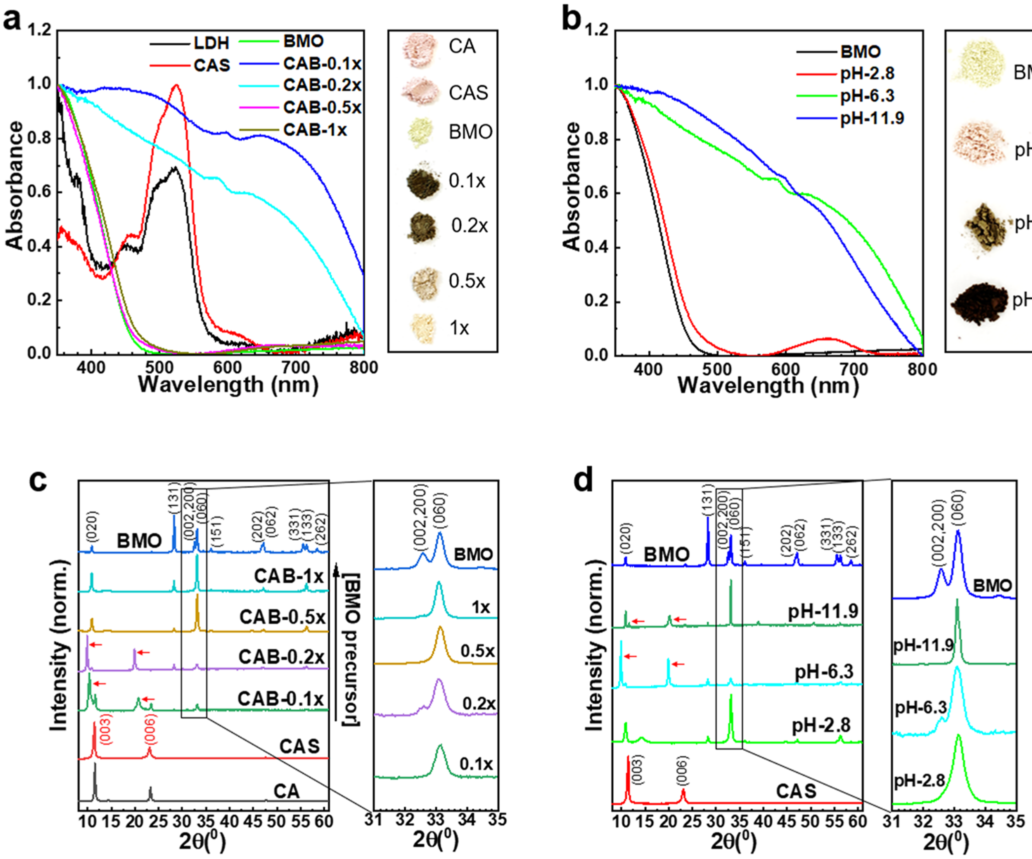

Figure 1. Normalized UV−vis DRS spectra of the (a) LDH−BMO composites prepared with varying amounts of BMO precursors (1x = 5 mM Bi) while keeping the [LDH] and [SDS] constant. (b) CAB-0.2x samples prepared at different pH values. X-ray diffractograms of the (c) precursor series and (d) pH series. Peaks belonging to the LDH in the composites have been indicated by horizontal red arrows.

Characterization. UV−vis absorbance spectra were obtained using a Cary 60 UV−Vis spectrometer (Agilent, Santa Clara, CA, USA). Diffuse reflectance UV−vis spectra were measured on a Cary 5000 spectrometer (Agilent, Santa Clara, CA, USA). Transmission electron microscopy was carried out on a JOEL JEM 1011 (Tokyo, Japan) to investigate the morphologies of the different samples. High-resolution transmission electron microscopy (Talos F200X, FEI, USA) was also used to investigate the morphologies of the different samples and to obtain high-angle annular dark field-scanning transmission electron microscopy (HAADF-STEM) images and electron-dispersive X-ray spectroscopy (EDX) mappings. The crystal structure of the as-prepared samples was determined using a PANalytical X'PERT Pro diffractometer (Phillips, Netherlands). Zeta potentials were measured using a Malvern Zeta-sizer Nano ZS (Malvern Instruments, UK). Fourier transformed infrared (FTIR) spectra were recorded on a Bruker Invenio R using golden gate ATR; 128 scans were averaged and recorded at a resolution of 4 cm^{-1}. N_2 adsorption−desorption isotherms were measured on an Autosorb iQ automated gas sorption analyzer (Quantacore instruments, Boynton Beach, FL, USA). Samples were degassed at 150 °C for 6 h prior to commencing N_2 adsorption, and 100−150 mg of powder was used for the analysis. The isotherms were obtained at 77 K, and the surface area was estimated using Brunauer−Emmett−Teller (BET) equation by choosing 11 points on the isotherms between 0.05 to 0.30 relative pressure values to ensure a good fit.

Dye Adsorption. MB and MO dyes were used to study the adsorption behavior of LDH-BMO particles. Sorbent dispersions were prepared by first sonicating 20 mg of the powder in 2 mL of deionized (DI) water for 15 min. For a given experiment, 0.2 mL of particle dispersion was added to an aqueous solution of MB (75 μM) and a solution of MO (1 mM) to achieve a final sorbent concentration of 1 mg/mL. These dispersions were left undisturbed in the dark for 36 h, following which their UV−vis spectra were recorded. Concentrations of MB (λ = 664 nm, ε = 95,000) and MO (λ = 466 nm, ε = 25,100) were calculated using the Beer−Lambert law. MB and MO supernatants were diluted 4× and 20×, respectively, before recording the UV−vis spectra. To study the kinetics of dye adsorption, UV−vis spectra were recorded at specific time points after the addition of the particles (1 mg/mL) with MO (250 μM). At specific time points, 2 mL aliquots were withdrawn from the dye suspension and centrifuged at 5500 rpm for 2 min to remove any suspended particles, after which the spectrum was recorded. The supernatants were diluted 10 times before recording the spectra. The isotherm experiments were conducted between the [MO] range (0.1 mM to 4 mM) using a fixed amount of adsorbent (2 mg, 1 mg/mL) with an equilibrium time of 36 h.

Photoelectrochemical Characterization. Samples were prepared by dispersing 3 mg of powder in 1.5 mL of PVA (10 mg/mL) by ultrasonication for 10 min. A total of 0.75 mL of this dispersion was dropped onto a clean fluorine-doped tin oxide (FTO) substrate. These substrates were then left for drying overnight under ambient conditions. Ag paint was applied on the edges of these substrates to ensure proper contact with the cell. A Zahner Zennium XC electrochemical workstation (ZAHNER-Elecktrik GmbH & Co. KG, Germany) was used for characterizing the photoelectrochemical response of the samples. A three-electrode cell was used with Ag/AgCl, Pt wire, and 0.2 M Na_2SO_4 as the reference electrode, counter electrode, and electrolyte, respectively. Samples were illuminated with a solar simulator (SS-F5-3A, Enli Tech Company, Taiwan) with a power of 110 mW/cm^2 at 400 nm and no applied voltage bias. Electrochemical impedance spectroscopy (EIS) was carried out at sinusoidal AC perturbation of 10 mV over the frequency range of 0.1 to 10^6 Hz.

RESULTS AND DISCUSSION

Figure 1a shows the UV−vis spectra of the different LDH−BMO hybrids along with the control samples. The absorption edges of CAB-0.5x and CAB-1x match closely to that of the BMO control, which lies at ∼490 nm. In contrast, CAB-0.1x and CAB-0.2x, prepared at low [Bi/Mo], absorb light across the entire visible spectrum, which in the case of CAB-0.1x, extends into the near-infrared region. The LDH alone, both pillared and pristine, absorbs strongly between 450 and 550 nm. The color of the hybrids' changes from gray to yellow with the increase in [Bi/Mo] (right panel of Figure 1a). This dependence of color on the [Bi/Mo] was hypothesized to be due to the change in the reaction pH, caused by the hydrolysis of the Bi precursor, $Bi(NO_3)_3$. Hence, to test this hypothesis, samples CAB-0.2x and CAB-1x were synthesized at different pH values.

The UV−vis spectra of CAB-0.2x prepared at different pH values show that a reaction pH > 6 results in the formation of composites with broadband light absorption (Figure 1b). For CAB-1x, broadband absorption manifested only at a reaction pH of 6.3 (Figure S1a). This change in color from light yellow to gray has been previously observed and was attributed to the presence of O vacancies in BMO.[47−49] This change in color suggests a relationship between reaction pH and the formation of O vacancies in BMO in the hybrids. Interestingly, this color change with variation of pH was not observed in our earlier study of the composites of BMO with Laponite.[26] Thus, apart from the reaction pH, the template particle also seems to play a role in defect formation in BMO. This suggests a role of ion leaching from the template particle to BMO, which has been previously observed in the growth of $ZnIn_2S_4$ in Laponite.[25]

Figure 1c shows the X-ray diffractograms of the samples synthesized with SDS-modified LDH using different amounts of BMO precursors and the BMO control. Diffraction peaks from the LDH lie at 11.56 and 23.27° and are due to the reflections from the (003) and (006) crystallographic planes, respectively (Figure S2). These same peaks are also seen in CAS and can also be seen in CAB-0.1x and CAB-0.2x synthesized at low [Bi/Mo], whereas samples prepared at higher precursor amounts show no peaks from the LDH. Interestingly, CAS shows a broadening of both (003) and (006) peaks, most likely resulting from the intercalation of SDS molecules (Figure S2). In contrast to a previous study,[50] no visible shift in these peaks to lower angles was observed. This discrepancy can be attributed to the three times higher SDS:LDH weight ratio used in ref 49 compared to the present study.

The peaks at 10.89, 28.28, 32.64, 33.13, 36.04, 46.83, 47.12, 55.60, 56.23, and 58.5° correspond to the reflections from the (020), (131), (200), (060), (151), (202), (062), (331), (133), and (262) planes of BMO, respectively.[39] These peaks correspond to γ-Bi_2MoO_6 (γ-BMO). Interestingly, when BMO was synthesized with only cetyltrimethylammonium bromide (CTAB), the intensity ratio of (060) to (200/002) peaks was 0.55,[26] whereas in the present case of BMO synthesized with SDS, the intensity ratio of the same peaks is 2.24. This difference in growth direction could plausibly be due to the different charges of CTAB (cationic) and SDS (anionic), which may facilitate the adsorption of these surfactants onto different facets of BMO. Strangely, such a difference in the crystal structure of BMO due to SDS and CTAB has not been reported.[51,52] Among the composites, both the (003) and (006) peaks of LDH shift to lower angles in CAB-0.1x and CAB-0.2x, indicating expansion of interlayer spacing. In CAB-0.5x and CAB-1x, peaks of LDH are not observed, which could be due to the high amounts of BMO masking the signal of LDH. Also, the SDS-modified LDH seems to completely inhibit the growth of the (002, 200) crystallographic planes of BMO in all the LDH−BMO hybrid samples with the exception of CAB-0.2x (Figure 1c), where the intensity of this peak is reduced compared to the BMO control.

Since differences in optical properties were observed with reaction pH in the hybrids, its effect on the underlying crystal structure was also investigated. When CAB-0.2x was synthesized at pH 2.8, the (060) peak of BMO becomes the most prominent reflection (Figure 1d). LDH diffraction peaks decreasing at pH 2.8 compared to the other pH values suggest that acidic conditions may degrade the LDH. At pH 6.3 (CAB-0.2x) and pH 11.9, peaks from both the LDH and BMO can be identified. In the latter sample, the (006) peak of the LDH shifts from 23.07 to 20.13°, implying an expansion of $d_{(006)}$ by 0.27 Å compared to CAS. In the case of CAB-1x synthesized at different reaction pH values, the peaks from the LDH appear only at the pH of 6.3, and the (060) peak of BMO is the most prominent reflection (Figure S1b). Comparing the pH series of CAB-0.2x and CAB-1x, it can be seen that the reflections from BMO are always more prominent in the latter regardless of the pH, likely due to the increased amount of BMO present.

The anionic surfactant SDS was used in this study to pillar the LDH. A series of samples were also synthesized to explore the effect of [SDS] by keeping the concentrations of LDH and BMO precursors the same as that used for CAB-0.2x. Upon increasing the [SDS] during the reaction, both the (003) and (006) reflections of the LDH shift toward lower angles (Figure S3). This is starkly seen between 0.25S and 0.5S, where [SDS] was doubled and the (003) and (006) planes of LDH shift from 11.58 to 10.03° and 23.36 to 20.06°, respectively. Hence, it can be inferred that increasing [SDS] increases the interlayer spacing, which allows more Bi/Mo precursor to access the interlayer space of the LDH.

To investigate the presence and fate of LDH after the hydrothermal growth of BMO, FT-IR spectroscopy was performed (Figure S4). The characteristic −OH peak of the LDH between 3000 and 3700 cm^{-1} is present in all samples except the BMO control. For the pristine LDH, peaks below 800 cm^{-1} can be ascribed to the M-O vibrations and M-O-H bending.[34] The presence of the peak at 1358 cm^{-1} suggests the presence of NO_3^- in the interlayer spacing of LDH.[50] This is reasonable given that $Al(NO_3)_3$ was used as the precursor in the synthesis of LDH. The peak at 1591 cm^{-1} could be due to the H_2O bending vibration. In the SDS-modified LDH, the peaks at 2924 cm^{-1} could be attributed to SDS and are also seen in CAB-0.2x. For the hybrids, peaks due to BMO can be seen at 835 and 791 cm^{-1}, with the exception of CAB-0.2x, where only the former peak is visible. These peaks can be assigned to the symmetric and asymmetric stretch of MoO_6 octahedra relating to the motion of apical O.[53,54] The higher intensity of the 835 cm^{-1} peak in CAB-0.5x and CAB-1x indicates higher amounts of BMO in these hybrids compared to CAB-0.2x. The peak at 1084 cm^{-1} seen in all the composite samples can be attributed to the presence of $Al(OH)_3$.[55] The absence of this peak in the LDH control points toward some degradation of LDH during the hydrothermal growth of BMO with the LDH.

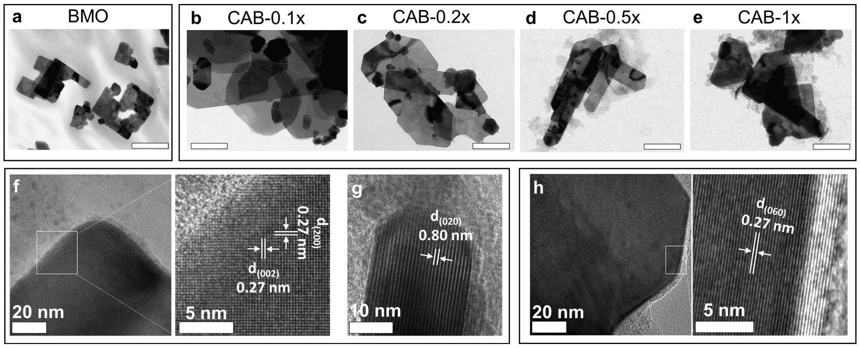

Figure 2. TEM images of LDH−BMO hybrids prepared at different BMO precursor concentrations with [LDH] and [SDS] fixed. (a) BMO control prepared with SDS and no LDH. CAB samples prepared at (b) 0.5 mM, (c) 1 mM, (d) 2.5 mM, and (e) 5 mM BMO precursor concentrations (Bi basis) using SDS-pillared LDH. (f) HR-TEM image of CAB-1x particles (images on the right show zoomed-in lattice planes). (g) HR-TEM image of CAB-1x with the (020) stacking plane of BMO indicated. (h) HR-TEM image of CAB-0.2x. Scale bars in (a)−(e) are 200 nm.

The TEM images of the CAB particles and BMO control are shown in Figure 2. In the case of BMO control synthesized with SDS, particles form in a regular squarish manner, similar to the regular square sheets of BMO that were obtained with CTAB.[26] Moreover, the BMO control shows additional protrusions jutting out partially from the edges (Figure 2a and Figure S6). The LDH control crystallizes into irregular circular disks ranging from ∼100 nm to more than 500 nm in size (Figure S5). In the case of samples CAB-0.1x and CAB-0.2x, darker BMO particles can be seen resting atop larger (and lighter) platelets of LDH. In contrast to the control BMO sample, the structure of CAB-0.5x particles seems to be more elongated.

HAADF-STEM mappings were performed to identify the regions belonging to BMO and LDH in CAB-0.2x. When synthesized at pH 6.3, BMO particles grow atop the LDH, which is shown by the separated localization of elements belonging to BMO and LDH (Figure 3). The high-magnification HAADF-STEM image clearly shows that the BMO crystal rests atop the larger LDH platelets (Figure 3). When synthesized at pH 2.8, a mixture of anisotropic particles composed of elements belonging to both LDH and BMO, and BMO particles atop LDH showing no co-localization of the elements, were observed (Figure S8a,b). At the pH of 11.9, the weak Mo signal in EDX contrasts with the results of Figure 1d, where peaks belonging to BMO could be clearly observed (Figure S8c).

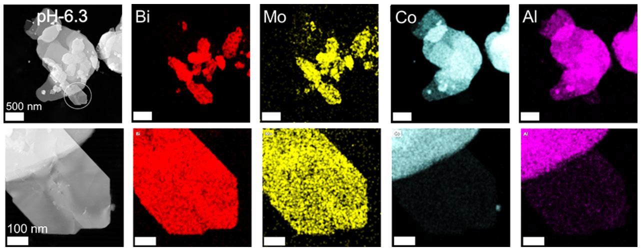

Figure 3. HAADF-STEM mappings of CAB-0.2x (pH 6.3). A zoomed-in elemental mapping of the circled region is shown in the bottom panel. Elements Bi, Mo, Co, and Al are shown from left to right. The corresponding EDX spectra are shown in Figure S7.

Dye Adsorption. In the case of MO adsorption, clear water is observed after the sedimentation of CAB-0.2x particles (Figure 4a). However, with the cationic dye MB, dye can still be seen in the solution. The controls CAS and BMO remove ∼47 and 0%, respectively, from the MO solution ([MO] = 1 mM). Among the hybrids, CAB-0.1x, CAB-0.2x, and CAB-0.5x remove 80, ∼100, and ∼92% of the MO, respectively, whereas CAB-1x does not adsorb MO (Figure 4b,c). Hence, the adsorption performance of these hybrids improves with increasing concentration of BMO precursor at first, which then peaks for CAB-0.2x and declines with a further increase in [Bi/Mo] thereafter (Figure 4b). This indicates that the onset of sorbent activity is sensitive to the [Bi/Mo]:[LDH] and that maximum sorbent action is seen when the aforementioned ratio is 0.63 mM:mg/mL. Interestingly, a similar ratio was found to be the critical value for the best sorbent action in Laponite−Bi_2MoO_6 hybrids.[26]

In the case of MB, samples CAS, BMO, CAB-0.1x, CAB-0.2x, CAB-0.5x, and CAB-1x adsorbed 8, 26, ∼6, 6, 9.5, and ∼10% of MB, respectively (Figure 4c). Hence, it can be inferred that the LDH−BMO composites are ineffective toward the removal of cationic species from aqueous solution. CAB-0.5x has specific adsorption values of 0.92 mmol/g and 7.5 μmol/g for the dyes MO and MB, respectively. Similarly, CAB-0.2x shows specific adsorption values of 1 mmol/g and 3.27 μmol/g for MO and MB, respectively. Interestingly, as the concentration of the precursor is doubled from 0.5 mmol (CAB-0.1x) to 1 mmol (CAB-0.2x), the adsorption of MO increases, whereas that of MB decreases. Since CAB-0.1x, CAB-0.5x, and CAB-0.2x uptake negligible amounts of MB, they essentially function as a selective sorbent of anionic species and might be useful toward ionic separation of chemical entities.

The adsorption of MO on CAB-0.2x was further investigated by examining the kinetics of the adsorption (Figure 4d and Figure S10a). For CAB-0.2x, close to 22% of MO is adsorbed in the first few minutes, and by 35 min, MO has been completely sequestered from the solution. In the case of sample CAS, only 28% of MO is removed by the end of the experiment. Dye adsorption kinetics were estimated by calculating psuedo-first-order rate constants. From Figure 4d, it can be seen that CAB-0.2x shows more than a 20× increase in the dye adsorption rate constant. Hence, CAB-0.2x not only adsorbs more dye, but it also adsorbs it quicker than the CAS control. However, CAB-0.2x exhibits sluggish adsorption kinetics compared to the Laponite−BMO hybrids, which were able to instantaneously adsorb MB,[26] likely due to the

https://doi.org/10.1021/acsami.2c14979
ACS Appl. Mater. Interfaces 2022, 14, 51921−51930

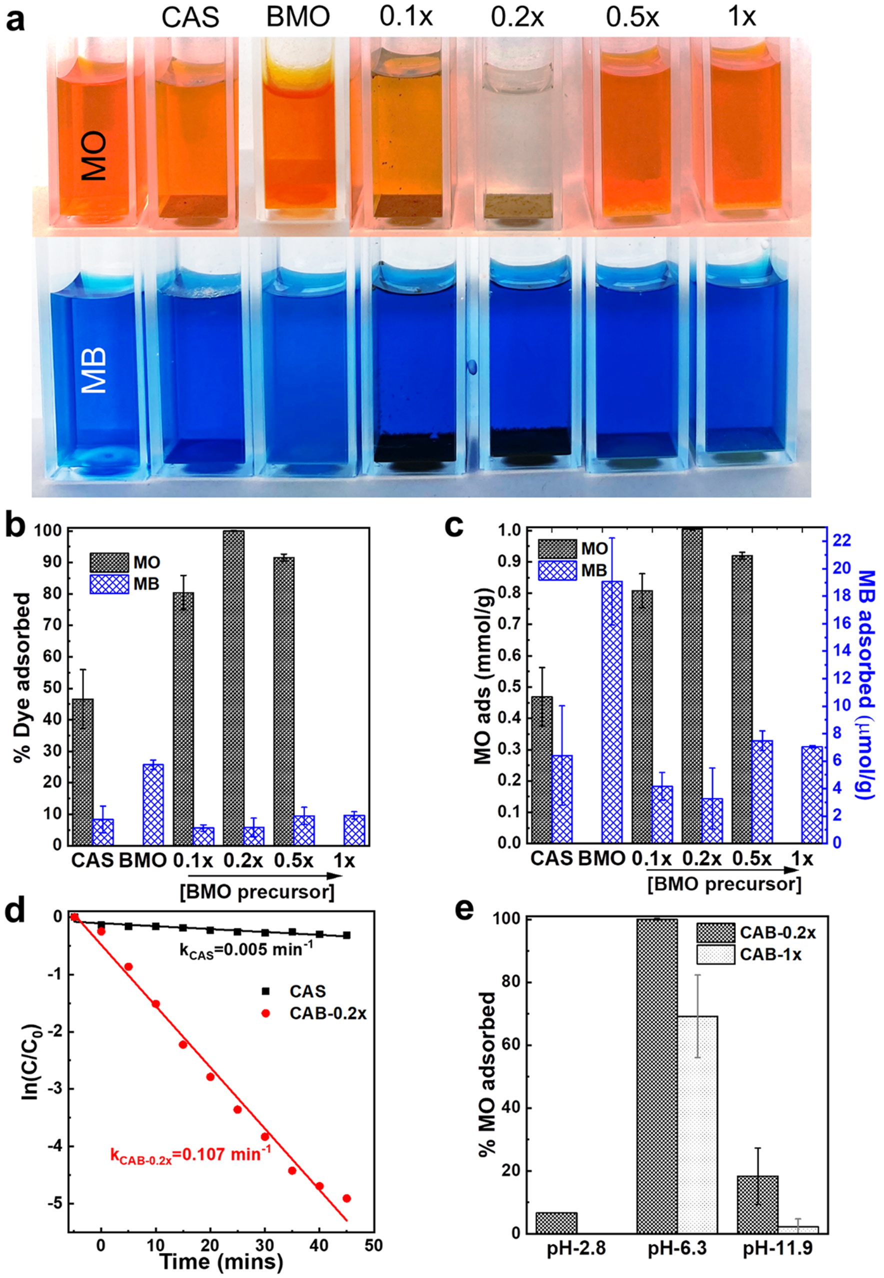

Figure 4. (a) Photographs of cuvettes showing adsorption of methyl orange (top) and methylene blue (bottom). (b) Adsorption of MO (1 mM) and MB (75 μM) by the LDH−BMO hybrids prepared by varying [Bi/Mo]. (c) Specific adsorptivity of the different composites shown in (a). (d) Kinetics of methyl orange adsorption, [MO] = 250 μM. (e) Effect of reaction pH on the adsorption of dyes; [MO] = 1 mM, [MB] = 75 μM. The [particle] = 1 mg/mL in all the above experiments.

absence of porosity in the LDH−BMO composites (Figure 5c).

As SDS was used to pillar the LDH, the effect of [SDS] on the MO adsorption performance was also examined. The adsorption performance of these CAB hybrids was found to be sensitive to [SDS] (Figure S11a). Even though CAB-0S (synthesized without SDS) adsorbs less MO than the CAS control, the introduction of SDS into the reaction improves the sorbent action of the CAB hybrids. Between CAB-0S and CAB-0.25S, the MO removal increases from ∼10% in the former to 25.7% in the latter. As the [SDS] is doubled further (sample CAB-0.5S), 91.1% of MO is removed from the solution. The sorption performance of the CAB hybrids then peaks at the [SDS] = 1.6 mM (sample CAB-1S/ CAB-0.2x), where ∼100% of the dye is sequestered from the solution. With a further increase in the SDS concentration to 3.2 mM (sample CAB-2S), the removal of MO decreases slightly to 92.8%, thereafter. Hence, the pillaring of LDH with SDS is critical to the formation of highly sorbent LDH−BMO composite particles, where excessive SDS above the anion exchange capacity of the LDH can reduce sorption, likely due to the nontemplated BMO growth. From the above results, it is clear that BMO growth with pillared LDH is crucial for enhancing adsorption. This may result from the maximized interface between BMO and LDH when synthesized in this manner. Consequently, the contact between BMO and LDH could result in the redistribution of charges at the interface, which might aid the sorption process.

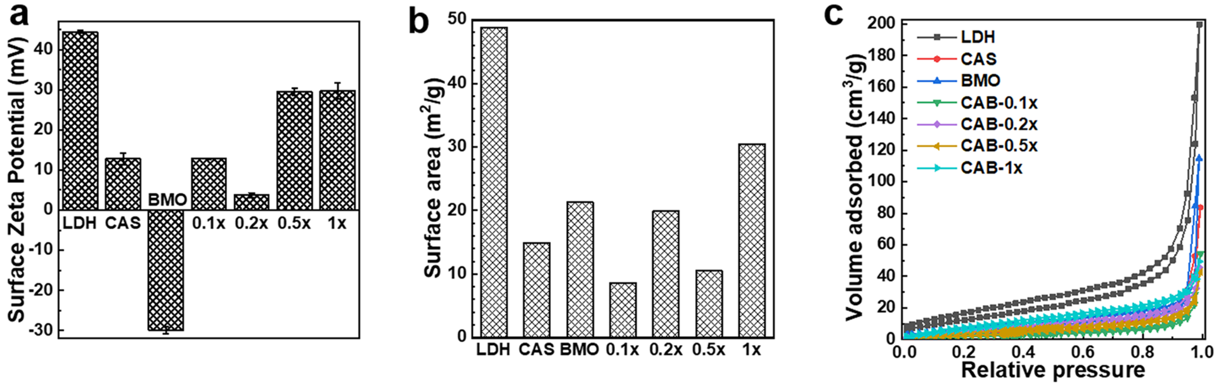

Figure 5. (a) Zeta potential of the LDH−BMO hybrids; (b) BET surface area; and (c) N_2 adsorption−desorption isotherms measured at 77 K.

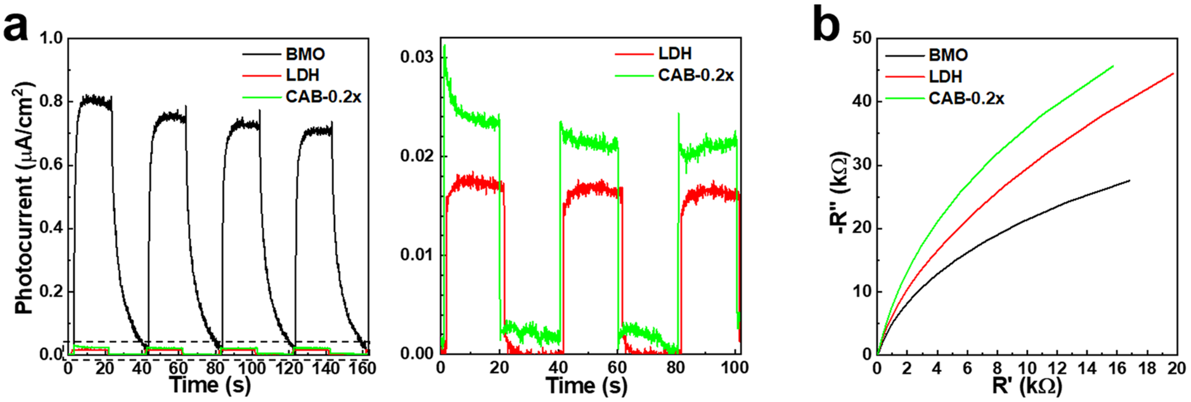

Figure 6. (a) Transient photocurrent response of CAB-0.2x along with the controls (the highlighted region is shown on the right). (b) EIS Nyquist plots of the same samples.

Samples synthesized at different pH values were also investigated for MO adsorption capacity. Sample CAB-0.2x sequestered 7, ∼100, and 18% of MO when synthesized at reaction pH values of 2.8, 6.3, and 11.9, respectively (Figure 4e). CAB-1x removes 69% of MO when synthesized at a reaction pH of 6.3, whereas at pH 2.8 and 11.9, it adsorbs ∼0 and 2% of MO from the solution, respectively. Thus, it can be inferred that the adsorption performance of these CAB hybrids not only depends on the amount of the precursors used but is also sensitive to the reaction pH, where pH values close to neutral conditions favor optimal sorbent performance.

Since particle surface properties are pertinent to the action of a sorbent, these hybrids were further characterized for their surface zeta potential and surface area. In Figure 5a, it can be seen that LDH, CAS, and all the CAB hybrids show a positive zeta potential with the exception of BMO, which has a highly negative zeta potential (−30 mV). As the LDH is pillared with the anionic surfactant SDS, the zeta potential drops from 44.4 to 12.8 mV, indicating the impregnation of LDH with the surfactant molecules. Among the CAB hybrids, the zeta potential decreases from 12.8 mV in CAB-0.1x to 3.7 mV in CAB-0.2x and CAB-0.5x and CAB-1x have zeta potentials of 29.5 and 29.7 mV, respectively. Hence, the surface charge in these hybrids is dominated by the charge of the LDH. Hence, by comparing the results of MO adsorption (Figure 4b,c) and zeta potential, it can be inferred that the adsorption of MO is not solely driven by the surface charge of these hybrids.

The surface areas of LDH, CAS, BMO, CAB-0.1x, CAB-0.2x, CAB-0.5x, and CAB-1x were found to be 48.8, 15, 7, 21.3, 19.9, 9, and 30.5 m^2/g, respectively (Figure 5b). Hence, BMO growth with LDH results in a decrease in the surface area of the composites as compared to pristine LDH. The lack of prominent hysteresis in the adsorption−desorption isotherms suggests a nonporous nature for both controls and composites (Figure 5c). From the present and previous study,[26] it can also be inferred that at low [Bi/Mo]:[Clay/LDH], the BMO growth does not alter the inherent porosity profile of the template particles. It is interesting to note that the sample with the greatest adsorptivity (CAB-0.2x) possesses a surface area that is only ∼33% greater than that of CAS. Since an increased surface area cannot be solely responsible for the improved adsorption capacity (of over 300%), this suggests that the growth of BMO at the LDH interface enhances adsorption.

The comparison of the sorption capacity of the different LDH-based sorbents is shown in Table S2. The adsorptivity of CAB-0.2x (1.95 mmol/g, calculated by the Langmuir−Freundlich model (Figure S10b)) lies on the order as those of the best performing LDH-based materials (∼6 mmol/g).[32] Interestingly, the growth of BMO with SDS-modified LDH enhances the adsorptivity of the composite by 338% compared to CAS. To compare the sorptive activity of the surface of the different sorbents, the adsorption capacity was normalized to the surface area. Based on this metric, CAB-0.2x shows a specific adsorption of 0.098 mmol/m^2 and is surpassed by only two other LDH-based sorbents.

In the previous study, the nanoclay-BMO sorbents were reused by photocatalytically degrading the adsorbed dye.[26] For this system, it was not feasible to evaluate the photocatalytic performance of CAB-0.2x by dye degradation experiments because the characteristic absorption band of MO is lost behind the broadband absorption of the sample (Figure S12). Therefore, the photoactivity of the samples was examined by chopped light voltammetry. The BMO control shows an order of magnitude higher photocurrent density (0.81 μA/cm^2) than the LDH control (0.017 μA/cm^2) and CAB-0.2x (0.023 μA/cm^2) (Figure 6a). CAB-0.2x shows a slightly higher photocurrent than the pristine LDH. Since the photocurrent of the composite is of the same order as the LDH, it seems that the photocurrent in CAB-0.2x is dominated by the LDH. The interfacial charge-carrier transfer of these samples was characterized by EIS. BMO shows the smallest arc radius followed by CA, and CAB-0.2x exhibits the highest radius, thus indicating that CAB-0.2x shows the highest interfacial charge transfer resistance followed by CA and BMO controls. Hence, from these measurements, it can be surmised that the growth of BMO on LDH slightly improves the photocurrent and also increases the interfacial charge transfer resistance. This indirectly proves that the LDH−BMO hybrids can potentially be used for photocatalytic degradation of the adsorbed dye.

CONCLUSIONS

The CoAl LDH−BMO hybrids synthesized in this work exhibited improvement in their adsorption capacity over that of pillared LDH, which are known sorbents of molecular species. The best performing sample, CAB-0.2x, showed an improvement of ~337% in maximum adsorptivity compared to the SDS-modified LDH. The selective sorption of anionic dye demonstrates the potential of this system for ionic separation of molecular species dissolved in aqueous media. The adsorption performance of these composites was found to be sensitive to the reaction pH, presence of pillaring agent, and [Bi/Mo]:[LDH]. Furthermore, the reaction pH influenced the optical properties of the hybrids significantly, where broadband light absorption could be achieved in the samples synthesized at pH ~ 6.

Our previous[26] and present studies taken together point toward a general propensity of Aurivillius oxides grown onto pillared clays (or clay-like materials) to enhance adsorption capacity of the pillared substrate. This enhancement in adsorptivity peaks at the [clay]:[Bi/Mo] of 0.63 mmol:g. Since at low [Bi/Mo]:[clay/LDH], the BMO crystal growth initiates from the basal sites of LDH (or clay) where surfactants are adsorbed, this proximal growth of BMO is suspected to be pivotal in enhancing the adsorption capacity of these composites compared to pillared LDH or clay. Also, due to the small amount of BMO grown, the porosity profile of the template remains conserved. Interestingly, the reaction pH and [Bi/Mo] did not change the direction of BMO growth in the composites compared to the growth of BMO in Laponite.[26] This implies that only the amount of BMO grown, rather than the specific orientation of the crystal, is crucial for the enhancement observed in these composites. Since the surface area of CAB-0.2x is slightly greater than that of the pillared-LDH, it is to be noted that the improvement in sorption is most likely due to the change in the nature of the surface of the composite compared to the LDH.

Further improvements in the present system can be achieved by studying the dependence of dye adsorption on the morphology of the template particles (LDHs in this case). As has been shown previously, the adsorptivity of the LDHs is closely related to their morphology.[33,34] Hence it seems likely that by growing BMO on LDH possessing high adsorptivity, the sorption performance of LDH−BMO hybrids can be boosted even further. Moreover, the photogenerated current in CAB-0.2x indicates that these particles can potentially be reused by photocatalytically degrading the adsorbed dye. Previous work has also established that the sorption performance can be further enhanced by encapsulation with a thin polymer shell.[56] The choice of LDH, apart from improving the adsorption performance, can also influence the optical properties of the composite and heterojunction formation, which could further enhance photocatalytic performance. Furthermore, ion leaching from the LDH may be responsible for defect formation in BMO, particularly O vacancies, as such leaching-induced defect formation has been previously observed in the growth of $ZnIn_2S_4$ in Laponite.[25] If ion leaching from the LDH substrate can be exploited for controlling the doping or formation of defects in BMO, this might also result in interesting photophysical properties. Thus, this work demonstrates that not only can the selectivity and adsorptivity of clay-based Aurivillius oxide sorbent composites be enhanced but also that the synthetic strategy of organic modification to template growth at interfaces can be generalized to other ionic layered materials.

ASSOCIATED CONTENT

Supporting Information

The Supporting Information is available free of charge at https://pubs.acs.org/doi/10.1021/acsami.2c14979.

> Additional UV−vis spectra; X-ray diffractograms; FTIR spectra; additional TEM images; EDX spectra; additional HAADF-STEM elemental mappings; UV−vis spectra from the dye adsorption experiments; adsorption isotherm; and UV−vis spectra from the photocatalytic dye degradation experiments (PDF)

AUTHOR INFORMATION

Corresponding Authors

Sanjay Jatav − *Institute of Physical Chemistry, University of Hamburg, 20146 Hamburg, Germany*; Email: sanjay.jatav@chemie.uni-hamburg.de

Eric H. Hill − *Institute of Physical Chemistry, University of Hamburg, 20146 Hamburg, Germany; The Hamburg Centre for Ultrafast Imaging (CUI), 22761 Hamburg, Germany*; orcid.org/0000-0003-3063-1447; Email: eric.hill@chemie.uni-hamburg.de

Authors

Marcel Herber − *Institute of Physical Chemistry, University of Hamburg, 20146 Hamburg, Germany*; orcid.org/0000-0002-7097-1502

Hongxiao Xiang − *Institute of Physical Chemistry, University of Hamburg, 20146 Hamburg, Germany*

Complete contact information is available at: https://pubs.acs.org/10.1021/acsami.2c14979

Notes

The authors declare no competing financial interest.

ACKNOWLEDGMENTS

This research was funded by the DAAD from the funds of German Federal Ministry of Education and Research (BMBF), under the MOPGA-GRI program (57565165). E.H.H. is supported by the Cluster of Excellence “Advanced Imaging of Matter” of the Deutsche Forschungsgemeinschaft (DFG) EXC

2056-project ID 390715994. H.X. is supported by funds from the DFG project ID 447787198. We thank the Central Division of Electron Microscopy (BEEM) of TUHH for providing access to an FEI Talos F200X. We thank the Weller/Vossmeyer groups for providing access to a Cary 5000 UV−vis−NIR spectrometer. We thank Dr. Hauke Heller of the Institute of Physical Chemistry and Sandra Koenig and Prof. Michael Froeba of the Institute of Inorganic Chemistry for providing access to a gas sorption analyzer and assistance with BET surface area measurements.

REFERENCES

(1) Persson, L.; Carney Almroth, B. M.; Collins, C. D.; Cornell, S.; de Wit, C. A.; Diamond, M. L.; Fantke, P.; Hassellöv, M.; MacLeod, M.; Ryberg, M. W.; Søgaard Jørgensen, P.; Villarrubia-Gómez, P.; Wang, Z.; Hauschild, M. Z. Outside the Safe Operating Space of the Planetary Boundary for Novel Entities. *Environ. Sci. Technol.* **2022**, *56*, 1510−1521.

(2) Wang, Z.; Walker, G. W.; Muir, D. C. G.; Nagatani-Yoshida, K. Toward a Global Understanding of Chemical Pollution: A First Comprehensive Analysis of National and Regional Chemical Inventories. *Environ. Sci. Technol.* **2020**, *54*, 2575−2584.

(3) Ng, A.; Weerakoon, D.; Lim, E.; Padhye, L. P. Fate of Environmental Pollutants. *Water Environ. Res.* **2019**, *91*, 1294−1325.

(4) Tang, Y.; Yin, M.; Yang, W.; Li, H.; Zhong, Y.; Mo, L.; Liang, Y.; Ma, X.; Sun, X. Emerging Pollutants in Water Environment: Occurrence, Monitoring, Fate, and Risk Assessment. *Water Environ. Res.* **2019**, *91*, 984−991.

(5) Cousins, I. T.; Johansson, J. H.; Salter, M. E.; Sha, B.; Scheringer, M. Outside the Safe Operating Space of a New Planetary Boundary for Per- and Polyfluoroalkyl Substances (PFAS). *Environ. Sci. Technol.* **2022**, *56*, 11172−11179.

(6) Chopra, A. K.; Sharma, M. K.; Chamoli, S. Bioaccumulation of Organochlorine Pesticides in Aquatic System-an Overview. *Environ. Monit. Assess.* **2011**, *173*, 905−916.

(7) Gerber, R.; Smit, N. J.; Van Vuren, J. H. J.; Nakayama, S. M. M.; Yohannes, Y. B.; Ikenaka, Y.; Ishizuka, M.; Wepener, V. Bioaccumulation and Human Health Risk Assessment of DDT and Other Organochlorine Pesticides in an Apex Aquatic Predator from a Premier Conservation Area. *Sci. Total Environ.* **2016**, *550*, 522−533.

(8) Mehra, S.; Singh, M.; Chadha, P. Adverse Impact of Textile Dyes on the Aquatic Environment as Well as on Human Beings. *Toxicol. Int.* **2021**, *28*, 165−176.

(9) Ercan, O.; Tarcin, G. Overview on Endocrine Disruptors in Food and Their Effects on Infant's Health. *Glob. Pediatr.* **2022**, *2*, No. 100019.

(10) Ghassabian, A.; Vandenberg, L.; Kannan, K.; Trasande, L. Endocrine-Disrupting Chemicals and Child Health. *Annu. Rev. Pharmacol. Toxicol.* **2022**, *62*, 573−594.

(11) Hansen, P. D.; Dizer, H.; Hock, B.; Marx, A.; Sherry, J.; McMaster, M.; Blaise, C. Vitellogenin - A Biomarker for Endocrine Disruptors. *TrAC, Trends Anal. Chem.* **1998**, *17*, 448−451.

(12) Dias, A. C. V.; Gomes, F. W.; Bila, D. M.; Sant'Anna, G. L.; Dezotti, M. Analysis of Estrogenic Activity in Environmental Waters in Rio de Janeiro State (Brazil) Using the Yeast Estrogen Screen. *Ecotoxicol. Environ. Saf.* **2015**, *120*, 41−47.

(13) Meijide, F. J.; Rey Vázquez, G.; Piazza, Y. G.; Babay, P. A.; Itria, R. F.; Lo Nostro, F. L. Effects of Waterborne Exposure to 17β-Estradiol and 4-Tert-Octylphenol on Early Life Stages of the South American Cichlid Fish Cichlasoma Dimerus. *Ecotoxicol. Environ. Saf.* **2016**, *124*, 82−90.

(14) Aves, A. R.; Revell, L. E.; Gaw, S.; Ruffell, H.; Schuddeboom, A.; Wotherspoon, E.; Larue, M.; Mcdonald, A. J. First Evidence of Microplastics in Antarctic Snow. *Cryosphere* **2022**, *16*, 2127−2145.

(15) Mirzaei, A.; Chen, Z.; Haghighat, F.; Yerushalmi, L. Removal of Pharmaceuticals from Water by Homo/Heterogonous Fenton-Type Processes − A Review. *Chemosphere* **2017**, *174*, 665−688.

(16) Kurniawan, T. A.; Chan, G. Y. S.; Lo, W. H.; Babel, S. Physico-Chemical Treatment Techniques for Wastewater Laden with Heavy Metals. *Chem. Eng. J.* **2006**, *118*, 83−98.

(17) Hofman-Caris, R.; Hofman, J. Limitations of Conventional Drinking Water Technologies in Pollutant Removal. *Handb. Environ. Chem.* **2019**, *67*, 21−51.

(18) Pincus, L. N.; Lounsbury, A. W.; Zimmerman, J. B. Toward Realizing Multifunctionality: Photoactive and Selective Adsorbents for the Removal of Inorganics in Water Treatment. *Acc. Chem. Res.* **2019**, *52*, 1206−1214.

(19) Pincus, L. N.; Melnikov, F.; Yamani, J. S.; Zimmerman, J. B. Multifunctional Photoactive and Selective Adsorbent for Arsenite and Arsenate: Evaluation of Nano Titanium Dioxide-Enabled Chitosan Cross-Linked with Copper. *J. Hazard. Mater.* **2018**, *358*, 145−154.

(20) Richardson, S. D.; Plewa, M. J.; Wagner, E. D.; Schoeny, R.; DeMarini, D. M. Occurrence, Genotoxicity, and Carcinogenicity of Regulated and Emerging Disinfection by-Products in Drinking Water: A Review and Roadmap for Research. *Mutat. Res., Rev. Mutat. Res.* **2007**, *636*, 178−242.

(21) Lavonen, E. E.; Gonsior, M.; Tranvik, L. J.; Schmitt-Kopplin, P.; Köhler, S. J. Selective Chlorination of Natural Organic Matter: Identification of Previously Unknown Disinfection Byproducts. *Environ. Sci. Technol.* **2013**, *47*, 2264−2271.

(22) Baig, U.; Faizan, M.; Sajid, M. Effective Removal of Hazardous Pollutants from Water and Deactivation of Water-Borne Pathogens Using Multifunctional Synthetic Adsorbent Materials: A Review. *J. Cleaner Prod.* **2021**, *302*, No. 126735.

(23) Jatav, S.; Furlan, K. P.; Liu, J.; Hill, E. H. Heterostructured Monolayer MoS_2 Nanoparticles toward Water-Dispersible Catalysts. *ACS Appl. Mater. Interfaces* **2020**, *12*, 19813−19822.

(24) Liu, J.; Jatav, S.; Hill, E. H. Few-Layer In_2S_3 in Laponite Interlayers: A Colloidal Route Toward Heterostructured Nanohybrids with Enhanced Photocatalysis. *Chem. Mater.* **2020**, *32*, 10015−10024.

(25) Liu, J.; Jatav, S.; Herber, M.; Hill, E. H. Few-Layer $ZnIn_2S_4$/Laponite Heterostructures: Role of Mg2+Leaching in Zn Defect Formation. *Langmuir* **2021**, *37*, 4727−4735.

(26) Jatav, S.; Liu, J.; Herber, M.; Hill, E. H. Facet Engineering of Bismuth Molybdate via Confined Growth in a Nanoscale Template toward Water Remediation. *ACS Appl. Mater. Interfaces* **2021**, *13*, 18713−18723.

(27) Liu, J.; Jatav, S.; Wessel, P.; Hill, E. H. Templating Unidirectional Bismuth Oxyiodide Crystal Growth with Layered Silicates for Enhanced Photocatalysis. *J. Phys. Chem. C* **2022**, *126*, 4975−4983.

(28) Forano, C; Hibino, T; Leroux, F; Taviot-Gueho, C. Chapter 13.1 Layered Double Hydroxides. In *Handbook of Clay Science*, 2nd ed.; Elsevier, 2006; pp. 1021−1095.

(29) Mishra, G.; Dash, B.; Pandey, S. Layered Double Hydroxides: A Brief Review from Fundamentals to Application as Evolving Biomaterials. *Appl. Clay Sci.* **2018**, *153*, 172−186.

(30) Meyn, M.; Beneke, K.; Lagaly, G. Anion-Exchange Reactions of Layered Double Hydroxides. *Inorg. Chem.* **1990**, *29*, 5201−5207.

(31) Kuthati, Y.; Kankala, R. K.; Lee, C. H. Layered Double Hydroxide Nanoparticles for Biomedical Applications: Current Status and Recent Prospects. *Appl. Clay Sci.* **2015**, *112*, 100−116.

(32) Goh, K. H.; Lim, T. T.; Dong, Z. Application of Layered Double Hydroxides for Removal of Oxyanions: A Review. *Water Res.* **2008**, *42*, 1343−1368.

(33) Gao, H.; Cao, R.; Xu, X.; Xue, J.; Zhang, S.; Hayat, T.; Alharbi, N. S.; Li, J. Surface Area- and Structure-Dependent Effects of LDH for Highly Efficient Dye Removal. *ACS Sustainable Chem. Eng.* **2019**, *7*, 905−915.

(34) Chen, Y.; Jing, C.; Zhang, X.; Jiang, D.; Liu, X.; Dong, B.; Feng, L.; Li, S.; Zhang, Y. Acid-Salt Treated CoAl Layered Double Hydroxide Nanosheets with Enhanced Adsorption Capacity of Methyl Orange Dye. *J. Colloid Interface Sci.* **2019**, *548*, 100−109.

(35) Zou, J.; Wang, Z.; Guo, W.; Guo, B.; Yu, Y.; Wu, L. Photocatalytic Selective Oxidation of Benzyl Alcohol over ZnTi-LDH:

The Effect of Surface OH Groups. *Appl. Catal. B Environ.* **2020**, *260*, No. 118185.
(36) Bhat, S. S. M.; Jang, H. W. Recent Advances in Bismuth-Based Nanomaterials for Photoelectrochemical Water Splitting. *ChemSusChem* **2017**, *10*, 3001−3018.
(37) Zhang, L.; Li, Y.; Li, Q.; Fan, J.; Carabineiro, S. A. C.; Lv, K. Recent Advances on Bismuth-Based Photocatalysts: Strategies and Mechanisms. *Chem. Eng. J.* **2021**, *419*, No. 129484.
(38) Sim, L. T.; Lee, C. K.; West, A. R. High Oxide Ion Conductivity in Bi_2MoO_6 Oxidation Catalyst. *J. Mater. Chem.* **2002**, *12*, 17−19.
(39) Chankhanittha, T.; Somaudon, V.; Watcharakitti, J.; Piyavarakorn, V.; Nanan, S. Performance of Solvothermally Grown Bi_2MoO_6 Photocatalyst toward Degradation of Organic Azo Dyes and Fluoroquinolone Antibiotics. *Mater. Lett.* **2020**, *258*, No. 126764.
(40) Ren, J.; Wang, W.; Shang, M.; Sun, S.; Gao, E. Heterostructured Bismuth Molybdate Composite: Preparation and Improved Photocatalytic Activity under Visible-Light Irradiation. *ACS Appl. Mater. Interfaces* **2011**, *3*, 2529−2533.
(41) Li, H. H.; Li, K. W.; Wang, H. Hydrothermal Synthesis and Photocatalytic Properties of Bismuth Molybdate Materials. *Mater. Chem. Phys.* **2009**, *116*, 134−142.
(42) Kumar, R.; Sudhaik, A.; Raizada, P.; Hosseini-Bandegharaei, A.; Thakur, V. K.; Saini, A.; Saini, V.; Singh, P. An Overview on Bismuth Molybdate Based Photocatalytic Systems: Controlled Morphology and Enhancement Strategies for Photocatalytic Water Purification. *J. Environ. Chem. Eng.* **2020**, *8*, No. 104291.
(43) Hu, F.; Cui, E.; Liu, H.; Wu, J.; Dai, Y.; Yu, G. Layered Bi_2MoO_6 /LDH Hetero-Structured Composites with Enhanced Visible Light Photocatalytic Activity. *J. Mater. Sci.: Mater. Electron.* **2019**, *30*, 2572−2584.
(44) Li, H.; Deng, Q.; Liu, J.; Hou, W.; Du, N.; Zhang, R.; Tao, X. Synthesis, Characterization and Enhanced Visible Light Photocatalytic Activity of Bi_2MoO_6/Zn-Al Layered Double Hydroxide Hierarchical Heterostructures. *Catal. Sci. Technol.* **2014**, *4*, 1028−1037.
(45) Yang, X. J.; Wu, L.; Hu, R.; Xing, J.; Zhou, G.; Lu, S.; Wu, J.; Li, P.; Liu, D. Hollow Microspherical Bi_2MoO_6/Zn-Ti Layered Double Hydroxide Heterojunction for Efficient Visible-Light Photocatalytic Degradation of Organic Contaminants. *New J. Chem.* **2022**, *46*, 1704−1712.
(46) Johnston, A. L.; Lester, E.; Williams, O.; Gomes, R. L. Understanding Layered Double Hydroxide Properties as Sorbent Materials for Removing Organic Pollutants from Environmental Waters. *J. Environ. Chem. Eng.* **2021**, *9*, No. 105197.
(47) Sharma, M.; Kumar, A.; Krishnan, V. Influence of Oxygen Vacancy Defects on Aurivillius Phase Layered Perovskite Oxides of Bismuth towards Photocatalytic Environmental Remediation. *Nanotechnology* **2022**, *33*, 275702.
(48) Kumar, J.; Ruckenstein, E. Structural Changes in Thin Films of the 1:1 Bismuth Molybdate under Reduction and Oxidation Conditions. *J. Catal.* **1976**, *45*, 198−215.
(49) Zhi-Cheng, J.; Li-Dun, A.; Yuan-Gen, Y. XPS Study of Ion-Induced Chemical Effect on β-Bismuth Molybdate Catalyst. *Appl. Surf. Sci.* **1985**, *24*, 134−146.
(50) Liu, Y.; Yu, Z.; Wang, Q.; Zhu, X.; Long, R.; Li, X. Application of Sodium Dodecyl Sulfate Intercalated Co−Al LDH Composite Materials (RGO/PDA/SDS-LDH) in Membrane Separation. *Appl. Clay Sci.* **2021**, *209*, No. 106138.
(51) Guo, W.; Li, H.; Ma, H.; Teng, W. Different Surfactants-Assisted Hydrothermal Fabrication and Photocatalytic Properties of Bi_2MoO_6 for Methylene Blue Degradation under Simulated Sunlight Irradiation. *J. Chem.* **2014**, *2014*, No. 436485.
(52) Zhu, Y. N.; Mu, J. J.; Zheng, G. H.; Dai, Z. X.; Zhang, L. Y.; Ma, Y. Q.; Zhang, D. W. Morphology, Photocatalytic and Photoelectric Properties of Bi_2MoO_6 Tuned by Preparation Method, Solvent, and Surfactant. *Ceram. Int.* **2016**, *42*, 17347−17356.
(53) Zhang, J.; Liu, Z.; Ma, Z. Facile Formation of $Bi_2O_2CO_3$ /Bi_2MoO_6 Nanosheets for Visible Light-Driven Photocatalysis. *ACS Omega* **2019**, *4*, 3871−3880.
(54) Maswanganyi, S.; Gusain, R.; Kumar, N.; Fosso-Kankeu, E.; Waanders, F. B.; Ray, S. S. Bismuth Molybdate Nanoplates Supported on Reduced Graphene Oxide: An Effective Nanocomposite for the Removal of Naphthalene via Adsorption-Photodegradation. *ACS Omega* **2021**, *6*, 16783−16794.
(55) Yang, X.; Wang, X.; Feng, Y.; Zhang, G.; Wang, T.; Song, W.; Shu, C.; Jiang, L.; Wang, C. Removal of Multifold Heavy Metal Contaminations in Drinking Water by Porous Magnetic Fe_2O_3@AlO(OH) Superstructure. *J. Mater. Chem. A* **2013**, *1*, 473−477.
(56) Jatav, S.; Herber, M.; Xiang, H.; Hill, E. H. Surface-Encapsulated Bismuth Molybdate-Layered Silicate Hybrids as Sorbents for Photocatalytic Filtration Membranes. *ACS Appl. Mater. Interfaces* **2022**, *14*, 22790−22798.

https://doi.org/10.1021/acsami.2c14979

Chapter 6

In_2S_3 Growth Templated by Aluminogermanate Nanotubes towards Efficient Visible Light Photocatalysts

This chapter has been published as: Jatav, S.; Xiang H.; Herber, M.; Paineau E.; Hill, E. H. In_2S_3 Growth Templated by Aluminogermanate Nanotubes towards Efficient Visible Light Photocatalysts in *Solar RRL*, **2023**, 7 (4), 2200947.

The chapters 2–5 examined the (photo)catalytic nanohybrids in which semiconductor growth was templated using discoidal clays, namely, laponite and CoAl layered double hydroxide. This chapter presents an investigation of photocatalytic nanohybrids prepared using a tubular clay, imogolite and a different semiconductor, namely, In_2S_3.

In_2S_3 Growth Templated by Aluminogermanate Double-Walled Imogolite Nanotubes Toward Efficient Visible Light Photocatalysts

Sanjay Jatav, Hongxiao Xiang, Marcel Herber, Erwan Paineau,* and Eric H. Hill*

Different strategies combining semiconductors and nanomaterials have been explored to enhance the performance of visible light photocatalysts. This work reports the hydrothermal growth of In_2S_3 on the aluminogermanate double-walled imogolite nanotubes and the photocatalytic properties of the resulting composites. The reaction conditions are optimized to ensure the linear growth of In_2S_3, while preserving the tubular structure of imogolite nanotubes. The imogolite–In_2S_3 composites show enhanced photocatalytic degradation of methyl orange compared to the control In_2S_3, exhibiting a fourfold increase in the photocatalytic dye degradation rate constant. Interestingly, these composites present a negative photocurrent response, indicating the generation of mobile holes, whereas both In_2S_3 and imogolite by themselves exhibit typical positive photocurrent behavior. The improvement in the photocatalytic dye degradation and the negative photocurrent response is attributed to the interface formation between In_2S_3 and imogolite in these composites and the *p*-type character of the latter. Templating the colloidal synthesis of semiconducting nanoparticles in confined spaces could bring a step change in the design of catalytic and photocatalytic materials.

1. Introduction

Less-energy-intensive means for water decontamination are being sought due to increasing demand, dwindling fossil fuel reserves, and problems associated with their use.[1,2] In this vein, solar means of decontaminating water are becoming attractive.[3,4] Indium sulfide, In_2S_3, is a III–V semiconductor which has been studied for its photocatalytic and photovoltaic properties.[5–7] Apart from possessing interesting optical properties, In_2S_3 is also appealing because of its low toxicity and stability under ambient settings.[8,9] One of the strategies for improving the performance of In_2S_3 is to combine it with other materials. For instance, composites with graphene,[10] ZnO,[11] and MnS[12] have shown improvement in photocatalytic performance over pristine In_2S_3. In a previous study, we reported that in addition to conventional carbon-based materials (graphene, nanotubes), metal sulfides, and oxides, layered silicate clays can also be used to enhance the photophysical properties of In_2S_3.[13] Such laponite–In_2S_3 nanohybrids, comprising thin layers of In_2S_3, showed an order of magnitude enhancement in photocurrent generation and photocatalytic efficiency compared to the In_2S_3 control. The possibility of templating In_2S_3 growth using a 1D template nanoparticle, and the resulting photocatalytic properties, led to the growth of In_2S_3 on aluminogermanate double-walled imogolite nanotubes (GWINTs).

Imogolite is a clay nanotube with a general structural formula $(OH)_3Al_2O_3X(R)$ (with X = Si, Ge; R = OH, CH_3...), which appears as a promising 1D template.[14,15] INTs have the advantage to present a well-defined minimum in their strain energy,[16] resulting in nanotubes with monodispersed diameters.[17,18] In addition, the synthesis process is relatively straightforward, enabling to control the morphology (single vs double-walled structures, aspect ratio...) and the surface properties of the inner cavity by changing the nature of the precursors.[19–21] Thanks to their unique colloidal properties,[22] INTs have demonstrated their ability to effectively stabilize metal nanoparticles on their external surface[23–25] but, to date, the growth of semiconductor nanowires with INTs has not been truly explored.

Herein, the hydrothermal growth of In_2S_3 was performed in the presence of the colloidal dispersion of INT to obtain photocatalytic INT-In_2S_3 composites. By carefully controlling the reaction conditions, the tubular morphology of INT could be preserved and the In_2S_3 growth confined exclusively onto these tubes. These In_2S_3-decorated INTs exhibited a fourfold enhancement in their photocatalytic dye degradation rate compared to the pristine In_2S_3, even though the former has a wider bandgap. In addition, the mechanism responsible for

S. Jatav, H. Xiang, M. Herber, E. H. Hill
Institute of Physical Chemistry
University of Hamburg
20146 Hamburg, Germany
E-mail: eric.hill@chemie.uni-hamburg.de

E. Paineau
Université Paris-Saclay, CNRS, Laboratoire de Physique des Solides
91405 Orsay, France
E-mail: erwan-nicolas.paineau@universite-paris-saclay.fr

The ORCID identification number(s) for the author(s) of this article can be found under https://doi.org/10.1002/solr.202200947.

DOI: 10.1002/solr.202200947

the negative photocurrent response of the composite, which contrasts with the photocurrent response of the pristine INT and In_2S_3 control samples, has been proposed.

2. Results

XRD was performed in order to verify the effective growth of In_2S_3 and the presence of INT. The diffraction peaks from In_2S_3 cannot be observed in the composites, which implies the presence of scant amount of In_2S_3 in the composites (**Figure 1**a). Due to the finite radial dimensions of the nanotubes, the related diffractograms display large oscillations between 5° and 15° 2θ that are typical of the form factor of double-walled nanotubes.[26]In the case of composites, the signature of INTs is still present but the nanotubes undergo structural transformation after being exposed to hydrothermal conditions during the reactions. By the 3-h time point, the appearance of additional peaks indicates the formation of another phase. In particular, the peak at 14.3° matches well with the (020) crystal plane of boehmite.[27,28] All the composites show the increase of a broad peak centered at $2\theta \approx 62°$ with increasing reaction time, which can be ascribed to the (080) plane of boehmite.[27] Thus, from XRD, it can be surmised that the hydrothermal transformation of INT to boehmite can be controlled by varying the reaction duration.

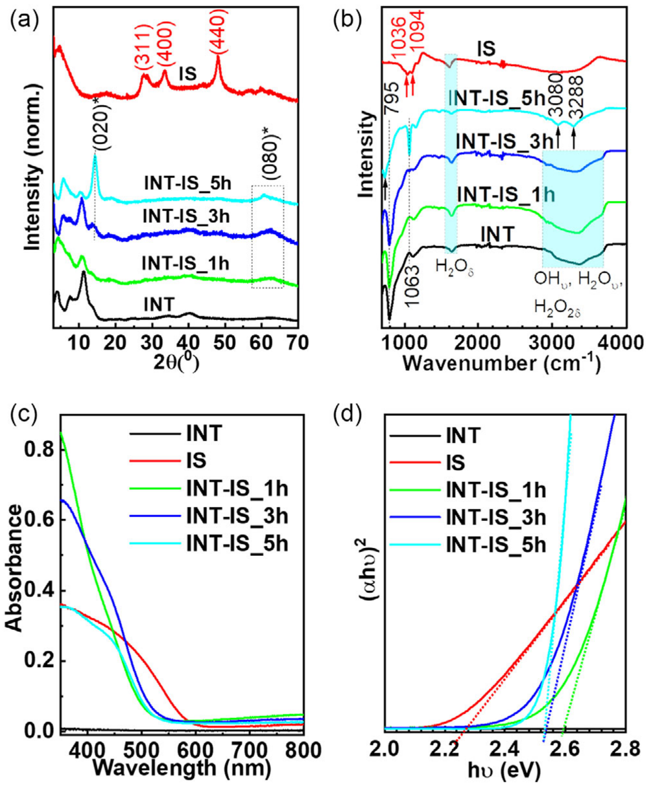

Figure 1. a) X-Ray diffractograms of the INT-In_2S_3 composites. *represents peaks belonging to boehmite. b) FTIR spectra. c) DRS UV–vis spectra of the INT–In_2S_3 composites. d) Tauc plots of the INT–IS composites. Dotted lines show the bandgap calculated by the Kubelka–Munk method.

These samples were further characterized by FTIR spectroscopy. The sharp peak at 795 cm^{-1} and the presence of a broad band between 2800 and 4000 cm^{-1} can be assigned to the Ge–O–Al stretch and to the υ stretching mode and bending mode of hydroxyl groups in water alongside the stretching vibrations of –OH groups belonging to INT, respectively (Figure 1b).[29,30] These bands are present in all the INT–IS composites except INT-IS_5h. The bands at 750, 1063, 1150, 3080, and 3288 cm^{-1} correspond to the torsional mode of Al–O, symmetric Al–O–H δ stretch, asymmetric Al–O–H δ stretch, symmetric Al–OH υ stretch, and asymmetric Al–OH υ stretch, respectively. These bands indicate the formation of boehmite.[31] The 1063 cm^{-1} band is also present in the INT-IS_3h sample, however with diminished intensity compared to INT-IS_5h. The bands in IS control seen at 1036 and 1094 cm^{-1} are due to the S–O stretch and υ stretch of CS present in the S source thioacetamide.[32,33] The absence of these bands in the composites indicates a relatively low amount of In_2S_3 present in these samples. Overall, FTIR characterization corroborates the observations from XRD.

The UV–vis–DRS spectra of the samples show that the light absorption in the composites is primarily due to the presence of In_2S_3, since INT has negligible absorption in the wavelength range measured (Figure 1c). Interestingly, the composites present a blueshift of the absorption band edge compared to the IS control, the largest blueshift being observed in INT-IS_1h. This blueshift is plausibly due to the small size of In_2S_3 particles present in these composites (**Figure 2**).[34] The bandgap of the samples was calculated using the Kubelka–Munk method (Figure 1d).[35,36] The bandgaps of IS, INT-IS_1h, INT-IS_3h, and INT-IS_5h were found to be 2.27, 2.59, 2.54, and 2.53 eV, respectively.

Pristine IS forms irregularly shaped sheets (Figure 2a), with a thickness of ≈5 nm (Figure S1, Supporting Information). The INT sample shows tubes having a diameter ≈4.5 nm and an average length ≈88 nm (Figure 2b), similar to those reported

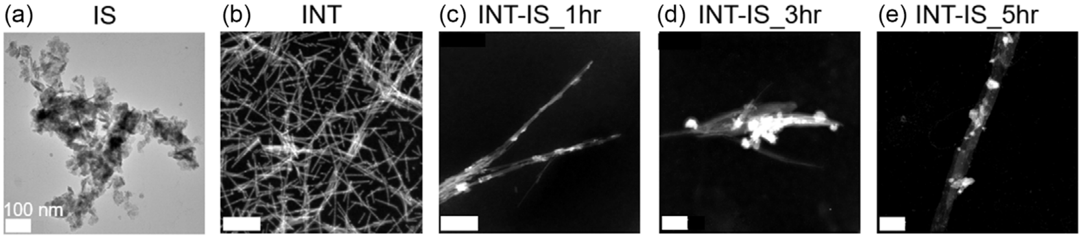

Figure 2. a) Bright-field TEM image of IS. HAADF–STEM images of b) INT, c) INT-IS_1h, d) INT-IS_3h, and e) INT-IS_5h. All scale bars are 100 nm. Additional images of these samples are presented in Figure S1, Supporting Information.

previously.[21] In the case of the sample INT-IS_1h, the tubular morphology of INT is largely preserved, but the tubes seem to be linked together into bundles after In_2S_3 growth (Figure 2c, S1, Supporting Information). The brighter spots represent In_2S_3, due to the increased atomic number of In relative to Ge and Al. In the presence of INT, In_2S_3 grows atop INT; however, the reaction time drastically affects the morphology of the grown In_2S_3. Furthermore, as the reaction time is increased to 3 and 5 h, the INT's tubular morphology is transformed into elongated sheets (Figure 2d,e and S1, Supporting Information). The XRD and FTIR results suggest that this change in morphology is due to the transition from imogolite to boehmite at longer reaction times. The absence of isolated In_2S_3 particles in the hybrids suggests that the surfactant modification of the INT surface as well as the In and S precursor concentrations chosen ensured the nucleation of In_2S_3 crystals on the INT.

HAADF–STEM EDX mappings were performed on the samples for a closer examination of In_2S_3 growth on INT and state of INT after the hydrothermal reactions (**Figure 3**). In the case of the sample INT-IS_1h, the continuous growth of In_2S_3 along the tube axis was observed, in addition to the growth of separate In_2S_3 particles along the tube length (Figure S1, Supporting Information). From the EDX spectra, it can be seen that peaks belonging to all the constituent elements are present for the sample INT-IS_1h (Figure S2a, Supporting Information). However, for the sample INT-IS_5h, the characteristic peaks of Ge ($K\alpha$ and $L\alpha$) have almost disappeared, indicating the transformation of INT to boehmite (Figure S2a, Supporting Information). From above mappings of the same sample, it can also be evidenced that after 5 h, the slender tubes seen in INT-IS_1h are transformed into elongated sheets, which signifies the conversion of INT into boehmite.

Photocatalytic performance of these composites was evaluated by photocatalytic degradation of the dye MO in visible light (>400 nm). MO is used as it does not photolyze upon illumination in the visible region. INTs also afford no dye degradation under visible light illumination (**Figure** 4a). The photocatalytic degradation of MO by IS is significantly lower than that of INT-IS_1h. The former could degrade ≈50% of the dye in 2 h, whereas the latter, having the same amount of In_2S_3 as IS, degraded ≈90% MO in the same time. The analysis of the dye degradation kinetics shows that the pseudo-first-order rate constant is enhanced by almost four times for INT-IS_1h compared to the IS control (Figure 4a). Since $[In_2S_3]$ was identical during the photocatalytic dye degradation with the samples INT-IS_1h and IS control, these results suggest that the introduction of INT induces a synergetic effect which enhances the photocatalytic activity of In_2S_3. It is to be noted that this improvement in photocatalysis occurs even with INT-IS_1h having a ≈14% larger bandgap than IS control. Laponite–In_2S_3 composites reported by Liu et al also showed improved photocatalysis despite a drastically increased bandgap.[13] Upon comparison, the INT-IS hybrids show a 19% increase in photocatalytic dye degradation rate compared to laponite–In_2S_3 composites. Moreover, the INT-In_2S_3 composite after 1 h of growth shows increased photocatalytic dye degradation compared with the boehmite-dominated sample synthesized with 5 h of growth (Figure S4a, Supporting Information). This suggests that the transformation of INT into boehmite is detrimental to the photocatalytic performance of the INT-IS hybrids. Also, the photocatalytic activity of INT-IS_1h decreased significantly after three reuse cycles, pointing to photodegradation of the hybrid during use (Figure S4b, Supporting Information). While this may result from loss of particles during the recovery step, it may also result from the photodegradation of the hybrid. The photoactivity was further investigated using chopped light voltammetry with a solar simulator as the light source.

Samples INT and IS generate similar amount of photocurrent upon illumination (Figure 4c). It was noted that INT showed no photocatalytic activity upon illumination with only visible light, suggesting that INT is photoactive only in the UV region of the spectrum due to its low light absorption in the visible range (Figure 1c). INT and IS by themselves showed a typical positive photocurrent response; however, the composite INT-IS_1h displayed a negative photocurrent response. This points toward some effect of the interface between INT and IS, which allows increased mobility of photogenerated holes. A similar negative photocurrent response was observed in the composites of reduced graphene oxide (RGO)–WS_2 by Rath et al.[37] They attributed this behavior to the *p*-type nature of RGO and the formation of diffusion barrier

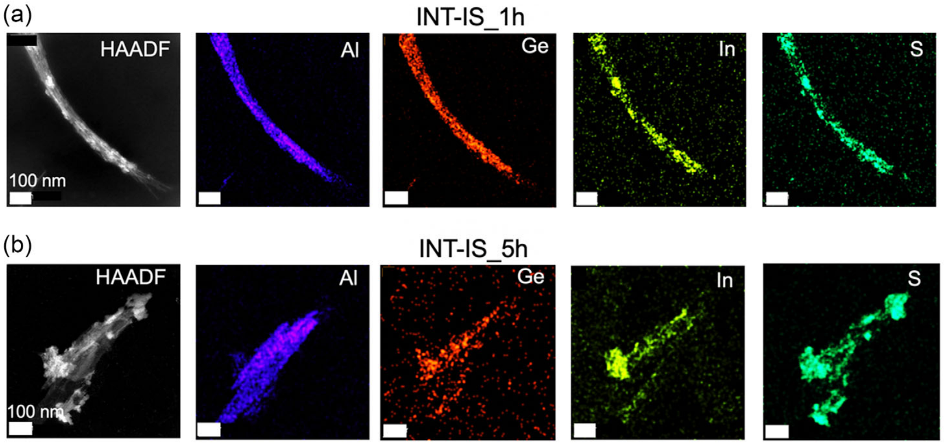

Figure 3. HAADF–STEM EDX mappings of a) INT-IS_1h and b) INT-IS_5h. EDX spectra of these mappings are presented in the Figure S2, Supporting Information.

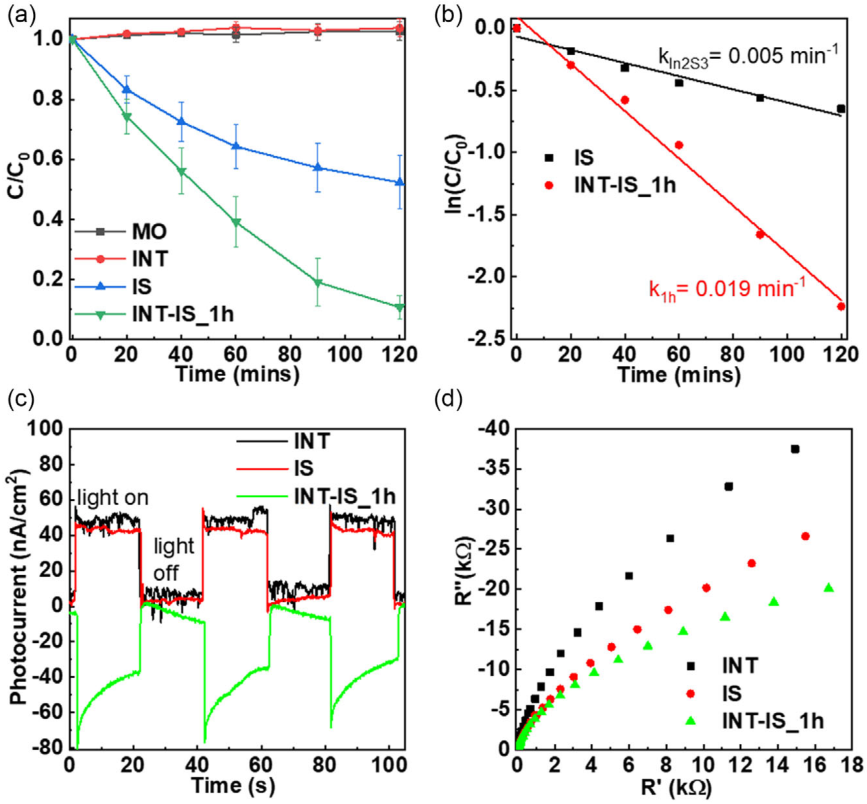

Figure 4. a) Photocatalytic dye degradation of MO (corresponding UV–vis spectra are shown in Figure S3, Supporting Information), b) apparent first order rate constant for MO photodegradation, ([MO] = 15.25 μM, [particles] = 0.25 mg mL^{-1}), c) transient photocurrent response, and d) Nyquist plots of the composite and controls.

between the valence band of RGO and conduction band of WS_2. As INT exhibits *p*-type characteristics,[38] it seems plausible that a similar mechanism might be operating in INT-IS_1h. Interfacial charge transfer resistance was examined by EIS. Since the radius of the arc corresponds to the resistance, it can be seen that INT-IS_1h shows the lowest interfacial charge transfer resistance followed by IS and then INT. The low interfacial resistance might be one of the factors contributing toward enhancing the photocatalytic dye degradation performance of INT-IS_1h.

3. Conclusions

By optimizing the reaction conditions, the growth of In_2S_3 was templated by surfactant-modified INT. The morphology of In_2S_3 changed from anisotropic platelets to a mix of linear growths along the INT particles after 1 h of growth, to small particles along the INT/boehmite structure at longer reaction times. These In_2S_3-decorated INT exhibited a ≈400% enhancement in the photocatalytic dye degradation rate of MO over pristine In_2S_3, even though the bandgap was increased by 14% in the composite. Moreover, the *p*-type character of INT and the formation of the interface with In_2S_3 also engendered a negative photocurrent response not seen in the parent constituent materials themselves. The increased photocatalytic performance of the INT-IS can be attributed to the high mobility of photogenerated holes, which can then directly lead to oxidative reactions of MO. The present study revealed that just like the discoidal clay, laponite, a tubular clay, imogolite, can also template the growth of In_2S_3, enhancing the resulting photocatalytic properties. This work shows that such morphology-based templating approaches can be utilized in a more general sense and will encourage further research into the composites of functional materials with clays in general and imogolite in particular. While further systematic studies are required to elucidate the role of the interface in enhancing photocatalysis, previously reported clay-templated syntheses of photocatalysts such as Bi_2MoO_6,[39] BiOI,[40] $ZnIn_2S_4$,[41] and MoS_2[42] suggest that there is yet a rich landscape of imogolite-based nanohybrid photocatalysts left to explore.

4. Experimental Section

Chemicals: Tetraethoxygermane (TEOG), urea ($CO(NH_2)_2$), dodecyltrimethylammonium bromide (DTAB), thioacetamide (TAA), indium chloride ($InCl_3.5H_2O$), and methyl orange (MO) were purchased from Sigma-Aldrich Chemical Reagent Co., Ltd. Aluminum perchlorate nonahydrate ($Al(ClO_4)_3{\cdot}9H_2O$) and polyvinyl alcohol (PVA, molecular weight 88 000–97 000 g mol^{-1}, 87–89% hydrolyzed) were procured from Alfa Aesar and Na_2SO_4 (>99%) was obtained from Chemsolute.

Synthesis: Ge Double-Walled Imogolite Nanotubes (GDWINT): Aluminogermanate double-walled nanotubes were synthesized according to previously reported methods.[43]Typically, 50 mL of 0.2 M $Al(ClO_4)_3$ and

50 mL of 0.2 M $CO(NH_2)_2$ were mixed under stirring in a PFTE beaker. 1.11 mL of TEOG was added to obtain a molar ratio [Ge]:[Al]:[urea] = 1:2:2. The mixture was then transferred in an acid digestion bomb (Zeoclave, Maximator, France). The hydrothermal treatment was performed under autogenous pressure at 140 °C for 5 days. After cooling down the autoclave, the resulting dispersion was dialyzed with ultrapure water (resistivity 18 MΩ cm) using semipermeable membranes (Spectra/Por, 10 kDa). The final solid concentration in GDWINT was determined by weight loss upon drying.

Synthesis: Hydrothermal In2S3 Growth on INT: An aqueous dispersion of GDWINT (1.5 mL, 10 mg mL^{-1}) was added to 23.5 mL deionized water in a 50 mL Teflon beaker. Subsequently, DTAB (78 µL, 0.1 M) was added to the above GDWINT dispersion under stirring. A previously prepared 5 mL solution of TAA (11 mg) and $InCl_3.5H_2O$ (5.43 mg) was added to the Teflon beaker and stirred for 5 min. Then this beaker was sonicated for 5 min and sealed in a hydrothermal autoclave (DAB-2, Berghof Instruments, Germany). The reaction was carried out at 180 °C for 1, 3, and 5 h. These samples were labeled as INT-IS_1h, INT-IS_3h, and INT-IS_5h, respectively. In_2S_3 control was prepared using 50 times the amount of In and S precursor used for synthesizing the composites. The In_2S_3 control was labelled as IS. All the above samples were washed five times with water and two times with ethanol and then dried at 60 °C for 24 h. The synthesis scheme is shown (**Scheme 1**).

Characterization: Crystal structure of the samples was determined by X-Ray diffraction (XRD) on a PANalytical X'PERT Pro diffractometer (Philips, Netherlands) using Cu Kα radiation (1.54 Å). Fourier-transform infrared (FTIR) spectra were measured on a Bruker Invenio R using golden gate ATR. 128 scans were averaged and recorded at a resolution of 4 cm^{-1}. A Cary 5000 UV–vis–NIR spectrometer (Agilent Inc., Santa Clara, CA, USA) was used for measuring diffuse reflectance UV–visible spectra of the samples with an integrating sphere. High-resolution transmission electron microscopy (HRTEM), high-angle-annular dark-field scanning transmission electron microscopy (HAADF–STEM), and electron-dispersive X-ray spectroscopy (EDX) mapping were performed on a Talos F200X (FEI, USA) equipped with four silicon drift EDX detectors.

Photocatalytic Dye Degradation: 5 mg of the composite was added to a solution of methyl orange (15.25 µM, 20 mL), resulting in the final photocatalyst concentration of 0.25 mg mL^{-1}. This dispersion was illuminated with a 300 W Xe lamp (LSE340, LOT-Oriel GmbH & Co. KG, Germany) using a >400 nm long-pass filter (FEL0400, Thorlabs, Newton, NJ, USA) to remove UV light. Before illumination, the dye suspension was stirred for 30 min to reach adsorption–desorption equilibrium. 1.5 mL aliquots were withdrawn at specific time points and centrifuged (4500 rpm, 10 min), after which the UV–vis absorbance spectra were recorded using a Cary 60 UV–vis spectrometer (Agilent Inc., Santa Clara, CA, USA). The same amount of INT was used in the control dye degradation experiments. For the In_2S_3 control experiments, an equivalent amount of In_2S_3 to that present in the composite was used (0.84 mg).

Photoelectrochemical Characterization: A Zahner Zennium XC electrochemical workstation was used for photoelectrochemical measurements. A three-electrode setup was used with an FTO photoanode, Ag/AgCl, and platinum wire functioning as working, reference, and counter electrodes, respectively. Chopped light voltammetry was carried out at an applied potential of 0 V (vs Ag/AgCl) with light pulse period of 20 s. Solar simulator (SS-F5-3 A, Enli Tech Company, Taiwan) was used as the illumination source. Electrochemical impedance spectroscopy (EIS) was carried out with a sinusoidal AC perturbation of 10 mV applied over the frequency range of 0.1–1 MHz. The samples were prepared by dispersing the powders (0.84 mg for IS and 5 mg for INT-IS_1h and INT) in 1.5 mL of PVA (10 mg mL^{-1}) and then drop casting 0.75 mL of the dispersion on the FTO substrate.

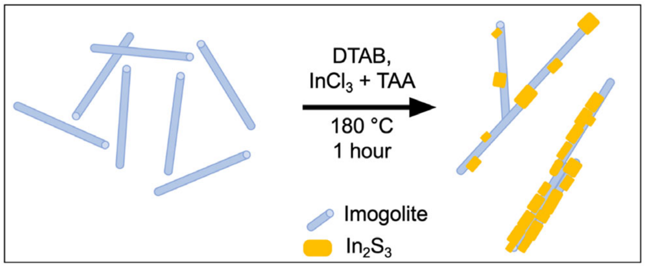

Scheme 1. Hydrothermal growth of In_2S_3 on imogolite nanotubes.

Supporting Information

Supporting Information is available from the Wiley Online Library or from the author.

Acknowledgements

This research was funded by the German Academic Exchange Service (DAAD) from the funds of the German Federal Ministry of Education and Research, BMBF (57565165). E.H.H. is supported by the Cluster of Excellence "Advanced Imaging of Matter" of the Deutsche Forschungsgemeinschaft (DFG) EXC 2056-project ID 390715994. This project received financial support from the CNRS through the International Emerging Actions program (IEA00669, SECOWIN). The authors are grateful to the Central Division of Electron Microscopy (BEEM) of TUHH for providing access to an FEI Talos F200X. The authors thank Professor Manfred Eich of the Institute of Optical and Electronic Materials of TUHH for providing the photoelectrochemistry setup and Dr. Fatemeh Ebrahimi for useful discussions. The authors thank the Weller/Vossmeyer groups for providing access to a Cary 5000 UV–vis–NIR spectrometer.

Open Access funding enabled and organized by Projekt DEAL.

Conflict of Interest

The authors declare no conflict of interest.

Data Availability Statement

The data that support the findings of this study are available from the corresponding author upon reasonable request.

Keywords

clays, imogolite, In_2S_3, nanotubes, photocatalysis, water remediation

Received: October 19, 2022
Revised: November 15, 2022
Published online:

---

[1] C. J. Vörösmarty, P. B. McIntyre, M. O. Gessner, D. Dudgeon, A. Prusevich, P. Green, S. Glidden, S. E. Bunn, C. A. Sullivan, C. R. Liermann, P. M. Davies, *Nature* **2010**, *467*, 555.
[2] H. S. Wheater, P. Gober, *Water Resour. Res.* **2015**, *51*, 5406.
[3] B. J. M. Chaúque, F. G. Brandão, M. B. Rott, *J. Environ. Chem. Eng.* **2022**, *10*.
[4] A. Ruiz-Aguirre, J. G. Villachica-Llamosas, M. I. Polo-López, A. Cabrera-Reina, G. Colón, J. Peral, S. Malato, *Energy* **2022**, *260*, 125199.
[5] S. Rengaraj, S. Venkataraj, C. W. Tai, Y. Kim, E. Repo, M. Sillanpää, *Langmuir* **2011**, *27*, 5534.
[6] Y. Liu, C. Chen, Y. He, Z. Zhang, M. Li, C. Li, X. B. Chen, Y. Han, Z. Shi, *Small* **2022**, *18*, 2201556.

[7] X. Tang, S. Yi, Q. Yuan, Q. Shu, D. Han, L. Feng, *Sol. RRL* **2022**, *6*, 1.
[8] M. Murugalakshmi, G. Mamba, S. A. Ansari, V. Muthuraj, T. I. T. Nkambule, *Colloids Surfaces A Physicochem. Eng. Asp.* **2022**, *634*, 127969.
[9] H. Qiu, S. Fang, G. Huang, J. Bi, *Environ. Res.* **2020**, *190*, 110018.
[10] M. Q. Yang, B. Weng, Y. J. Xu, *Langmuir* **2013**, *29*, 10549.
[11] Z. Braiek, T. Roques-Carmes, I. Ben Assaker, M. Gannouni, P. Arnoux, S. Corbel, R. Chtourou, *J. Photochem. Photobiol. A Chem.* **2019**, *368*, 307.
[12] J. Tan, M. Yu, Z. Cai, X. Lou, J. Wang, Z. Li, *J. Colloid Interface Sci.* **2021**, *588*, 547.
[13] J. Liu, S. Jatav, E. H. Hill, *Chem. Mater.* **2020**, *32*, 10015.
[14] E. Paineau, *Appl. Sci.* **2018**, *8*.
[15] J. Govan, N. Arancibia-Miranda, M. Escudey, B. Bonelli, F. Tasca, *Mater. Chem. Front.* **2021**, *5*, 6779.
[16] L. Guimarães, A. N. Enyashin, J. Frenzel, T. Heine, H. A. Duarte, G. Seifert, *ACS Nano* **2007**, *1*, 362.
[17] G. Monet, M. S. Amara, S. Rouzière, E. Paineau, Z. Chai, J. D. Elliott, E. Poli, L. M. Liu, G. Teobaldi, P. Launois, *Nat. Commun.* **2018**, *9*.
[18] E. Paineau, G. Monet, V. Peyre, C. Goldmann, S. Rouzière, P. Launois, *Langmuir* **2019**, *35*, 12451.
[19] G. I. Yucelen, D. Y. Kang, R. C. Guerrero-Ferreira, E. R. Wright, H. W. Beckham, S. Nair, *Nano Lett.* **2012**, *12*, 827.
[20] M. S. Amara, E. Paineau, S. Rouzière, B. Guiose, M. E. M. Krapf, O. Taché, P. Launois, A. Thill, *Chem. Mater.* **2015**, *27*, 1488.
[21] E. Paineau, S. Rouzière, G. Monet, C. C. Diogo, I. Morfin, P. Launois, *J. Colloid Interface Sci.* **2020**, *580*, 275.
[22] E. Paineau, M. E. M. Krapf, M. S. Amara, N. V. Matskova, I. Dozov, S. Rouzière, A. Thill, P. Launois, P. Davidson, *Nat. Commun.* **2016**, *7*, 1.
[23] S. Imamura, T. Kokubu, T. Yamashita, Y. Okamoto, K. Kajiwara, H. Kanai, *J. Catal.* **1996**, *160*, 137.
[24] W. J. Hsu, I. A. M. Ibrahim, Y. H. Lin, Z. H. Yang, G. I. Yucelen, J. W. Han, D. Y. Kang, *ACS Appl. Nano Mater.* **2019**, *2*, 6677.
[25] C. Hamon, E. , P. Launois, E. Paineau, *J. Phys. Chem. Lett.* **2021**, *12*, 5052.
[26] G. Monet, S. Rouzière, D. Vantelon, C. Coelho Diogo, D. Maurin, J. L. Bantignies, P. Launois, E. Paineau, *J. Phys. Chem. C* **2021**, *125*, 12414.
[27] T. C. Alex, A. J. Kailath, R. Kumar, *Metall. Mater. Trans. B Process Metall. Mater. Process. Sci.* **2020**, *51*, 443.
[28] X. Zhang, P. L. Huestis, C. I. Pearce, J. Z. Hu, K. Page, L. M. Anovitz, A. B. Aleksandrov, M. P. Prange, S. Kerisit, M. E. Bowden, W. Cui, Z. Wang, N. R. Jaegers, T. R. Graham, M. Dembowski, H. W. Wang, J. Liu, A. T. N'Diaye, M. Bleuel, D. F. R. Mildner, T. M. Orlando, G. A. Kimmel, J. A. La Verne, S. B. Clark, K. M. Rosso, *ACS Appl. Nano Mater.* **2018**, *1*, 7115.
[29] G. Monet, E. Paineau, Z. Chai, M. S. Amara, A. Orecchini, M. Jimenéz-Ruiz, A. Ruiz-Caridad, L. Fine, S. Rouzière, L. M. Liu, G. Teobaldi, S. Rols, P. Launois, *Nanoscale Adv.* **2020**, *2*, 1869.
[30] E. Paineau, P. Launois, *Crystals* **2020**, *10*, 1.
[31] Z. Wang, J. Gong, J. Ma, J. Xu, *RSC Adv.* **2014**, *4*, 14708.
[32] R. R. Iyengar, D. N. Sathyanarayana, C. C. Patel, *J. Inorg. Nucl. Chem.* **1972**, *34*, 1088.
[33] N. Chaudhari, L. Mandal, O. Game, S. Warule, D. Phase, S. Jadkar, S. Ogale, *ACS Appl. Mater. Interfaces* **2015**, *7*, 17671.
[34] J. Ning, K. Men, G. Xiao, L. Zhao, L. Wang, B. Liu, B. Zou, *J. Colloid Interface Sci.* **2010**, *347*, 172.
[35] P. Makuła, M. Pacia, W. Macyk, *J. Phys. Chem. Lett.* **2018**, *9*, 6814.
[36] D. Chen, Z. Liu, *ACS Sustain. Chem. Eng.* **2018**, *6*, 12328.
[37] S. Ratha, A. J. Simbeck, D. J. Late, S. K. Nayak, C. S. Rout, *Appl. Phys. Lett.* **2014**, *105*.
[38] J. Park, J. Lee, S. Chang, T. Park, B. Han, W. H. Jin, W. Yi, *Bull. Korean Chem. Soc.* **2008**, *29*, 1048.
[39] S. Jatav, J. Liu, M. Herber, E. H. Hill, *ACS Appl. Mater. Interfaces* **2021**, *13*, 18713.
[40] J. Liu, S. Jatav, P. Wessel, E. H. Hill, *J. Phys. Chem. C* **2022**, *126*, 4975.
[41] J. Liu, S. Jatav, M. Herber, E. H. Hill, *Langmuir* **2021**, *37*, 4727.
[42] S. Jatav, K. P. Furlan, J. Liu, E. H. Hill, *ACS Appl. Mater. Interfaces* **2020**, *12*, 19813.
[43] M. S. Amara, E. Paineau, M. Bacia-Verloop, M. E. M. Krapf, P. Davidson, L. Belloni, C. Levard, J. Rose, P. Launois, A. Thill, *Chem. Commun.* **2013**, *49*, 11284.

Chapter 7

Epilogue and Outlook

7.1 Summary

The different clay-semiconductor composites examined in this thesis demonstrates that clays can act as suitable substrates for synthesizing high performance functional hybrids for wastewater remediation. Interestingly, not only did clays improve the catalytic and photocatalytic performance of MoS_2 and In_2S_3, in the composites of Bi_2MoO_6 with laponite and LDH, Bi_2MoO_6 growth improved the adsorption capacity of these clays. Interestingly, these improvements in the performance of the semiconductor-clay hybrids were contingent upon the organic modification of the clays prior to the reaction. This in-turn indicates the criticality of surfactants for achieving the optimum templating of the semiconductor growth during the hydrothermal reaction.

In addition to improving the (photo)catalytic performance, these clays affected the semiconductor crystal growth in two ways: by confining the crystal growth (seen in MoS_2 and In_2S_3) or by altering the usual crystal growth direction as seen in the case of Laponite-Bi_2MoO_6 composites. In laponite-MoS_2 layered nanohybrids, since MoS_2 growth was confined to the interlayer spacing of laponite particles, this reduction in size increased the number of catalytic edge sites on MoS_2 and resulted in improving the catalytic degradation of dyes. In addition to enhanced catalytic activity, these laponite-MoS_2 hybrids also showed improved dispersibility and stability in aqueous medium compared to pristine MoS_2. Hence, the clay, laponite was not only able to confine and isolate MoS_2 monolayer growth, but also able to provide aqueous stability and dispersibility to these hybrids. The sandwich structure of these hybrids proposed in chapter 2 ([110]) was supported by the X-ray scattering and electron microscopy studies. However, the presence of isolated monolayers of MoS_2 in the hybrids was most spectacularly manifested in the observation of photoluminescence from these hybrid (Fig 7.1), since photoluminescence is only observed for monolayer MoS_2.[72]

The In_2S_3 growth on surfactant-modified imogolite resulted in enhancing the photocatalytic performance of these composites, just like previously reported laponite-In_2S_3 nanohybrids.[111] Although, the reduced size of In_2S_3 in imogolite-In_2S_3 nanohybrids increased the bandgap by 14%, it did not hinder the photocatalytic performance. Moreover, the formation of interface between the p-type imogolite nanotubes and In_2S_3 elicited a negative photocurrent response, which was not observed in the individual constituent materials.

In clay-Bi_2MoO_6 hybrids, the carefully controlled growth of Bi_2MoO_6 on surfactant-modified laponite and CoAl layered double hydroxide (LDH) resulted in the formation of photocatalytic hybrids with enhanced adsorptivity compared to only surfactant-modified clays.[112, 113] For laponite-Bi_2MoO_6 hybrids, the emergence of enhanced sorption capacity was concomitant with a change in the crystal growth habit of Bi_2MoO_6. The surfactant-modified laponite enabled a change in the crystal growth direction from [100] to [010] direction. This resulted in the preponderance of 100-facet dominated Bi_2MoO_6 in the laponite-Bi_2MoO_6 photocatalytic hybrids. The sorption enhancement and faceting were observed only in the cases when [Bi]:[laponite] was in the range of 0.16–0.63 mM:mg/mL. Also, these hybrids exhibited near-spontaneous adsorption of dye which prompted their use in a filtration setup. In a follow-up study, we reported the filtration of dye contaminated water by these laponite-Bi_2MoO_6 particles deposited onto a cellulose acetate membrane filters and found that a thin cross-linked shell of polymer blend of butyl acrylate and styrene can improve their dye adsorption capacity further.[114]

Furthermore, by switching from a cationic laponite to an anionic CoAl LDH substrate, LDH-Bi_2MoO_6 photocatalytic sorbent composites were obtained, which were proficient at selective adsorption of anionic species (chapter-4).[113] However, in contrast to laponite-Bi_2MoO_6, no drastic change in the growth direction of Bi_2MoO_6 was observed in these LDH-Bi_2MoO_6 composites . The optical properties of the LDH-Bi_2MoO_6 hybrids were sensitive to the reaction pH, in contrast to their laponite counterparts; where broadband light absorption could be achieved in the former at reaction pH ~6. Where the dye sorption behavior is concerned, both the clay-Bi_2MoO_6 hybrids showed enhancements compared to their surfactant-modified clay templates. Also, both the hybrids showed peak adsorption performance at the [Bi]:[clay] of 0.63 mmol:g. However, they differed substantially where the kinetics of dye adsorption were concerned. The laponite-Bi_2MoO_6 showed near-instantaneous adsorption of entire dye in the solution, whereas for LDH-Bi_2MoO_6 hybrids that was not the case. This might be due the much higher surface area of laponite compared to the LDH. And the reuse of these particles can be achieved by photocatalytic degradation of the adsorbed dye.

It is also to be noted that since the synthesis of these hybrids was carried out in aqueous media without any harmful solvents, the hydrothermal method provides an environmentally benign approach for obtaining high performance clay-semiconductor hybrids. In addition, incorporating clays reduces the amount of semiconductor required in the composite; therefore, allowing for less use of metallic precursors and rendering the production of such composites cheap.

7.2 Future Research Avenues

The work covered in this dissertation gave rise to many interesting lines of research. In this section some of those lines of research are emphasized and based on that some recommendations for future research are pointed out below.

Piezoresponse of Laponite-MoS_2 Layered Particles

One of the interesting properties associated with MoS_2 is the emergence of photoluminescence (PL) in the monolayer limit.[72] In this thesis the presence of monolayer/few-layers MoS_2 separated by laponite particles was supported by XRD and HRTEM in [110]. Additionally, the presence of isolated MoS_2 mono-layers in these nanohybrids was further confirmed by PL spectroscopy (Fig 7.1). Another interesting phenomenon associated with few/mono-layers of MoS_2 is the emergence of piezoelectricity.[115] Piezoelectricity refers to the generation of voltage under the application of mechanical stress. This has been studied previously by operating atomic force microscopy in the piezo force mode. Hence, it would be interesting to investigate piezoelectricity in these laponite-MoS_2 layered nanohybrids and study their efficacy as transducers or mechanical sensors.

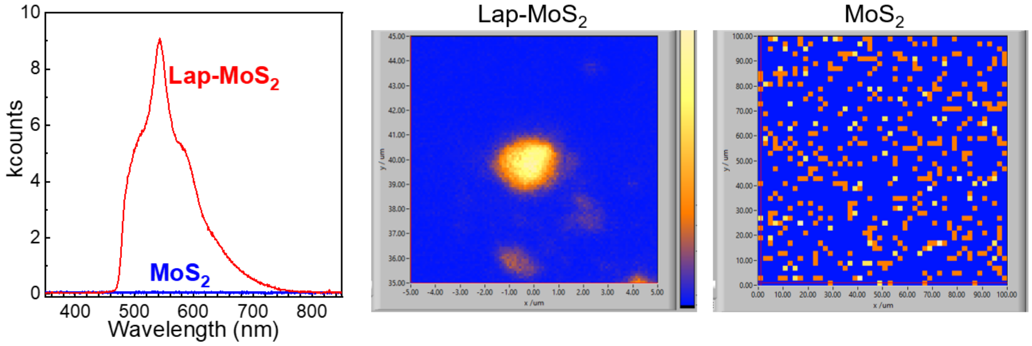

Figure 7.1: Left, photoluminescence spectra of laponite-MoS_2 and prisine MoS_2. Middle, confocal PL image of laponite-MoS_2 and right, confocal PL image of MoS_2.

Sorbent Photocatalytic Imogolite-In_2S_3 Hybrids

The imogolite-In_2S_3 nanohybrids reported in Chapter 6 [116] were explored further. Previously, in [116], only the surfactant DTAB was used during the synthesis of imogolite-In_2S_3, which showed enhanced photocatalytic activity compared to pristine In_2S_3. These subsequent experiments focused on the effect of surfactant chain-length used during the synthesis on the photocatalytic performance of imogolite-In_2S_3 nanohybrids. The surfactants used were C_8TAB (OTAB), C_{12}TAB (DTAB) and C_{16}TAB (CTAB). The hybrids prepared with C_{12}TAB performed slightly better than the ones prepared using C_8TAB during the photocatalytic degradation experiments. Interestingly, the imogolite-In_2S_3 hybrids synthesized with C_{16}TAB showed enhanced adsorption of methyl orange (Fig. 7.2b). Henceforth, the focus of the investigation was narrowed onto these the imogolite-In_2S_3 hybrids synthesized with C_{16}TAB. Further studies revealed that the adsorption performance of these hybrids was sensitive to the [CTAB] used during the synthesis of these hybrids (Fig. 7.2b). The bulk of future work will focus on the structural and morphological characterization of these CTAB-based imogolite-In_2S_3 hybrids. In addition, the performance stability of these hybrids will be assessed by the adsorption-photocatalytic cyclic reuse of these hybrid particles.

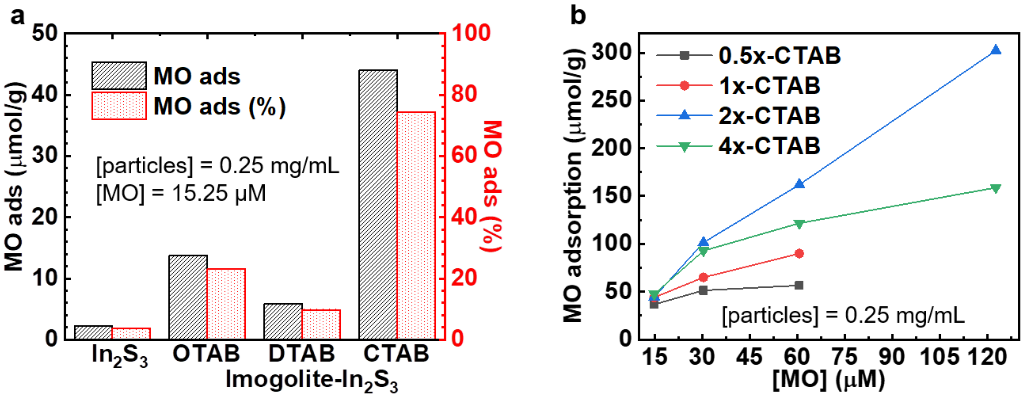

Figure 7.2: (a) Methyl orange (MO) adsorption by imogolite-In_2S_3 hybrids prepared using different surfactants. (b) Adsorption isotherms of the imogolite-In_2S_3 hybrids prepared at different [CTAB]; 1x = 0.26 mM.

Incorporating 2D Materials in Laponite-Bi_2MoO_6 Filtration Membranes

A more practical and efficient way to use photocatalytic sorbent hybrids would be to incorporate them onto a membrane substrate. Previously, we accomplished this using surface modified laponite-Bi_2MoO_6 particles deposited on cellulose acetate membranes.[114] Although these hybrid particles modified membranes were effective at filtering dyes out of their solution and could be reused by photocatalytically degrading the adsorbed dye, hence providing a facile means to defoul these membranes. However, the flow rate achieved through these was very low (2mL/min) to be of any practical significance. Incorporating 2D materials like g-C_3N_4 in the design of the aforementioned filtration membranes might be helpful toward attaining high flow-rate water filtration membranes. In addition, g-C_3N_4 nanosheets can be functionalized readily, which allows for tuning their interlayer distance.[117] This strategy can be exploited to tailor channel dimensions or pore size in these hybrid water filtration membranes and hence provide a means to control flow-rate.

Bibliography

[1] David Halliday, Robert Resnick, and Jearl Walker. *Fundamentals of Physics*. John Wiley & Sons, 2013.

[2] Nicholas Georgescu-Roegen. The Entropy Law and the Economic Problem. *Valuing the Earth: Economics, Ecology, Ethics*, pages 75–88, 1993.

[3] François Jarrige and Thomas Le Roux. *The Contamination of the Earth: A History of Pollutions in the Industrial Age*. MIT Press, 2020.

[4] Herman E Daly. On Economics as a Life Science. *Journal of Political Economy*, 76(3):392–406, 1968.

[5] Johan Rockström, Will Steffen, Kevin Noone, Åsa Persson, F Stuart Chapin III, Eric Lambin, Timothy M Lenton, Marten Scheffer, Carl Folke, Hans Joachim Schellnhuber, et al. Planetary Boundaries: Exploring the Safe Operating Space for Humanity. *Ecology and Society*, 14(2), 2009.

[6] Richard B Alley. *The Two-Mile Time Machine: Ice Cores, Abrupt Climate Change, and Our Future*. Princeton University Press, 2014.

[7] Andrew Y Glikson and C Battista. *The Event Horizon: Homo Prometheus and the Climate Catastrophe*. Springer, 2021.

[8] Linn Persson, Bethanie M. Carney Almroth, Christopher D. Collins, Sarah Cornell, Cynthia A. de Wit, Miriam L Diamond, Peter Fantke, Martin Hassellöv, Matthew MacLeod, Morten W. Ryberg, et al. Outside the Safe Operating Space of the Planetary Boundary for Novel Entities. *Environmental Science & Technology*, 56(3):1510–1521, 2022.

[9] Zhanyun Wang, Glen W. Walker, Derek C.G. Muir, and Kakuko Nagatani-Yoshida. Toward a Global Understanding of Chemical Pollution: A First Comprehensive Analysis of National and Regional Chemical Inventories. *Environmental Science & Technology*, 54(5):2575–2584, 2020.

[10] Julian Cribb. *Surviving the 21st Century: Humanity's Ten Great Challenges and How We Can Overcome Them.* Springer, 2016.

[11] Alex R Aves, Laura E Revell, Sally Gaw, Helena Ruffell, Alex Schuddeboom, Ngaire E Wotherspoon, Michelle LaRue, and Adrian J McDonald. First Evidence of Microplastics in Antarctic Snow. *The Cryosphere*, 16(6):2127–2145, 2022.

[12] Imogen E. Napper, Bede F.R. Davies, Heather Clifford, Sandra Elvin, Heather J. Koldewey, Paul A. Mayewski, Kimberley R. Miner, Mariusz Potocki, Aurora C. Elmore, Ananta P. Gajurel, et al. Reaching New Heights in Plastic Pollution–Preliminary Findings of Microplastics on Mount Everest. *One Earth*, 3(5):621–630, 2020.

[13] Sanae Chiba, Hideaki Saito, Ruth Fletcher, Takayuki Yogi, Makino Kayo, Shin Miyagi, Moritaka Ogido, and Katsunori Fujikura. Human Footprint in the Abyss: 30 Year Records of Deep-Sea Plastic Debris. *Marine Policy*, 96:204–212, 2018.

[14] Ellen MacArthur Foundation. The New Plastics Economy: Rethinking the Future of Plastics & Catalysing Action, 2017.

[15] Manon de Pierpont. Drowning in Plastic-Noyés sous le Plastique, 2020.

[16] Karl Gruber. Cleaning Up Our Future Health. *Nature*, 555(7695):S20–S22, 2018.

[17] Ian T. Cousins, Jana H. Johansson, Matthew E. Salter, Bo Sha, and Martin Scheringer. Outside the Safe Operating Space of a New Planetary Boundary for Per-and Polyfluoroalkyl Substances (PFAS). *Environmental Science & Technology*, 56(16):11172–11179, 2022.

[18] Evanthia Diamanti-Kandarakis, Jean-Pierre Bourguignon, Linda C Giudice, Russ Hauser, Gail S Prins, Ana M Soto, R Thomas Zoeller,

and Andrea C Gore. Endocrine-Disrupting Chemicals: An Endocrine Society Scientific Statement. *Endocrine Reviews*, 30(4):293–342, 2009.

[19] Corey J.A. Bradshaw, Paul R. Ehrlich, Andrew Beattie, Gerardo Ceballos, Eileen Crist, Joan Diamond, Rodolfo Dirzo, Anne H. Ehrlich, John Harte, Mary Ellen Harte, et al. Underestimating the Challenges of Avoiding a Ghastly Future. *Frontiers in Conservation Science*, 1:1–9, 2021.

[20] Line Mathiesen, Tina Buerki-Thurnherr, Jana Pastuschek, Leonie Aengenheister, and Lisbeth E Knudsen. Fetal Exposure to Environmental Chemicals; Insights from Placental Perfusion Studies. *Placenta*, 106:58–66, 2021.

[21] Sani Rachman Soleman, Tomoko Fujitani, Yukiko Fujii, and Kouji H Harada. Levels of Octachlorostyrene in Mothers' Milk and Potential Exposure Among Infants in Sendai City, Japan 2012. *International Journal of Environmental Research and Public Health*, 17(9):3064, 2020.

[22] Liqin Hu, Dan Luo, Limei Wang, Meng Yu, Shizhen Zhao, Youjie Wang, Surong Mei, and Gan Zhang. Levels and Profiles of Persistent Organic Pollutants in Breast Milk in China and Their Potential Health Risks to Breastfed Infants: A Review. *Science of the Total Environment*, 753:142028, 2021.

[23] Martin van den Berg, Karin Kypke, Alexander Kotz, Angelika Tritscher, Seoung Yong Lee, Katarina Magulova, Heidelore Fiedler, and Rainer Malisch. WHO/UNEP Global Surveys of PCDDs, PCDFs, PCBs and DDTs in Human Milk and Benefit–Risk Evaluation of Breastfeeding. *Archives of Toxicology*, 91:83–96, 2017.

[24] Jon D. Onstot, Randall E. Ayling, and John S. Stanley. Characterization of HRGC/MS Unidentified Peaks from the Analysis of Human Adipose Tissue. Volume 1: technical approach. Washington (DC): US Environmental Protection Agency Office of Toxic Substances (560/6–87–002a), 1987.

[25] John Elkington. *The Poisoned Womb: Human Reproduction in a Polluted World*. Penguin Group USA, 1986.

[26] Enid Gilbert-Barness. Teratogenic Causes of Malformations. *Annals of Clinical & Laboratory Science*, 40(2):99–114, 2010.

[27] Theo Colburn, Dianne Dumanoski, and John Peterson Myers. *Our Stolen Future: Are We Threatening our Fertility, Intelligence, and Survival? A Scientific Detective Story.* Plume, 1997.

[28] Shanna H. Swan and Stacey Colino. *Count Down: How Our Modern World is Threatening Sperm Counts, Altering Male and Female Reproductive Development, and Imperiling the Future of the Human Race.* Simon and Schuster, 2022.

[29] Sungpyo Kim and Diana S. Aga. Potential Ecological and Human Health Impacts of Antibiotics and Antibiotic-Resistant Bacteria from Wastewater Treatment Plants. *Journal of Toxicology and Environmental Health, Part B*, 10(8):559–573, 2007.

[30] Zeqing Long, Qiangang Li, Ting Wei, Guangming Zhang, and Zhijun Ren. Historical Development and Prospects of Photocatalysts for Pollutant Removal in Water. *Journal of Hazardous Materials*, 395:122599, 2020.

[31] M. Ali Omar. *Elementary Solid State Physics: Principles and Applications.* Pearson Education India, 1975.

[32] Yen-Ju Lai and Duu-Jong Lee. Pollutant Degradation with Mediator Z-scheme Heterojunction Photocatalyst in Water: A Review. *Chemosphere*, 282:131059, 2021.

[33] Heinrich Dieter Müller and Friedrich Steinbach. Decomposition of Isopropyl Alcohol Photosensitized by Zinc Oxide. *Nature*, 225(5234):728–729, 1970.

[34] John H Carey, John Lawrence, and Helle M Tosine. Photodechlorination of PCB's in the Presence of Titanium Dioxide in Aqueous Suspensions. *Bulletin of Environmental Contamination and Toxicology*, 16:697–701, 1976.

[35] Vered Heleg and Itamar Willner. Photocatalysed CO_2-Fixation to Formate and H_2-Evolution by Eosin-modified Pd–TiO_2 Powders. *Journal*

of the Chemical Society, Chemical Communications, (18):2113–2114, 1994.

[36] Roland Marschall and Lianzhou Wang. Non-Metal Doping of Transition Metal Oxides for Visible-Light Photocatalysis. *Catalysis Today*, 225:111–135, 2014.

[37] Mohammad Reza Delsouz Khaki, Mohammad Saleh Shafeeyan, Abdul Aziz Abdul Raman, and Wan Mohd Ashri Wan Daud. Application of Doped Photocatalysts for Organic Pollutant Degradation-A Review. *Journal of Environmental Management*, 198:78–94, 2017.

[38] Yu Xiaodan, Wu Qingyin, Jiang Shicheng, and Guo Yihang. Nanoscale ZnS/TiO_2 Composites: Preparation, Characterization, and Visible-Light Photocatalytic Activity. *Materials Characterization*, 57(4-5):333–341, 2006.

[39] Ruibin Jiang, Benxia Li, Caihong Fang, and Jianfang Wang. Metal/Semiconductor Hybrid Nanostructures for Plasmon-Enhanced Applications. *Advanced Materials*, 26(31):5274–5309, 2014.

[40] Cheng Hu, Na Tian, Yihe Zhang, and Hongwei Huang. Facet-Selective Charge Separation in Two-Dimensional Bismuth-based Photocatalysts. *Catalysis Science & Technology*, 11(11):3659–3675, 2021.

[41] Cui Ying Toe, Marlene Lamers, Thomas Dittrich, Hassan A Tahini, Sean C Smith, Jason Scott, Rose Amal, Roel van de Krol, Fatwa F Abdi, and Yun Hau Ng. Facet-Dependent Carrier Dynamics of Cuprous Oxide Regulating the Photocatalytic Hydrogen Generation. *Materials Advances*, 3(4):2200–2212, 2022.

[42] Mu Xiao, Zhiliang Wang, Miaoqiang Lyu, Bin Luo, Songcan Wang, Gang Liu, Hui-Ming Cheng, and Lianzhou Wang. Hollow Nanostructures for Photocatalysis: Advantages and Challenges. *Advanced Materials*, 31(38):1801369, 2019.

[43] Mohd. A. Khan, Muhammad A. Nadeem, and Hicham Idriss. Ferroelectric Polarization Effect on Surface Chemistry and Photo-catalytic Activity: A Review. *Surface Science Reports*, 71(1):1–31, 2016.

[44] Qiuhui Zhu, Ke Zhang, Danqing Li, Nan Li, Jingkun Xu, Detlef W Bahnemann, and Chuanyi Wang. Polarization-Enhanced Photocatalytic Activity in Non-Centrosymmetric Materials based Photocatalysis: A Review. *Chemical Engineering Journal*, 426:131681, 2021.

[45] Faiza Bergaya and Gerhard Lagaly. *Handbook of Clay Science*. Newnes, 2013.

[46] Saeed Farrokhpay, Bulelwa Ndlovu, and Dee Bradshaw. Behaviour of Swelling Clays versus Non-Swelling Clays in Flotation. *Minerals Engineering*, 96:59–66, 2016.

[47] Barbara S. Neumann. Improvements in or Relating to Synthetic Clay-like Minerals. *British Patent Application No*, 1054111, 1962.

[48] Kirill Shafran, Christopher Jeans, Simon J. Kemp, and Kevin Murphy. Dr Barbara S. Neumann: Clay Scientist and Industrial Pioneer; Creator of Laponite®. *Clay Minerals*, 55(3):256–260, 2020.

[49] Mark Kroon, Willem L. Vos, and Gerard H. Wegdam. Structure and Formation of a Gel of Colloidal Disks. *Physical Review E*, 57(2):1962, 1998.

[50] C. Rodrigo Pierozan, Abdurrahman Almikati, Gregorio Silva Araujo, and G. Jorge Zornberg. Optical and Physical Properties of Laponite for Use as Clay Surrogate in Geotechnical Models. *Geotechnical Testing Journal*, 45:79–100, 2022.

[51] Hendrik Van Olphen. *An Introduction to Clay Colloid Chemistry: For Clay Technologists, Geologists, and Soil Scientists*. 1977.

[52] Santosh L. Tawari, Donald L. Koch, and Claude Cohen. Electrical Double-Layer Effects on the Brownian Diffusivity and Aggregation Rate of Laponite Clay Particles. *Journal of Colloid and Interface Science*, 240(1):54–66, 2001.

[53] Khushboo Suman and Yogesh M Joshi. Microstructure and Soft Glassy Dynamics of an Aqueous Laponite Dispersion. *Langmuir*, 34(44):13079–13103, 2018.

[54] Dudley W Thompson and James T Butterworth. The Nature of Laponite and its Aqueous Dispersions. *Journal of Colloid and Interface Science*, 151(1):236–243, 1992.

[55] Nóra Hegyesi, Richárd T. Vad, and Béla Pukánszky. Determination of the Specific Surface Area of Layered Silicates by Methylene Blue Adsorption: The Role of Structure, pH and Layer Charge. *Applied Clay Science*, 146:50–55, 2017.

[56] Fabio Carniato, Giorgio Gatti, and Chiara Bisio. An Overview of the Recent Synthesis and Functionalization Methods of Saponite Clay. *New Journal of Chemistry*, 44(24):9969–9980, 2020.

[57] Paul A. Wheeler, Junzuo Wang, James Baker, and Lon J. Mathias. Synthesis and Characterization of Covalently Functionalized Laponite Clay. *Chemistry of materials*, 17(11):3012–3018, 2005.

[58] Rafael Celis, M. Carmen Hermosin, and Juan Cornejo. Heavy Metal Adsorption by Functionalized Clays. *Environmental science & technology*, 34(21):4593–4599, 2000.

[59] W.T. Tsai, C.W. Lai, and K.J. Hsien. Effect of Particle Size of Activated Clay on the Adsorption of Paraquat from Aqueous Solution. *Journal of Colloid and Interface Science*, 263(1):29–34, 2003.

[60] Robert A. Schoonheydt, Tom Pinnavaia, Gerhard Lagaly, and Nick Gangas. Pillared clays and pillared layered solids. *Pure and Applied Chemistry*, 71(12):2367–2371, 1999.

[61] C.T. Cowan and D. White. Adsorption by Organo-Clay Complexes. In *Clays and Clay Minerals*, pages 459–467. Elsevier, 1962.

[62] Max M. Mortland, Sun Shaobai, and Stephen A. Boyd. Clay-Organic Complexes as Adsorbents for Phenol and Chlorophenols. *Clays and Clay minerals*, 34:581–585, 1986.

[63] Stephen A Boyd, Sun Shaobai, Jiunn-Fwu Lee, and Max M Mortland. Pentachlorophenol Sorption by Organo-Clays. *Clays and Clay minerals*, 36:125–130, 1988.

[64] Jiunn-Fwu Lee, Max M. Mortland, Cary T. Chiou, Daniel E. Kile, and Stephen A. Boyd. Adsorption of Benzene, Toluene, and Xylene by Two Tetramethylammonium-Smectites having Different Charge Densities. *Clays and Clay Minerals*, 38:113–120, 1990.

[65] WF Jaynes and Stephen A. Boyd. Clay Mineral Type and Organic Compound Sorption by Hexadecyltrimethlyammonium-Exchanged Clays. *Soil Science Society of America Journal*, 55(1):43–48, 1991.

[66] Stephen A. Boyd, Max M. Mortland, and Cary T. Chiou. Sorption Characteristics of Organic Compounds on Hexadecyltrimethylammonium-Smectite. *Soil Science Society of America Journal*, 52(3):652–657, 1988.

[67] Shmuel Yariv and Harold Cross. Introduction to Organo-Clay Complexes and Interactions. In *Organo-Clay Complexes and Interactions*, pages 51–124. CRC Press, 2001.

[68] W.F. Jaynes and George F. Vance. BTEX Sorption by Organo-Clays: Cosorptive Enhancement and Equivalence of Interlayer Complexes. *Soil Science Society of America Journal*, 60(6):1742–1749, 1996.

[69] Zijing Xia, Wen Chen, Rahul Shevate, Yuqin Wang, Feng Gao, Di Wang, Omar A. Kazi, Anil U. Mane, Sang Soo Lee, Jeffrey W. Elam, et al. Tunable Ion Transport with Freestanding Vermiculite Membranes. *ACS Nano*, 16(11):18266–18273, 2022.

[70] Kaline Pagnan Furlan, José Daniel Biasoli de Mello, and Aloisio Nelmo Klein. Self-Lubricating Composites Containing MoS_2: A Review. *Tribology International*, 120:280–298, 2018.

[71] Kin Fai Mak, Changgu Lee, James Hone, Jie Shan, and Tony F Heinz. Atomically Thin MoS_2: A New Direct-Gap Semiconductor. *Physical Review Letters*, 105(13):136805, 2010.

[72] Branimir Radisavljevic, Aleksandra Radenovic, Jacopo Brivio, Valentina Giacometti, and Andras Kis. Single-layer MoS_2 Transistors. *Nature Nanotechnology*, 6(3):147–150, 2011.

[73] Berit Hinnemann, Poul Georg Moses, Jacob Bonde, Kristina P. Jørgensen, Jane H. Nielsen, Sebastian Horch, Ib Chorkendorff, and

Jens K. Nørskov. Biomimetic Hydrogen Evolution: MoS_2 Nanoparticles as Catalyst for Hydrogen Evolution. *Journal of the American Chemical Society*, 127(15):5308–5309, 2005.

[74] Thomas F. Jaramillo, Kristina P. Jørgensen, Jacob Bonde, Jane H. Nielsen, Sebastian Horch, and Ib Chorkendorff. Identification of Active Edge Sites for Electrochemical H_2 evolution from MoS_2 Nanocatalysts. *Science*, 317(5834):100–102, 2007.

[75] Desheng Kong, Haotian Wang, Judy J. Cha, Mauro Pasta, Kristie J. Koski, Jie Yao, and Yi Cui. Synthesis of MoS_2 and $MoSe_2$ Films with Vertically Aligned Layers. *Nano Letters*, 13(3):1341–1347, 2013.

[76] Laura Guardia, Juan I. Paredes, Jose M Munuera, Silvia Villar-Rodil, Miguel Ayan-Varela, Amelia Martinez-Alonso, and Juan MD Tascón. Chemically Exfoliated MoS_2 Nanosheets as an Efficient Catalyst for Reduction Reactions in the Aqueous Phase. *ACS Applied Materials & Interfaces*, 6(23):21702–21710, 2014.

[77] Kang Peng, Liangjie Fu, Jing Ouyang, and Huaming Yang. Emerging Parallel Dual 2D Composites: Natural Clay Mineral Hybridizing MoS_2 and Interfacial Structure. *Advanced Functional Materials*, 26(16):2666–2675, 2016.

[78] Kang Peng, Liangjie Fu, Huaming Yang, Jing Ouyang, and Aidong Tang. Hierarchical MoS_2 Intercalated Clay Hybrid Nanosheets with Enhanced Catalytic Activity. *Nano Research*, 10(2):570–583, 2017.

[79] L.T. Sim, C.K. Lee, and A.R. West. High Oxide Ion Conductivity in Bi_2MoO_6 Oxidation Catalyst. *Journal of Materials Chemistry*, 12(1):17–19, 2002.

[80] James L. Callahan, Robert K. Grasselli, Ernest C. Milberger, and H. Arthur Strecker. Oxidation and Ammoxidation of Propylene over Bismuth Molybdate Catalyst. *Industrial & Engineering Chemistry Product Research and Development*, 9(2):134–142, 1970.

[81] Yushan Dong, Shuming Dong, Bin Liu, Chenghao Yu, Jing Liu, Dan Yang, Piaoping Yang, and Jun Lin. 2D Piezoelectric Bi_2MoO_6 Nanoribbons for GSH-Enhanced Sonodynamic Therapy. *Advanced Materials*, 33(51):2106838, 2021.

[82] Baskar Senthilkumar, Ramakrishnan Kalai Selvan, Leonid Vasylechko, and Manickam Minakshi. Synthesis, Crystal Structure and Pseudocapacitor Electrode Properties of γ-Bi_2MoO_6 Nanoplates. *Solid State Sciences*, 35:18–27, 2014.

[83] Kunda J. Samdani, Jeong Hwa Park, Dong Woo Joh, and Kang Taek Lee. Self-Assembled Bi_2MoO_6 Nanopetal Array on Carbon Spheres toward Enhanced Supercapacitor Performance. *ACS Sustainable Chemistry & Engineering*, 6(12):16702–16712, 2018.

[84] Aniruddha K. Kulkarni, Mohaseen S. Tamboli, Digambar Y. Nadargi, Yogesh A. Sethi, Sharad S. Suryavanshi, Anil V. Ghule, and Bharat B. Kale. Bismuth Molybdate (α-$Bi_2Mo_3O_{12}$) Nanoplates via Facile Hydrothermal and its Gas Sensing Study. *Journal of Solid State Chemistry*, 281:121043, 2020.

[85] Xuelian Wu, Yun Hau Ng, Wibawa H. Saputera, Xiaoming Wen, Yi Du, Shi Xue Dou, Rose Amal, and Jason Scott. The Dependence of Bi_2MoO_6 Photocatalytic Water Oxidation Capability on Crystal Facet Engineering. *ChemPhotoChem*, 3(12):1246–1253, 2019.

[86] Shuguan Li, Liqi Bai, Ning Ji, Shixin Yu, Sen Lin, Na Tian, and Hongwei Huang. Ferroelectric Polarization and Thin-Layered Structure Synergistically Promoting CO_2 Photoreduction of Bi_2MoO_6. *Journal of Materials Chemistry A*, 8(18):9268–9277, 2020.

[87] Tammanoon Chankhanittha, Varanya Somaudon, Jidapa Watcharakitti, Voranan Piyavarakorn, and Suwat Nanan. Performance of Solvothermally Grown Bi_2MoO_6 Photocatalyst toward Degradation of Organic Azo Dyes and Fluoroquinolone Antibiotics. *Materials Letters*, 258:126764, 2020.

[88] Hanbo Yu, Longbo Jiang, Hou Wang, Binbin Huang, Xingzhong Yuan, Jinhui Huang, Jin Zhang, and Guangming Zeng. Modulation of Bi_2MoO_6-Based Materials for Photocatalytic Water Splitting and Environmental Application: A Critical Review. *Small*, 15(23):1901008, 2019.

[89] Rohit Kumar, Anita Sudhaik, Pankaj Raizada, Ahmad Hosseini-Bandegharaei, Vijay Kumar Thakur, Adesh Saini, Vipin Saini, and

Pardeep Singh. An Overview on Bismuth Molybdate based Photocatalytic Systems: Controlled Morphology and Enhancement Strategies for Photocatalytic Water Purification. *Journal of Environmental Chemical Engineering*, 8(5):104291, 2020.

[90] Yongxing Xing, Rongqing Cheng, Haipeng Li, Zhiliang Liu, and Chunfang Du. Mannitol-Assisted Synthesis of Ultrathin Bi_2MoO_6 Architectures: Excellent Selective Adsorption and Photocatalytic Performance. *Journal of Nanoparticle Research*, 21(2):1–14, 2019.

[91] A. Martinez-de La Cruz and S. Obregón Alfaro. Synthesis and Characterization of γ-Bi_2MoO_6 Prepared by Co-Precipitation: Photoassisted Degradation of Organic Dyes under Vis-Irradiation. *Journal of Molecular Catalysis A: Chemical*, 320(1-2):85–91, 2010.

[92] Xiao Xu, Xing Ding, Xianglong Yang, Pei Wang, Shu Li, Zhexue Lu, and Hao Chen. Oxygen Vacancy Boosted Photocatalytic Decomposition of Ciprofloxacin over Bi_2MoO_6: Oxygen Vacancy Engineering, Biotoxicity Evaluation and Mechanism Study. *Journal of Hazardous Materials*, 364:691–699, 2019.

[93] Zan Dai, Fan Qin, Huiping Zhao, Jie Ding, Yunling Liu, and Rong Chen. Crystal Defect Engineering of Aurivillius Bi_2MoO_6 by Ce Doping for Increased Reactive Species Production in Photocatalysis. *ACS Catalysis*, 6(5):3180–3192, 2016.

[94] Chunquan Li, Zhiming Sun, Wanzhong Zhang, Caihong Yu, and Shuilin Zheng. Highly Efficient g-C_3N_4/TiO_2/Kaolinite Composite with Novel Three-Dimensional Structure and Enhanced Visible Light Responding Ability towards Ciprofloxacin and S. aureus. *Applied Catalysis B: Environmental*, 220:272–282, 2018.

[95] Ping Chen, Qianxin Zhang, Yuehan Su, Lingzhi Shen, Fengliang Wang, Haijin Liu, Yang Liu, Zongwei Cai, Wenying Lv, and Guoguang Liu. Accelerated Photocatalytic Degradation of Diclofenac by a Novel CQDs/BiOCOOH Hybrid Material Under Visible-Light Irradiation: Dechloridation, Detoxicity, and a New Superoxide Radical Model Study. *Chemical Engineering Journal*, 332:737–748, 2018.

[96] Jialiang Liang, Fuyang Liu, Jun Deng, Mian Li, and Meiping Tong. Efficient Bacterial Inactivation with Z-scheme AgI/Bi_2MoO_6 under Visible Light Irradiation. *Water Research*, 123:632–641, 2017.

[97] G.A. Steigmann, H.H. Sutherland, and J. Goodyear. The Crystal Structure of β-In_2S_3. *Acta Crystallographica*, 19(6):967–971, 1965.

[98] Shu-Hong Yu, Lei Shu, Yong-Sheng Wu, Jian Yang, Yi Xie, and Yi-Tai Qian. Organothermal Synthesis and Characterization of Nanocrystalline ß-Indium Sulfide. *Journal of the American Ceramic Society*, 82(2):457–460, 1999.

[99] Z. Braiek, A. Brayek, M. Ghoul, S. Ben Taieb, M. Gannouni, I. Ben Assaker, A. Souissi, and R. Chtourou. Electrochemical Synthesis of ZnO/In_2S_3 Core–Shell Nanowires for Enhanced Photoelectrochemical Properties. *Journal of Alloys and Compounds*, 653:395–401, 2015.

[100] Wenjuan Huang, Lin Gan, Haotian Yang, Nan Zhou, Renyan Wang, Wanhui Wu, Huiqiao Li, Ying Ma, Haibo Zeng, and Tianyou Zhai. Controlled Synthesis of Ultrathin 2D β-In_2S_3 with Broadband Photoresponse by Chemical Vapor Deposition. *Advanced Functional Materials*, 27(36):1702448, 2017.

[101] Yi Liu, Liyong Du, Kuikun Gu, and Mingzhe Zhang. Effect of Tm Dopant on Luminescence, Photoelectric Properties and Electronic Structure of In_2S_3 Quantum Dots. *Journal of Luminescence*, 217:116775, 2020.

[102] Wei Chen, Jan-Olov Bovin, Alan G Joly, Shaopeng Wang, Fuhai Su, and Guohua Li. Full-Color Emission from In_2S_3 and In_2S_3: Eu^{3+} Nanoparticles. *The Journal of Physical Chemistry B*, 108(32):11927–11934, 2004.

[103] Sebastian Siol, Tara P Dhakal, Ganesh S Gudavalli, Pravakar P Rajbhandari, Clay DeHart, Lauryn L Baranowski, and Andriy Zakutayev. Combinatorial Reactive Sputtering of In_2S_3 as an Alternative Contact Layer for Thin Film Solar Cells. *ACS Applied Materials & Interfaces*, 8(22):14004–14011, 2016.

[104] He Li, Zhihao Yuan, Carla Bittencourt, Xiaojiang Li, Wei Li, Minfang Chen, Wenjiang Li, and Rony Snyders. Anion Exchange Synthesis of

Hollow β-In_2S_3 Nanoparticles: Adsorption and Visible Light Photocatalytic Performances. *Journal of Environmental Chemical Engineering*, 7(1):102910, 2019.

[105] Zhibin Wu, Xingzhong Yuan, Guangming Zeng, Longbo Jiang, Hua Zhong, Yingcong Xie, Hui Wang, Xiaohong Chen, and Hou Wang. Highly Efficient Photocatalytic Activity and Mechanism of Yb^{3+}/Tm^{3+} codoped β-In_2S_3 from Ultraviolet to Near Infrared Light towards Chromium (VI) Reduction and Rhodamine B Oxydative Degradation. *Applied Catalysis B: Environmental*, 225:8–21, 2018.

[106] Cuiling Ai, Dandan Zhou, Qian Wang, Xiangwen Shao, and Yingjie Lei. Optimization of Operating Parameters for Photocatalytic Degradation of Tetracycline using In_2S_3 under Natural Solar Radiation. *Solar Energy*, 113:34–42, 2015.

[107] Jaspal Singh and R.K. Soni. Enhanced Sunlight Driven Photocatalytic Activity of In_2S_3 Nanosheets Functionalized MoS_2 Nanoflowers Heterostructures. *Scientific Reports*, 11(1):15352, 2021.

[108] Haibo Qiu, Shengqiong Fang, Guocheng Huang, and Jinhong Bi. A Novel Application of In_2S_3 for Visible-Light-Driven Photocatalytic Inactivation of Bacteria: Kinetics, Stability, Toxicity and Mechanism. *Environmental Research*, 190:110018, 2020.

[109] Roberta Hofman-Caris and Jan Hofman. *Limitations of Conventional Drinking Water Technologies in Pollutant Removal*, pages 21–51. Springer International Publishing, Cham, 2019.

[110] Sanjay Jatav, Kaline P. Furlan, Junying Liu, and Eric H. Hill. Heterostructured Monolayer MoS_2 Nanoparticles toward Water-Dispersible Catalysts. *ACS Applied Materials & Interfaces*, 12(17):19813–19822, 2020.

[111] Junying Liu, Sanjay Jatav, and Eric H. Hill. Few-Layer In_2S_3 in Laponite Interlayers: A Colloidal Route toward Heterostructured Nanohybrids with Enhanced Photocatalysis. *Chemistry of Materials*, 32(23):10015–10024, 2020.

[112] Sanjay Jatav, Junying Liu, Marcel Herber, and Eric H. Hill. Facet Engineering of Bismuth Molybdate via Confined Growth in a Nanoscale

Template toward Water Remediation. *ACS Applied Materials & Interfaces*, 13(16):18713–18723, 2021.

[113] Sanjay Jatav, Marcel Herber, Hongxiao Xiang, and Eric H. Hill. Layered Double Hydroxide–Bismuth Molybdate Hybrids toward Water Remediation via Selective Adsorption of Anionic Species. *ACS Applied Materials & Interfaces*, 14(46):51921–51930, 2022.

[114] Sanjay Jatav, Marcel Herber, Hongxiao Xiang, and Eric H. Hill. Surface-Encapsulated Bismuth Molybdate-Layered Silicate Hybrids as Sorbents for Photocatalytic Filtration Membranes. *ACS Applied Materials & Interfaces*, 14(20):22790–22798, 2022.

[115] Hanyu Zhu, Yuan Wang, Jun Xiao, Ming Liu, Shaomin Xiong, Zi Jing Wong, Ziliang Ye, Yu Ye, Xiaobo Yin, and Xiang Zhang. Observation of Piezoelectricity in Free-standing Monolayer MoS_2. *Nature Nanotechnology*, 10(2):151–155, 2015.

[116] Sanjay Jatav, Hongxiao Xiang, Marcel Herber, Erwan Paineau, and Eric H. Hill. In_2S_3 Growth Templated by Aluminogermanate Double-Walled Imogolite Nanotubes towards Efficient Visible Light Photocatalysts. *Solar RRL*, 7(4):2200947, 2023.

[117] Mohammed Majdoub, Zakaria Anfar, and Abdallah Amedlous. Emerging Chemical Functionalization of g-C_3N_4: Covalent/Noncovalent Modifications and Applications. *ACS Nano*, 14(10):12390–12469, 2020.

Appendix A

Chemicals

Chemicals	**Pictogram**	**Hazard Statements**	**Precautionary Statements**
Thioacetamide		302-315 319-350-412	273-280- 305+350+338 302+352
$Bi(NO_3)_3$		272-315-319- 335	221-280-302+ 352-304+340- 305+351+338
$InCl_3$		302-314	260-280-321 303+351+338- 305+351+338
$Al(NO_3)_3$		272-315-319	220-280-302+352- 305+351+338
$Co(NO_3)_2$		272-302-317- 318-334-341- 350i-360F-410	201-220-273-280- 304+340- 342+311

Chemicals	**Pictogram**	**Hazard Statements**	**Precautionary Statements**
Methyl orange		301	270-301+310
Methylene blue		302	270-301+312
Rhodamine B		302-318-412	264-270-273-280-301+312-305+351+338
$(CH_2)_6N_4$		228-317	210-280 333+313
Sodium dodecyl sulfate		228-302+332-315-318-335 412	210-261-280-302+352-305+351+338-312
$C_{19}H_{42}BrN$		302-315-318-335-373-410	273-280-302+352-305+351+338-310
Ammonium persulfate		272-302-315-317-319-334-335	261-280 305+351+338-302+352

Chemicals	**Pictogram**	**Hazard Statements**	**Precautionary Statements**
Styrene		226-304-315-319-332-361d-372	210-260-331-301+310 302+352-305+351+338-370+378
Butyl Acrylate		226-319-315- 332-317 335-303+313-412-401	280-271-260-280-210 273-243-241-272-264-242-240 312-305+351+338-304+340-303+361+353
Methylenbis-(acrylamide)		301-312+332 340-350-361fd 372	260-280 301+310 302+352

List of H- and P-statements

H-statements

H226	Flammable liquid and vapour
H228	Flammable solid
H272	May intensify fire; oxidizer
H301	Toxic if swallowed
H302	Harmful if swallowed
H304	May be fatal if swallowed and enters airways
H312	Harmful in contact with skin
H314	Causes severe skin burns and eye damage
H315	Causes skin irritation
H317	May cause an allergic skin reaction
H318	Causes serious eye damage
H319	Causes serious eye irritation
H332	Harmful if inhaled
H334	May cause allergy/ asthma symptoms/ breathing difficulties if inhaled
H335	May cause respiratory irritation
H340	May cause genetic defects
H341	Suspected of causing genetic defects
H350	May cause cancer
H350i	May cause cancer by inhalation
H360F	May damage fertility
H361d	Suspected of damaging the unborn child
H361fd	Suspected of damaging fertility. Suspected of damaging the unborn child
H372	Causes damage to organs through prolonged or repeated exposure
H373	May cause damage to organs through prolonged or repeated exposure
H401	Toxic to aquatic life
H410	Very toxic to aquatic life with long-lasting effects
H412	Harmful to aquatic life with long-lasting effects
H302+H332	Harmful if swallowed or if inhaled
H312+H332	Harmful in contact with skin or if inhaled
H303+H313	May be harmful if swallowed or in contact with skin

P-statements

P201	Obtain special instructions before use
P210	Keep away from heat, hot surfaces, sparks, sources open flames and other ignition
P220	Keep away from clothing and other combustible materials
P221	Take any precaution to avoid mixing with combustibles
P240	Ground and bond container and receiving equipment
P241	Use explosion-proof equipment
P242	Use only non-sparking tools
P243	Take precautionary measures against static discharge
P260	Do not breathe dust/fume/gas/mist/vapours/ spray
P261	Avoid breathing dust/fume/gas/mist/vapours/ spray
P264	Wash thoroughly after handling
P270	Do not eat, drink or smoke when using this product
P271	Use only outdoors or in a well-ventilated area
P272	Contaminated work clothing should not be allowed out of the workplace
P273	Avoid release to the environment
P280	Wear protective gloves/protective clothing
P301	IF SWALLOWED:
P302	IF ON SKIN:
P305	IF IN EYES:
P310	Immediately call a POISON CENTER or doctor/physician
P312	Call a POISON CENTER/doctor if you feel unwell
P321	Specific treatment
P301+P310	IF SWALLOWED: Immediately call a POISON CENTER/doctor
P301+P312	IF SWALLOWED: Call a POISON CENTER/ doctor if you feel unwell
P302+P352	IF ON SKIN: Wash with plenty of water
P304+P340	IF INHALED: Remove person to fresh air and keep comfortable for breathing
P333+P313	If skin irritation or rash occurs: Get medical advice/attention
P342+P311	If experiencing respiratory symptoms: Call a POISON CENTER/doctor
P370+P378	In case of fire: Use… to extinguish
P303+P351+P338	IF IN EYES: Rinse cautiously with water for several minutes. Remove contact lenses if present and easy to do

P303+P361+P353	IF ON SKIN (or hair): Take off immediately all contaminated clothing. Rinse skin with water [or shower]
P305+P350+P338	IF IN EYES: Rinse cautiously with water for several minutes. Remove contact lenses, if present and easy to do

Appendix B

Supplementary Information for Chapter 2

Heterostructured Monolayer MoS_2 Nano-particles toward Water-Dispersible Catalysts

Supporting Information: Heterostructured Monolayer MoS_2 Nanoparticles Toward Water-Dispersible Catalysts

Sanjay Jatav, Kaline P. Furlan, Junying Liu, Eric H. Hill*
Institute of Advanced Ceramics, Hamburg University of Technology, Hamburg 21073;
eric.hill@tuhh.de

Contents:

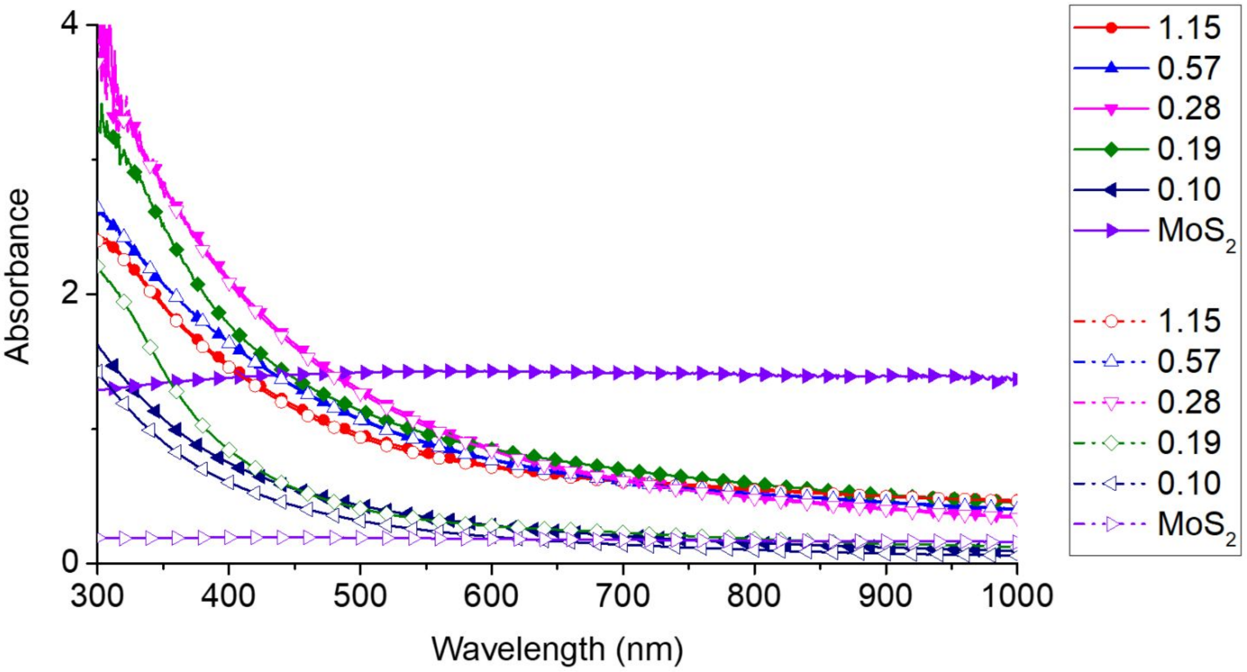

Figure S1. UV-Vis spectra of Lap-MoS_2 synthesized at different Mo:Lap precursor ratios by mass, in aqueous dispersion before and after 48 hr. Filled symbols indicates initial spectrum and empty symbols with dotted lines indicates samples after 48 hr of settling.

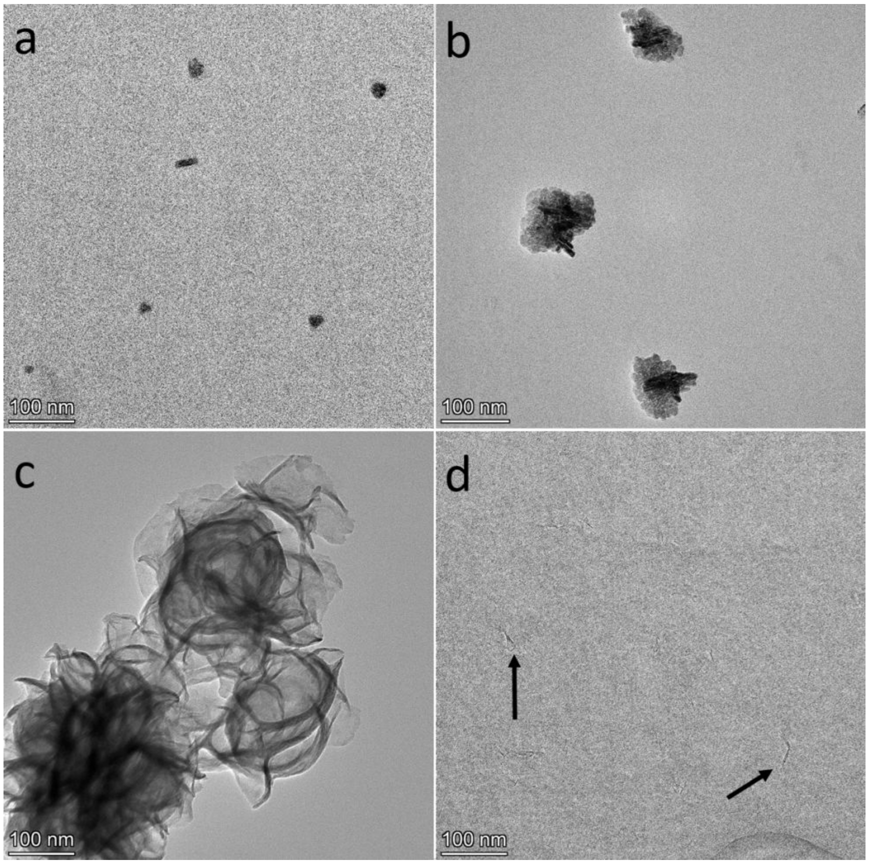

Figure S2. Lap-MoS_2 synthesized hydrothermally (a) with, and (b) without stirring during reaction, and controls for (c) MoS_2 and (d) Laponite®-RD.

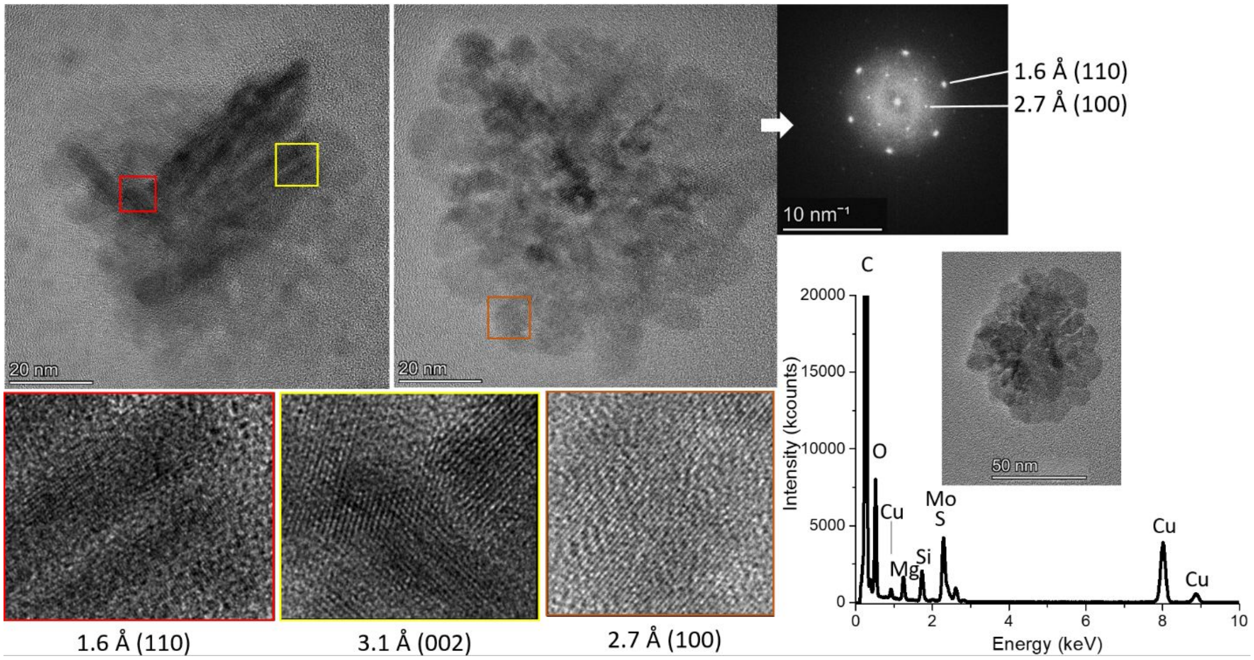

1.6 Å (110) 3.1 Å (002) 2.7 Å (100)

Figure S3. HRTEM images of Lap-MoS_2 synthesized without stirring, with corresponding electron diffraction patterns and EDX spectrum.

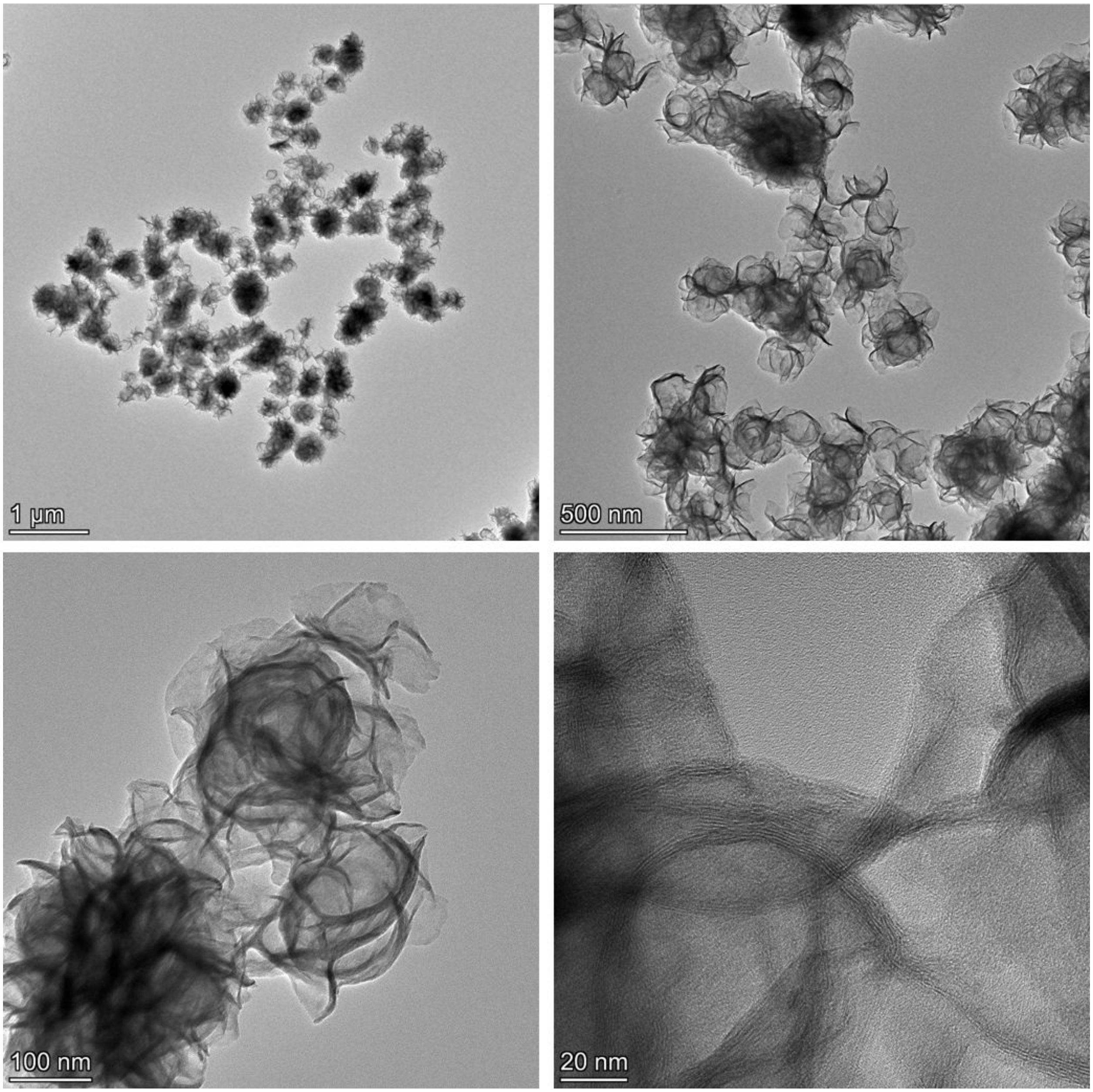

Figure S4. HRTEM images of the MoS_2 control samples synthesized without Laponite-RD®.

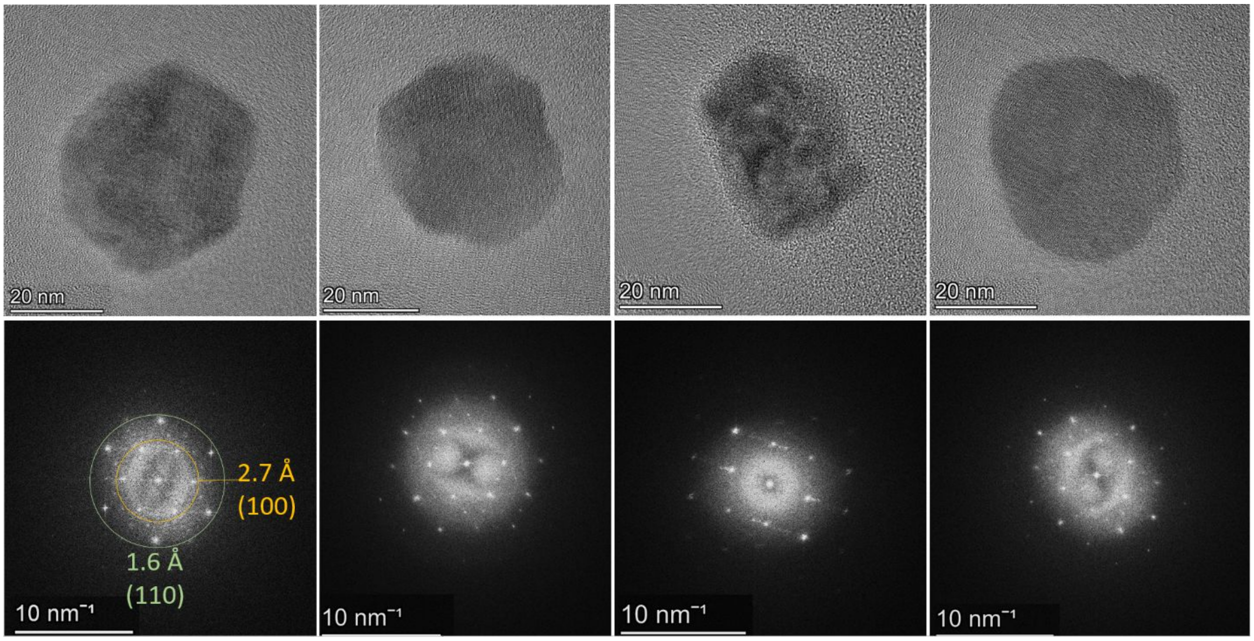

Figure S5. TEM images of Lap-MoS_2, including electron diffraction patterns showing (100) and (110) planes of MoS_2.

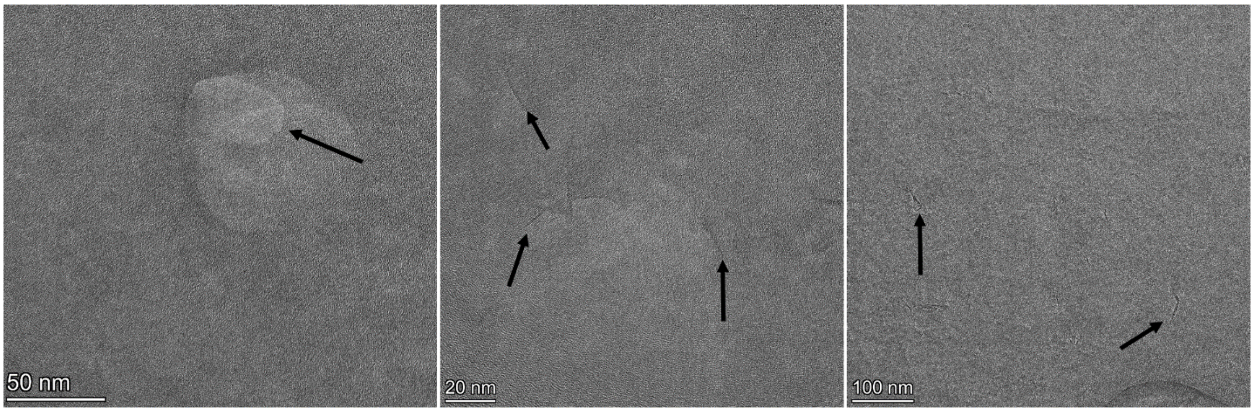

Figure S6. HRTEM images of Laponite-RD® control.

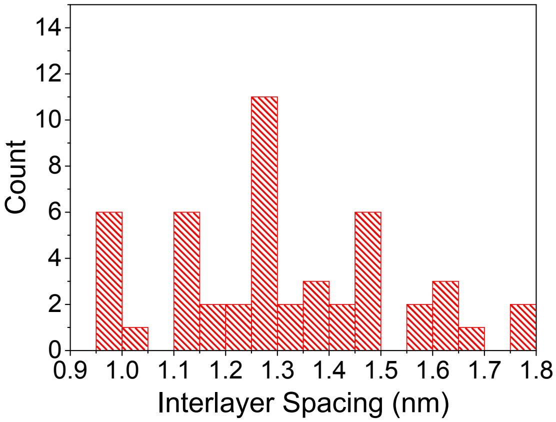

Figure S7. Distribution histogram of 48 interlayer spacings measured by HRTEM.

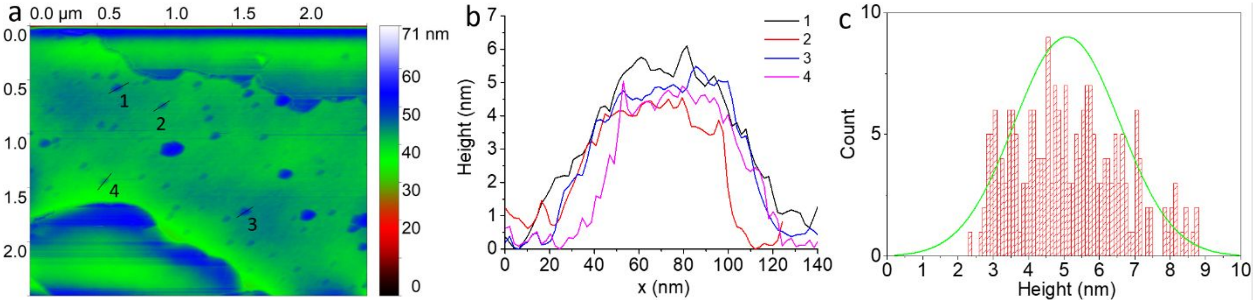

Figure S8. (a) Height-map of Lap-MoS$_2$ particles on Si wafer. (b) Height profiles of the lines shown in (a). (c) Distribution plot of Lap-MoS$_2$ heights measured by AFM, with a total of 217 particles measured.

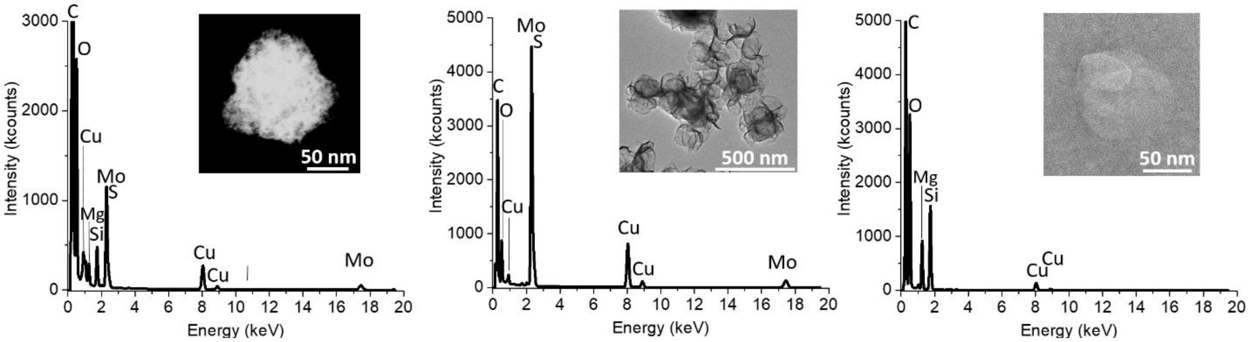

Figure S9. Full range of EDX spectra of Lap-MoS$_2$, MoS$_2$, and Lap (from left to right) shown in **Figure 4**.

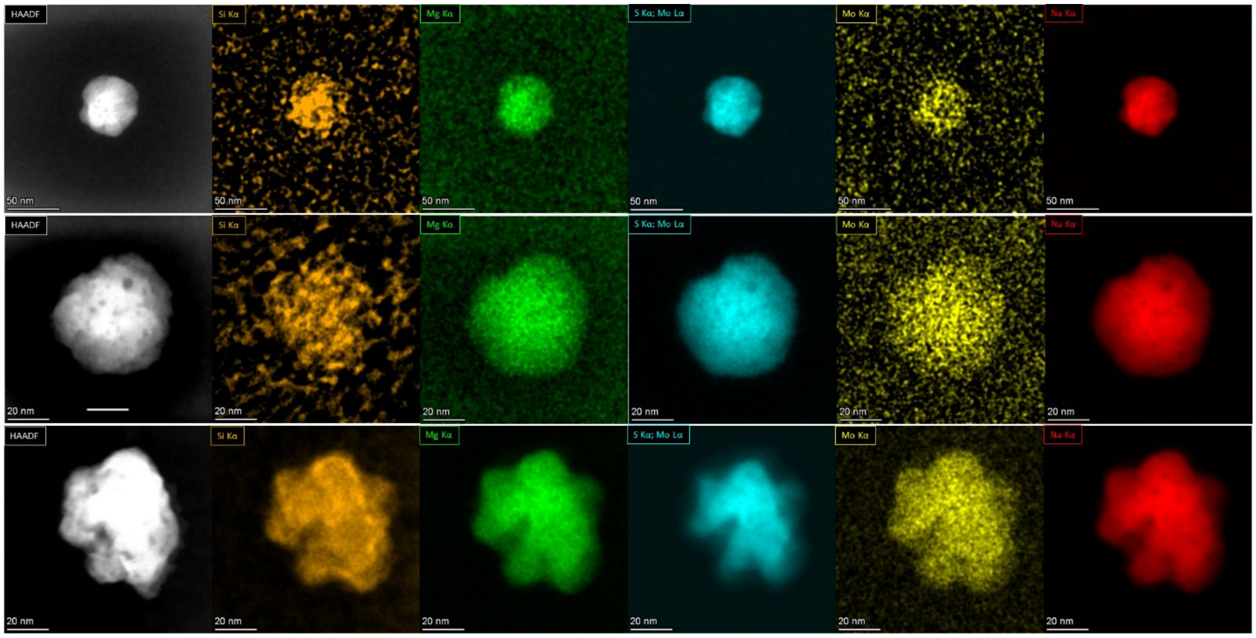

Figure S10. HAADF-STEM EDX mappings of Lap-MoS$_2$ particles. Silicon is visible in the background in some cases due to the presence of typical vacuum greases which can contaminate the sample during prolonged electron beam exposure.

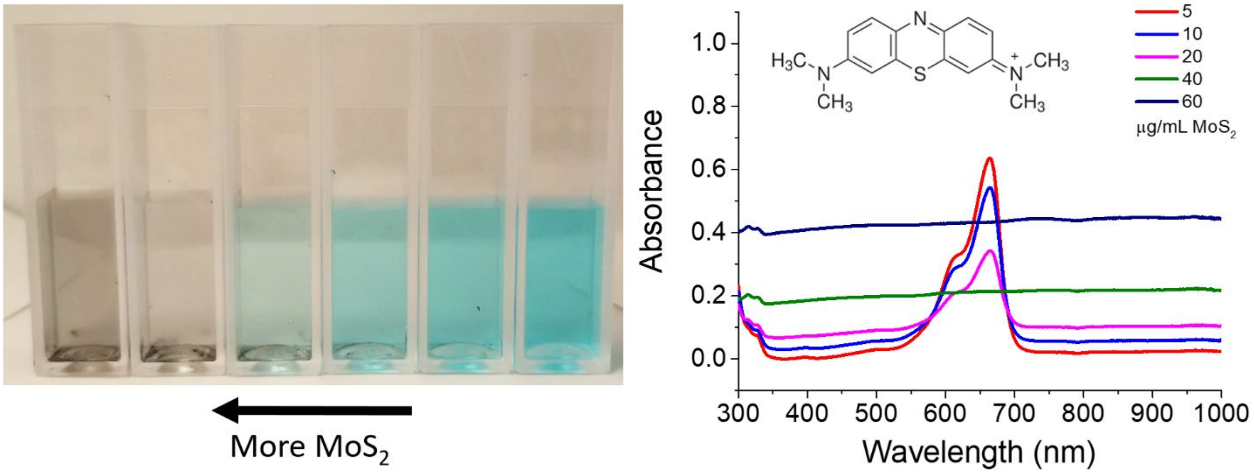

Figure S11. Absorption spectra and corresponding photograph of a 10 μM methylene blue solution with increasing amounts of MoS$_2$.

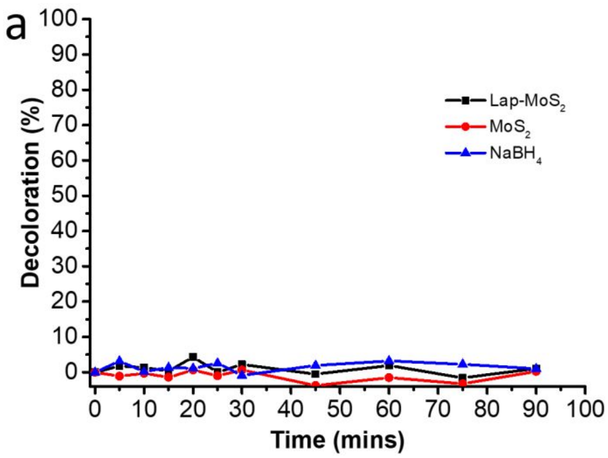

Figure S12. Control catalytic experiments: (a) MO (67 μM) with 20 μg/mL catalysts and (b) 4-NA with 10 μg/mL catalysts; Those with catalysts have no NaBH$_4$, NaBH$_4$ trace includes no catalyst.

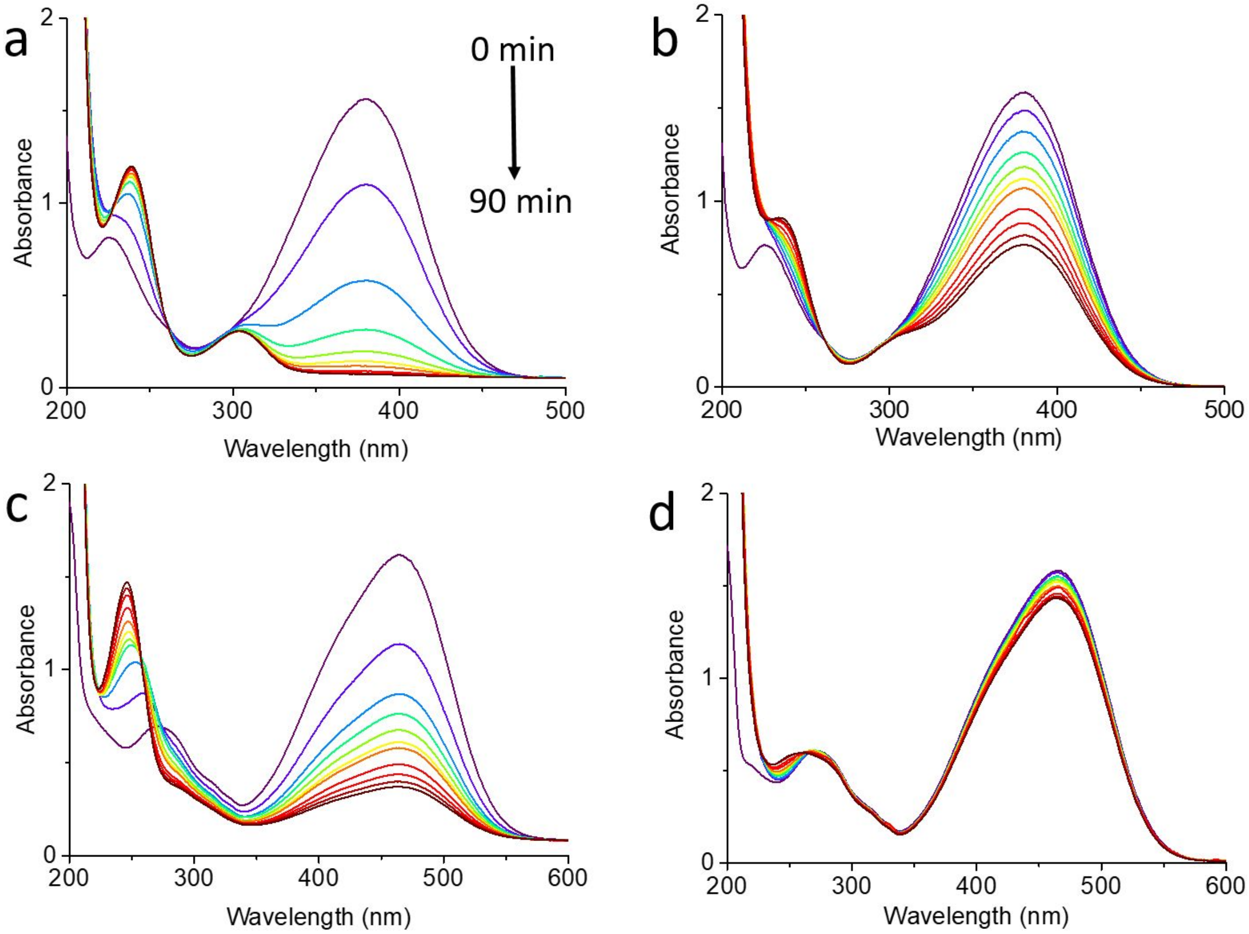

Figure S13. UV-Visible spectra at different timepoints of catalytic degradation by NaBH$_4$: 4-NA (0.12 mM) by 10 μg/mL (a) Lap-MoS$_2$ and (b)MoS$_2$; MO (67 μM) by 20 μg/mL (c) Lap-MoS$_2$ and (d)MoS$_2$

Appendix C

Supplementary Information for Chapter 3

Facet Engineering of Bismuth Molybdate via Confined Growth in a Nanoscale Template toward Water Remediation

Supporting Information

Facet Engineering of Bismuth Molybdate via Confined Growth in a Nanoscale Template toward Water Remediation

Sanjay Jatav, Junying Liu, Marcel Herber, Eric H. Hill*

*e-mail: eric.hill@chemie.uni-hamburg.de

Institute of Physical Chemistry, University of Hamburg, Grindelallee 117, 20146 Hamburg, Germany

The Hamburg Centre for Ultrafast Imaging (CUI), Luruper Chausee 149, 22761 Hamburg, Germany

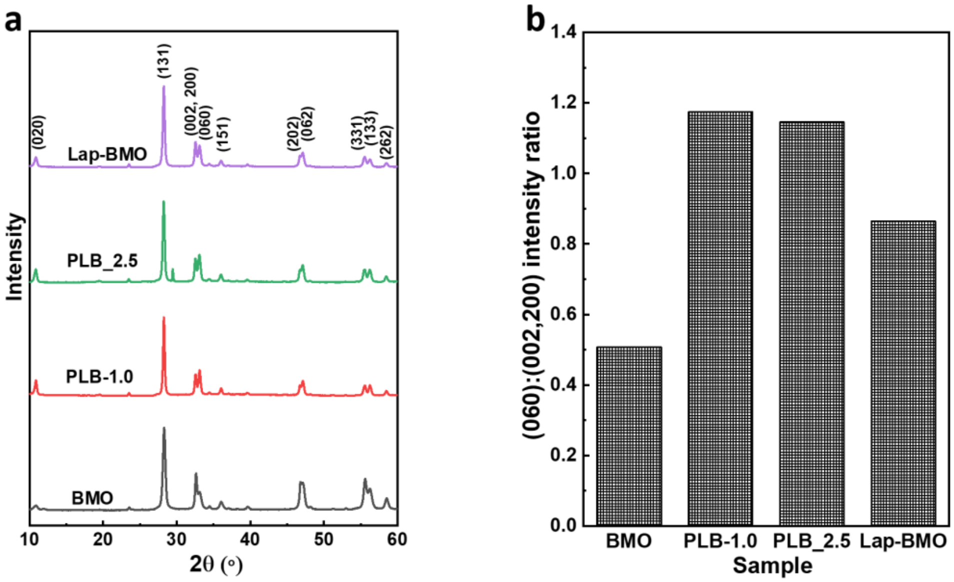

Figure S1. (a) X-ray diffractograms of BMO prepared with 2.5x increased concentration of all reactants, keeping the ratio of [BMO precursor]:[CTAB-Lap] unchanged. (b) Intensity ratio of (060):(002,200) peaks for the different samples. Lap-BMO refers to the sample prepared using unpillared Lap (no CTAB).

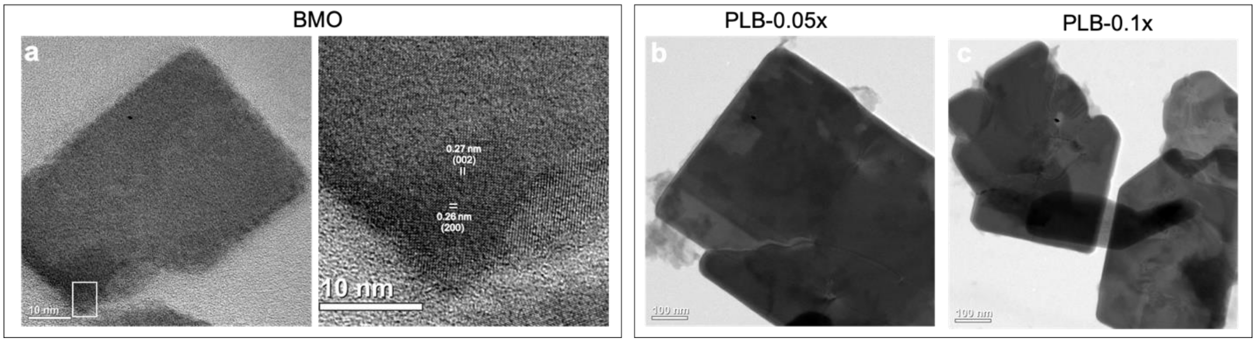

Figure S2. HRTEM micrograph of (a) BMO control; PLB samples prepared at (b) 0.25 mM, (c) 0.5 mM BMO precursor concentration (Bi basis) using CTAB-pillared Lap.

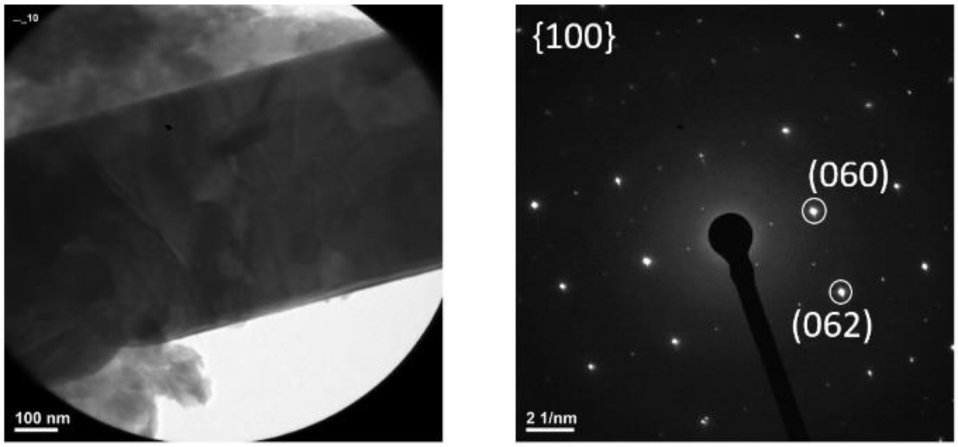

Figure S3. Selected area electron diffraction image from the sample PLB-0.2x.

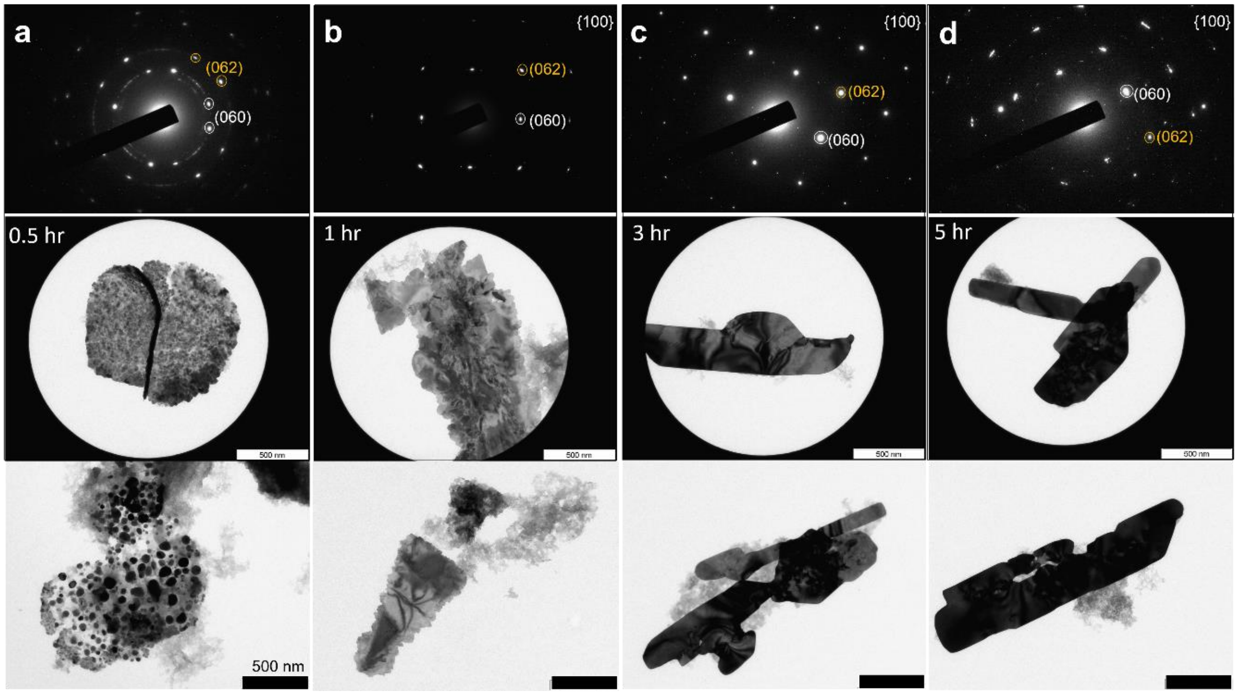

Figure S4. Selected area electron diffraction patterns, corresponding transmission electron micrographs, and additional micrographs (from top to bottom) of PLB-0.2x synthesized with reaction times of (a) 30 min; (b)1 hour; (c) 3 hours; (d) 5 hours. Scale bars are 500 nm.

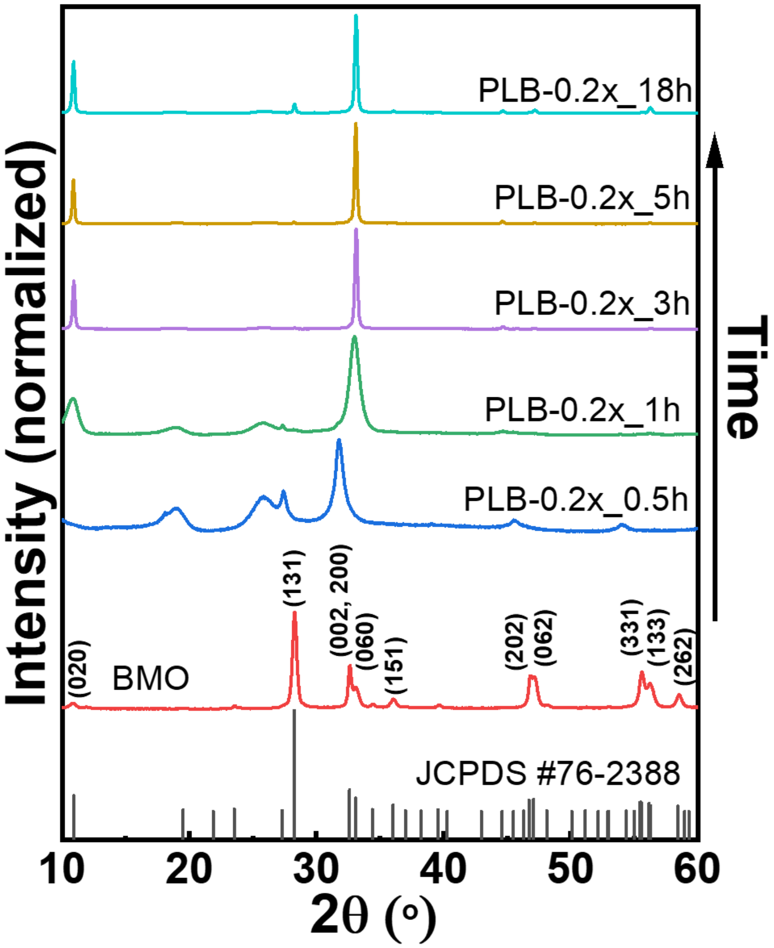

Figure S5. (a) X-ray diffractograms of PLB-0.2x samples synthesized for different durations.

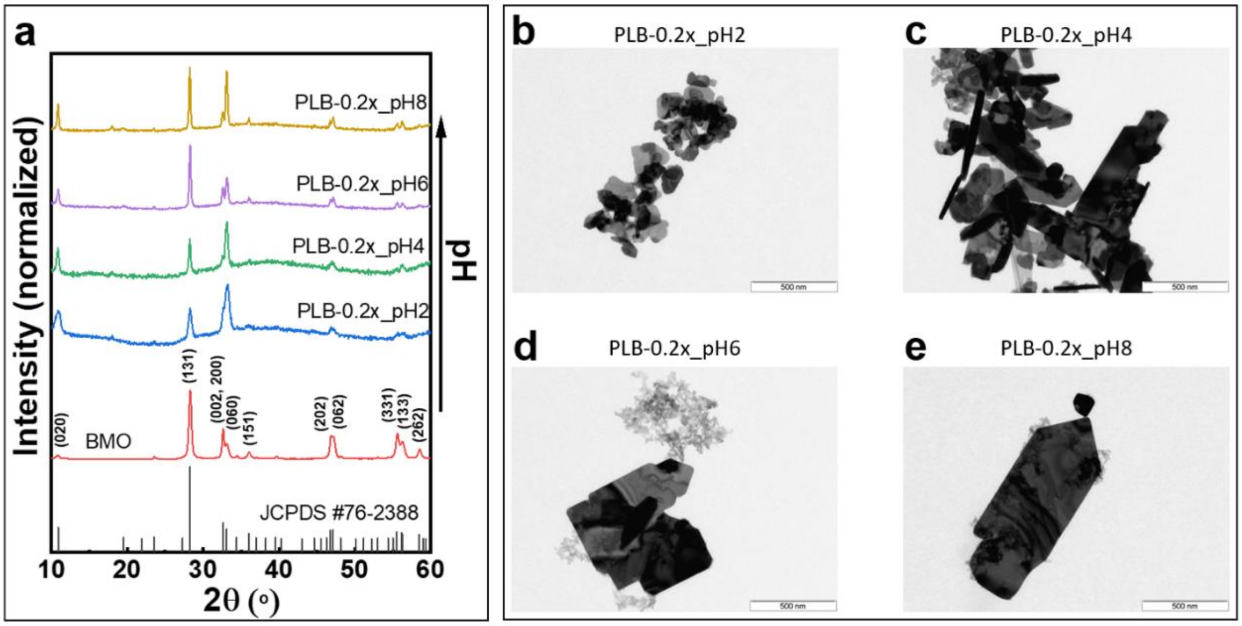

Figure S6. (a) X-ray diffractograms from the pH series of samples. TEM micrograph of PLB-0.2x synthesized at a pH of (b) 2.04, (c) 4.24, (d) 6.3 and (e) 8.24.

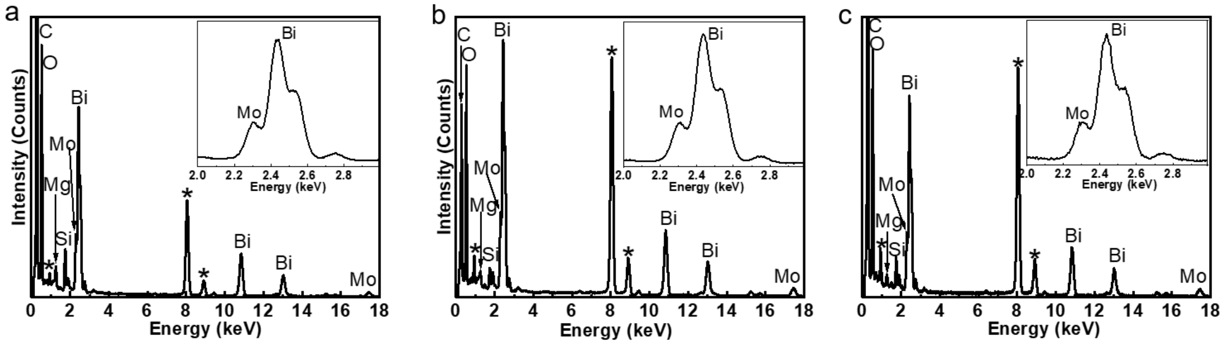

Figure S7. EDX spectra corresponding to the HAADF-STEM EDX maps of PLB-0.2x shown in (a)**Figure 3a**; (b) **Figure 3b**; (c) **Figure 3c**. * refers to Cu peaks from the TEM grid.

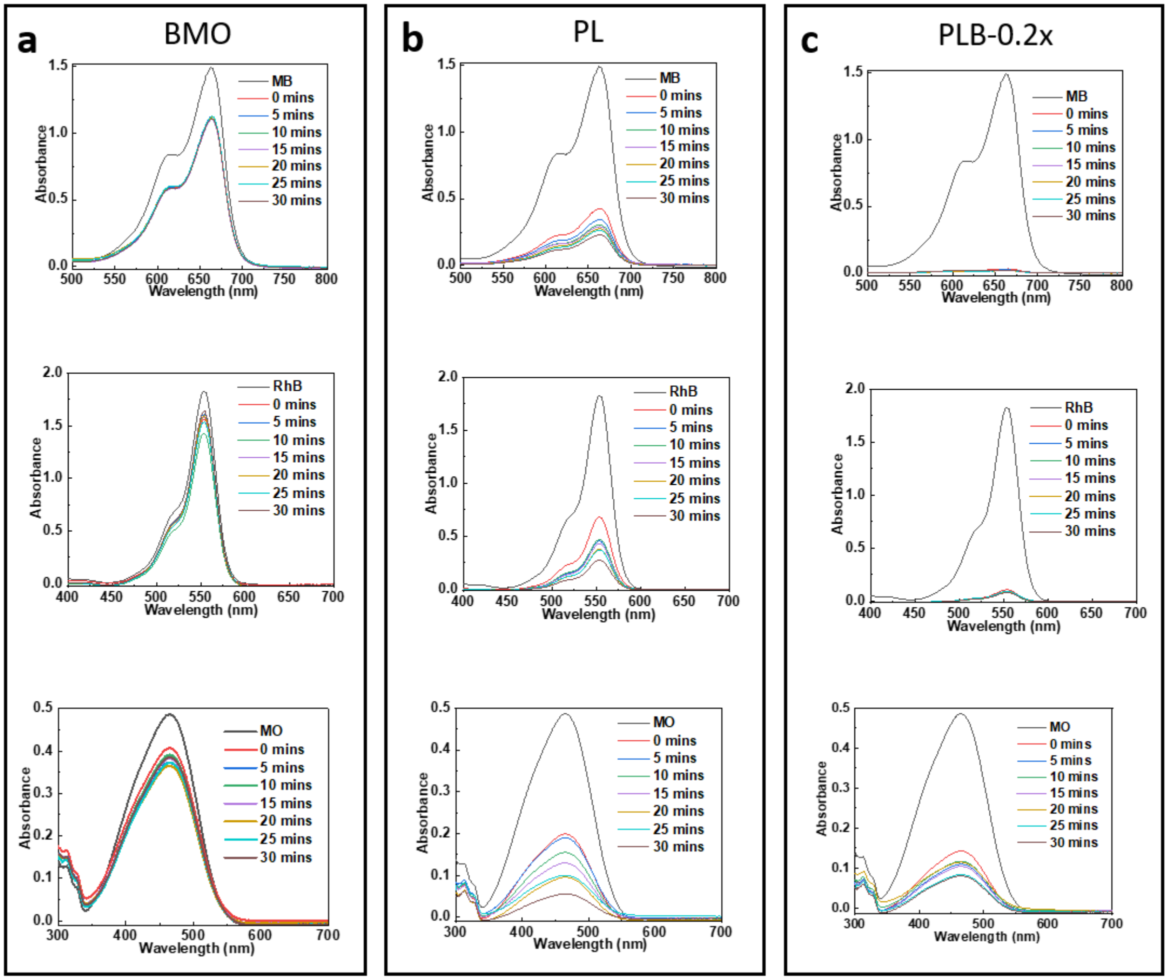

Figure S8. UV-vis spectra from the adsorption kinetics study. Panels (a), (b) and (c) show the different dyes absorbed by BiMo, PL and PLB-0.2x, respectively over a span of 30 mins. The [dye]= 75 µM and [particles]= 1 mg/mL.

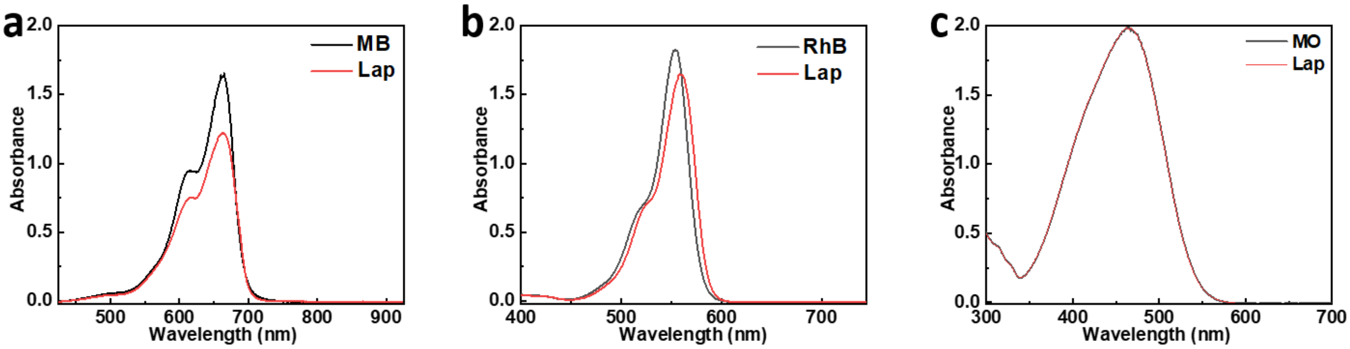

Figure S9. UV-vis spectra recorded 36 hours after the addition of Lap (a) MB (b) RhB (c) MO.

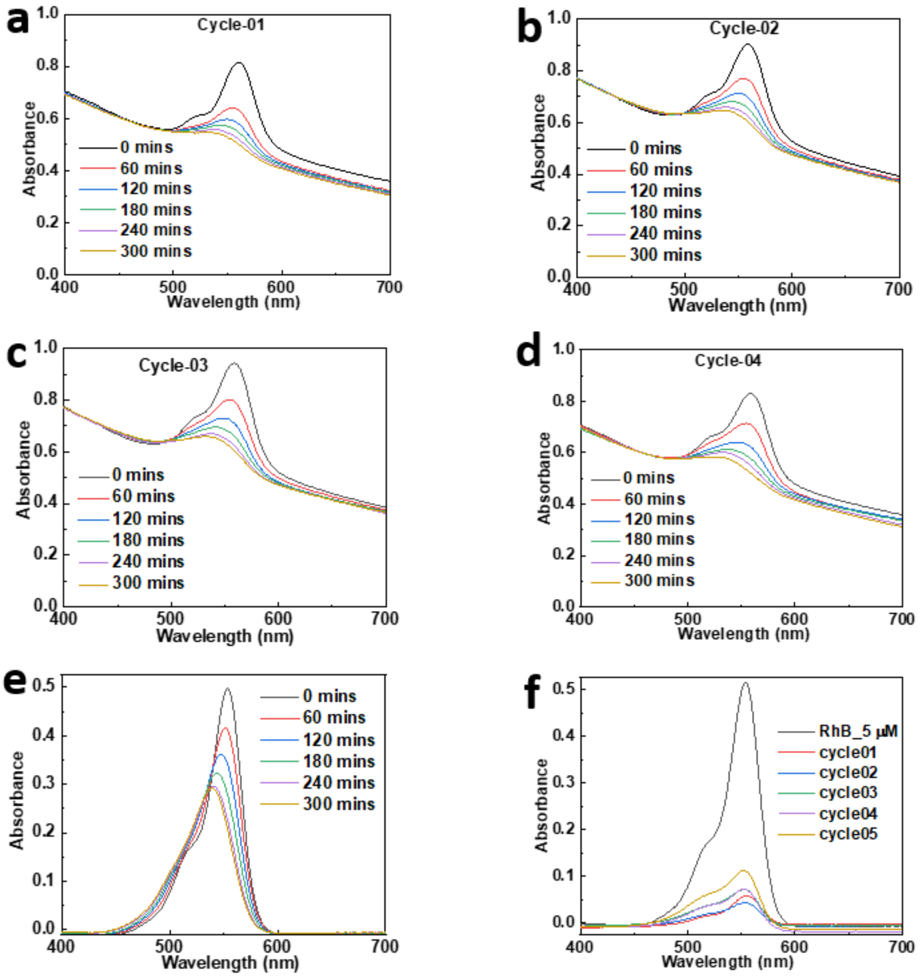

Figure S10. UV-vis spectra from the recycling experiments of PLB-0.2x sample using 5 µM RhB. (a-e) shows RhB photodegradation of over subsequent cycles using PLB-0.2x particles as photocatalysts. (e) Photodegradation of 5 µM RhB in light. (f) Amount of dye adsorbed after every adsorption cycle.

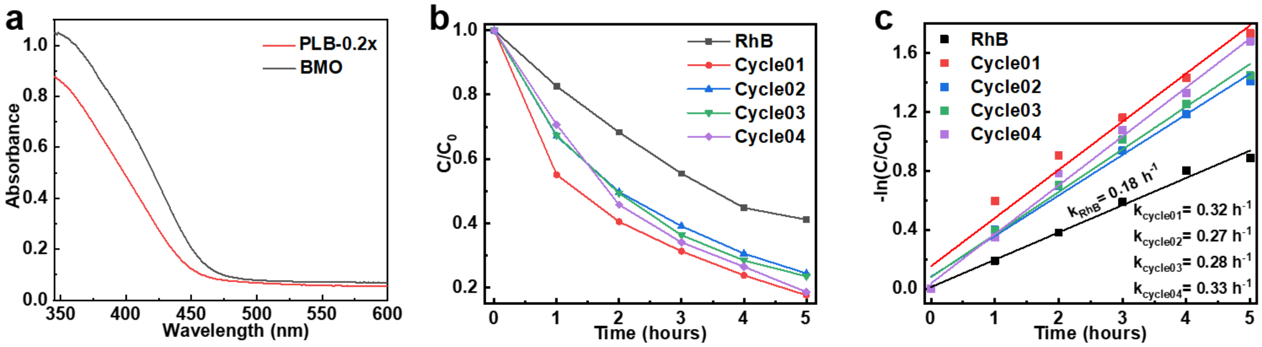

Figure S11. (a) UV-vis diffuse reflectance spectra of PLB-0.2x and BMO control sample. (b) Amount of dye degraded during different cycles, (c) kinetics of photodegradation using PLB-0.2x at different cycles.

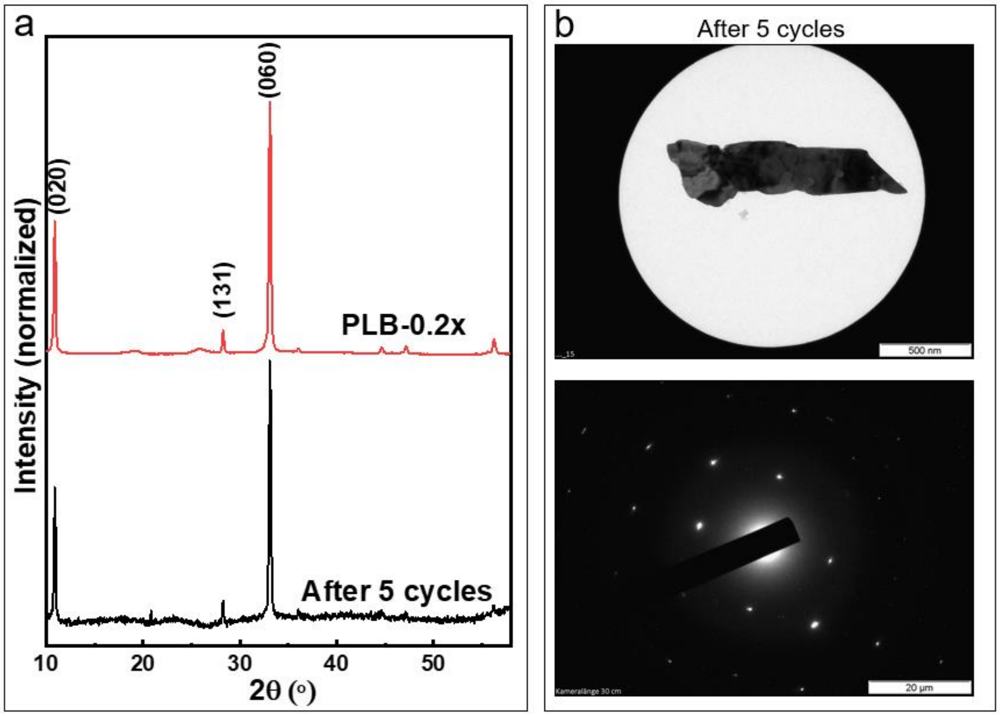

Figure S12. (a) X-ray diffractograms of of PLB-0.2x before after 5 cycles of photodegradation. (b) TEM image and corresponding SAED pattern of the PLB-0.2x sample after 5 cycles of photocatalytic RhB degradation. HRTEM and SAED pattern of PLB-0.2x is shown in **Figure S4**.

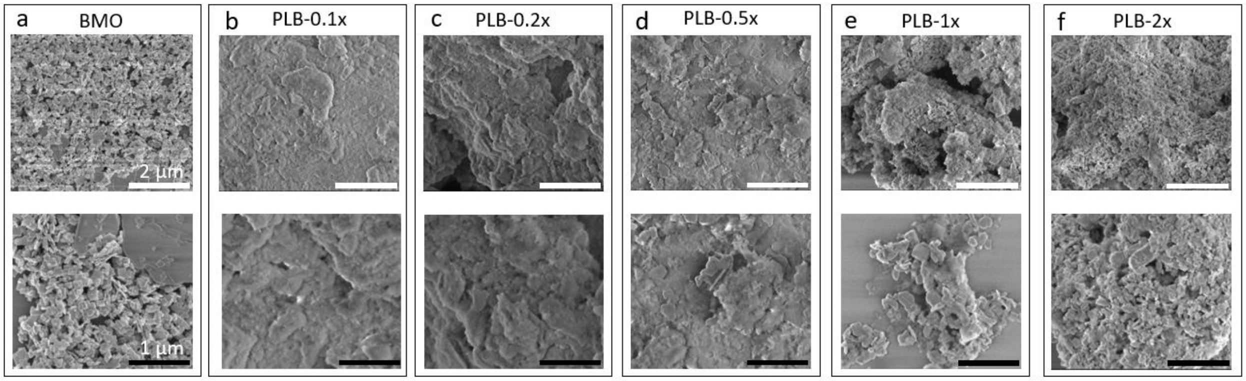

Figure S13. SEM micrographs of (a) BMO control (b) PLB-0.1x (c) PLB-0.2x (d) PLB-0.5x (e) PLB-1x (f) PLB-2x. Scale bars in top and bottom panel are 2 and 1 µm, respectively.

Table S1: Comparison of dye adsorption capacity. 150 µM RhB and MB were used for determining the given dye capacities of PLB-0.2x.

Material	**Dye**	**Adsorption capacity (µmol/mg)**	**Ref**
Bi_2MoO_6	MB	7.6	1
AgI- Bi_2MoO_6/Vermiculite	Malachite green	57.3	2
Bi_2MoO_6	RhB	4.82	3
PLB-0.2x	RhB	77.37	This work
PLB-0.2x	MB	106.84	This work
Zr-Pillared Montmorillonite	MB	109.42	4
Al-Pillared Montmorillonite	MB	37.51	4

References

(1) Zhang, L.; Xu, T.; Zhao, X.; Zhu, Y. Controllable Synthesis of Bi2MoO6 and Effect of Morphology and Variation in Local Structure on Photocatalytic Activities. *Appl. Catal. B Environ.* **2010**, *98* (3–4), 138–146.

(2) Zhu, P.; Wang, R.; Duan, M.; Chen, Y.; Hu, M.; Luo, X.; Teng, H. Efficient Adsorption and Photocatalytic Degradation of Dyes by AgI-Bi2MoO6/Vermiculite Composite under Visible Light. *ChemistrySelect* **2019**, *4* (41), 12022–12031.

(3) Yang, Z.; Shen, M.; Dai, K.; Zhang, X.; Chen, H. Controllable Synthesis of Bi 2 MoO 6 Nanosheets and Their Facet-Dependent Visible-Light-Driven Photocatalytic Activity. *Appl. Surf. Sci.* **2018**, *430*, 505–514.

(4) Gil, A.; Assis, F. C. C.; Albeniz, S.; Korili, S. A. Removal of Dyes from Wastewaters by Adsorption on Pillared Clays. *Chem. Eng. J.* **2011**, *168* (3), 1032–1040.

Appendix D

Supplementary Information for Chapter 4

Surface-Encapsulated Bismuth Molybdate-Layered Silicate Hybrids as Sorbents for Photocatalytic Filtration Membranes

Supporting information

Surface Encapsulated Bismuth Molybdate – Layered Silicate Hybrids as Sorbents for Photocatalytic Filtration Membranes

Sanjay Jatav†, Marcel Herber†, Hongxiao Xiang†, Eric H. Hill*†‡

†Institute of Physical Chemistry, University of Hamburg, Grindelallee 117, 20146 Hamburg, Germany

‡The Hamburg Center for Ultrafast Imaging (CUI), Luruper Chausee 149, 22761 Hamburg, Germany

*eric.hill@chemie.uni-hamburg.de

Table S1: %Organic content estimated from TGA.

Sample Name	% Organic content
Lap-BMO	13.25
BA	17.64
BS-C	38.703
M-BS-C	32.87

Table S2: Specific adsorption of MB per Lap-BMO calculated from Figure S6a,b.

Sample Name	MB adsorbed (µmol/g)	MO adsorbed (µmol/g)
Lap-BMO	95.12	56.78
BS	89.69	26.67
BS-C	124.98	52.81
M-BS-C	112.96	31.77

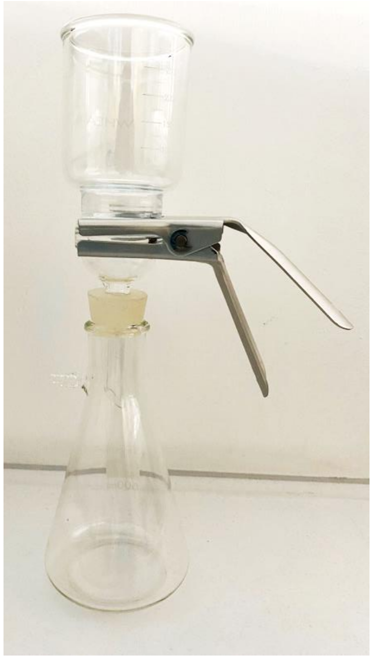

Figure S1: The filtration setup

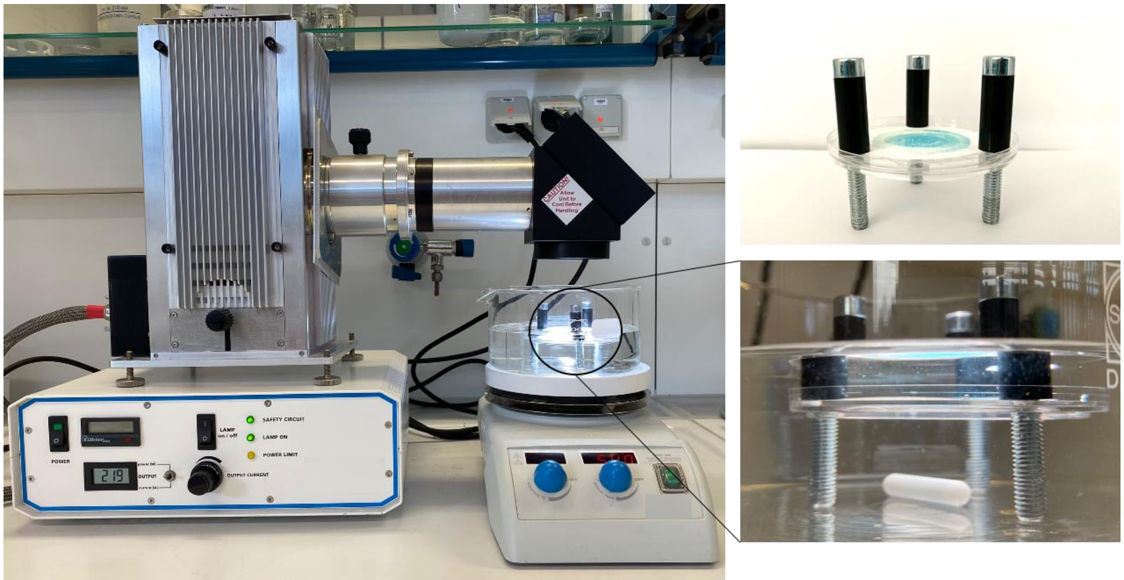

Figure S2: The photodegradation setup and the fixture used to hold the filter paper in place.

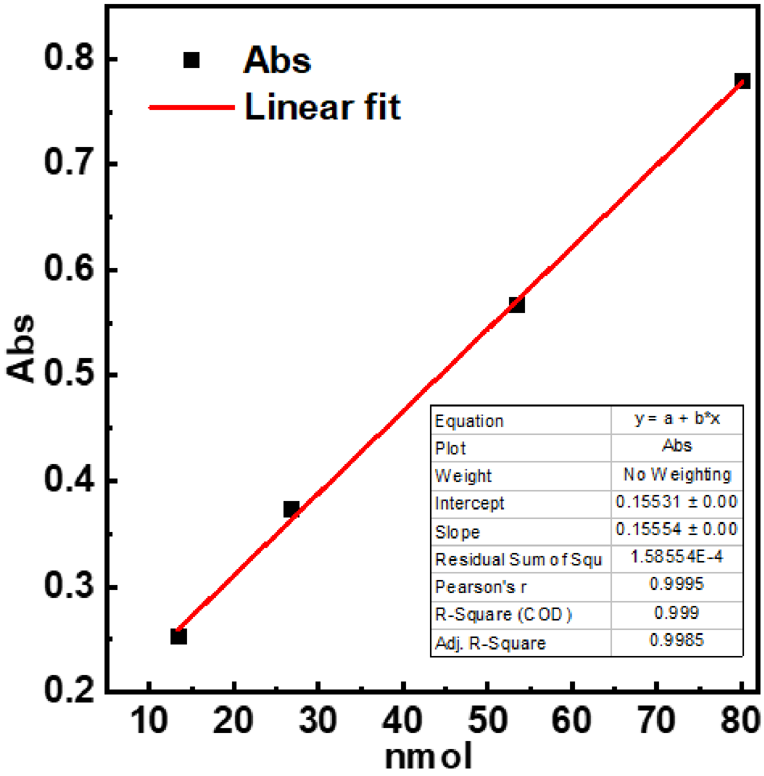

Equation	y = a + b*x
Plot	Abs
Weight	No Weighting
Intercept	0.15531 ± 0.00
Slope	0.15554 ± 0.00
Residual Sum of Squ	1.58554E-4
Pearson's r	0.9995
R-Square (COD)	0.999
Adj. R-Square	0.9985

Figure S3: Calibration curve (absorbance at 664 nm) for estimating the quantity of MB adsorbed on filter membranes via diffuse reflectance UV-Vis spectroscopy.

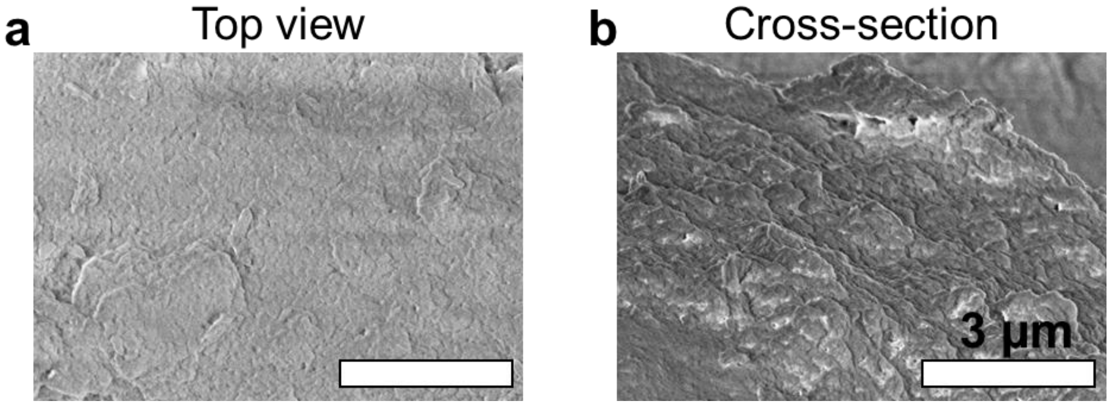

Figure S4: SEM image of filter coated with Lap-BMO particles. (a) Top view and (b) cross-sectional view. Scale bar in both images corresponds to 3 µm.

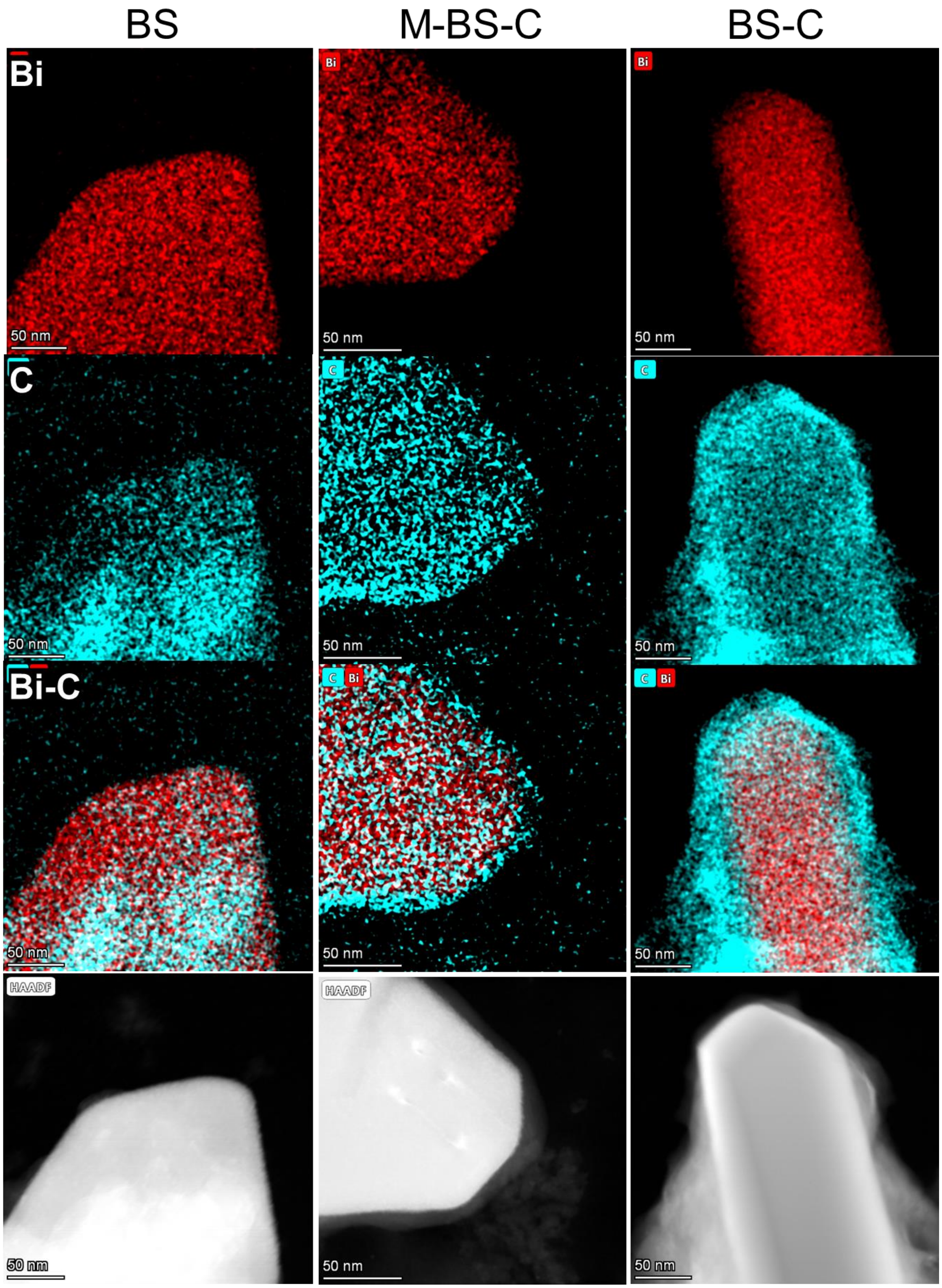

Figure S5: HAADF-STEM EDX elemental maps of the polymer encapsulated Lap-BMO particles. All scale bars correspond to 50 nm.

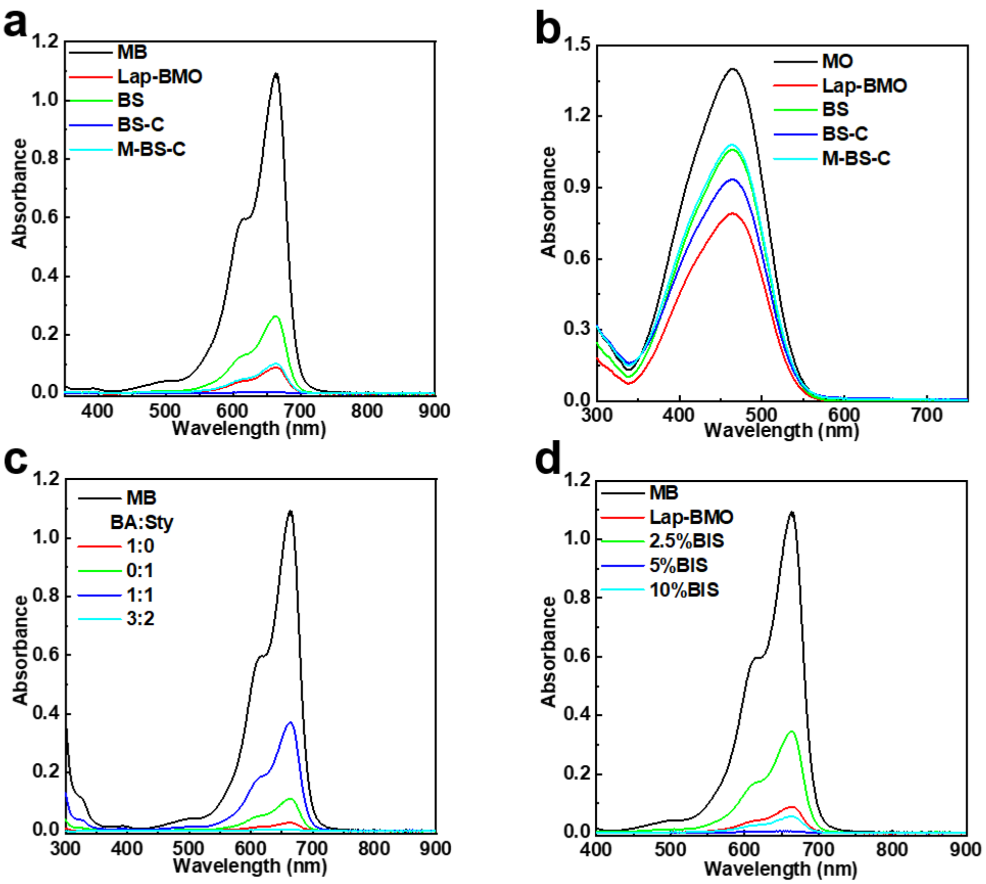

Figure S6: UV-vis spectra from the dye adsorption experiments presented in Figure 3. (a) MB adsorption, (b) MO adsorption. (c) UV-vis spectra for the samples prepared using different BA:Sty ratios and (d) different amount of crosslinker concentration. 20 mL of 53.4 µM dye solution was poured through all the samples.

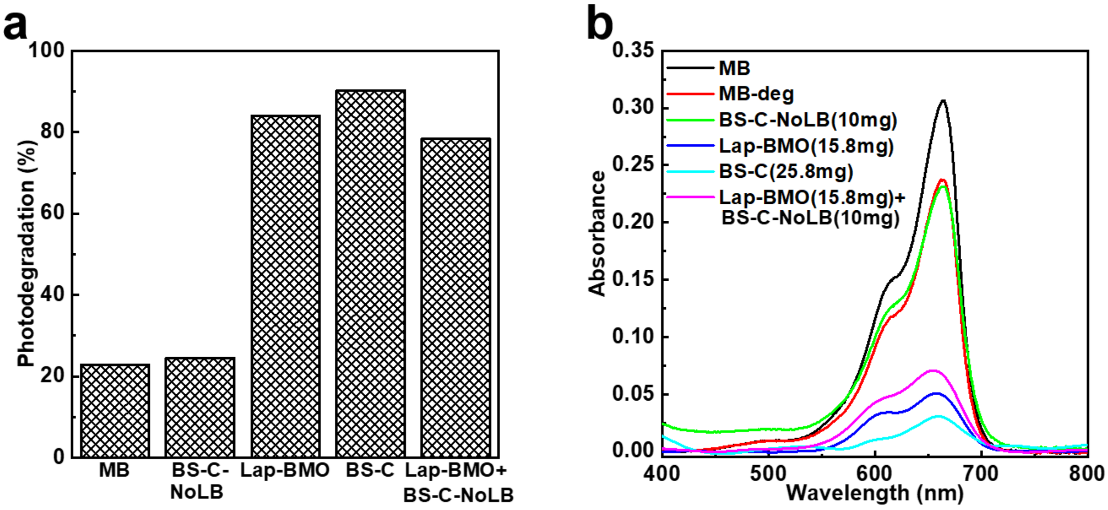

Figure S7: (a) Photocatalytic degradation of MB in aqueous solution, (b) UV-vis spectra corresponding to (a). [MB] = 13.35 µM.

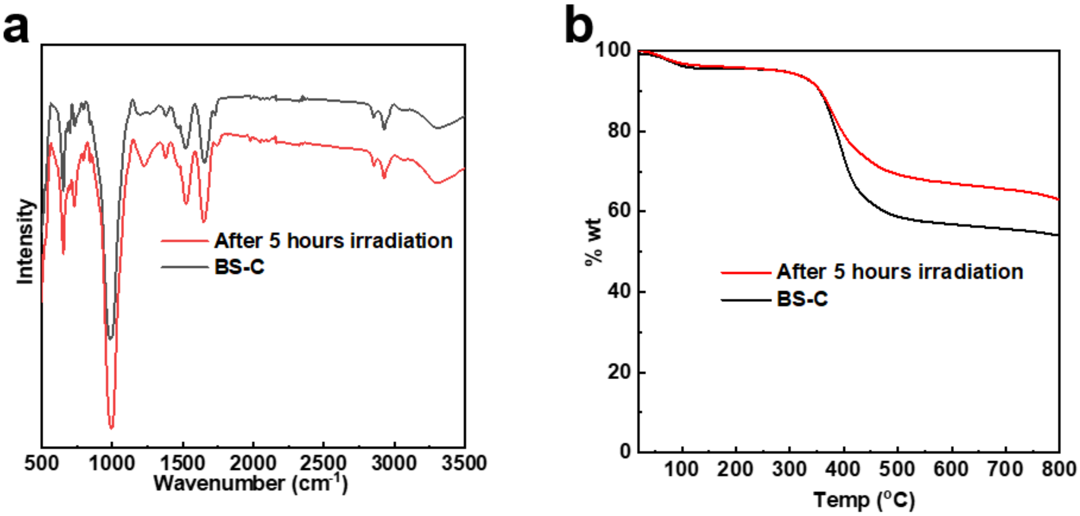

Figure S8: (a) FTIR spectra and (b) TGA curves for the sample BS-C before and after 5 hours of illumination.

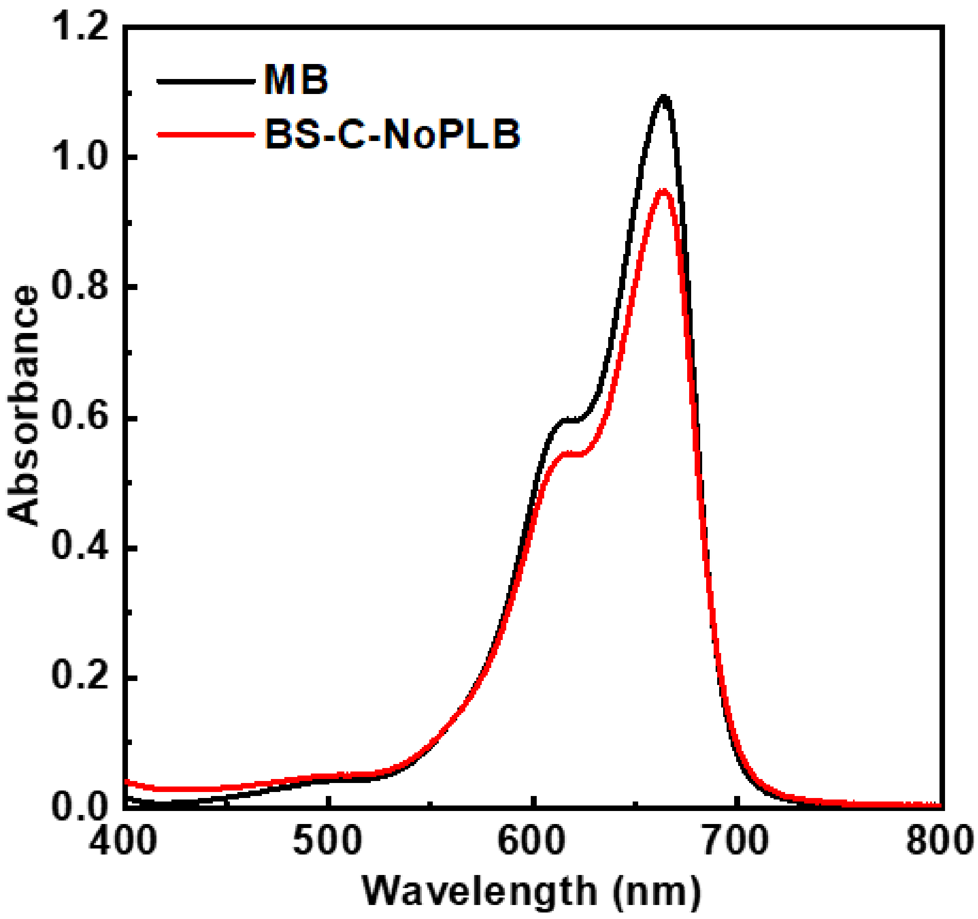

Figure S9: MB removal by BS-C-NoLB. [MB] = 53.4 µM and concentration of [BS-C-NoLB] = 1 mg/mL.

Table S3: Comparison with of adsorption capacity with other materials

Material	Membrane/ Substrate	Model Pollutant	Conc. (µM)/ [volume used (mL)]	Dye adsorbed (µmol/g)	Ref.
BS-C	Cellulose acetate	MB	53.4/ [100]	191.83	This work
Ti_3C_2Tx	Poly amide	MB	6.25	131.31	1
Activated carbon	Poly amide	MB	6.25	171.87	1
TiO_2/ Graphene oxide (GO)	Polyether Sulfone (PES)	RhB	20.876/ [14]	48.61	2
PVDF	PVDF	Crystal Violet	24.51/ [25]	3.35†	3
Meldrum acid-CNF	PVDF	Crystal violet	24.51/ [25]	9.765†	3

Ca-Alignate/ MWCNTs	PHB nanofibers	Brilliant Blue	63.06/ [10]	23†	4
GO-MnO_2	-	MB	468.9/ [50]	550†	5
Arginine-activated carbon	-	MB	46.89 / [250]	690†	6

†Specific adsorption not measured under flow conditions

References

(1) Kim, S.; Yu, M.; Yoon, Y. Fouling and Retention Mechanisms of Selected Cationic and Anionic Dyes in a $Ti_3C_2T_x$ MXene-Ultrafiltration Hybrid System. *ACS Appl. Mater. Interfaces* **2020**, *12* (14), 16557–16565.

(2) Xu, C.; Cui, A.; Xu, Y.; Fu, X. Graphene Oxide-TiO_2 Composite Filtration Membranes and Their Potential Application for Water Purification. *Carbon.* **2013**, *62*, 465–471.

(3) Gopakumar, D. A.; Pasquini, D.; Henrique, M. A.; De Morais, L. C.; Grohens, Y.; Thomas, S. Meldrum's Acid Modified Cellulose Nanofiber-Based Polyvinylidene Fluoride Microfiltration Membrane for Dye Water Treatment and Nanoparticle Removal. *ACS Sustain. Chem. Eng.* **2017**, *5* (2), 2026–2033.

(4) Guo, J.; Zhang, Q.; Cai, Z.; Zhao, K. Preparation and Dye Filtration Property of Electrospun Polyhydroxybutyrate–Calcium Alginate/Carbon Nanotubes Composite Nanofibrous Filtration Membrane. *Sep. Purif. Technol.* **2016**, *161*, 69–79.

(5) Verma, M.; Tyagi, I.; Kumar, V.; Goel, S.; Vaya, D.; Kim, H. Fabrication of GO–MnO_2 Nanocomposite Using Hydrothermal Process for Cationic and Anionic Dyes Adsorption: Kinetics, Isotherm, and Reusability. *J. Environ. Chem. Eng.* **2021**, *9* (5), 106045.

(6) Naushad, M.; Alqadami, A. A.; AlOthman, Z. A.; Alsohaimi, I. H.; Algamdi, M. S.; Aldawsari, A. M. Adsorption Kinetics, Isotherm and Reusability Studies for the Removal of Cationic Dye from Aqueous Medium Using Arginine Modified Activated Carbon. *J. Mol. Liq.* **2019**, *293*, 111442.

Appendix E

Supplementary Information for Chapter 5

Layered Double Hydroxide - Bismuth Molybdate Hybrids toward Water Remediation via Selective Adsorption of Anionic Species

Supporting Information

Layered Double Hydroxide - Bismuth Molybdate Hybrids toward Water Remediation via Selective Adsorption of Anionic Species

Sanjay Jatav,[*†] Marcel Herber,[†] Hongxiao Xiang,[†] Eric H. Hill[*†‡]

[†]Institute of Physical Chemistry, University of Hamburg, Grindelallee 117, 20146 Hamburg, Germany

[‡]The Hamburg Centre for Ultrafast Imaging (CUI), Luruper Chausee 149, 22761 Hamburg, Germany

*corresponding authors: eric.hill@chemie.uni-hamburg.de, sanjay.jatav@chemie.uni-hamburg.de

Table S1. Sample names and reaction pH

Sample name	pH
BMO	2.4
CAB-0.1x	6.4
CAB-0.2x	6.3
CAB-0.5x	3.7
CAB-1x	2.8

Table S2. Amount of BMO in composites

Sample	Max. BMO content (%)
CAB-0.1x	9.01
CAB-0.2x	16.37
CAB-0.5x	33.11
CAB-1x	49.75

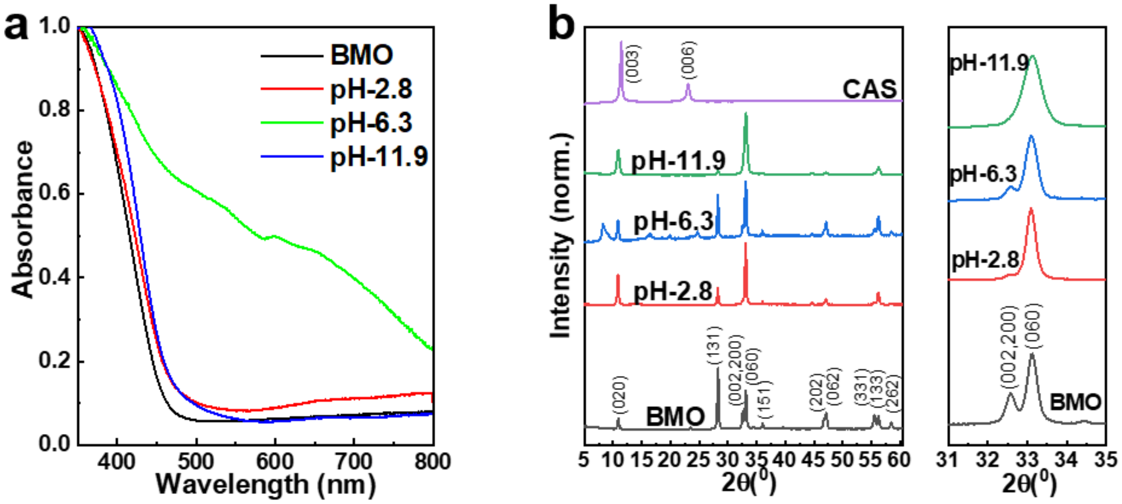

Figure S1: (a) Normalized UV-vis spectra, (b) X-ray diffractograms of the of CAB-1x prepared at different pH.

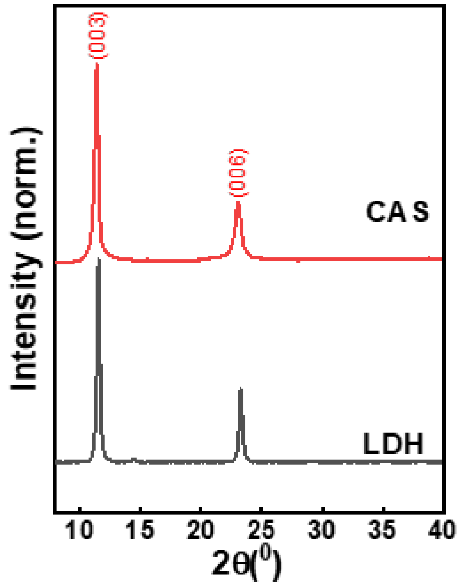

Figure S2: X-ray diffractograms of LDH and SDS-pillared LDH.

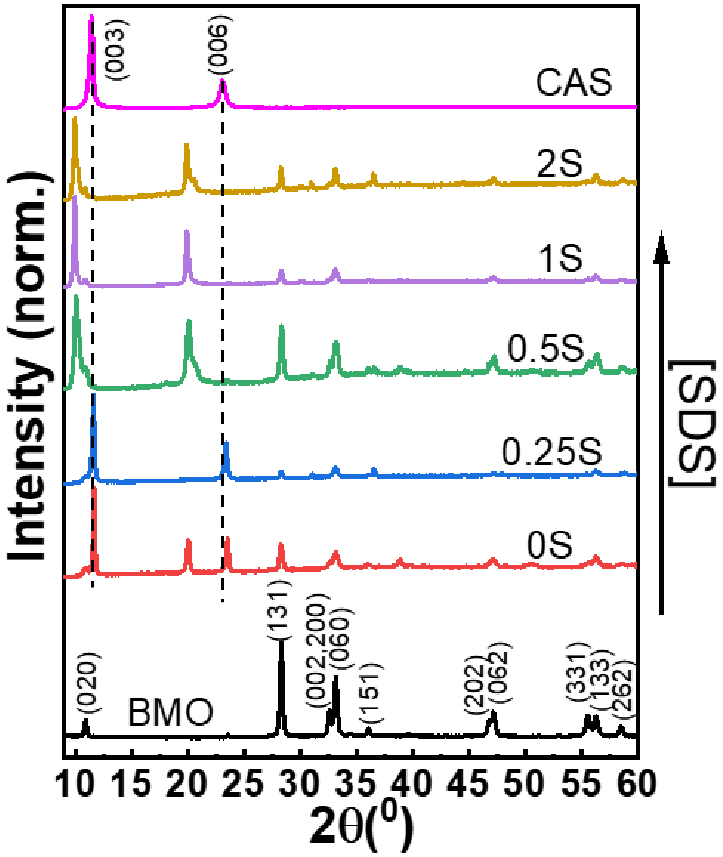

Figure S3: X-ray diffractograms of the of CAB-0.2x samples prepared at different [SDS].

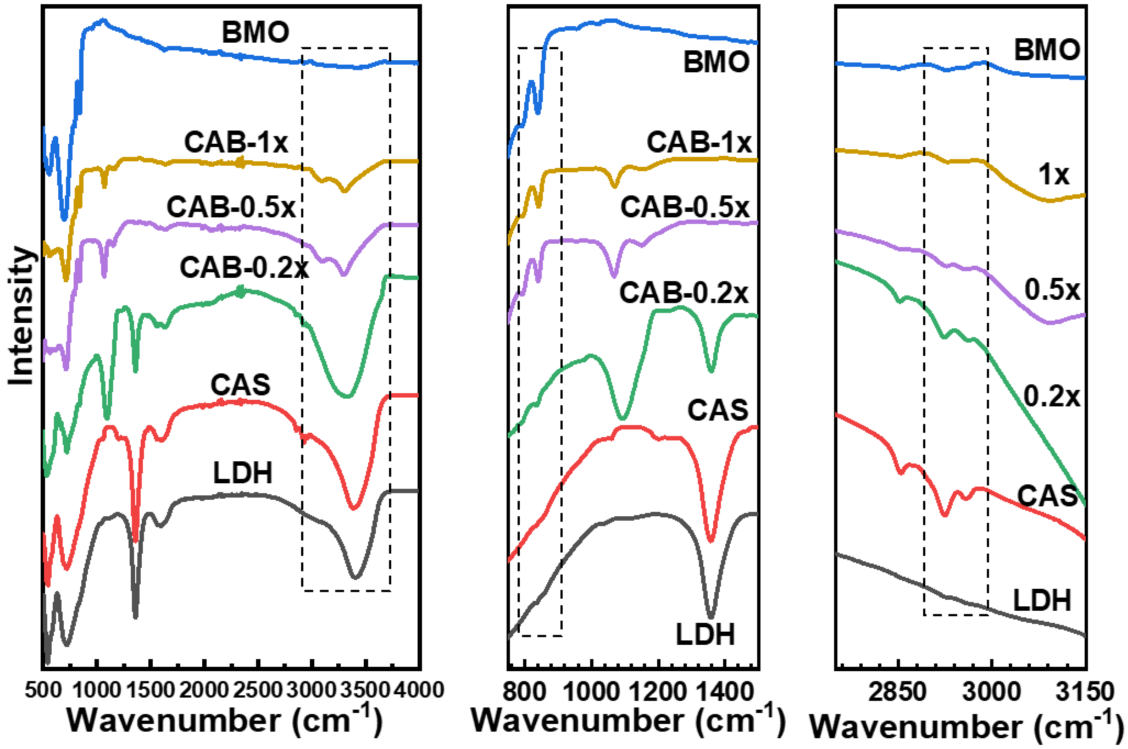

Figure S4: FTIR spectra of the CoAl-BMO samples prepared at different [Bi/Mo] precursor.

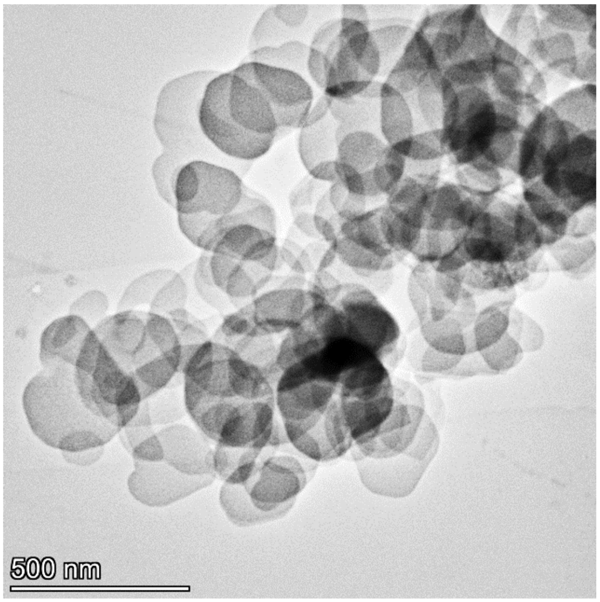

Figure S5: TEM image of the CoAl LDH.

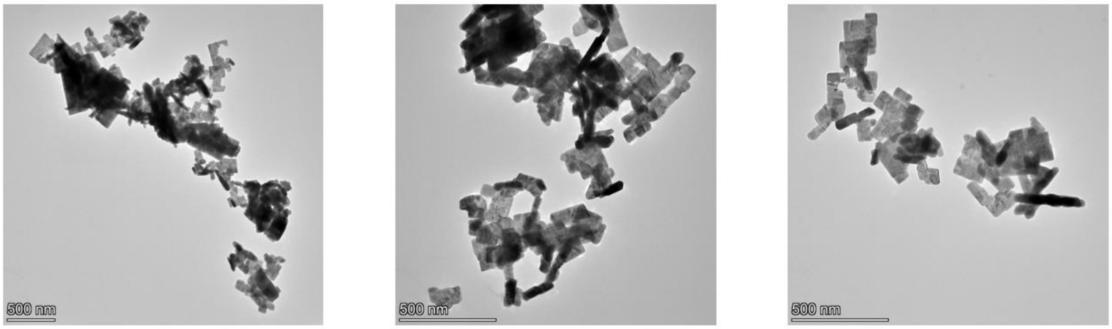

Figure S6: TEM images of the BMO control.

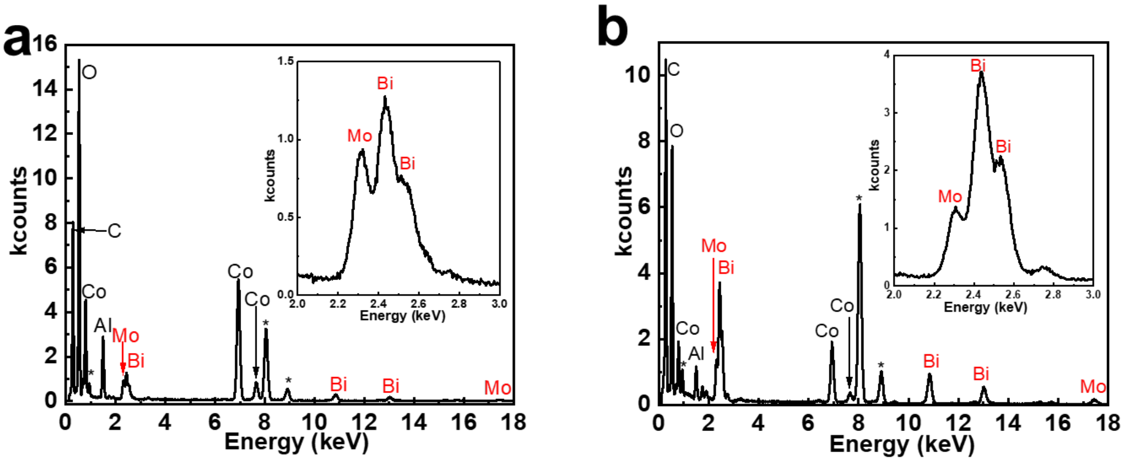

Figure S7: EDX spectra of the HAADF-STEM mapping shown in **Figure 3** (a) top panel, (b) bottom panel. * refers to the peaks due to Cu.

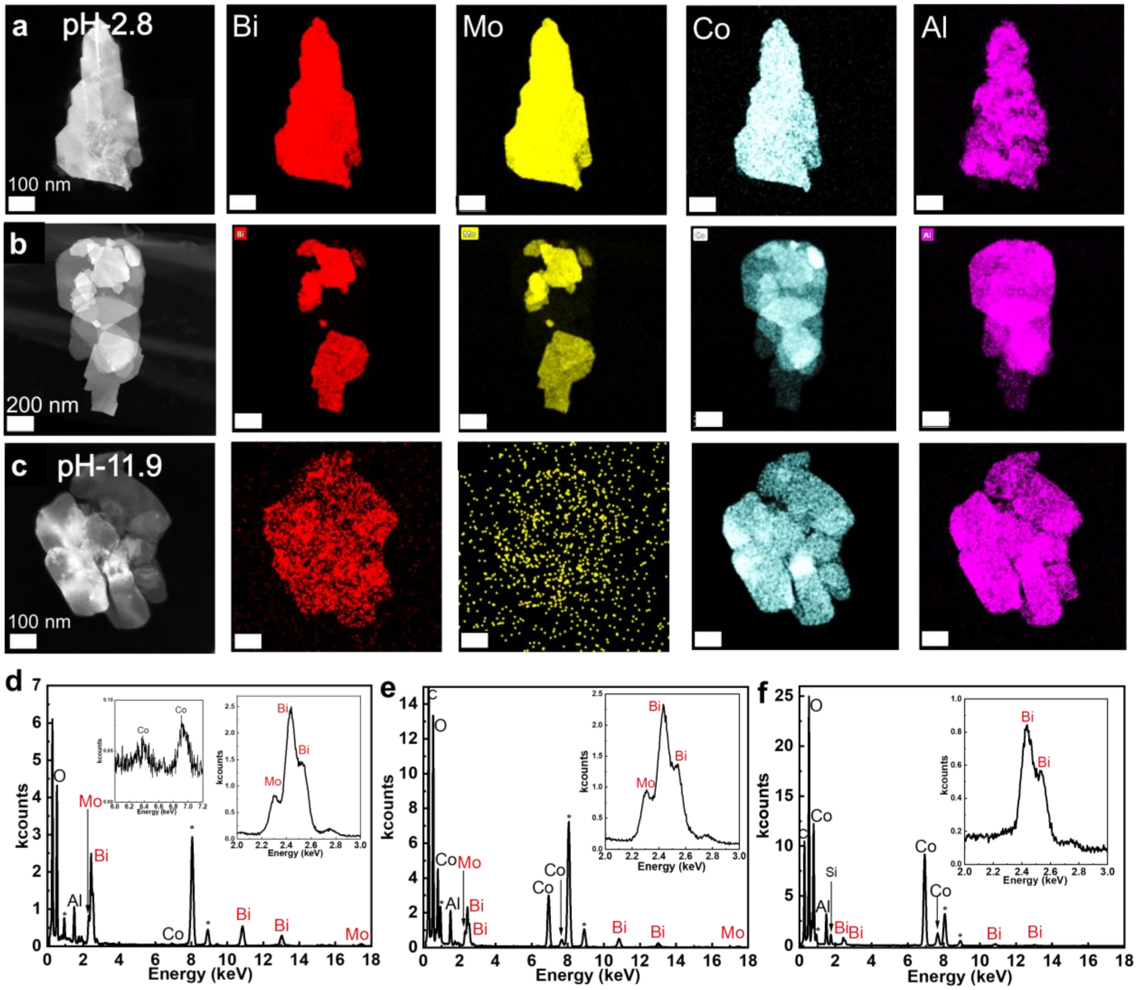

Figure S8: HAADF-STEM mappings of samples CAB-0.2x samples prepared at pH of (a, b) 2.8, (c) 11.9. and corresponding EDX spectra (d) of (a), (e) of (b), and (f) of (c). * refers to the peaks due to Cu.

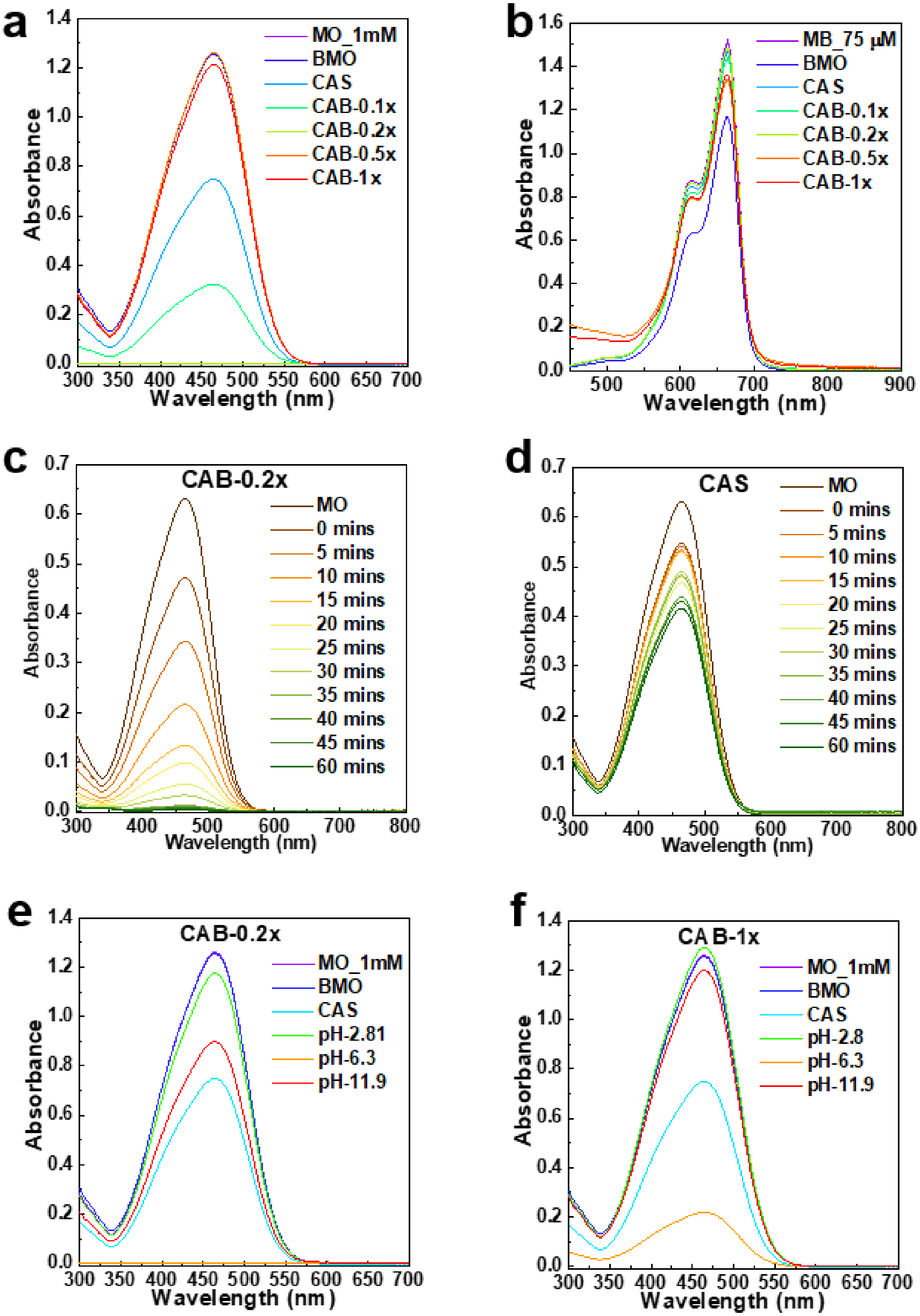

Figure S9: (a-b) UV-vis spectra of the samples shown in **Figure 4b, c**. (c-d) UV-vis spectra from the adsorption kinetics experiment (**Figure 4d**). (e-f) UV-vis spectra of the samples shown in **Figure 4e**.

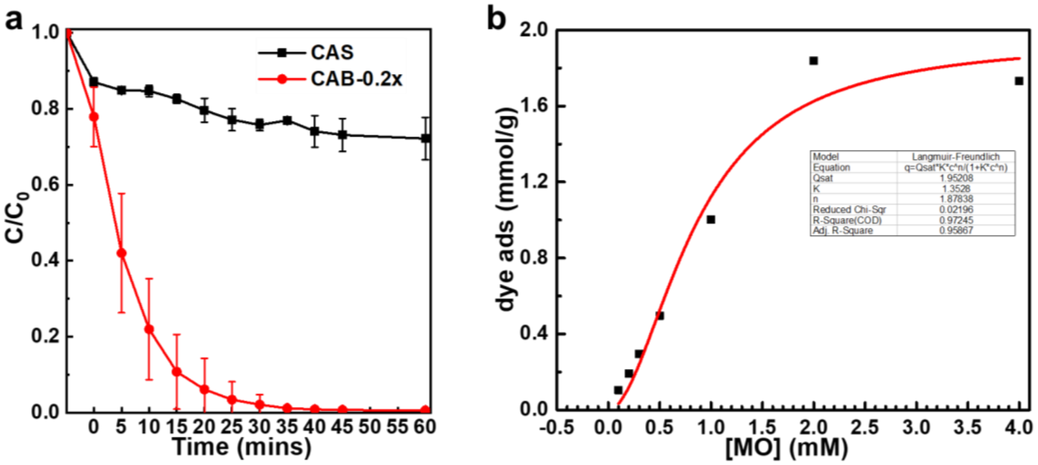

Figure S10: (a) Kinetics of methyl orange adsorption, [MO] = 250 µM; (b) Adsorption isotherm, [CAB-0.2x] = 1 mg/mL.

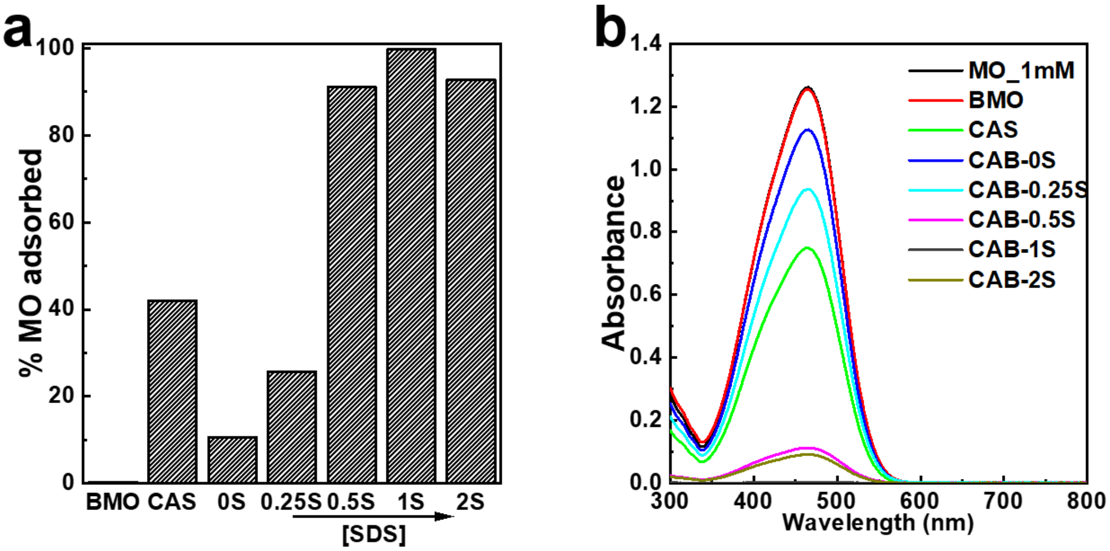

Figure S11: (a) MO removal and (b) UV-vis spectra of the samples prepared at different [SDS].

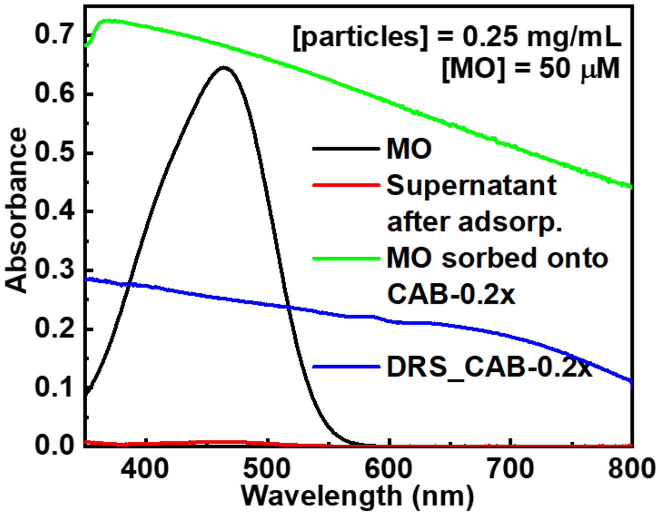

Figure S12: UV-vis spectra before and after MO adsorption on CAB-0.2x. Diffuse reflectance spectrum (DRS) of CAB-0.2x is shown in blue.

Table S3: Comparison of adsorption capacity with other materials

Material	Model Pollutant	Charge	Dye adsorbed (mmol/g)	Dye adsorbed (mmol/ m^2)	Ref.
CoAl w/ SDS	**MO**	**Anionic**	**0.42**	**0.009**	**This work**
CAB-0.2x	**MO**	**Anionic**	**1.95**	**0.096**	**This work**
Flower-like hollow CoAl	MO	Anionic	6.69	0.049	1
Flower-like solid CoAl	MO	Anionic	6.04	0.019	1
CoAl platelet	MO	Anionic	3.72	0.216	1
CoAl w/ Cl$^-$	MO	Anionic	2.45	0.123	2
CoAl	Eriochrome Black T	Anionic	0.91	0.022	3
MgAl	”	Anionic	1.17	0.017	3
Surface Modified Laponite-BMO	MB	Cationic	0.19	0.003	4
Ti_3C_2Tx	MB	Cationic	0.13	0.014	5
Activated carbon	MB	Cationic	0.17	-	5
GO-MnO_2	MB	Cationic	0.55	0.021	6
Arginine- activated carbon	MB	Cationic	0.69	-	7
MOF-235	MO	Anionic	1.46	-	8
Porous Ionic Polymer	MO	Anionic	2.98	-	9

References

(1) Gao, H.; Cao, R.; Xu, X.; Xue, J.; Zhang, S.; Hayat, T.; Alharbi, N. S.; Li, J. Surface Area- and Structure-Dependent Effects of LDH for Highly Efficient Dye Removal. *ACS Sustain. Chem. Eng.* **2019**, *7* (1), 905–915.

(2) Chen, Y.; Jing, C.; Zhang, X.; Jiang, D.; Liu, X.; Dong, B.; Feng, L.; Li, S.; Zhang, Y. Acid-Salt Treated CoAl Layered Double Hydroxide Nanosheets with Enhanced Adsorption Capacity of Methyl Orange Dye. *J. Colloid Interface Sci.* **2019**, *548*, 100–109.

(3) Zubair, M.; Jarrah, N.; Manzar, M. S.; Al-Harthi, M.; Daud, M.; Mu'azu, N. D.; Haladu, S. A. Adsorption of Eriochrome Black T from Aqueous Phase on MgAl-, CoAl- and NiFe- Calcined Layered Double Hydroxides: Kinetic, Equilibrium and Thermodynamic Studies. *J. Mol. Liq.* **2017**, *230*, 344–352.

(4) Jatav, S.; Herber, M.; Xiang, H.; Hill, E. H. Surface-Encapsulated Bismuth Molybdate-Layered Silicate Hybrids as Sorbents for Photocatalytic Filtration Membranes. *ACS Appl. Mater. Interfaces* **2022**, *14* (20), 22790–22798.

(5) Kim, S.; Yu, M.; Yoon, Y. Fouling and Retention Mechanisms of Selected Cationic and Anionic Dyes in a $Ti_3C_2T_x$ MXene-Ultrafiltration Hybrid System. *ACS Appl. Mater. Interfaces* **2020**, *12* (14), 16557–16565.

(6) Verma, M.; Tyagi, I.; Kumar, V.; Goel, S.; Vaya, D.; Kim, H. Fabrication of GO–MnO_2 Nanocomposite Using Hydrothermal Process for Cationic and Anionic Dyes Adsorption: Kinetics, Isotherm, and Reusability. *J. Environ. Chem. Eng.* **2021**, *9* (5), 106045.

(7) Naushad, M.; Alqadami, A. A.; AlOthman, Z. A.; Alsohaimi, I. H.; Algamdi, M. S.; Aldawsari, A. M. Adsorption Kinetics, Isotherm and Reusability Studies for the Removal of Cationic Dye from Aqueous Medium Using Arginine Modified Activated Carbon. *J. Mol. Liq.* **2019**, *293*, 111442.

(8) Haque, E.; Jun, J. W.; Jhung, S. H. Adsorptive Removal of Methyl Orange and Methylene Blue from Aqueous Solution with a Metal-Organic Framework Material, Iron Terephthalate (MOF-235). *J. Hazard. Mater.* **2011**, *185* (1), 507–511.

(9) Yang, S.; Hou, Y.; Xiong, S.; Chen, F.; Jiang, Y.; Pan, C.; Tang, J.; Yu, G. Processable Hypercrosslinked Ionic Networks for Effective Removal of Methyl Orange. *Sep. Purif. Technol.* **2021**, *258*, 117986.

Appendix F

Supplementary Information for Chapter 6

In_2S_3 Growth Templated by Imogolite towards Efficient Visible Light Photocatalysts

Supporting Information

In$_2$S$_3$ Growth Templated by Aluminogermanate Double-Walled Imogolite Nanotubes towards Efficient Visible Light Photocatalysts

Sanjay Jatav, Hongxiao Xiang, Marcel Herber, Erwan Paineau, and Eric H. Hill**

S. Jatav, H. Xiang, M. Herber, E. H. Hill
Institute of Physical Chemistry, University of Hamburg, 20146 Hamburg, Germany
E-mail: eric.hill@chemie.uni-hamburg.de

E. Paineau
Université Paris-Saclay, CNRS, Laboratoire de Physique des Solides, 91405 Orsay, France
E-mail: erwan-nicolas.paineau@universite-paris-saclay.fr

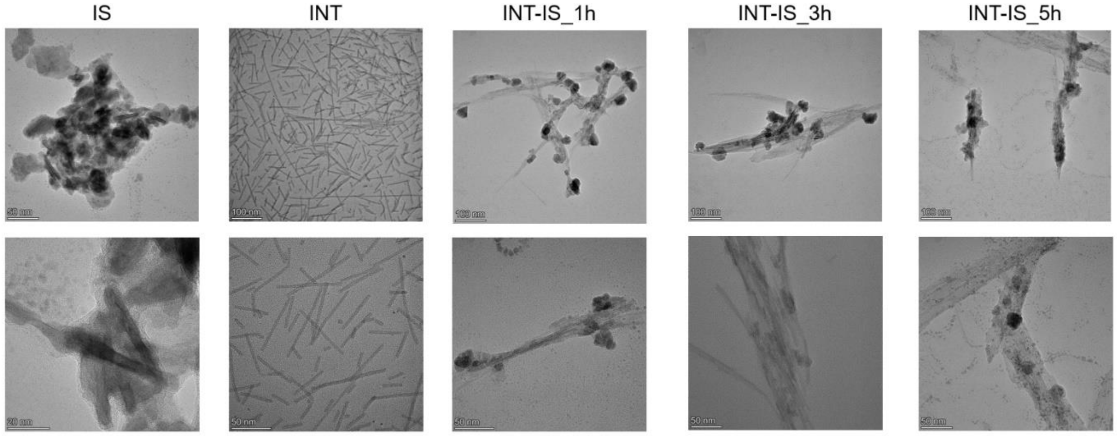

Figure S1. Additional TEM images of the samples.

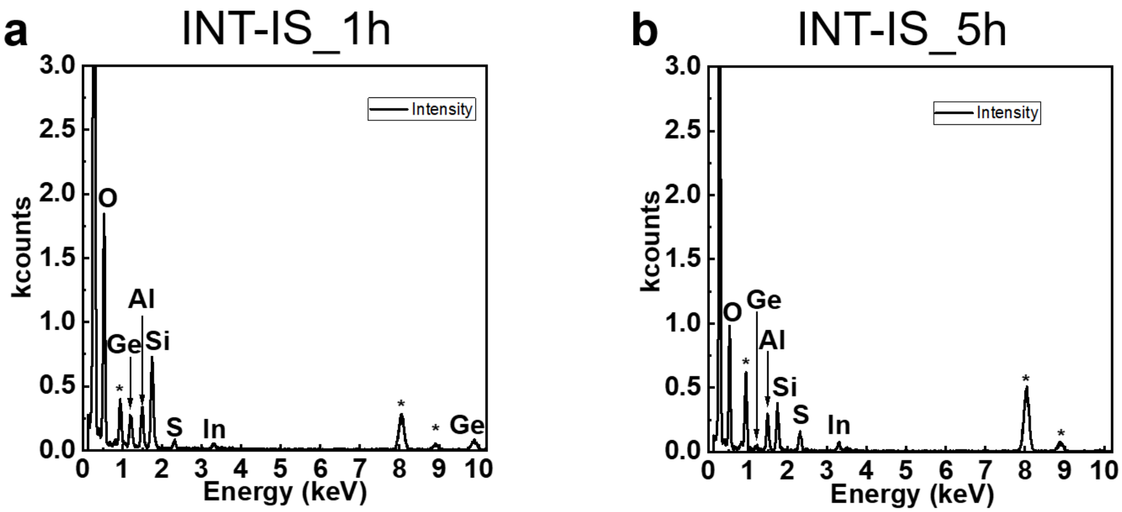

Figure S2. EDX spectra of the HAADF-STEM mappings corresponding to (a) Figure 3(a); (b) Figure 3(b).

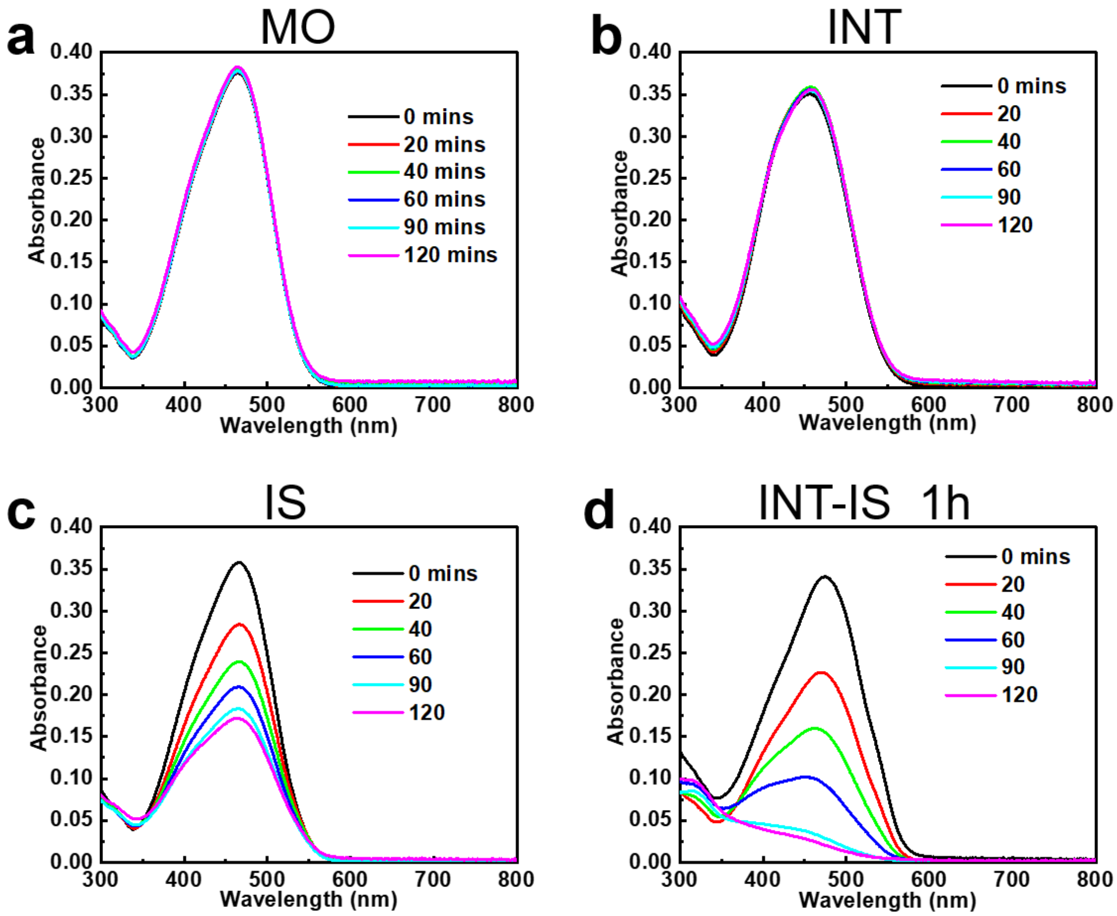

Figure S3. UV-vis spectra from photocatalytic dye degradation experiments shown in **Figure 4a**. (a) Methyl orange (b) INT control (c) IS control and (d) INT-IS_1h.

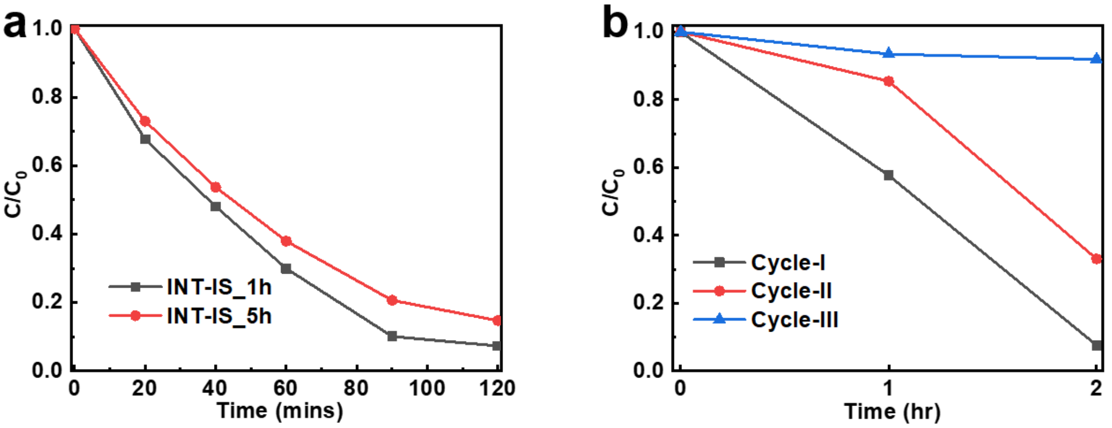

Figure S4. (a) Photocatalytic degradation of MO (b) Photocatalytic recycling of INT-IS_1h. [MO] = 15.25 µM, [particles] = 0.25 mg/mL.

ACKNOWLEDGEMENTS

Just like how the plan of a building is conceived first in the mind of an architect prior to it's construction, the architect for the work presented in this thesis has been my advisor, Dr. Eric H. Hill at the Institute of Physical Chemistry, University of Hamburg (UHH). Ergo, my first and infinite debt is to Eric, who gave me the chance to work with him. I am also deeply grateful to him for his valuable guidance, constant support and critical commentary which helped me immensely in my research journey and inculcated in me scientific rigor.

I express my deep gratitude to Prof. Alf Mews at the Institute of Physical Chemistry, University of Hamburg for agreeing to be my co-advisor and allowing me to use facilities at his disposal. Also, I convey my heartfelt thanks to him for raising critical points and asking pertinent and puzzling questions during my presentations. These made me reflect critically on my work and helped to make the work more thorough.

Dr. Erwan Paineau from CNRS, Paris, France provided us with the Imogolite nanotubes whenever we needed them. I am very grateful to Erwan for his cordiality and also the exchange opportunity. This made me appreciate X-ray scattering techniques even more.

One of the primary reasons for taking-up academic research was the inspiration I drew from my teachers during my undergraduate studies at IIT-Madras. I am beholden to them because my life prospects would've been very different if not worse, had our paths never intersected. Deserving a particular mention is Prof. Ratnakumar Annabatula at the Department of Mechanical Engineering, who tended to my curiosity regarding the subject matter of materials science and guided me during my formative years. Along the same vein, I express my most heartfelt gratitude to Prof. Dillip K. Satapathy at the Department of Physics, for allowing me to work with him, offering me opportunities when I had none and always motivating me to give my best.

Since a work like this can not be done without the support of others, deserving a particular mention are the Hill-people, both former and present, namely, Junying, Swaathini, Marcel, Hongxiao, Benedetta, Kai, Swetanshu, Patrick, Silvano and Christian who with their cordiality and friendliness (and delectable cuisines) created the ideal atmosphere that made possible the accomplishments of this enterprise.

During the course of my dissertation at UHH I got to work very closely with the Mews group. I would like to give a shout out to them for helping out and providing support that we dearly needed to make things sail smoothly. I would especially like to single out Dr. Charlotte Ruhmlieb for her sage advises and helping us out when we had just moved to UHH. I would also like to thank Felix, Roman, Moritz, Florian, Mareike, Jannic, Sebastian, Daniel, Thomas and Maria for always being helpful whenever it was needed.

The work presented herein would've been incomplete without the assistance of the central facilities at the Institute; hence, I would like to offer a special thanks to Stefan Werner at the electron microscopy and Nina Schober at the X-ray diffraction facilities for ploughing through the samples thrown at them. Without those measurements this work would not bear the sheen that it bears now.

Early part of the work presented herein was accomplished at Hamburg University of Technology (TUHH). Since, we were working out of the Institute of Advanced Ceramics at TUHH, I would like to thank Prof. Gerold Schneider for hosting us and his group for their cordiality and the useful discussions. I was very lucky to share the workspace with Sandra, Gregor, Kai and Wernfreid. I also enjoyed the company of Busra, Jasmine, Yen, Benedickt. Due to the assistance of Anja and Manfred many things were able to go along smoothly.

Transmission electron microscopy (TEM) was critical to the investigations carried out in this thesis and a large part of it was done at the Electron Microscopy Unit (BEEM) at TUHH. Here I would especially like to single out Dr. Surya Snata Rout and Dr. Tobias Krekeler who were my closest helpmates when things became way out of whack for me. I am also very thankful to Prof. Manfred Eich at the Institute of Optical Materials, TUHH for providing access to the photoelectrochemical setup and Dr. Fatemeh Ebrahimi for sharing her insights of electrochemistry.

This thesis was completed during the COVID-19 pandemic and as a result home became more distant a place than I'd imagined. My days here were made bearable at worst and enjoyable at best due to the company of amazing people, who became my friends here in Hamburg. I would like to convey my most heartfelt gratitude to Mohammad, Rafael, Ilka, Paul, Nathan, Eoin, Armin, Diego, Fran, Ribas, Kaline, Diletta, Berta, Pia, Thorsten, Nikola, Matz, Tina, Jan, Dianna, Alex, Cristina and Vincent for befriending me, sharing food and laughter with me, and most importantly, taking good care

of me. I'll be forever indebted to you all for allowing an outsider like myself to become a part of your life.

Though I had to move away from home for my PhD, fortunately, I was still able keep in touch with my friends. I would like to express my deepest gratitude to Purab, Shreyas, Vipul, Tarun, Mohit and Vishal. Though our friendship was stretched through the space, despite of becoming leaner, our bonds grew deeper and stronger. Also during this while I was fortuitously able to reconnect with my school friends Prerna, Prabh and Arnesh here in Europe and would like to thank them for always taking time out for me whenever I wanted to see them.

Last but not the least without the support of my sisters Shweta and Swati and my parents none of this would have materialized. I would like to thank them for their patience, support, goodwill and immense blessings.

DECLARATION

,,I hereby declare on oath that this doctoral dissertation is written independently and solely by my own based on the original work of my PhD and has not used any other than the acknowledged resources and aids."

Date, Signature